

International Transactions on Electrical Energy Systems

Power Quality Improvement Techniques in Renewable Energy Integrated Microgrid Systems

Lead Guest Editor: Albert Alexander

Guest Editors: Umashankar Subramaniam and Ravi Samikannu





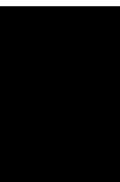
Power Quality Improvement Techniques in Renewable Energy Integrated Microgrid Systems

International Transactions on Electrical Energy Systems

**Power Quality Improvement
Techniques in Renewable Energy
Integrated Microgrid Systems**

Lead Guest Editor: Albert Alexander

Guest Editors: Umashankar Subramaniam and Ravi
Samikannu



Copyright © 2023 Hindawi Limited. All rights reserved.

This is a special issue published in "International Transactions on Electrical Energy Systems." All articles are open access articles distributed under the Creative Commons Attribution License, which permits unrestricted use, distribution, and reproduction in any medium, provided the original work is properly cited.

Associate Editors

Chitti Babu Baladhandautham , India
Antonio Bracale , Italy
Tomislav Capuder , Croatia
Chia Chi Chu , Taiwan
Gilsoo Jang , Republic of Korea
Dusmanta K. Mohanta , India
Daniela Proto, Italy
Ahmet Mete Vural , Turkey







Academic Editors

JAGABAR SATHIK M MOHAMED ALI,
India
Sobhy M. Abdelkader, United Kingdom
Johny Renoald Albert , India
Rodolfo Araneo, Italy
Enrique Rosales Asensio, Spain
Faroque Azam, India
Hamed Badihi , Finland
Ajay Kumar Bansal , India
Ajay Kumar Bansal, India
Ramesh Chand Bansal , Australia
Yukun Bao , China
Prasenjit Basak , India
Dr. CH Hussaian Basha, India
Youcef Belkhier, France
Jaouher Ben Ali, Tunisia
Sujin Bureerat , Thailand
Dhanamjayulu C , India
Murthy Cherukuri , India
Paulo Costa , Portugal
Michele De Santis , Italy
Mouloud Azzedine Denai , United Kingdom
Harsh Dhiman , India
Sheng Du , China
Youssef Errami , Morocco
Davide Falabretti , Italy
Salvatore Favuzza , Italy
Aymen Fлах , Tunisia
Ci-Wei Gao , China
Samuele Grillo , Italy


Yueshi Guan, China
Zhitao Guan, China
Nitin K. Gupta , India
Reza Jalilzadeh Hamidi, USA
Santoshkumar Hampannavar , India
Tianqi Hong , USA
Wei-tzer Huang , Taiwan
Kyeon Hur, Republic of Korea
Kamran Iqbal , USA
Hamed Jafari Kaleybar, Italy
Jyotheeswara Reddy Kalvakurthi, India
Kangli Liu, China
Shaofeng Lu , China
Ibrahim Mahariq, Kuwait
Anjaneer Kumar Mishra , India
Manohar Mishra, India
Adel Oubelaid, Algeria
Dr. Narendra Babu P , India
Gayadhar Panda, India
Dr. N. Prabakaran , India
Santi A. Rizzo, Italy
Julio Rosas-Caro , Mexico
Mohammad Sadi , USA
Akshay Kumar Saha , South Africa
Lalit Chandra Saikia , India
Irfan Sami, Republic of Korea
Subrata kumar Sarker, Bangladesh
Gulshan Sharma , South Africa
Pawan Sharma, Norway
Yiming Shen , China
Dr. Arvind R. Singh , South Africa
Sudhakar babu T , India
Shafaat Ullah, Pakistan
Jesus Valdez-Resendiz , Mexico
Kusum Verma , India
Yu-Chi Wu , Taiwan
Rui Yao, China

Contents




Intelligent Controller Design and Fault Prediction Using Machine Learning Model

Kailash Kumar , Suyog Vinayak Pande , T. Ch. Anil Kumar, Parvesh Saini , Abhay Chaturvedi ,
Pundru Chandra Shaker Reddy , and Krishna Bikram Shah 
Research Article (9 pages), Article ID 1056387, Volume 2023 (2023)






PV Based Standalone DC -Micro Grid System for EV Charging Station with New GWO-ANFIS MPPTs under Partial Shading Conditions

R. Ragul, N. Shanmugasundaram, Mariaraja Paramasivam, Suresh Seetharaman, and Sheela L. Mary Immaculate 
Research Article (14 pages), Article ID 2073742, Volume 2023 (2023)





Analysis and Implementation of Sliding Mode Controller-Based Variable Frequency Drive Using the SCADA System

Belqasem Aljafari , L. Ashok Kumar, V. Indragandhi , and V. Subramaniaswamy 
Research Article (16 pages), Article ID 7194119, Volume 2022 (2022)



A Grid-Connected Solar PV/Wind Turbine Based Hybrid Energy System Using ANFIS Controller for Hybrid Series Active Power Filter to Improve the Power Quality

Pazhanimuthu Cholamuthu, Baranilingesan Irusappan, Suresh Kalichikadu Paramasivam , Senthil Kumar Ramu , Suresh Muthusamy , Hitesh Panchal, Ramakrishna S S Nuvvula , Polamarasetty P Kumar, and Baseem Khan 
Research Article (14 pages), Article ID 9374638, Volume 2022 (2022)



Prophetic Energy Assessment with Smart Implements in Hydroelectricity Entities Using Artificial Intelligence Algorithm

Abdullah Saleh Alqahtani, Pravin R. Kshirsagar , Hariprasath Manoharan , Praveen Kumar Balachandran , C. K. Yogesh, and Shitharth Selvarajan 
Research Article (12 pages), Article ID 2376353, Volume 2022 (2022)





An Innovative Solution for Battery Draining in 5G Devices Using Alternate Routing Model

M. Sivasubramanian, J. Vignesh, V. Senthil kumar, S. Sumathi, R. Sathish, Kumar Parasuraman, B Santhosh Kumar, M Kathirvelu, Leena Bojaraj, Srihari K , and Negasi Tsegay Sbhat 
Research Article (8 pages), Article ID 8924801, Volume 2022 (2022)







Environmental Fault Diagnosis of Solar Panels Using Solar Thermal Images in Multiple Convolutional Neural Networks

Tamilselvi Selvaraj, Ramasubbu Rengaraj, GiriRajanbabu Venkatakrishnan, SoundhariaGanesan Soundararajan, Karuppiiah Natarajan, PraveenKumar Balachandran , PrinceWinston David, and Shitharth Selvarajan 
Research Article (16 pages), Article ID 2872925, Volume 2022 (2022)

A Review on Potential Opportunities to Preheat the Batteries Using a Finned Solar Air Energizer to Enhance Power Quality and Thermal Management in Low-Temperature Surroundings





P. K. Dhal, J. Uma, Piyush Gaur, D. Prasad, Melvin Victor Depoures , A. Rajkumar, M. Ramesh , Praveen Bhai Patel , and Habtewolde Ababu Birhanu 
Review Article (11 pages), Article ID 6276789, Volume 2022 (2022)

Integrating Industrial Appliances for Security Enhancement in Data Point Using SCADA Networks with Learning Algorithm

Alaa O. Khadidos , Adil O. Khadidos , Hariprasath Manoharan , Khaled H. Alyoubi , Abdulrhman M. Alshareef , and Shitharth Selvarajan 




Research Article (11 pages), Article ID 8685235, Volume 2022 (2022)

Diagnosis of Broken Bars in V/F Control Induction Motor Drive Using Wavelets and EEV Estimation for Electric Vehicle Applications

Senthil Kumar Ramu , Gerald Christopher Raj Irudayaraj, Gunapriya Devarajan , V. Indragandhi, V. Subramaniaswamy , and J. Sam Alaric 

Research Article (13 pages), Article ID 9474640, Volume 2022 (2022)

A Modified Seven-Level Inverter with Inverted Sine Wave Carrier for PWM Control

Arun Vijayakumar , Albert Alexander Stonier , Geno Peter , Praghash Kumaresan , and Elenor M. Reyes

Research Article (12 pages), Article ID 7403079, Volume 2022 (2022)

Research Article

Intelligent Controller Design and Fault Prediction Using Machine Learning Model

Kailash Kumar ¹, **Suyog Vinayak Pande** ², **T. Ch. Anil Kumar**,³ **Parvesh Saini** ⁴,
Abhay Chaturvedi ⁵, **Pundru Chandra Shaker Reddy** ⁶, and **Krishna Bikram Shah** ⁷

¹College of Computing and Informatics, Saudi Electronic University, Riyadh 11673, Saudi Arabia

²Department of Electronics and Telecommunication Engineering,

Mukesh Patel School of Technology Management and Engineering, Shirpur Campus, Shirpur, Maharashtra, India

³Department of Mechanical Engineering, Vignan's Foundation for Science Technology and Research, Vadlamudi, Guntur, Andhra Pradesh 522213, India

⁴Electrical Engineering, Graphic Era Deemed to Be University, Dehradun, India

⁵Department of Electronics and Communication Engineering, GLA University, Mathura 281406, Uttar Pradesh, India

⁶Department of Computer Science and Engineering, Geethanjali College of Engineering and Technology, Hyderabad, Telangana, India

⁷Department of Computer Science and Engineering, Nepal Engineering College, Changunarayan, Bhaktapur, Nepal

Correspondence should be addressed to Kailash Kumar; kk9844456@gmail.com and Krishna Bikram Shah; krishnabs@nec.edu.np

Received 9 September 2022; Revised 14 October 2022; Accepted 24 November 2022; Published 29 April 2023

Academic Editor: Ravi Samikannu

Copyright © 2023 Kailash Kumar et al. This is an open access article distributed under the Creative Commons Attribution License, which permits unrestricted use, distribution, and reproduction in any medium, provided the original work is properly cited.

In a solar power plant, a solid phase transformer and an optimization coordinated controller are utilized to improve transient responsiveness. Transient stability issues in a contemporary electrical power system represent one of the difficult tasks for an electrical engineer due to the rise in uncertain renewable energy sources (RESs) as a result of the need for green energy. The potential for terminal voltage to be adversely impacted by this greater RES raises the possibility of electrical device damage. It is possible to use a solid state transformer (SST) or smart transformer to address a transient response issue. These devices are frequently employed to interact between RES and a power grid. SST features a variety of regulated converters to maintain the necessary voltage levels. This method can therefore simultaneously lessen power fluctuations and transient responsiveness. In order to improve the quality of RES power injections and the electrical system's transient stability, this work provides a controller design for a solar photovoltaic (SPV) system that is connected to the grid by SST. The optimization of a controller model is proposed by modifying a PI controller taken from a commercial one. With the use of IEEE 39 standard buses, the proposed controller is tested. When evaluating the effectiveness of a suggested controller, it is important to take into account a variety of solar radiation patterns as well as a time delay uncertainty that can range from 425 ms to 525 ms. According to simulation results, the proposed controller can be employed to lessen power fluctuation brought on by unpredictable RES. Additionally, the proposed coordinated regulation of SPV and SST can prevent catastrophic damage in the event of substantial disturbances like a circuit breaker collapsing to expand a power line due to a fault by inhibiting significant voltage cycles within an electronic appliance's rated voltage limit. The results indicate that a transitory stability issue in a modern power system caused by an unforeseen increase in RES may be addressed utilizing the suggested controllers as alternatives.

1. Introduction

Owing to the fact that wind energy is one of the most promising renewable energy sources in the world, it is predicted that wind generation systems will offer ample

electricity and have good grid integration [1, 2]. In order to obtain a more stable operation of the controller and increase system efficiency, wind power production systems need more sophisticated, unique, and robust control methodologies. Large amounts of pure, sustainable energy are

produced when energy is extracted from water. But so far, only 30% of this energy has been created [3–5]. In comparison to other renewable energy sources, hydropower and especially hydropower facilities are more cost-effective, run more effectively, and are environmentally friendly. Hydropower plants are highly automated and cost-effective to run. To preserve the caliber and dependability of the power source, the major components of the power system must be regularly monitored and safeguarded. The data gathering, monitoring, and protection system handles this responsibility. Turbines need to be safeguarded from abnormal situations as well as short circuits. A failure is a long-term disruption of a system's capacity to fulfil the needed function under certain operational conditions [6, 7]. A defect is an unpermitted deviation of at least one characteristic or characteristic attribute of the system from the accepted or conventional state [8–10].

An enormous amount of prior data (usually more than 100,000 items) is needed to train the decision model, which is a common challenge for machine learning algorithms. This size requires the controller to have robust storage capabilities as well as strong computational capabilities. In a real network, a variety of devices work together to determine if a node is accessible. The controller will have a very significant burden if it monitors and forecasts the state of every piece of equipment on that scale. Selecting a machine learning technique that can train a highly accurate model using less data is essential. At a data amount of less than 5,000, the SVM method has a high efficiency and excellent accuracy, making it ideal for use in real applications.

Since some flaws might cause system failure if they occur frequently, early fault identification is crucial for maintaining system functionality for a long time.

The two main divisions of fault detection techniques are model-based approaches and signal processing-based (feature-based) methods. Model-based techniques are built on the foundations of system modeling and model evaluation. In order to extract information about issues, mathematical or statistical operations are carried out in signal processing-based methods or artificial intelligence (AI) approaches are utilized to appropriately handle signal features. Feature-based methods are more suited for remote monitoring since sensor data may be sent to the processing facility via a number of methods and give in situ observations.

To develop a reliable fault detection algorithm using feature-based approaches, information identifying the state of each observed element is necessary. These facts are gathered via a variety of sensor data. A few examples of the signals that could be used are ultrasonic tests, vibrations, torque, stress, temperatures, electrical output, lubricating oil quality, and centralized management signals.

Research questions served as the basis for the study that is being presented here. They were designed to characterize the pertinent research in terms of publication sources and scientific areas while also examining the strengths and limitations of the most recent machine learning techniques for mechanical fault detection and fault prognosis in manufacturing equipment. Five

academic databases were searched for relevant papers, and after applying a set of criteria, the primary studies were chosen.

2. Literature Review

For a 1.5 MW doubly fed induction generator (DFIG) in a grid-connected wind energy conversion system (WECS), the authors in [11, 12] presented optimal design and tuning of fuzzy logic controllers (FLCs) using sophisticated methodologies like the particle swarm optimizer (PSO), the gray wolf optimization (GWO), the moth-flame optimizer (MFO), and the multi-verse optimizer (MVO). The grid-side converter, current regulator, and rotor-side converter of the back-to-back DFIG wind turbine all have FLC scaling factors that are optimized. It is suggested that a multi-objective optimization methodology be used to reduce the steady-state errors of these controllers in order to enhance the dynamic performance of the DFIG wind energy system when variable wind speed circumstances are present. The suggested optimized controller and PI controller are also compared, along with the various FLC optimization strategies employing PSO, GWO, MFO, and MVO. This study's key contribution is its suggestion of a novel control approach for a WECS based on DFIG. Utilizing PSO, GWO, MFO, and MVO algorithms to regulate the d-q element of the stator and rotor currents to manage the active and reactive power of the DFIG will maximize MIMO-FLC transformation matrix. In order to determine the behavior of the proposed controller in the event of a transformation from a low to a high gust, the proposed controller's operation is tested in variable wind speeds. By contrasting the various techniques, it is discovered that the MFO-FLC controller is the best optimized controller and exhibits excellent behavior in these conditions. For the next generation of energy systems, we suggest a revolutionary intelligent fault-tolerant adaptive control methodology in [13, 14]. Based on reliable fault-tolerant control, this design enhances local controllers coupled to energy systems, such as renewable energy-based power producers (FTC). For the monitoring and management of energy systems, this local controller works in conjunction with an area controller. A dual heuristic programming (DHP) action-critic neural network architecture along with a predictive identifier is created with this goal in mind. The area controller's major goal is to communicate with the local controller, supplement local controller, and share information about the grid state in accordance with an ideal control plan. To control reactive power management at the common point of coupling, the controller's effectiveness is tested on a wind-generating system's two-area power grid (CPP). Simulation experiments show that the suggested architecture is capable of enhancing the power grid's stabilization when there are renewable energy resources present. On Pulau Ubin island, an intelligent microgrid with a high proportion of clean and renewable energy resources was designed and put into operation to meet current and projected electrical demand. In the midst of heavily urbanized Singapore, Pulau Ubin is one of the few remaining pockets of "village" life that captures the character of

Singapore in its formative years. The system design has taken into account all potential energy sources, the effectiveness of energy conversion, power demand, and environmental and financial considerations. Electricity is produced using doubly fed induction generators that are fueled by photovoltaic (PV) cells and biodiesel. In order to maximize the utilization of renewable energy sources and to increase battery life, an energy storage system has been suitably sized. Smart grid technologies have been used to optimize energy production, monitor energy usage, handle instant energy flow, preserve electricity performance, and generate fault notifications. These technologies include smart meters, microgrid controllers, and remote monitoring systems with SCADA functions. This project also acts as a testing ground for sophisticated grid control technologies, clean and renewable energy generation, and storage under an intelligent microgrid architecture. The use of these smart grid characteristics to grid-connected microgrids has considerable promise. If this system is implemented successfully, it can serve as an example of sustainable development for many regions of Asia, where almost 40% of the population lacks access to power [15–20]. In this study, PowerFlexHouse, a research center for investigating the technical possibilities of active load control in a distributed power system with a high penetration of renewable energy, is introduced. A study of the software platform on which building controllers can be used is followed by a description of the facility based on a distributed power system (SYSLAB). Finally, this study demonstrates how to create a thermal model predictive controller for this distributed power system's power consumption estimation. Studies on how this intelligent house responds to a hybrid power grid can be done thanks to the PowerFlexHouse's control. With the help of our demand side control study, we intend to significantly increase grid dependability as well as energy efficiency and user power costs [16, 21–24]. Whenever the generator malfunctions and also the machine starts to function as a synchronous motor linked to the electricity grid, the original power source—the motor or turbine—is typically damaged. The proposed protection has been created to prevent this from happening. It becomes necessary to immediately identify these variables in this scenario because the generator turns into an active load, increasing the temperature and seriously damaging the main turbine. In order to prevent reverse power flow and maintain the quality and dependability of supply, this study suggests a novel controller for a neuro-fuzzy system. The fuzzy system network has drawn the attention of numerous scientists and engineers. The modification of the membership function as a reverse mechanism derived from the fuzzy logic controller is this work's novel characteristic. The smart grid is built on a network of smart meters. In this project, wireless sensor network-based Zigbee technology was used to construct smart grid meters. Due to its small battery and low power consumption, the Zigbee network of wireless sensors has more value than other wireless communication systems in terms of providing high-performance measurements. The OPNET simulation is used in this study to depict the Zigbee network. The operating properties of the star, tree, and mesh were understood by parameter analysis based

on performance. This strategy is applicable to any network that DG manages. The suggested intelligent protection system intends to improve the availability of the DG units during faults, ensure selectivity of protection, and shorten the time it takes to eradicate problems. Using cutting-edge sensors, a neural fuzzy system, and a Zigbee network, a new protective mechanism is elaborated. By reducing the duration of failure and solving the issue of the system's long-term disconnection, the intelligent algorithm ensures the selectivity of the protection [25–29].

3. Proposed Work

The objective function, which is expressed as the reduction of power loss over a year, can be described as

$$O = \text{MIN} N_d * \left[\sum_{\tau=1}^{M_t} l(S) + \sum_{\tau=1}^{M_t} l_P(W) + \sum_{\tau=1}^{M_t} l_P(SP) \right], \quad (1)$$

where M_t stands for the maximum number of hours in a day and N_d stands for the number of days in each season. S , W , and SP stand for the different seasons of summer, winter, and spring. Figure 1 describes the objective function for the proposed approach.

To produce a stable power supply with maximal voltage stability, which is expressed in equation (1), and the power balance is a significant limitation.

$$G(1)_{ap} - \sum_{k=1}^n k_l - \sum_{bh=1}^{nbh} l_{P(bh)} = 0, \quad (2)$$

where $G(1)_{ap}$ represents the grid active power and k_l and $l_{P(bh)}$ are the demand and power loss for the grid, respectively. To ensure voltage regulation, the resistance value at every bus is denoted as

$$\text{Min}_V \leq V_r \leq \text{Max}_V, \quad (3)$$

where Min_V and Max_V represent the lower and upper bounds of the voltage. Bounds of the voltage and also zero phase of angle are calculated as follows:

$$\begin{aligned} \mu_1 &= 0, \\ V_1 &= 1. \end{aligned} \quad (4)$$

Distributed generation is a key tactic for tackling the growing demand for power usage. Numerous earlier studies focused on the ideal power flow in the scattered network, but they did not sufficiently consider the reliability of the distribution network. The structure of demand forecasting in control center is shown in Figure 2.

The distributed generation should be deployed as efficiently as possible, as shown in Figure 3, to reduce power losses and the associated expenses. A variety of factors, including location characteristics, active power loss, voltage stability, voltage variation, load requirements, and DG capacity, impact the placement of distributed generation, which is related to the size and placement of the distributed generation that is appropriate. Accurate forecasting of the load demand is required in order to choose the size and

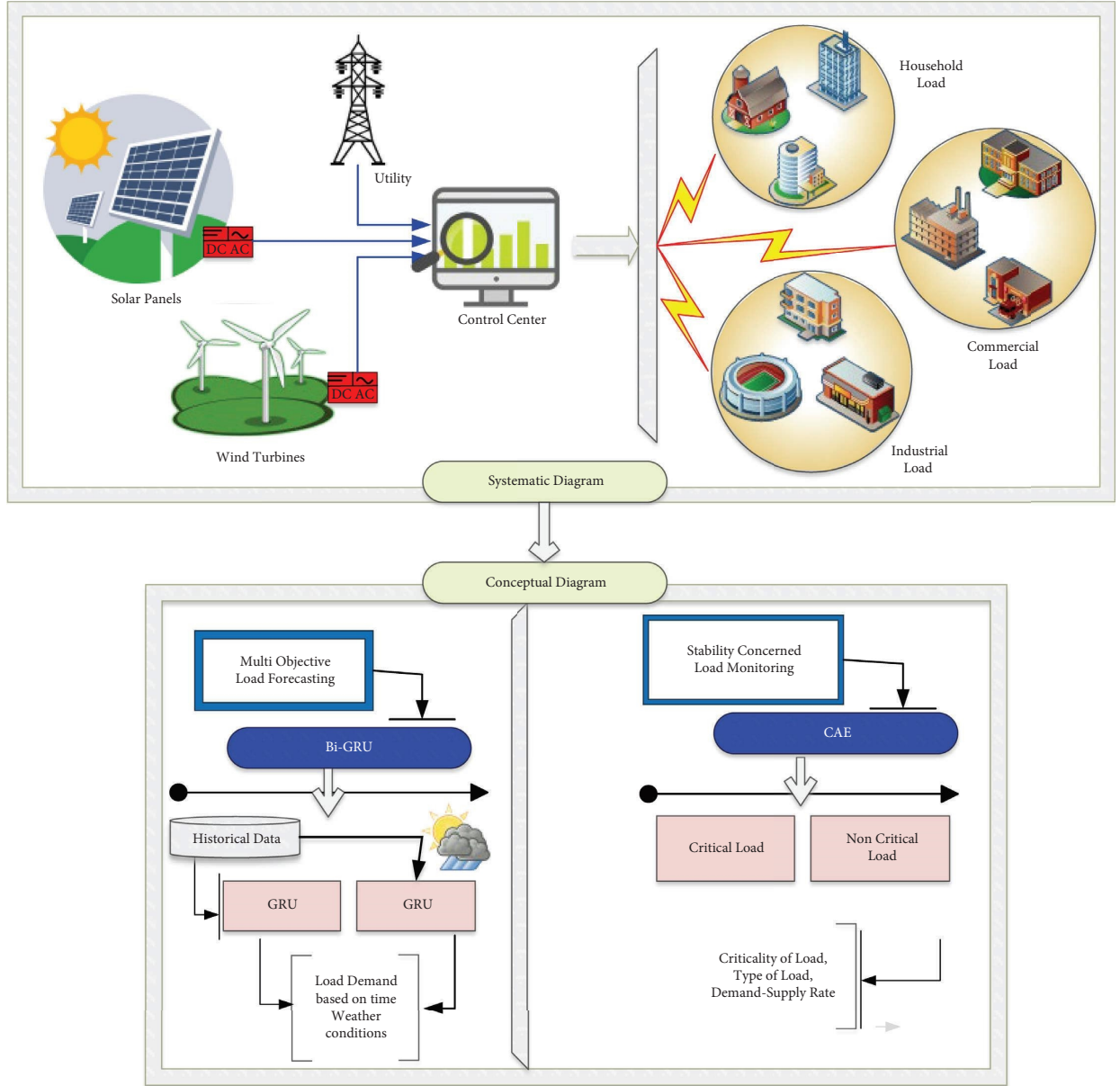


FIGURE 1: System flowchart.

location of the distributed generation. One illustration of a geographic feature is where DG is located. Other examples include the placement of solar power plants depending on local temperature and irradiance and wind turbines based on local wind speed.

- (i) The objective function to improve in this article is the position and size of the RDGs, which are determined using a heuristic algorithm.
- (ii) The following is a mathematical calculation for optimum sizing, according to solar RDG. The following information is based on the anticipated generation of electricity P_S and the location of SDG.

$$P_{SDGE,i} = n_{s,i} \times P_{SG} \quad \forall i \in d, \quad (5)$$

where $n_{s,i}$ represents the number of SDGs for the i th bus, P_{SG} represents the expected power generation, and d is the candidate bus. The projected generation rate for the solar RDG is computed as follows if the size and position are optimized.

$$P_{SDG,i} = n_{s,i} \times P_{SDG,R} \quad (6)$$

where $P_{SDG,R}$ is the discrete size rate of solar RDG.

3.1. Wind Turbine RDG. We can determine the ideal size and position of the RDG wind turbines based on the anticipated rate of power generation P_{WG} , which is shown below.

$$P_{WDGE,i} = n_{w,i} \times P_{WG} \quad \forall i \in d, \quad (7)$$

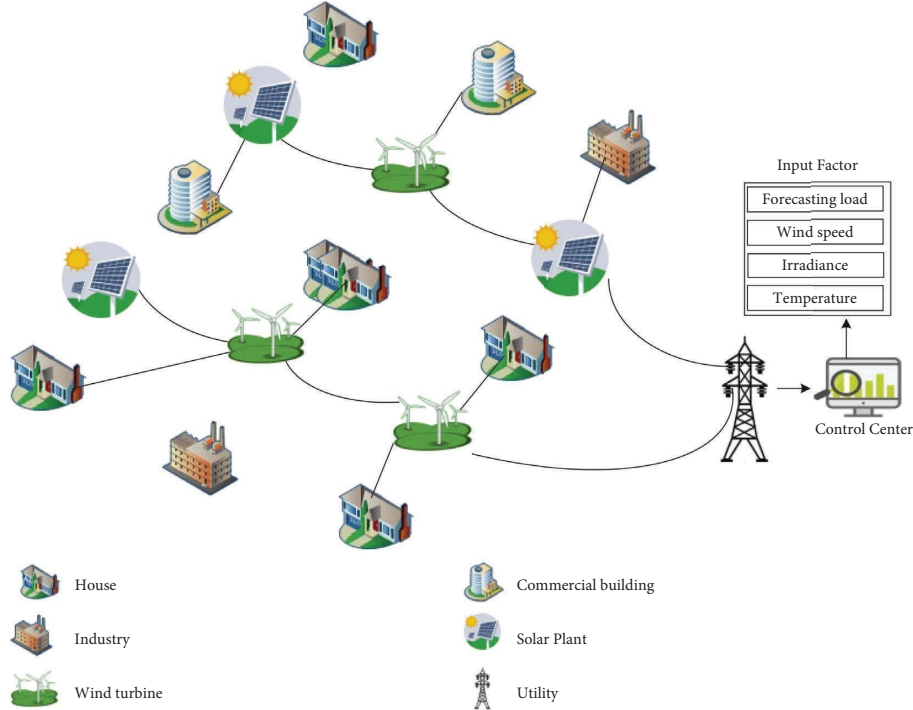


FIGURE 2: Demand forecasting in control center.

where $N_{w,i}$ and p_{WG} represent, respectively, the quantity of wind turbines and the anticipated power output of the wind turbine. Next, the position and rated size of the WDG are determined as follows:

$$P_{wDG,i} = n_{w,i} \times P_{wDG,R}, \quad (8)$$

where $P_{SDG,R}$ is the discrete size rate of wind RDG. The suggested multi-objective golden eagle optimization (MOGEO) algorithm comprises two phases that are explained in the following in terms of its computational complexity.

3.1.1. Initial Population. The method employs $O(N_p \times N_d)$ time to initialize each golden eagle's step vectors, position vector, and as memory. This algorithm's main loop accepts $O(N_p \times N_d \times N_i \times N_o \times N_a)$ as inputs. Finally, we determine that the suggested MOGEO method has a total complexity of $O(N_p \times N_d \times N_i \times N_o \times N_a)$.

The GEO, which has quick convergence and has proven to be more effective than other meta-heuristic optimization algorithms, performs the task of placing scattered generations in the best possible position. Also, the GEO algorithm is used to accurately find the best solutions for the complex optimization problem discussed above. The golden eagle, which consists of several bird species including hawks and eagles, is the model for this method. The following are some examples of the main characteristics and how they function. It has greater predisposition at the first stage to normalize the transition for the final stage by following a spiral (round) trajectory that restores the search path for the attack. It continues to have propensity to attack and cruise during every flight time. It searches the prey for eagle information.

The crowding score (CS) i , which is derived using the crowding distance concept and is defined as follows, is used in MOGEO to assess fitness. The Pareto front value for this distance was calculated between the two values that were closest to each other throughout time using the following formulas.

$$CS_i = \frac{1}{n} \sum_{j \in j} \frac{(f_{i+,j} - f_{i,j}) - (f_{i,j} - f_{i-,j})}{f_j^{\max} - f_j^{\min}}, \quad (9)$$

where $f_{i-,j}$, $f_{i,j}$, and $f_{i+,j}$ are the three successive members of the archive which are arranged according to the optimization's objective values and objective functions. The following method is used to calculate a new score based on the roulette wheel procedure. S_i is calculated as follows:

$$S_i = 1 - CS_i. \quad (10)$$

The following are some examples of the main characteristics and how they function: It has a greater predisposition at the first stage to normalize the transition for the final stage by following a spiral (round) trajectory that restores the straight and searching path for the attack. It continues to have a propensity to attack and cruise during every flight time. It searches the prey for eagle information. At the conclusion of this procedure, the total number of solar and wind RDGs and their positions are determined. Number of iterations, initial conditions, distance scores, and termination criteria of the algorithm are computed. Here, the fitness of the agent is determined while minimizing the losses using a distance-based objective function between two nearby sets of data. The placements of initialized parameters are then modified. If the termination criteria are satisfied, the

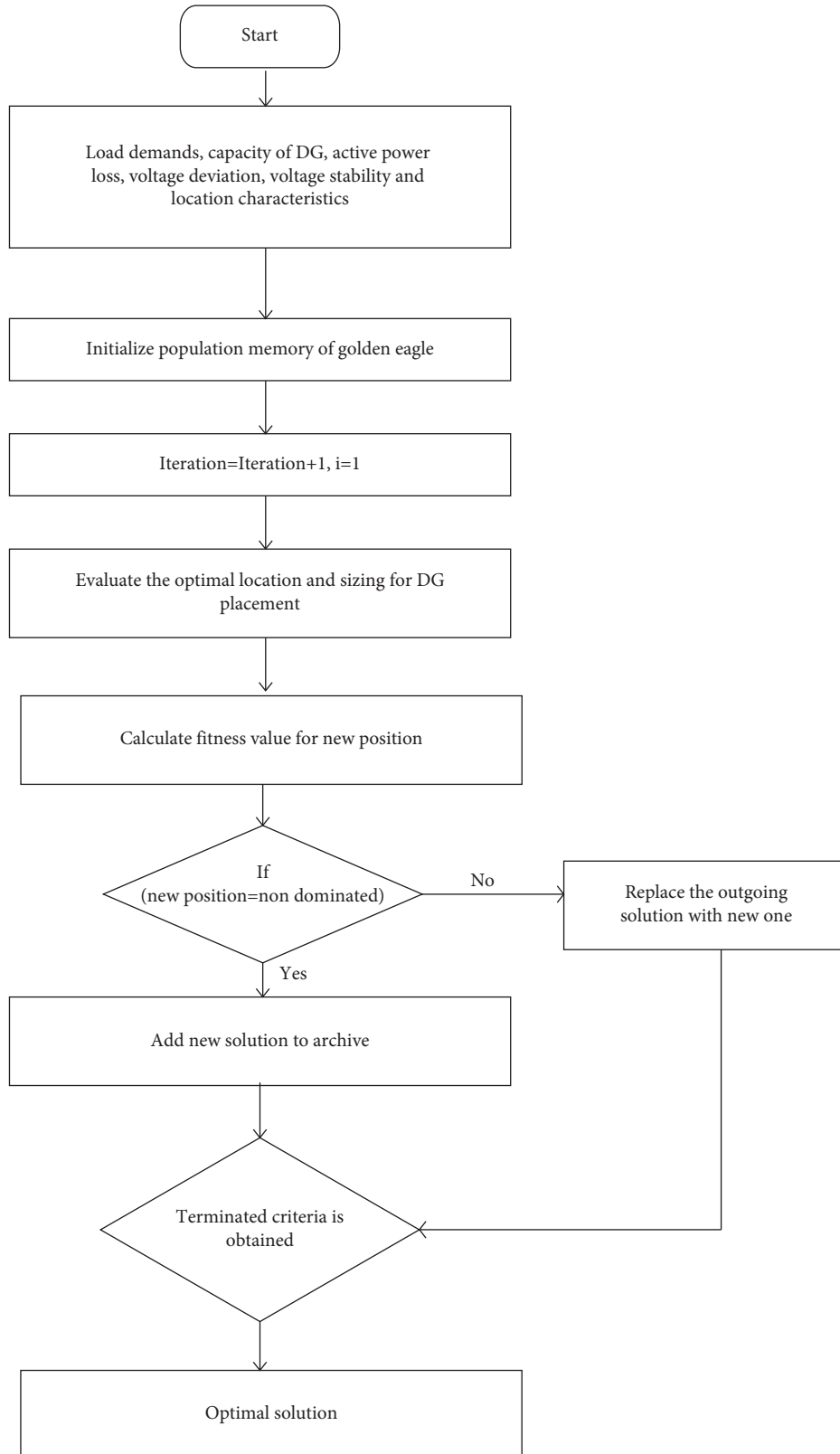


FIGURE 3: Flowchart for optimization of load demand in control center.

optimal fitness values are preserved; if not, the method is repeated until the best fitness value is reached.

4. Results and Discussion

The word “power loss” refers to the amount of power that is lost during transmission. Reverse power flow is the outcome of distributed generators’ ineffective grid placement, which is the source of this. The proposed work is done using MATLAB tool for simulation. In terms of the quantity of RDGs, Figure 4 compares the power loss of our proposed GEO model with that of the existing models. With an increase in RDGs, the power loss is reduced. Our suggested model has a minimal power loss since the RDG is placed optimally taking into account the load demand, RDG capacity, site features, and other important considerations. The MOGEO algorithm is used to decide the size, placement, and number of RDGs. The current methodologies were ineffective at positioning the RDG optimally because they anticipated continuous active and reactive power of the load on the customer side. Additionally, the power flow is not stable when just exogenous influences are taken into account.

Table 1 presents the numerical study of power loss for our proposed GEO model and existing models with regard to the number of RDGs. It is discovered that the suggested model has an average power loss of 60.1 kW, but the existing techniques have a power loss of up to 90.5 kW, which has an impact on the steady power flow to the essential load.

Voltage stability is a crucial parameter for assessing how well a method can withstand acceptable voltage. Voltage instability results from the approach’s inability to meet load demand. In severe load situations, voltage stability should be attained to enable proper power supply. Figure 5 compares the voltage stability of our suggested solution and the current approaches in relation to the number of RDGs. Increasing the number of RDGs improves voltage stability, but doing so increases energy costs. As a result, it is important to find the ideal number of RDGs, which can be done using MOGEO. The forecasting of load demand gives the suggested technique great voltage stability in challenging load scenarios. The right placement of RDGs in the network and the achievement of voltage stability are made possible by the correct information of the load. The existing methods are less effective in determining the ideal size and location of RDGs because they lack prior knowledge of load demand.

Table 2 provides a numerical comparison of the voltage stability of the proposed GEO model and the currently used methods in relation to the number of RDGs. The consistency of the suggested model is 0.95 pu, whereas the stability of the previous techniques is only 0.86 pu. This leads us to the conclusion that our suggested method is more reliable at supplying electricity to crucial loads.

The voltage deviation is a measurement of the voltage difference from the reference voltage that has an impact on the functionality of the power system. The voltage divergence is caused by a dynamic variation in load demand. Figure 6 compares the voltage deviation between our proposed model and the existing techniques in relation to the

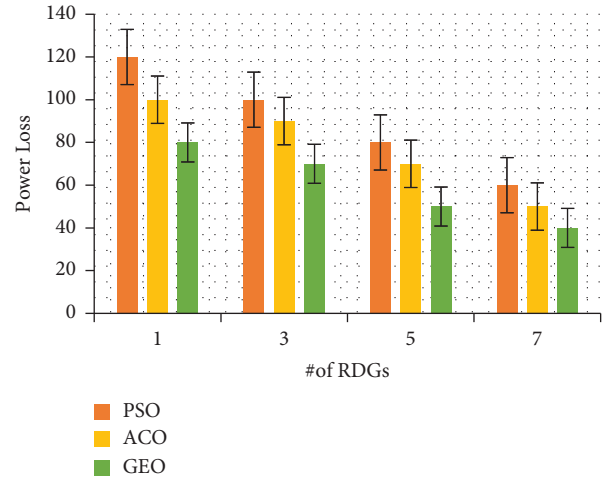


FIGURE 4: Power loss (critical load).

TABLE 1: Analysis of power loss.

Techniques	# of RDGs
PSO	90.5 ± 5
ACO	77.5 ± 4
GEO	60.1 ± 2

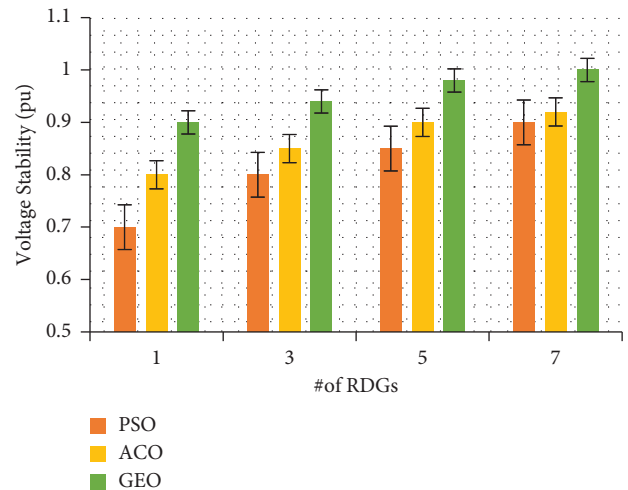


FIGURE 5: Voltage stability (critical load).

TABLE 2: Analysis of voltage stability (pu).

Techniques	# of RDGs
PSO	0.83 ± 0.5
ACO	0.86 ± 0.3
GEO	0.95 ± 0.1

number of RDGs. Less voltage variation occurs when the RDG count rises. Our suggested solution has less voltage damage than other existing systems because of the dynamic load monitoring. Utilizing the A2C-GAE, a steady power supply is offered based on the variation in load demand, with the load being dynamically divided into critical and non-

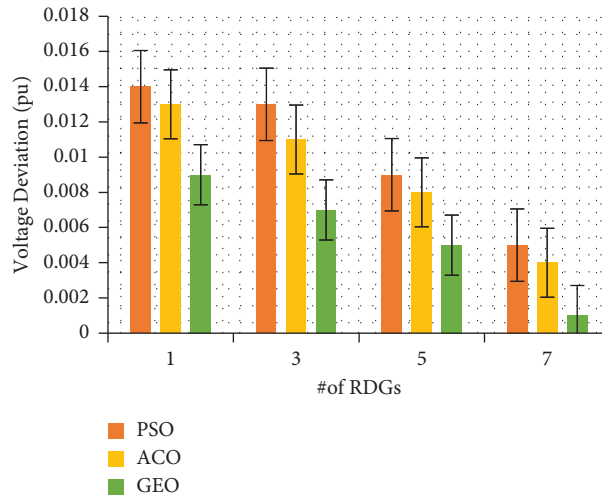


FIGURE 6: Voltage deviation (critical load).

TABLE 3: Analysis of voltage deviation (pu).

Techniques	# of RDGs
PSO	0.011 ± 0.005
ACO	0.009 ± 0.003
GEO	0.006 ± 0.001

critical categories. The present approaches assume a constant load demand, which raises voltage variances and affects system performance.

The voltage deviation with respect to the number of RDGs for both the current approaches and our proposed GEO methodology is numerically analyzed in Table 3. The proposed approach appears to have a voltage deviation of about 0.006 pu, whereas the voltage deviation of the existing methods can exceed 0.011 pu. The increased voltage variation of the current techniques degrades the performance of the power system, increasing the cost of revenue.

5. Conclusion and Future Work

This paper describes the design of a GEO-based controller that will be integrated into a microgrid that is connected to the grid and has the potential to store energy. The controller's goals are to regulate the rate of charge and discharge of the energy storage system (ESS) in order to lower end-user operational costs by running the ESS as an arbitrage device and minimizing power exchange between the main grid and microgrid. By deducting the load, the ESS's charge state, and the cost of power on the market from the available renewable energy, the suggested technique determines the charge and discharge rate of the ESS on a rolling horizon. In comparison to previous controllers with similar objectives, the recommended controller can reduce the energy exchange between the main grid and microgrid and achieve lower operating expenses. The aforementioned initiatives can be advanced using machine learning. A group of clever algorithms known as machine learning is capable of learning the underlying knowledge

contained in training data. The resulting decision model serves as direction for more work after the inherent information has been abstracted.

Data Availability

The datasets used and/or analyzed during the current study are available from the corresponding author on reasonable request.

Conflicts of Interest

The authors declare that they have no conflicts of interest.

References

- [1] L. Liu, M. Shafiq, V. R. Sonawane, M. Y. B. Murthy, P. C. S. Reddy, and K. C. K. Reddy, "Spectrum trading and sharing in unmanned aerial vehicles based on distributed blockchain consortium system," *Computers and Electrical Engineering*, vol. 103, Article ID 108255, 2022.
- [2] L. Sujihelen, R. Boddu, S. Murugaveni et al., "Node replication attack detection in distributed wireless sensor networks," *Wireless Communications and Mobile Computing*, vol. 2022, Article ID 7252791, 11 pages, 2022.
- [3] K. Ashok, R. Boddu, S. A. Syed, V. R. Sonawane, R. G. Dabhade, and P. C. S. Reddy, "GAN Base feedback analysis system for industrial IOT networks," *Automatika*, vol. 64, no. 2, pp. 259–267, 2023.
- [4] T. T. Teo, L. Thillainathan, W. L. Woo, and K. Abidi, "Intelligent controller for energy storage system in grid-connected microgrid," *IEEE Transactions on Systems, Man, and Cybernetics: Systems*, vol. 51, no. 1, pp. 650–658, 2021.
- [5] V. K. Tatikayala and S. Dixit, "AC side controller for grid connected hybrid renewable energy sources," in *Proceedings of the 2021 IEEE 2nd International Conference on Smart Technologies for Power, Energy and Control (STPEC)*, pp. 1–5, Bilaspur, Chhattisgarh, India, December, 2021.
- [6] A. Singhal, S. Varshney, T. A. Mohanaprakash et al., "Minimization of latency using multitask scheduling in industrial autonomous systems," *Wireless Communications and Mobile Computing*, vol. 2022, Article ID 1671829, 10 pages, 2022.

- [7] R. Sabitha, A. P. Shukla, A. Mehbodniya, L. Shakkeera, and P. C. S. Reddy, "A fuzzy trust evaluation of cloud collaboration outlier detection in wireless sensor networks," *Ad Hoc and Sensor Wireless Networks*, vol. 53, 2022.
- [8] I. Alsaïdan, P. Chaudhary, M. Alaraj, and M. M. Rizwan, "An intelligent approach to active and reactive power control in a grid-connected solar photovoltaic system," *Sustainability*, vol. 13, no. 8, p. 4219, 2021.
- [9] C. Raghavendran, M. Sadees, J. Preetha Roselyn, and D. Devaraj, "An intelligent energy management system for grid connected DFIG based wind system," in *Proceedings of the 2019 IEEE International Conference on Intelligent Techniques in Control, Optimization and Signal Processing (INCOS)*, pp. 1–5, Tamilnadu, India, April, 2019.
- [10] R. Dhanalakshmi, N. P. G. Bhavani, S. S. Raju et al., "Onboard pointing error detection and estimation of observation satellite data using extended kalman filter," *Computational Intelligence and Neuroscience*, vol. 2022, Article ID 4340897, 8 pages, 2022.
- [11] S. A. Nasef, A. A. Hassan, H. T. Elsayed, M. B. Zahran, M. K. El-Shaer, and A. Y. Abdelaziz, "Optimal tuning of a new multi-input multi-output fuzzy controller for doubly fed induction generator-based wind energy conversion system," *Arabian Journal for Science and Engineering*, vol. 47, no. 3, pp. 3001–3021, 2021.
- [12] S. Kamalasadán and R. Ghorbani, "Novel intelligent fault-tolerant adaptive control methodology for next generation energy systems," in *Proceedings of the 2012 IEEE Industry Applications Society Annual Meeting*, pp. 1–8, Las Vegas, NV, USA, October, 2012.
- [13] Y. Fan, V. Rimali, M. Tang, and C. V. Nayar, "Design and Implementation of stand-alone smart grid employing renewable energy resources on Pulau Ubin Island of Singapore," in *Proceedings of the 2012 Asia-Pacific Symposium on Electromagnetic Compatibility*, pp. 441–444, Singapore, May, 2012.
- [14] Y. Zong, A. Thavlov, D. Kullmann, O. Gehrke, and H. W. Bindner, "Model predictive controller design for a load management research facility in a distributed power system," *IFAC Proceedings Volumes*, vol. 43, no. 1, pp. 237–242, 2010.
- [15] P. C. S. Reddy, G. Suryanarayana, and S. Yadala, "Data analytics in farming: rice price prediction in Andhra Pradesh," in *Proceedings of the 2022 5th International Conference on Multimedia, Signal Processing and Communication Technologies (IMPACT)*, pp. 1–5, IEEE, Aligarh, India, November, 2022.
- [16] P. Li, B. Anduv, X. Zhu, X. Jin, and Z. Du, "Across working conditions fault diagnosis for chillers based on IoT intelligent agent with deep learning model," *Energy and Buildings*, vol. 268, Article ID 112188, 2022.
- [17] S. Rahamat Basha, C. Sharma, F. Sayeed et al., "Implementation of reliability antecedent forwarding technique using straddling path recovery in manet," *Wireless Communications and Mobile Computing*, vol. 2022, Article ID 6489185, 9 pages, 2022.
- [18] C. R. Rathish and A. Rajaram, "Hierarchical load balanced routing protocol for wireless sensor networks," *International Journal of Applied Engineering Research*, vol. 10, no. 7, pp. 16521–16534, 2015.
- [19] D. N. V. S. L. S. Indira, R. K. Ganiya, P. Ashok Babu et al., "Improved artificial neural network with state order dataset estimation for brain cancer cell diagnosis," *BioMed Research International*, vol. 2022, Article ID 7799812, 10 pages, 2022.
- [20] P. Ganesh, G. B. S. R. Naidu, K. Swaroopa et al., "Implementation of hidden node detection scheme for self-organization of data packet," *Wireless Communications and Mobile Computing*, vol. 2022, Article ID 1332373, 9 pages, 2022.
- [21] A. Rajaram and K. Sathiyaraj, "An improved optimization technique for energy harvesting system with grid connected power for green house management," *Journal of Electrical Engineering and Technology*, vol. 17, no. 5, pp. 2937–2949, 2022.
- [22] M. Dinesh, C. Arvind, S. Sreeja Mole et al., "An energy efficient architecture for furnace monitor and control in foundry based on industry 4.0 using IoT," *Scientific Programming*, vol. 2022, Article ID 1128717, 8 pages, 2022.
- [23] S. Kannan and A. Rajaram, "Enhanced stable path routing approach for improving packet delivery in MANET," *Journal of Computational and Theoretical Nanoscience*, vol. 14, no. 9, pp. 4545–4552, 2017.
- [24] R. P. P. Anand and A. Rajaram, "Effective timer count scheduling with spectator routing using stifle restriction algorithm in manet," *IOP Conference Series: Materials Science and Engineering*, vol. 994, no. 1, Article ID 012031, 2020.
- [25] P. C. Reddy and A. Sureshbabu, "An adaptive model for forecasting seasonal rainfall using predictive analytics," *International Journal of Intelligent Engineering and Systems*, vol. 12, no. 5, pp. 22–32, 2019.
- [26] C. R. Rathish and A. Rajaram, "Sweeping inclusive connectivity based routing in wireless sensor networks," *ARNP Journal of Engineering and Applied Sciences*, vol. 3, no. 5, pp. 1752–1760, 2018.
- [27] K. Mahalakshmi, K. Kousalya, H. Shekhar et al., "Public auditing scheme for integrity verification in distributed cloud storage system," *Scientific Programming*, vol. 2021, Article ID 8533995, 5 pages, 2021.
- [28] J. Divakaran, S. Malipatil, T. Zaid et al., "Technical study on 5G using soft computing methods," *Scientific Programming*, vol. 2022, Article ID 1570604, 7 pages, 2022.
- [29] Y. Sucharitha and P. C. Shaker Reddy, "An autonomous adaptive enhancement method based on learning to optimize heterogeneous network selection," *International Journal of Sensors, Wireless Communications and Control*, vol. 12, no. 7, pp. 495–509, 2022.

Research Article

PV Based Standalone DC -Micro Grid System for EV Charging Station with New GWO-ANFIS MPPTs under Partial Shading Conditions

R. Ragul,¹ N. Shanmugasundaram,¹ Mariaraja Paramasivam,² Suresh Seetharaman,³ and Sheela L. Mary Immaculate ⁴

¹Department of Electrical and Electronics Engineering, Vels Institute of Science, Technology & Advanced Studies (VISTAS), Chennai, Tamil Nadu, India

²Department of Electrical and Electronics Engineering, P. A. College of Engineering and Technology, Pollachi, Tamil Nadu, India

³Department of Electrical and Electronics Engineering, Kalaingar Karunanidhi Institute of Technology (KIT), Coimbatore, Tamil Nadu, India

⁴DEAN-PESAC, Pentecost University, Accra, Ghana

Correspondence should be addressed to Sheela L. Mary Immaculate; misheela@pentvars.edu.gh

Received 18 August 2022; Revised 11 October 2022; Accepted 24 November 2022; Published 15 March 2023

Academic Editor: Ravi Samikannu

Copyright © 2023 R. Ragul et al. This is an open access article distributed under the Creative Commons Attribution License, which permits unrestricted use, distribution, and reproduction in any medium, provided the original work is properly cited.

The goal of this article is to use MPPTs (maximum power point trackers) to extract maximum power from best configuration or combine renewable resources and energy storage systems that all work together in off-grid for electric vehicle charging. The grey wolf algorithm (GWO) searches the MPP at partial shading condition (PSC) with following two consideration one is high oscillations around GMPPs, and other is that they are unable to track the new GMPPs after it has changed positions because the seeking agents will be busy around the previous GMPPs captured. Hence, in this paper, the proposed research objective is to find solutions to these two difficulties. The issue of oscillations around GMPPs was handled by combining GWO with ANFISs (adaptive Neuro-Fuzzy inference system) to gently tune output produced power at GMPPs. ANFISs are distinguished by their near-zero oscillations and precise GMPPs capturing. The second issue called they are unable to track the new GMPPs after it has changed positions is addressed in this work by using novel initialization by GWOs (Grey wolf Optimizations). In the MATLAB-Simulink and experiments demonstrate the effectiveness of the suggested GWO-ANFIS MPPTs based off-grid station for EVs (Electrical Vehicle) battery charging.

1. Introduction

With the growing environmental concerns, governments throughout the world have established a variety of carbon emission limits. EVs that are powered entirely by electricity have the potential to replace gasoline and diesel vehicles. EVs enhance energy efficiency through effective fuel economy, especially when the power is generated from renewable sources such as solar and wind. When it comes to EVs in smart grids, that are more than simply an electrical burden, but also a power resource [1, 2], several proposals have been made [3–7] presented an

approach for modelling EVs as an additional load on the distribution network. Several scholars [8, 9] proposed a grid-connected PV system for EVs charging. In most cases, a backup battery is not required for a grid-connected system. There are two configurations for the grid-connected system. One is that the PV system works in conjunction with the utility grid to provide electricity to the load. As a result, the output of PV system is frequently less than load's power. The other is that the PV system is designed to provide the load with the needed power, and the utility grid serves as a backup source during solar power variations in this arrangement. With the ever-increasing

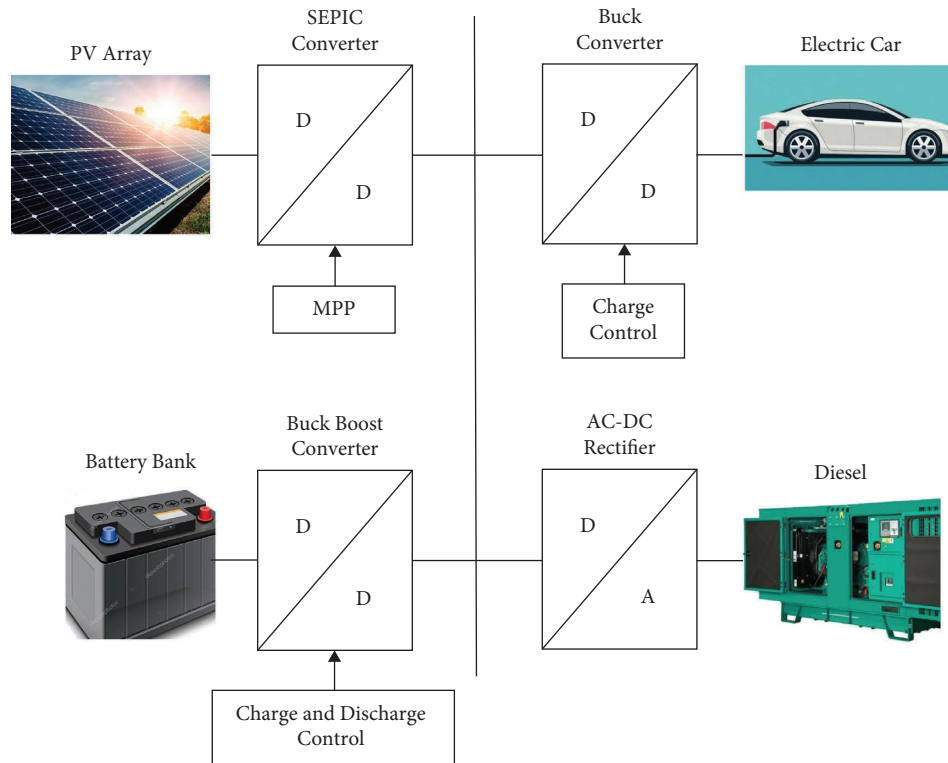


FIGURE 1: Off-grid charging station for EVs.

demand for electric vehicles, it became imperative to expand the number of charging stations. EVs require a high number of charging stations. As a result, EVs will be a substantial burden on the future distribution network system. The phrase “off-grid” of PV systems are not linked to main grids is known as a “stand-alone” PV systems. These stand-alone PV systems are ideal for electrifying small places in remote areas or small towns. They can also be used as charging points for EVs on long-distance routes as depicted in Figure 1. Many publications [10, 11] have discussed off-grid system design.

Due to seasonal weather conditions and the non-linear nature of solar irradiation, solar power output varies significantly, necessitating a hybrid application or backup systems [12]. Solar irradiance is not strongly connected across surrounding locations over short time periods, which is a critical factor in PV power output losses and swings [13]. MPPTs are considered significant components of PV systems for increased efficiency. Because of the non-linear features of PV arrays, it is unavoidable to design an effective maximum power point tracking system which is not only effective and improves the solar power system’s output power [14]. Furthermore, a variety of internal and external factors including series/parallel resistances, Diode factors, solar irradiations, PV array surfaces, internal temperatures, shadows and dirt impact on PV system’s output efficiencies. Because the dynamics of PV systems under PSCs change over time, MPPTs for PV powered systems must track GMPPs smoothly and steadily in a variety of situations including shades, degraded PVs, changes in PV arrays or PV characteristics.

A number of algorithms for MPPTs have been suggested for enhancing PV system’s effectiveness, including hill climbing [12], P&O (perturb and observe) [15–17], incremental conductance [18], however these techniques produce oscillations at MPPTs, resulting in power losses. IC technique [18] was developed to decrease these oscillations and increase module efficiency, however it only lowered the oscillations. P&O and IC approaches failed in time spans specified by changing atmospheric conditions. A scanning technique was presented [19–21] to estimate panel’s maximum power-delivering potential at any given operational condition for PV systems with rapidly changing and PSCs and insulations.

Soft computing methods employed for MPPTs in PV systems include PSOs (Particle Swarm Optimizations) [22], GWOs [23], CS, ACOs (Ant Colony Optimizations) [24], KHOs (Krill Herd Optimizations), FAs (Firefly algorithms) [25], ABCs (artificial bee colonies), MVOs (Multi-Verse Optimizations), ALOs (Ant Lion Optimizations), SCAs (Sine Cosine Algorithms), Dragonfly Algorithms, WOA (Whale Optimization Algorithms), MFOs (Moth-Flame Optimizations). Several studies [26, 27] have examined and introduced all of these approaches. In shaded or non-shaded circumstances where most approaches could catch the GMPPs. Nonetheless, they are affected by two major issues in PV applications. The first difficulty is with dynamic or time-varying GMPPs location in P-V curves, where most of these techniques may catch the initial GMPPs and stay around it, but not if the GMPP positions changes over a period of time. The second difficulty is that random variables associated with all of these soft computing techniques create substantial power swings near steady states. To overcome these two challenges, novel and efficient ways have been applied in this

study where the first issue is overcome by introducing re-initialization methods for soft computing methodologies while the second issue is resolved by using combination of soft computing techniques namely GWOs and ANFISs and where quick peak tracking and low oscillations around GMPPs differentiate ANFISs.

2. Related Work

Controller settings were optimised and adaptively modified using a predictive neural networks controller by Mohamed et al. [28]. The scheme anticipated control parameters by tracking grid current and dc-bus voltage mean square errors and eliminating them in a specified amount of time.

SMCs were proposed by Pahari and Subudhi [29] for control discontinuity based on high frequency conversions for driving closed loop systems to reach and stay on planned sliding surfaces. This approach considerably enhanced PV system's tracking speeds, however the step size of modulation depths of switching devices impacted system's dynamic and steady-state properties. When ΔU increased, Although tracking speeds increased, variations in PV array's output powers and voltages also increased. Pahari and Subudhi introduced Integral sliding mode controls to increase controller's steady state performances.

External voltage control, P&O, and an adaptive integral differential slip films were used to design their new sliding surface in Kihal et al. [30] and where derivative and integral terms eliminated overshoots during quick solar irradiation changes and reduced steady-state fluctuations.

The study in [31] was a novel model of adaptive PID controllers based on ANFISs proposed to address concerns in MPPTs approaches. It aided in maximising the output of DC pump in terms of speed. Their proposed controller was also used to test performances of EVs. To get the maximum power from solar-powered pump many methods have been tried and ANFISs have also been used to optimise performances of these intelligent systems. However, the approaches have certain flaws, necessitating the development of a new paradigm. As a result, in this research, a technique is developed in which a PID controller is used, and the combination of ANFISs and PID improves the performance of MPPTs. Moreover, this work's proposed combinations were tested on EVs.

Padmanaban et al. [32] presented grid-based PV systems with MPPT control mechanisms. Their work's ABC method converted ANFIS membership functions and their experimental study demonstrated that PV grid integrations were dependable and safe.

The author of [33] recommended modifying INC (Incremental Conductance) to track GMPPs of PV systems with PSCs without the application of any nature-inspired intelligence approaches like PSOs or other comparable algorithms. The work identified p-v curve as a mixture of areas and monitored global peaks by moving operating points from one region to another. In addition, the system incorporated varying sample times for quicker global peak tracking under extreme PSCs caused by unpredictable PV module shading patterns. Their PV module was modelled in

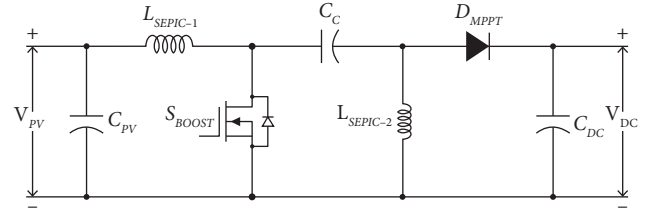


FIGURE 2: The SEPIC converter diagram.

combination with SEPIC converters for a battery charging applications using MATLAB/SIMULINK platform. The proposed technique was put to the test under various shading patterns to see how quickly and accurately their tracker tracked the power points. Finally, the suggested algorithm's idea was tested using PILs (Process-in-Loops) on TMS320F28027 LAUNCHPAD DSP board. Their result comparisons with recently published work in this sector showed that their suggested approach was more beneficial in terms of processing times.

Hence Evolutionary algorithms have reduced steady state oscillations and have advantage of ease in implementation and simplicity of computation.

3. Design Charging Station Converters

The power converter is the most important technology associated with PV systems. Maximum power from PV module is dragged from converter and sent to the load. This should be accomplished in grid-connected systems with least harmonic content in the current and a PF value greater than 0.9. The output voltage in off-grid systems should be adjusted to the necessary value. The suggested charging station in Figure 1 employs three DC-DC converter topologies. The SEPIC converter converts the fluctuating voltage from modules to a stable voltage, while the buck converter reduces the DC Bus voltage to voltage of the electric vehicle battery. The bidirectional converter is use d to control the battery bank's charging and discharging. The following sections detail the design of three DC-DC converters.

3.1. DC-DC SEPIC Converter. Figure 2 depicts Single Ended Primary Inductance Converter. [34] contains PV modules' input source voltage (V_{PV}), SEPIC inductor ($L_{SEPIC-1}$ and $L_{SEPIC-2}$), Coupling Capacitor (C_C), DC-link capacitor (C_{DC}), a diode (D_{MPPT}), MOSFET (Metal-Oxide-Semiconductor Field- Effect Transistor) (S_{MPPT}) as a switch and the output voltage (V_{DC}) (DC Bus Voltage). The SEPIC converter's output voltage can reduce or enhance the input PV voltage. Controlling or changing voltage may be done by adjusting the MOSFET's duty cycle.

As per the equation (34), the output voltage V_{DC} is proportionate to input voltage V_{PV} .

$$D_{MPPT} = \frac{V_{DC}}{V_{PV} + V_{DC}}, \quad (1)$$

here D_{MPPT} is duty cycle.

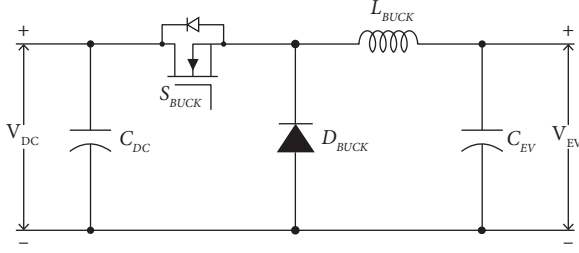


FIGURE 3: The buck converter diagram.

Equation (1) is used to determine the duty cycle of the SEPIC converter. Solar energy ranges between 0 and 1000 W/m² and temperature ranges from 25 to 75 degrees Celsius in the simulation.

SEPIC converter duty cycle is determined for a cell temperature of 25°C and irradiance of 1000 W/m² in non-shaded conditions. $V_{PV} = 116$ V, as you may have observed. When V_{DC} is equal to 110 V, $D_{MPPT(MIN)}$ at 110 V is 0.48.

If the two PV panels are shaded, the SEPIC Converter Duty Cycle is calculated at 25°C and 1000 W/m² at cell temperature of 25°C. As observed, $V_{PVmin} = 58$ V and $V_{DC} = 110$ V, resulting in $D_{MPPT(Max)}$ at 110 V of 0.65. Then inductance for continuous current, Coupling Capacitor of SEPIC converter is calculated below

3.1.1. Design of SEPIC Inductor. In the SEPIC converter, the inductance for continuous current is computed as follows [34]:

$$\begin{aligned} L_{SEPIC-1} \& L_{SEPIC-2} &= \frac{V_{PVmin}(D_{MPPT(Max)})}{\Delta I_{oMax} * F_{SW}} \\ &= 1.58 \text{ mH} \cong 1.6 \text{ mH}. \end{aligned} \quad (2)$$

The switching frequency, F_{SW} , has been set at 25 kHz. The ripple current ΔI_{oMax} is computed as follows: V_{IN} is the converter input voltage = 58 V. (taken as 13 percent of the total current):

$$\begin{aligned} \Delta I_{LBoost} &= 0.13 * I_{PV} \\ &= 0.13 * 7.34 \\ &= 0.95. \end{aligned} \quad (3)$$

3.1.2. Design of SEPIC Coupling Capacitor. Coupling capacitor C_c ripple voltage is:

$$\begin{aligned} C_C &= \frac{I_{PV}(1 - D_{MPPT(Max)})}{\Delta V_{CC} * F_{SW}} \\ &= \frac{7.35(1 - 0.65)}{12 * 25} \\ &= 8.5 \mu F \cong 10 \mu F. \end{aligned} \quad (4)$$

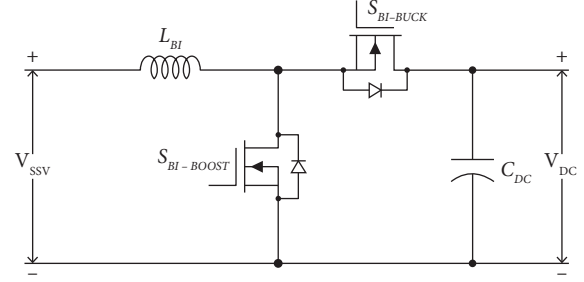


FIGURE 4: The bidirectional converter diagram.

3.2. DC-DC Buck Converter. Buck converter illustrated in Figure 3 [35] is made up of DC-link voltage as an input source (V_{DC}), buck inductor (L_{BUCK}), buck capacitor (C_{BUCK}), a diode (D), MOSFET (S) as a switch and the output voltage (V_{EV}) as an EVs battery voltage (350 V in Tesla S 100D cars).

The duty ratio is calculated as follows:

$$\begin{aligned} D_{BUCK} &= \frac{V_{EV}}{V_{DC}} \\ &= \frac{60}{110} \\ &= 0.545. \end{aligned} \quad (5)$$

3.2.1. Design of Buck Inductor and Buck Capacitor. The buck converter's inductance for continuous current is computed as follows [35]:

$$\begin{aligned} L_{BUCK} &= \frac{V_{DC} - V_{EV}}{\Delta I_{LBUCK} * F_{SW}} \\ &= \frac{110 - 60}{1.51 * 10,000} \\ &= 3.3 \text{ mH}, \end{aligned} \quad (6)$$

ΔI_{LBUCK} (The ripple current) is computed as (taken as 13% of the charge current):

$$\begin{aligned} \Delta I_{LBUCK} &= 0.13 * I_{CGB} \\ &= 0.013 * 11.66 \\ &= 1.51 \text{ A}. \end{aligned} \quad (7)$$

3.3. The Bidirectional Converter. The storage battery is supplied as a backup service during energy outages to smooth power storage produced by off-grid systems. As a consequence of the advantages listed below, this article recommends a bidirectional buck-boost converter, as illustrated in Figure 4 [23], regulate storage and delivery of electricity among PV system and battery bank:

- (i) It provides the most cost-effective solution with the fewest external components.
- (ii) It accomplishes voltage step-up and step-down using the fewest possible components.
- (iii) It has a decreased duty cycle when in operation.
- (iv) It has a high efficiency over a wide range of input and output voltages.
- (v) It is less costly than the majority of converters.

Based on power flow direction, the bidirectional converter may be configured in two operation modes: boost and buck [36] describes these modalities in detail.

3.3.1. *Design for the Bidirectional Converter.* The inductance (L_{BI}) can be represented in two different ways:

In Buck mode:

$$\begin{aligned} L_{BI-Buck} &= \frac{V_{DC} - V_{SSV}}{\Delta I_{BI-BUCK} * F_{SW}} \\ &= \frac{110 - 60}{2.08 * 10,000} \\ &= 2.4 \text{ mH}, \end{aligned} \quad (8)$$

$\Delta I_{BI-Buck}$ (ripple current) is computed as (taken as 13% of charge current):

$$\begin{aligned} \Delta I_{BI-BUCK} &= 0.13 * I_{CGS} \\ &= 0.13 * 16 \\ &= 2.08 \text{ A}. \end{aligned} \quad (9)$$

In Boost mode:

$$\begin{aligned} L_{BI-BOOST} &= \frac{V_{DC} - V_{SSV}}{\Delta I_{BI-BOOST} * F_{SW} * V_{DC}} \\ &= \frac{110 - 60}{1.65 * 10,000 * 110} \\ &= 0.02 \text{ mH}, \end{aligned} \quad (10)$$

here ΔI_{BI} (ripple current) under Boost mode is computed as (taken as 13% of the charge current):

$$\begin{aligned} \Delta I_{BI-BOOST} &= 0.13 * I_{CGS} \frac{V_{DC}}{V_{SSV}} \\ &= 0.13 * 6.95 * \frac{110}{60} \\ &= 1.65 \text{ A}, \end{aligned} \quad (11)$$

$L_{BI-Buck}$ is more than $L_{BI-BOOST}$ to make sure that inductor current can function during continuous conduction mode (CCM) [36], $L_{BI-BUCK}$ value is selected, that is, equal to

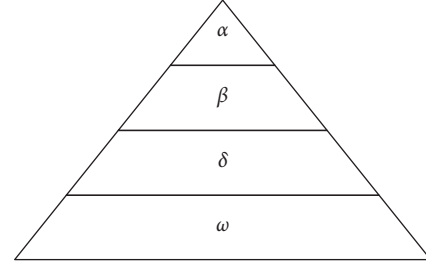


FIGURE 5: Leadership pyramid with four level (α , β , δ and ω).

2.4 mH here $D_{BI-BOOST}$ is duty cycle under Boost mode and computed as:

$$\begin{aligned} D_{BI-BOOST} &= 1 - \frac{V_{SSV}}{V_{DC}} \\ &= 1 - \frac{60}{110} \\ &= 0.455. \end{aligned} \quad (12)$$

4. Design of Closed Loop System

The Grey wolf Optimizer combined with ANFISs are implemented to track the new GMPPs after it has changed positions are discussed follows.

4.1. *Proposed Grey Wolf Optimizer Combined with ANFISs Global Maximum Power Point Tracking Techniques.* Due the PSC the PV array generates the several peaks is generated with various LMPPs and a single GMPPs so tracking of maximum power location is obtain by GWO algorithm. The GWO enhance power quality and ensure the efficiency of PVCs (photovoltaic cells) under PSCs (partial shading conditions) by varying the duty cycle with low iteration. Mirjalili et al. originally proposed Grey Wolf Optimizer in 2014 [23], and it is considered one of the most recent heuristic optimization techniques. This approach is based on the way grey wolves hunt food in the wild, pursuing, attacking, and killing them. Grey wolves prefer to live in packs of 5 to 10 individuals. They follow a strict social dominance structure with four levels of leadership. Leaders, named as alpha (α), and subleaders, which they call beta (β), etc, are referred to as leadership pyramids, as illustrated in Figure 5, where wolf dominance rises from top to bottom [37]. The alpha wolf holds duty cycle of maximum power by corresponding random search duty cycle set. Accordingly the second and third maximum powers are named as beta and delta respectively. The rest of maximum power solution at the duty cycle is denoted as omega. The tracking global maximum power behaviour of grey wolves, we suppose that the alpha, beta and delta have the better knowledge about the

global maximum power. Therefore, we save the first to three best powers obtained so far iterations and oblige the next iteration search duty cycle to update the duty cycle according to the best maximum power. GWOs are created to replicate grey wolves behaviour in the optimization domain. Grey wolf leadership hierarchy is established by assuming the leaders; wolves known as alpha (α), subleaders known as beta (β), lower rank wolves known as delta (δ), lowest rank wolves known as omega (ω).

Grey wolves encircle food in the hunt, as previously stated. The following equations are presented to analytically model encircling behaviour [23]:

$$\begin{aligned} \vec{E} &= |\vec{C} \cdot \vec{D}_p(t) - \vec{D}(t)|, \\ \vec{D}_p(t+1) &= \vec{D}_p(t) - \vec{A} \cdot \vec{E}, \end{aligned} \quad (13)$$

here t indicates current iteration, A , C are coefficient vectors whose values has capability to save balance between exploration and exploitation in searching region, D_p is prey's position vector, D represents grey wolf's position vector. Two coefficient vectors A and C are computed like:

$$\begin{aligned} \vec{A} &= 2\vec{a} \cdot \vec{r}_1 - \vec{a}, \\ C &= 2\vec{r}_2, \end{aligned} \quad (14)$$

here, coefficient a is decreasing linearly beginning 2 to 0, r_1 , r_2 are arbitrary vectors with value $[1, 0]$. Grey wolves hunt by circling their prey, and pack should follow the commands of alpha wolf (D_α) as a high priority, and orders of the beta wolves (D_β) and delta wolves (D_δ) as a lesser priority. The following equations can be used to model this leadership hierarchy numerically:

$$\begin{aligned} \vec{E}_\alpha &= |\vec{C}_1 \cdot \vec{D}_\alpha - \vec{D}|, \\ \vec{E}_\beta &= |\vec{C}_2 \cdot \vec{D}_\beta - \vec{D}|, \\ \vec{E}_\delta &= |\vec{C}_3 \cdot \vec{D}_\delta - \vec{D}|, \\ \vec{D}_1 &= \vec{D}_\alpha - \vec{A}_1 \cdot \vec{E}_\alpha, \\ \vec{D}_2 &= \vec{D}_\beta - \vec{A}_2 \cdot \vec{E}_\beta, \\ \vec{D}_3 &= \vec{D}_\delta - \vec{A}_3 \cdot \vec{E}_\delta, \\ \vec{D}_p(t+1) &= \frac{\vec{D}_1 + \vec{D}_2 + \vec{D}_3}{3}. \end{aligned} \quad (15)$$

The solution's exploration and exploitation are determined by a and A values, wherein $|A| \leq 1$, the wolves incline to exploitation (converge to prey) and $|A| \geq 1$, wolves tend to exploration (diverge from prey as it might be one of LMPPs). As stated in introduction, hybrid GWO-ANFIS is suggested to combine benefits of both approaches and monitor variant GMPPs under variation PSCs with almost negligible oscillations around GMPPs power. To monitor the variation GMPPs, GWOs with two re-

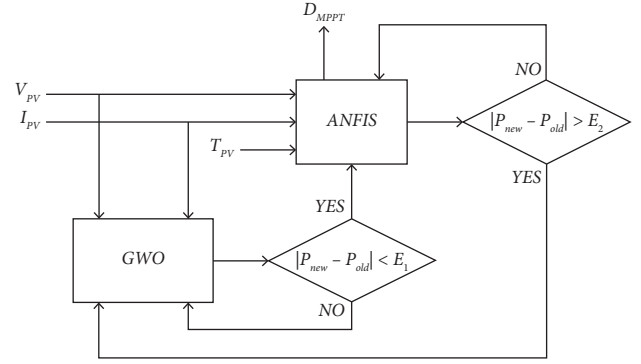


FIGURE 6: PV energy system with hybrid GWO-ANFIS based MPPTs.

initialization approaches is presented. GWOs is re-initialized to seek for GMPPs at first. After GWOs has caught initial GMPPs, it is ended depending on first condition and the role is given to ANFISs [38]. ANFISs are employed to soften the initial GMPPs captured by GWOs and track precise value of GMPPs with nearly minimal fluctuation around global power. Inputs of ANFISs are V_{PV} , I_{PV} and T_{PV} [28], which create the Duty (D_{MPPT}) output, whereas the ANFISs output is the DC-DC converter's optimum duty ratio (SEPIC converter) [39, 40]. In contrast, if the PSCs changes, ANFISs are terminated, and GWOs must be re-initialized to search for and follow new GMPPs, as illustrated in Figure 6.

This study proposes a combination of GWOs and ANFISs for taking full advantage of both techniques while overcoming their disadvantages. When it comes to capturing GMPPs of PV systems, GWOs are the most effective and have the fastest convergences, but it also has a lot of oscillations around GMPPs at steady states. ANFISs which are opposite of GWOs remain at local peaks with extremely low oscillations around GMPPs. As a result, GWOs were first used to quickly and effectively track GMPPs and subsequently ANFISs then start to behave like MPPTs with very low oscillations. As a result, GWOs are employed to follow the GMPPs and avoid local peaks at the start of MPPTs. Furthermore, at GMPPs, the drawback of major oscillations is avoided by pausing operations and enabling ANFISs to operate with extremely low oscillations. In order for GWOs to be terminated and ANFISs to complete the control of MPPTs on GMPPs that have already been captured, the following prerequisites must be met:

$$|P_{new} - P_{old}| \leq E_1, \quad (16)$$

here, P_{new} is current power obtained from PV system, P_{old} is pervious iteration value of simulation, E_1 is permissible limit before transferring control from GWOs to ANFISs, that is equivalent to 2% of generated power. Condition for terminating ANFISs and go back to GWOs to re-initialize the agents to search for new GMPPs under new PSCs via following conditions:

$$|P_{new} - P_{old}| \geq E_2, \quad (17)$$

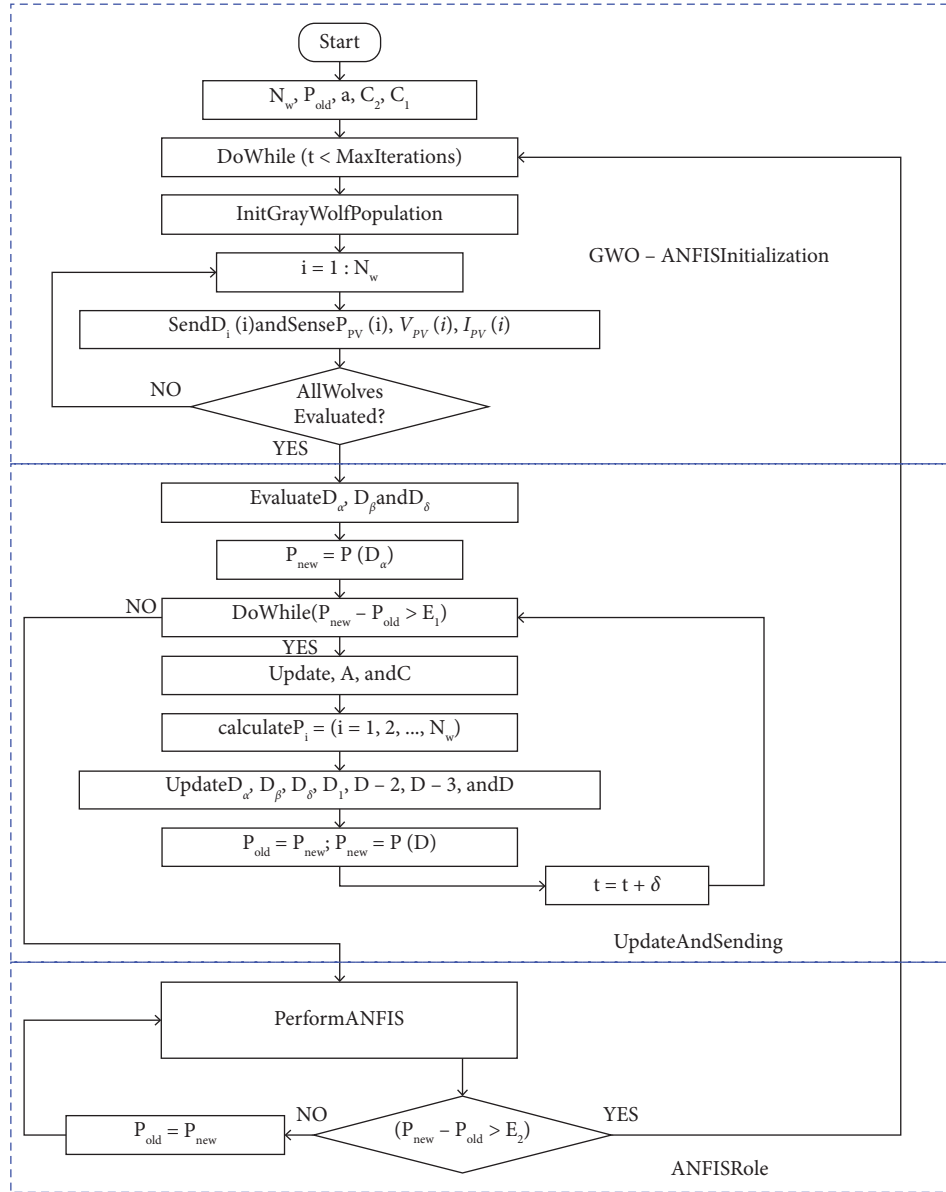


FIGURE 7: Flowchart of GWO-ANFIS based on PSCs change.

here E_2 is permissible limit before transferring control from ANFISs to GWOs, that equivalent to 5% of generated power.

There are two suggested initialization approaches for re-initializing the GWOs to begin looking for a new GMPPs. As previously stated, the goal of combining GWOs and ANFISs is to take advantages of both approaches, with GWOs being rapid and reliable MPPTs approach for tracking GMPPs under PSCs while ANFISs have lowest GMPP oscillations. GWOs will be unable to catch new GMPPs when they alters their position since all wolves will be looking in the prior GMPPs search zone. As a result, if the controller detects a change in PSCs, the agents of GWOs should be re-initialized to scan the search region for new GMPPs. ANFISs will follow GWOs once they have identified GMPPs until the controller detects another change in the PSCs.

If the condition stated in equation (27) is true, the controller will follow the PSCs modification. Figure 7 shows a flowchart which summarizes processes of hybrid GWO-ANFIS with PSCs modification re-initialized.

4.2. The Charge and Discharge Control. Power is transferred from and to the battery bank via the charging and discharging controller. The bidirectional converter in the stand-alone PV system with the battery bank illustrated in Figure 8 has four distinct control modes depending on magnitude of power produced by PV array, that is dependent on temperature and irradiance.

Mode 1. When obtained PV power is less than power needed by EVs battery, i.e. $PPV < PDDh$, and the charge status of SOC is greater than 40%, first control mode is used.

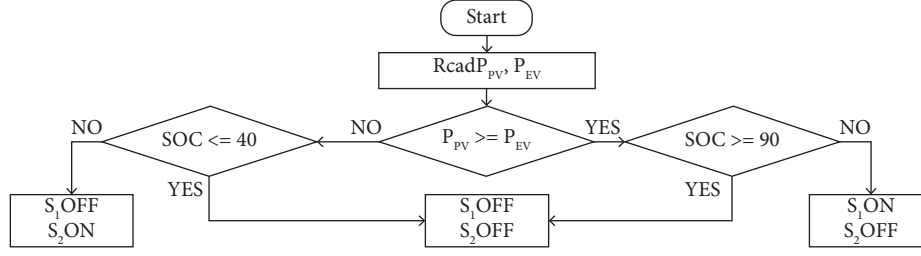


FIGURE 8: Four operating modes flowchart.

The bidirectional converter enters buck mode in this mode, where the controller sends a control signal to make switch 1 (S1) detached while also sending a control signal to make switch 2 (S2) connect. This mode uses storage batteries to offer additional power.

Mode 2. When obtained PV power is less than power needed by EVs battery, i.e. $PPV < PDDh$, and the charge status of SOC is less than 40%, the second control mode is used. In this mode, the controller sends a control signal to both switches 1 (S1) and 2 (S2), causing them to be disconnected.

Mode 3. When obtained PV power exceeds power needed by EVs battery, i.e., $PPV > PDDh$ and the charge status of SOC is less than 90% and more than 40%, the third control mode is used. PV array not only supplies power to EVs battery under maximum power point enabled management in this mode, but it also charges the battery bank with surplus power produced by PV array. In this mode, the controller sends a control signal to switch 1 (S1) to connect and a control signal to switch 2 (S2) to disconnect, causing the bidirectional converter to enter boost mode.

Mode 4. When the generated PV power exceeds the EVs battery's power demand, i.e., $PPV > PDDh$, and the storage battery's charge state (SOC) is greater than 90%, the fourth control mode is used. The PV array delivers power to EVs battery under maximum power point enabled management in this mode, and charge status of storage battery is maintained at more than 90% by constant voltage charging to prevent the battery from discharging. In this mode, the controller sends a control signal to both switches 1 (S1) and 2 (S2), causing them to be disconnected. The four operational modes are depicted in Figure 8's flowchart.

5. Simulation Result

Simulating the suggested TPC Converter for performance assessment with the Sim Power-System Toolbox is done in MATLAB/Simulink setting. DC-microgrid settings provided in Table 1 were used to obtain all simulation results in MATLAB 2021.

The solar irradiation fluctuates as per the following pattern in the simulation, while all other parameters remain constant. As a consequence of GWO-ANFIS MPPTs, the DC-microgrid is at steady state at $t = 0$ s, and the four PV at 1000 wb/m^2 create the current I_{PV} of 6.8 Amps, the PV output voltage V_{PV} of

TABLE 1: Parameters used in simulation.

Sl.no	Parameter	Value
1	PV MPP power (P_{MPP})	213.15 W
2	PV MPP voltage (V_{MPP})	29 V
3	PV MPP current (I_{MPP})	7.35 A
4	Series PV panel	4No's
5	Parallel PV panel	1No's
6	Storage system battery type	Lead-acid
7	Storage system battery nominal voltage (V_{SSV})	60 V
8	Storage system battery rated capacity	16 Ah
9	SEPIC converter inductors ($L_{SEPIC-1}$ & $L_{SEPIC-2}$)	1.6 mH
10	SEPIC converter coupling capacitor (C_C)	10 μ F
11	Buck converter inductor (L_{BUCK})	3.3 mH
12	Bidirectional converter inductor (L_{BI})	2.4 mH
13	DC link capacitor (C_{DC})	60 μ F

125.8 Volt, and the PV power P_{PV} of 856 watts as seen in Figure 9. There is no bypass diode conduct since all four PVs are operated in equal irradiance with just one global peak, as illustrated in Figure 10. As indicated in Figure 11, the EVs charging power P_{EV} from the DC micro grid is 700 Watts, with a nominal dc link voltage V_{EV} of 110 V and an EVs current I_{EV} of 6.36 Amps. The remaining PV power P_{ESS} of 150 Watts is stored in the ESS battery at a current I_{ESS} of -2.49 A and a voltage of 60.2 Volt, increasing the battery SOC from 40% to 60%, as illustrated in Figure 12.

Due to partial shade, the irradiation of Panels 3 and 4 drops to 300 wb/m^2 at $t = 0.2$ s. PV output voltage V_{PV} falls to 59.5 Volts, PV current I_{PV} reduces to 7.1 amps, and PV power P_{PV} falls to 422.5 Watts. As illustrated in Figure 10, this global power is tracked using the GWO-ANFIS MPPTs algorithm by removing the darkened panel at this instant bypass diode conduction. Even when the PV lighting varies, the DC bus voltage remains constant at 110 V thanks to the battery converter. At $t = 0$ s, the battery is charging, but as the PV output power decreases, it drains. Because the DC bus voltage remains constant at 110 V, EVs power P_{EV} is kept constant at 700 W, as illustrated in Figure 11. The remaining power P_{ESS} of 277.5 Watts obtained by PV is stored in ESS battery at a current I_{ESS} of 4.64 A and a voltage of 59.7 Volt, lowering the battery SOC from 40% as seen in Figure 12.

The PV panel and diesel generator are started with a produced power of 422.5 watts and 790 watts, respectively, as the ESS battery discharges below 40% SOC at $t = 0.4$ sec, as illustrated in Figures 9 and 13. To keep the EVs power P_{EV} at 700 W, the DC bus voltage is kept constant, as illustrated in Figure 11. He remaining power P_{ESS} of 512.5 watts charged in the ESS battery, increasing the SOC as illustrated in the Figure 12.

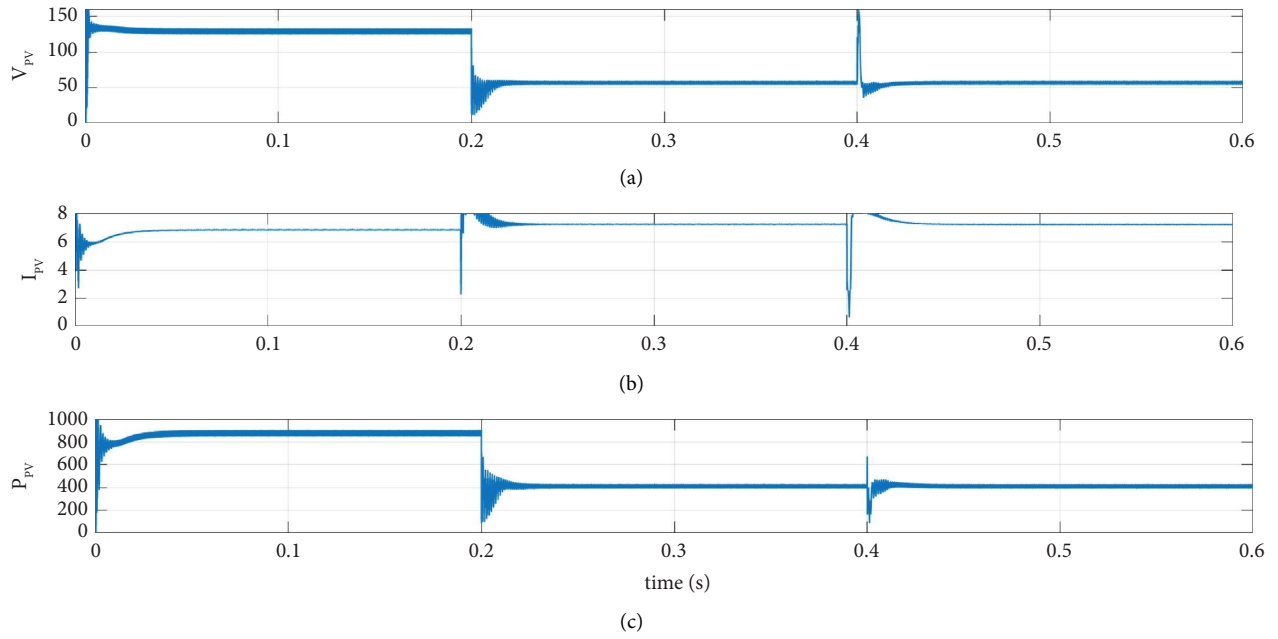


FIGURE 9: Simulation results (a) PV voltage (b) PV current (c) PV power.

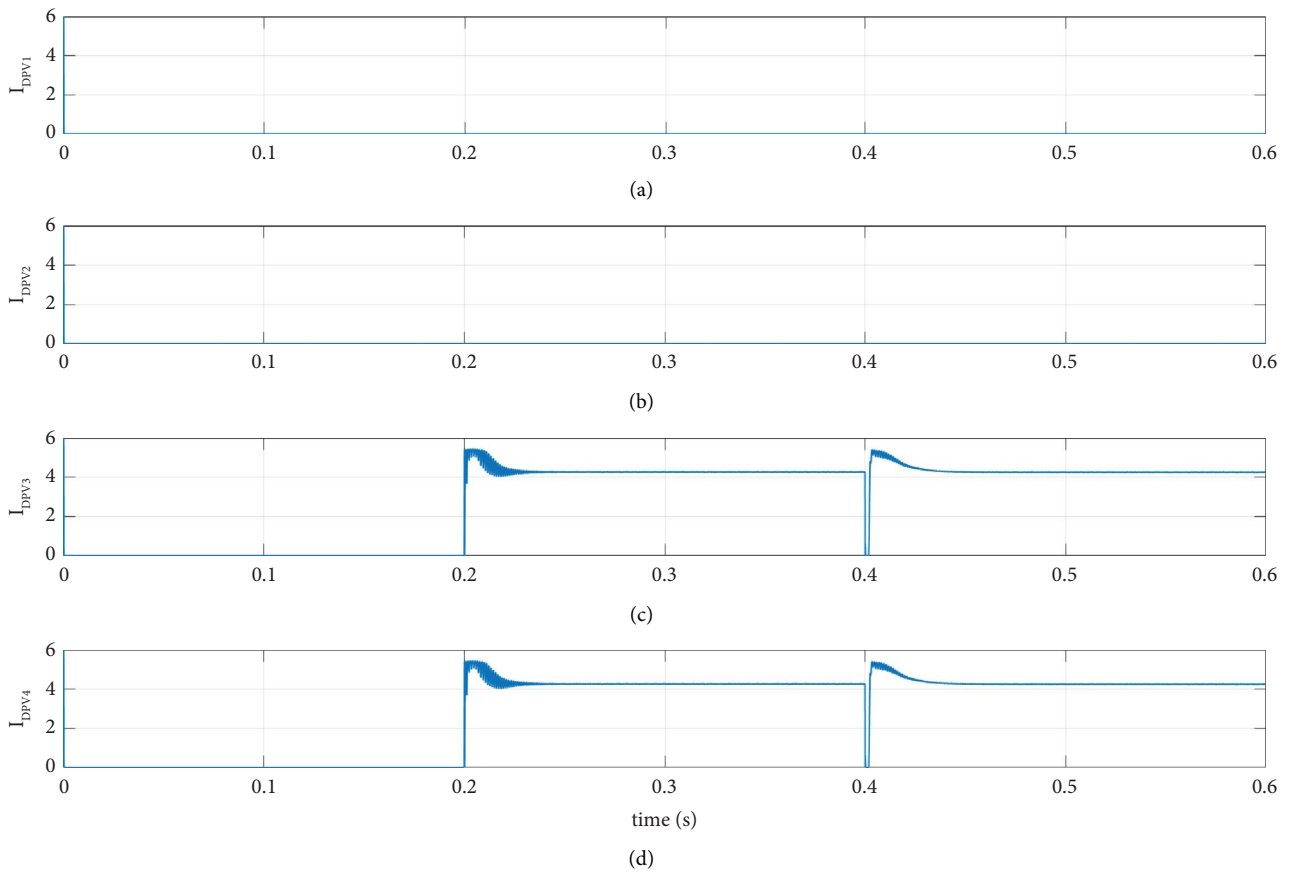


FIGURE 10: Simulation results (a) bypass diode PV -1 (b) bypass diode PV -2 (c) bypass diode PV -3 (d) bypass diode PV -4.

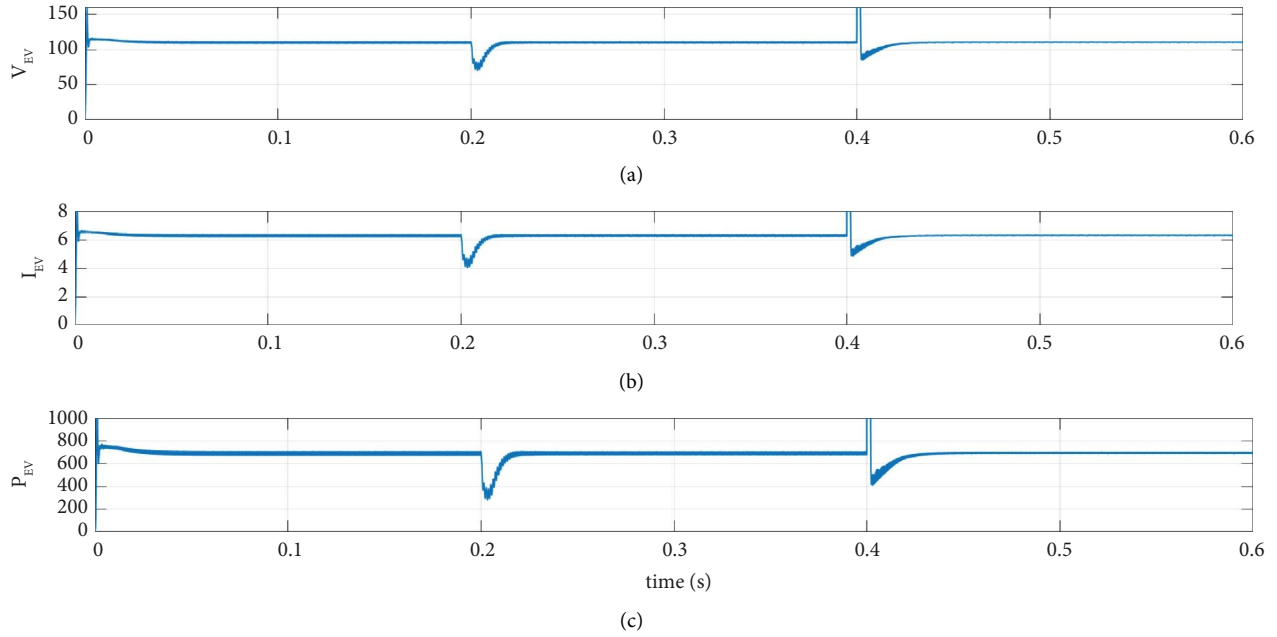


FIGURE 11: Simulation results (a) EVs voltage (b) EVs current (c) EVs power.

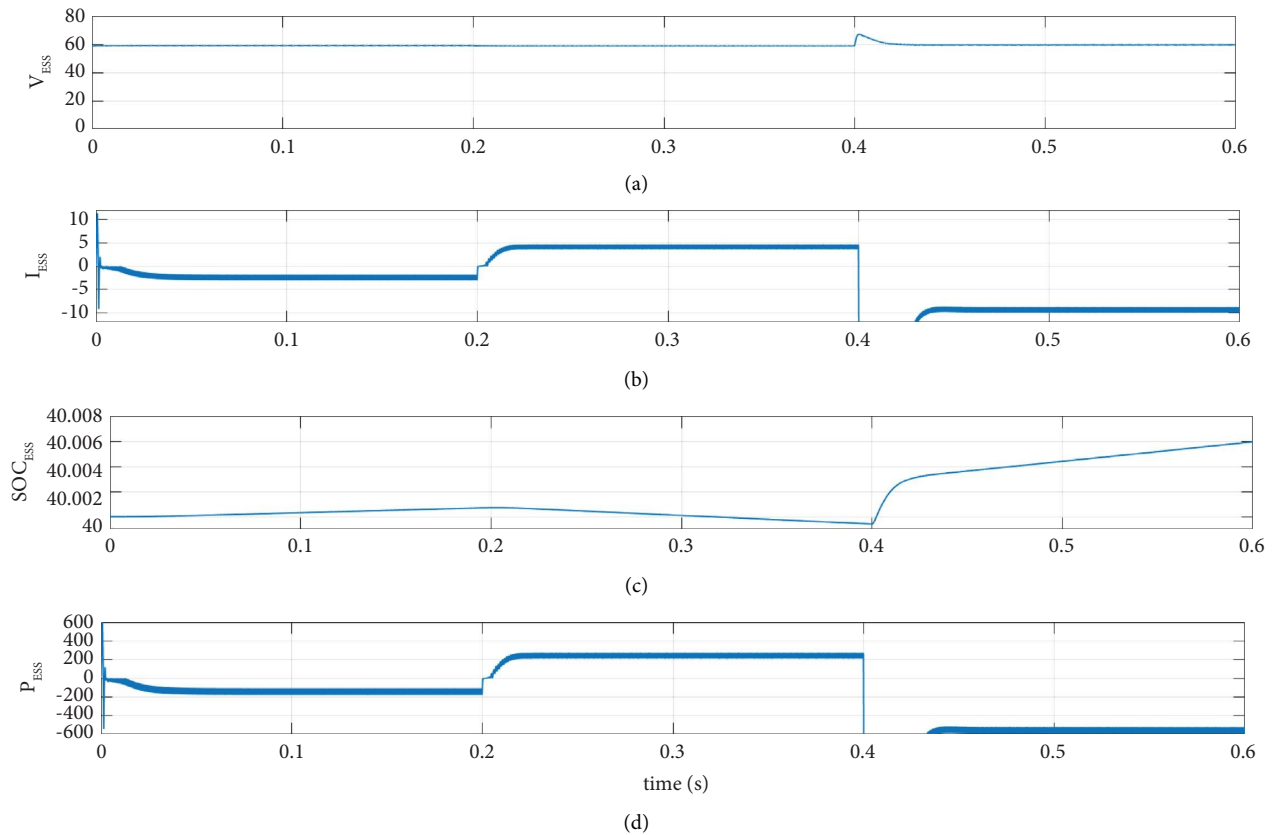


FIGURE 12: Simulation results (a) ESS voltage (b) ESS current (c) ESS SOC (d) ESS power.

6. Experimental Results

The proposed GWO-ANFIS tracking algorithm has been evaluated for its performance with P&O MPP tracking

algorithms. The evaluation tracked maximum power from PV array system to DC using a simple boost converter. Table 2 lists hardware parameter values of 4S configuration in Proposed GWO-ANFIS MPPT.

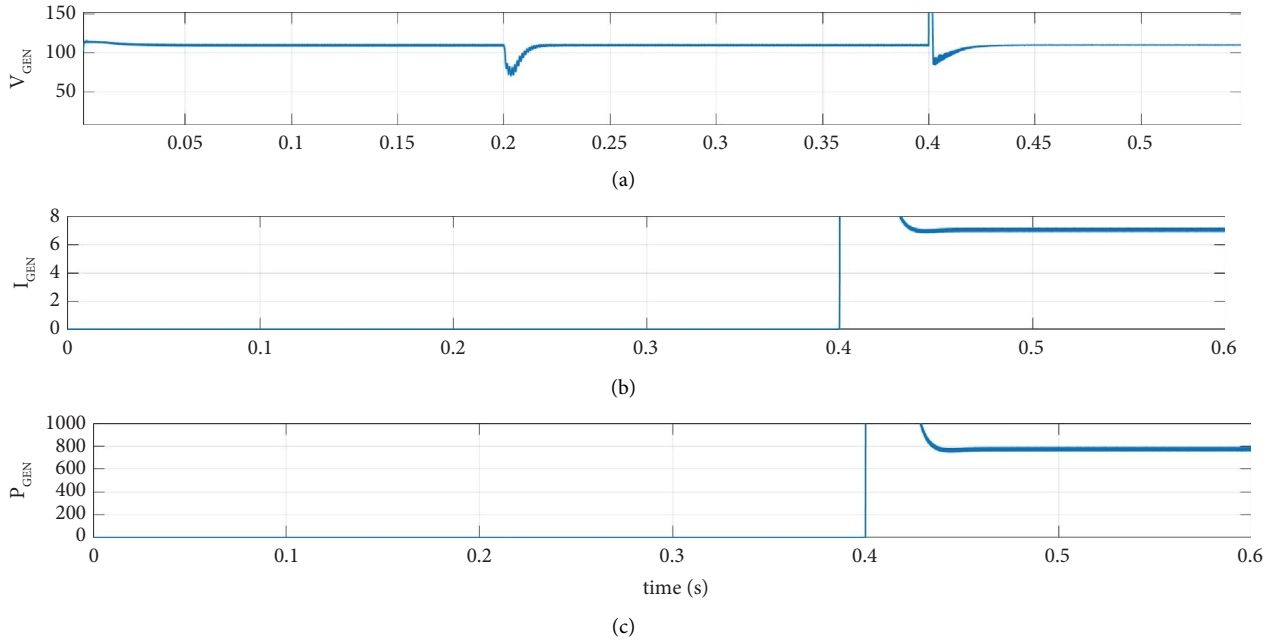


FIGURE 13: Simulation results (a) diesel generator voltage (b) diesel generator ESS current (c) diesel generator power.

TABLE 2: Hardware parameter values of 4S configuration.

Parameter	Value	Value
Boost inductance	4S	2.36 mH
DC filter capacitor	4S	200 μ F
Load resistor	4S	140 ohms
MOSFET 400 V, 10 A, N-channel		IRF740
Schottky diode 200 V, 10 A		MUR 10200
Maximum power PVC current (I_{mpp})		2.90 A
Maximum power PVC voltage (V_{mpp})		17.5 V
Maximum power PVC power (P_{mpp})		50 W
Open circuit PVC voltage (V_{oc})		21.8 V
Sort circuit PVC current (I_{sc})		3.20



FIGURE 14: Experimental results for proposed GWO-ANFIS MPPT method for 4S configuration. (a) Pattern 1. (b) Pattern 2.

To validate the effectiveness of the proposed MPPT, experiments were carried out on real PV array for both 4S. To create partial shading, transparent sheets of different shapes were placed on PV modules.

Figures 14(a) and 14(b) shows the PV voltage, PV current and PV power of GWO-ANFIS based MPPT control at 4S configuration with two different Pattern-1 and Pattern-2 respectively. The corresponding values are denoted in Table 3.

TABLE 3: Performance comparison of the proposed GWO-ANFIS MPPT method for 4S configuration.

Shading pattern	GP in watts	V_{PV}	I_{PV}	P_{PV} (W)	Track efficiency (%)
Pattern 1	108.2 W/75.5 V	75.7	1.41	106.74	98.65
Pattern 2	76.33 W/35.8 V	35.1	2.13	74.76	97.94

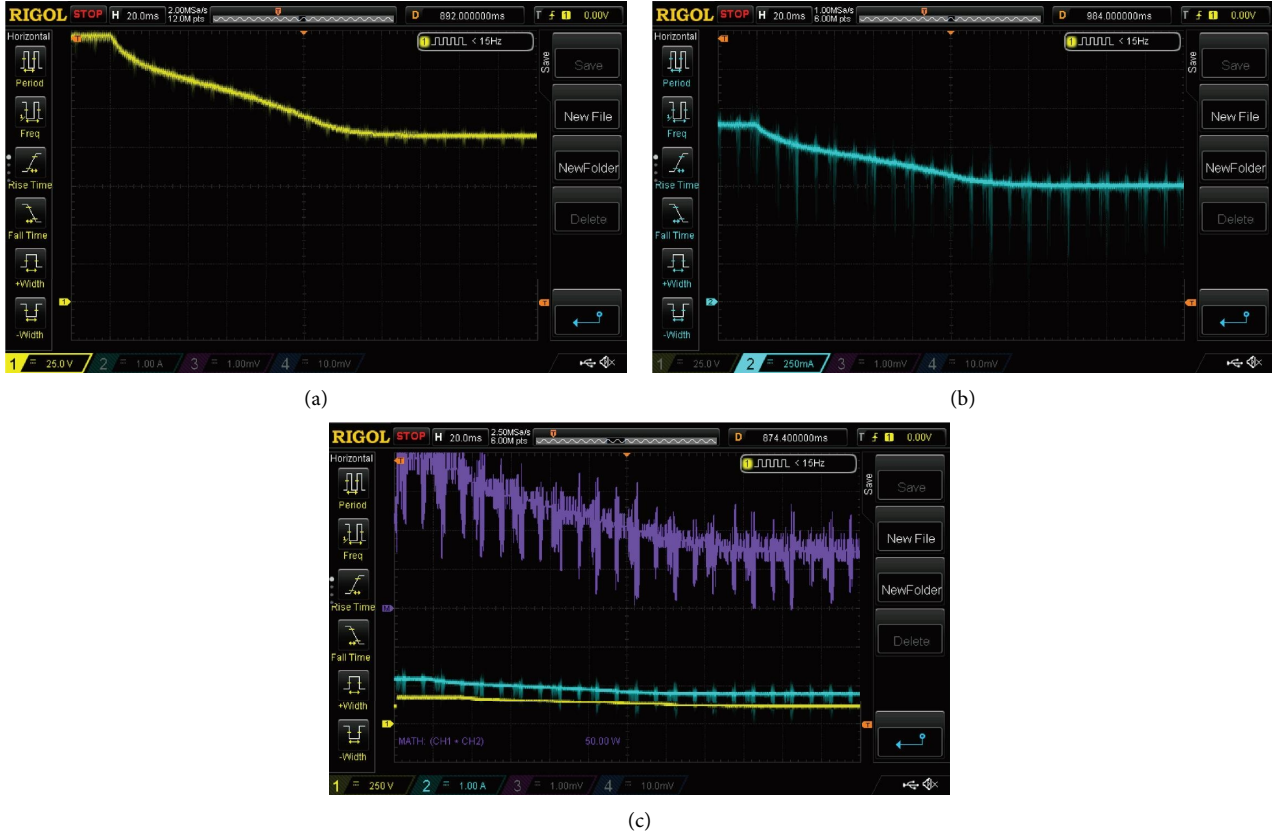


FIGURE 15: Experimental result of proposed GWO-ANFIS MPPT for pattern 2. (a) DC link voltage. (b) DC link current. (c) DC link power.

Figure 15. Shows the DC Voltage, DC current and DC power of Proposed GWO-ANFIS MPPT algorithm for Pattern2.

7. Conclusion

This article successfully built and simulated a charging station that use s a stand-alone PV system with an energy storage system to charge an EVs battery. The GWO-ANFIS method has been used with the MPPT controller. The P-V curve has several peaks due to partial shading; one GMPPs and many LMPPs. Heuristic approaches such as GWOs can readily capture the GMPPs before it starts hunting. The results showed that GWO-ANFIS with PSCs change re-initialization is the optimum approach for tracking the dynamic GMPPs. The combination of the ANFISs controller and the GWOs method significantly reduced output power oscillations. The charge and discharge phases of the battery energy storage were also effectively modelled and simulated employing the bidirectional converter. A bidirectional

converter logic controller has also been created and simulated. The logic controller's efficiency with the bidirectional controller was demonstrated by the findings. The suggested station's design and power management are discussed and evaluated in MATLAB/Simulink using three alternative modes of operation. The experimental verification is done for PV 4S configuration using GWO-ANFIS MPPT with Boost converter which proves that the maximum power is tracked in PSC at an efficiency 98.65%.

Data Availability

Data sharing not applicable to this article as no datasets were generated or analysed during the current study. No underlying data was collected or produced in this study.

Ethical Approval

In our work, no animals or human are involved.

Conflicts of Interest

The authors declare they have no conflicts of interest.

References

- [1] J. A. P. Lopes, F. J. Soares, and P. M. R. Almeida, "Integration of electric vehicles in the electric power system," *Proceedings of the IEEE*, vol. 99, no. 1, pp. 168–183, 2011.
- [2] A. S. B. Humayd and K. Bhattacharya, "A novel framework for evaluating maximum PEV penetration into distribution systems," *IEEE Transactions on Smart Grid*, vol. 9, no. 4, pp. 2741–2751, Jul 2018.
- [3] K. Clement-Nyns, E. Haesen, and J. Driesen, "The impact of charging plug-in hybrid electric vehicles on a residential distribution grid," *IEEE Transactions on Power Systems*, vol. 25, no. 1, pp. 371–380, 2010.
- [4] K. Qian, C. Zhou, M. Allan, and Y. Yuan, "Modeling of load demand due to EV battery charging in distribution systems," *IEEE Transactions on Power Systems*, vol. 26, no. 2, pp. 802–810, 2011.
- [5] J. Van Roy, N. Leemput, F. Geth, R. Salenbien, J. Buscher, and J. Driesen, "Apartment building electricity system impact of operational electric vehicle charging strategies," *IEEE Transactions on Sustainable Energy*, vol. 5, no. 1, pp. 264–272, 2014.
- [6] S. Shafiee, M. Fotuhi-Firuzabad, and M. Rastegar, "Investigating the impacts of plug-in hybrid electric vehicles on power distribution systems," *IEEE Transactions on Smart Grid*, vol. 4, no. 3, pp. 1351–1360, Sep 2013.
- [7] C. B. Harris and M. E. Webber, "The impact of vehicle charging loads on frequency regulation procurements in ERCOT," in *Proceedings of the ISGT 2014*, pp. 1–5, Washington, DC, USA, February, 2014.
- [8] E. Sortomme, M. M. Hindi, S. D. J. MacPherson, and S. S. Venkata, "Coordinated charging of plug-in hybrid electric vehicles to minimize distribution system losses," *IEEE Transactions on Smart Grid*, vol. 2, no. 1, pp. 198–205, Mar 2011.
- [9] M. Akmal, A. Jawad, and A. Al Tarabesheh, "Design and simulation solar grid-connected charger for electrical vehicles," in *Proceedings of the UKSim AMSS 20th International Conference on Modelling & Simulation*, Cambridge, UK, March 2018.
- [10] G. I. Rashed, "Applicability study of battery charging stations in off-grid for rural electrification – the case of Rwanda," in *Proceedings of the International Conference on Power Generation Systems and Renewable Energy Technologies (PGSRET)*, pp. 1–6, Istanbul, Turkey, August 2019.
- [11] M. Ishaq, U. H. Ibrahim, and H. Abubakar, "Design of an off grid photovoltaic system: a case study of government technical college, wudil, kano state," *International Journal of Scientific & Technology Research*, vol. 2, no. 12, pp. 172–181, December 2013.
- [12] F. J. Vivas, A. De las Heras, F. Segura, and J. M. Andújar, "A review of energy management strategies for renewable hybrid energy systems with hydrogen backup," *Renewable and Sustainable Energy Reviews*, vol. 82, pp. 126–155, Feb. 2018.
- [13] A. Amjad, L. Wuhua, and H. Xiangning, "Simple moving voltage average incremental conductance MPPTs technique with direct control method under nonuniform solar irradiance conditions," *International Journal of Photoenergy*, vol. 2015, Article ID 479178, 12 pages, Jan. 2015.
- [14] D. Verma, S. Nema, A. M. Shandilya, and S. K. Dash, "Maximum power point tracking (MPPTs) techniques: recapitulation in solar photovoltaic systems," *Renewable and Sustainable Energy Reviews*, vol. 54, pp. 1018–1034, Feb. 2016.
- [15] B. Subudhi and R. Pradhan, "A comparative study on maximum power point tracking techniques for photovoltaic systems," *IEEE Transactions on Sustainable Energy*, vol. 4, no. 1, pp. 89–98, Jan. 2013.
- [16] M. A. Elgendy, B. Zahawi, and D. J. Atkinson, "Assessment of perturb and observe MPPT algorithm implementation techniques for PV pumping applications," *IEEE Transactions on Sustainable Energy*, vol. 3, no. 1, pp. 21–33, Jan. 2012.
- [17] M. A. Elgendy, B. Zahawi, and D. J. Atkinson, "Operating characteristics of the P&O algorithm at high perturbation frequencies for standalone PV systems," *IEEE Transactions on Energy Conversion*, vol. 30, no. 1, pp. 189–198, Jun. 2015.
- [18] M. A. Elgendy, B. Zahawi, and D. J. Atkinson, "Assessment of the incremental conductance maximum power point tracking algorithm," *IEEE Transactions on Sustainable Energy*, vol. 4, no. 1, pp. 108–117, Jan. 2013.
- [19] M. A. G. de Brito, L. Galotto, L. P. Sampaio, G. d. A. e Melo, and C. A. Canesin, "Evaluation of the main MPPT techniques for photovoltaic applications," *IEEE Transactions on Industrial Electronics*, vol. 60, no. 3, pp. 1156–1167, Mar. 2013.
- [20] A. S. Mahdi, A. K. Mahamad, S. Saon, T. Tuwoso, H. Elmunsyah, and S. W. Mudjanarko, "Maximum power point tracking using perturb and observe, fuzzy logic and ANFIS," *SN Applied Sciences*, vol. 2, no. 1, 2020.
- [21] R. Kotti and W. Shireen, "Efficient MPPT control for PV systems adaptive to fast changing irradiation and partial shading conditions," *Solar Energy*, vol. 114, pp. 397–407, Mar. 2015.
- [22] K. Ishaque, Z. Salam, M. Amjad, and S. Mekhilef, "An improved particle swarm optimization (PSO)-Based MPPT for PV with reduced steady-state oscillation," *IEEE Transactions on Power Electronics*, vol. 27, no. 8, pp. 3627–3638, 2012.
- [23] S. Mirjalili, S. M. Mirjalili, and A. Lewis, "Grey wolf optimizer," *Advances in Engineering Software*, vol. 69, pp. 46–61, 2014.
- [24] L. L. Jiang, D. L. Maskell, and J. C. Patra, "A novel ant colony optimization-based maximum power point tracking for photovoltaic systems under partially shaded conditions," *Energy and Buildings*, vol. 58, pp. 227–236, 2013.
- [25] K. Sundareswaran, S. Peddapati, and S. Palani, "MPPTs of PV systems under partial shading conditions through a colony of flashing fireflies," *IEEE Transactions on Energy Conversion*, vol. 29, no. 2, pp. 463–472, Jun. 2014.
- [26] L. L. Jiang, R. Srivatsan, and D. L. Maskell, "Computational intelligence techniques for maximum power point tracking in PV systems: a review," *Renewable and Sustainable Energy Reviews*, vol. 85, pp. 14–45, 2018.
- [27] F. Belhachat and C. Larbes, "A review of global maximum power point tracking techniques of photovoltaic system under partial shading conditions," *Renewable and Sustainable Energy Reviews*, vol. 92, pp. 513–553, 2018.
- [28] A. A. Mohamed, H. Metwally, A. El-Sayed, and S. I. Selem, "Predictive neural network based adaptive controller for grid-connected PV systems supplying pulse-load," *Solar Energy*, vol. 193, pp. 139–147, 2019.
- [29] O. P. Pahari and B. Subudhi, "Integral sliding mode-improved adaptive MPPT control scheme for suppressing grid current harmonics for PV system," *IET Renewable Power Generation*, vol. 12, no. 16, pp. 1904–1914, 2018.

- [30] A. Kihal, F. Krim, A. Laib, B. Talbi, and H. Afghoul, "An improved MPPT scheme employing adaptive integral derivative sliding mode control for photovoltaic systems under fast irradiation changes," *ISA Transactions*, vol. 87, pp. 297–306, 2019.
- [31] S. Pareek and T. Kaur, "Hybrid ANFIS-PID based MPPTs controller for a solar PV system with electric vehicle load IOP conference series: materials science and engineering," *IOP Conference Series: Materials Science and Engineering*, vol. 1033, no. 1, Article ID 012012, 2021.
- [32] S. Padmanaban, N. Priyadarshi, M. Sagar Bhaskar, J. B. Holm-Nielsen, V. K. Ramachandaramurthy, and E. Hossain, "A hybrid ANFIS-ABC based MPPTs controller for PV system with anti-islanding grid protection: experimental realization," *IEEE Access*, vol. 7, Article ID 103377103389, 2019.
- [33] R. Kumar, S. Khandelwal, P. Upadhyay, and S. Pulipaka, "Global maximum power point tracking using variable sampling time and pv curve region shifting technique along with incremental conductance for partially shaded photovoltaic systems," *Solar Energy*, vol. 189, pp. 151–178, 2019.
- [34] K. Muralidhar and S. Susovon, "An adaptive voltage sensor based MPPTs for photovoltaic systems with SEPIC converter including steady state and drift analysis," *IEEE Transactions on Industrial Electronics*, vol. 62, no. 12, pp. 992–1000, Dec 2015.
- [35] S. Naeim, "Design of a DC/DC buck converter for ultra-low power applications in 65nm CMOS Process," Master's thesis, Linköping University, Linköping, Sweden, 2012.
- [36] C. Kuei-Hsiang, T. Ming-Chang, H. Chun-Hao, L. Yang-Guang, and H. Liang-Chiao, "Design and implementation of a bidirectional DC-DC converter for stand-alone photovoltaic systems," *International Journal of Computers, Communications & Control*, vol. 2, no. 3, 2013.
- [37] S. K. Cherukuri and S. R. Rayapudi, "Enhanced grey wolf optimizer based MPPT algorithm of PV system under partial shaded condition," *International Journal of Renewable Energy Development*, vol. 6, no. 3, 2017.
- [38] F. Liu, P. Yadav, A. M. Baschnagel, and A. B. McMillan, "MR-based treatment planning in radiation therapy using a deep learning approach," *Journal of Applied Clinical Medical Physics*, vol. 20, no. 3, pp. 105–114, 2019.
- [39] S. Remya, J. E. Paul, and D. B. Nair, "ANFIS based SEPIC converter for maximum power point tracking of photovoltaic modules," *International Journal of Engineering Trends and Technology*, vol. 30, no. 4, pp. 170–175, 2015.
- [40] M. S. Kumar, P. S. Manoharan, and R. Ramachandran, "Modelling and simulation of ANFIS-based MPPT for PV system with modified SEPIC converter," *International Journal of Business Intelligence and Data Mining*, vol. 15, no. 3, pp. 255–272, 2019.

Research Article

Analysis and Implementation of Sliding Mode Controller-Based Variable Frequency Drive Using the SCADA System

Belqasem Aljafari ¹, L. Ashok Kumar,² V. Indragandhi ³, and V. Subramaniaswamy ⁴

¹Department of Electrical Engineering, Najran University, Najran 11001, Saudi Arabia

²Department of Electrical Engineering, PSG College of Technology, Coimbatore, India

³School of Electrical Engineering, Vellore Institute of Technology, Vellore, India

⁴School of Computing, SASTRA University, Thanjavur, India

Correspondence should be addressed to V. Indragandhi; indragandhi.v@vit.ac.in and V. Subramaniaswamy; vsubramaniaswamy@gmail.com

Received 13 July 2022; Revised 6 September 2022; Accepted 11 October 2022; Published 18 November 2022

Academic Editor: Sheng Du

Copyright © 2022 Belqasem Aljafari et al. This is an open access article distributed under the Creative Commons Attribution License, which permits unrestricted use, distribution, and reproduction in any medium, provided the original work is properly cited.

Vector control of an asynchronous machine is traditionally accomplished by analogizing it to a separately excited DC machine. It provides decoupled torque and flux control that is perpendicular to each other, ensuring that neither vector interferes with the other. So, despite their close interconnection, torque and speed control are accomplished separately. The rotor flux is aligned with the direct axis of the synchronously rotating reference frame to achieve this. The PI controllers are critical in achieving the variable frequency drive (VFD) desired topology. The system employs three types of controllers: flux, speed, and torque. The flux controller is easy to tune, but the speed and torque controllers are more difficult to tune because the speed controller's output is the torque controller's reference signal. Furthermore, there is no well-defined method for tuning the controllers in a vector control system. However, perfect tuning is required for the machine's better dynamic behavior. It is clear from the above analysis that system identification is critical for tuning PI controllers. However, as an asynchronous machine, obtaining a decoupled system transfer function is extremely difficult. To solve this problem, the proposed system combines a seven-level pulse width modulation (PWM) inverter for vector control of a three-phase asynchronous nonstandard induction machine used in critical applications in nuclear power plants with a sliding mode control technique that eliminates the complexity of PI tuning. A second-order sliding mode controller could be used in the future to reduce the chattering and parameter variation effects. This controller can be enhanced with fuzzy logic principles to make it more robust and reliable, allowing it to be used in future drive designs for high-rating motors with critical applications.

1. Introduction

In many ways, the induction motor outperforms a separately excited DC motor in terms of performance, power-to-weight ratio, high-speed capability, low starting cost, high dependability, and robustness. The DC motor with a converter and a simple controller is the only option for most modern and superior industrial applications. However, DC motor face some unique challenges, such as commutating and maintenance. The DC motor has a few drawbacks, including a low torque-to-weight ratio and a lower unit capacity. AC motors, particularly induction motors, on the other hand,

because of their simple and rugged structure, high torque-to-weight ratio, and reliability, are well suited to mechanical drives. Control, however, is extremely difficult due to the combined effect of flux and the torque component of the current. The scalar control only shows the extent of the control variable's variation. To regulate the speed of an induction motor, a variable voltage, variable frequency power source is required. Maintaining the same terminal voltage to frequency proportion is critical in the v/f control procedure. The scalar control procedure has excellent steady-state performance but poor transient performance [1]. Voltage/frequency control keeps the stator flux linkage

in a steady state by preventing flux and torque from decoupling. As a result of the coupling effect, the drive's transient response is poor. By changing both components independently, the induction motor can be considered a separately excited DC motor [2, 3]. The vector control is accomplished by dividing the stator current into two orthogonal components: one is magnetizing current or the flux component of current, which is towards the flux linkage, and the other is the torque component of current, which is perpendicular to the flux linkage. The vector control or field-oriented control method can be divided into two types based on the flux acquisition method: direct and indirect.

Implementing various types of field-oriented control requires a variety of techniques. The majority of the methodologies require an exact estimate of the position of the rotor or speed. It necessitates the use of speed sensors such as shaft-mounted tachogenerators or digital shaft encoders [4, 5]. The speed sensors raise the drive's cost and size, reduce system reliability, and necessitate extra care when measuring noise. The direct field orientation method requires the rotor flux magnitude which is measured by using hall effect sensors or search coils. The performance and accuracy of the drive system are degraded by the hall effect sensors. At slower speeds, assessing rotor flux by integrating open-loop machine voltages is complicated. Indirect field orientation is straightforward and recommended. Its effectiveness is strongly dependent on accurate knowledge of machine parameters. The above issues have been the focus of induction motor control research. Many studies have been published on assessing rotor flux and speed from terminal voltages and currents rather than taking measurements. This removes the flux or speed sensor, allowing for sensor-free control [5–7].

The major problem with terminal quantity-based flux observers is their machine parameter's sensitivity, particularly stator resistance and rotor resistance of the voltage model flux observer and current model flux observer, respectively. To overcome this issue, different control strategies are attempted to enhance the estimation of rotor flux. Some of them are discussed further [8, 9]. The Kalman filter algorithm as well as its modifications are reliable observers for both linear and nonlinear systems. A modified Kalman filter is used to estimate the speed of induction motor drives which uses a vector controller. Unfortunately, this method has a number of drawbacks, including high computational demands and difficult design and tuning procedures. The rotor saliency method is used for determining the rotor position and speed using the signal injection technique. Stator terminals are injected with high-frequency signals. Appropriate signal processing and filtering of the high-frequency stator current detect the saliencies that are induced in the stator model of the induction motor. These techniques have been demonstrated to have the ability for a range of speeds and parameter-insensitive sensorless control, particularly at low speeds.

The inverter switching state is selected based on the flux position and errors in flux and torque, which are obtained in direct self-control (DTC). Fuzzy logic and artificial neural networks (ANN) have recently received a lot of attention to

address the issues of nonlinearity and uncertainty of system parameters. The essential features of neural networks are their way to generate good models of nonlinear systems, their decentralized and multithreaded structure, which renders neural-based control methods quicker, their ease of implementation by software or hardware, and their capacity to learn and adapt to the practices of any real process. In the influence of environmental disturbances or when the IFO drive system experiences defective decoupling due to rotor time constant variations, fuzzy controllers have been shown to enhance measurement accuracy [10–12]. Because fuzzy logic and neural networks have better tracking properties than traditional controllers, they are getting popular as estimators and controllers for a wide range of industrial applications.

The vector control's primary goal is to achieve decoupling. Desirable decoupling will not be achieved if the rotor parameters in use in the decoupling control law do not track their true values. Detuning of rotor variables due to a decrease in torque-producing abilities and magnetic saturation occurred by overexcitation reduces the efficiency of the motor drive. The dynamic control properties have also deteriorated. It is possible to achieve decoupling by adjusting parameters in real time, but it is a very difficult and complex process. Various online tuning methods for mitigating the severity of rotor variable variations have been reported. The rotor parameter detuning problem can be solved with a robust control technique. Apart from the aforementioned issue, induction motor drives have a number of other issues that demand the use of a powerful control technique. Load torque disruptions, parameter estimation in the model used in controller design and analysis, and the necessity to track complex paths rather than just step changes are all examples of these [13, 14]. A robust control method is required in these circumstances. One such method is sliding mode control. A sliding mode controller is appropriate for a specific type of nonlinear system. In the existence of modeling errors, parameter changes, and disruptions, this can be used if the upper bounds of their actual values are known. Certain plant uncertainties or the use of a simplified depiction of system dynamics can lead to inaccuracies in modeling. Sliding mode controller design addresses the issue of maintaining stability and performance in the existence of modeling errors in a structured way [15, 16].

The tracking control of motors and robot manipulators with a wide range of mechanical loads is best suited to the sliding mode control. Induction motors, known as actuators, should obey complex paths which are indicated for manipulator movements. When compared to adaptive controllers for parameter estimation, sliding mode controllers have the advantage of being computationally simple and robust to parameter variations. The disadvantage of sliding mode control is that it causes a large and abrupt change in control variables during the process, putting the system under a lot of stress. It also causes the system states to chatter. Soto, Yeung, and Utkin implemented sliding mode control to the induction motor drive. Control methods are applied to an indirect vector-controlled induction machine in a sliding mode for position and speed control. For

induction motor drives, adaptive input-output linearizing control with a sliding mode is addressed. The sliding mode controller is a great pick for dealing with that sort of problem because the amplitude and speed of the motor flux are controlled separately by sliding mode controllers with variable switching gains in this case.

For the speed control of induction machines, traditional control systems such as PI control have been used. Traditional PI controllers are characterized by a large overshoot and a long settling time. To address these issues, sliding mode control has been used to control electrical drive systems. A sliding mode controller (SMC) is a nonlinear, high-speed switching, feedback control strategy for controlling nonlinear plants that is both effective and reliable. The SMC, on the other hand, is prone to chattering due to its discontinuous switching control [17, 18]. In this article, a sliding mode controller is meant to control the speed of an induction motor inputted by a three-phase voltage source multilevel inverter using the space vector pulse width modulation. The proposed method is validated by simulation results. Due to the widespread usage of induction motors in torque-controlled applications, such as electric automobiles, high-precision torque estimation and control of induction motor drives is a crucial study area [19–21].

The chapter describes the modeling of the induction motor, in section 3 the field-oriented control is presented followed by speed estimation is given in section 5. Section 6 discusses the design of the sliding mode controller, section 7 provides the simulation results, and the work is concluded in section 8.

2. Modelling of the Induction Machine

Even though an induction motor's construction is simple because of its nonlinear characteristics and interdependent behavior in the state-space model, the speed control is very complex compared to DC Motors. Modern controllers for AC motor drives have been developed in response to rapid updates and advancements in variable frequency inverters, as well as the application of control theory. Fitting numerical modeling of the motor to upgrade the controller structure is part of the design. A suitable three-phase induction motor model is required to investigate the entire induction motor drive system. The presumption that is considered for modeling induction motor is by disseminating the stator winding to produce MMF sinusoidally in the air gap, equal mutual inductances, and by ignoring voltage and current harmonics, magnetic circuit saturation, hysteresis losses, eddy current losses, and skin effects.

By rotating the reference frame's d-axis and the stationary reference frame's q-axis, the quantities are assumed to be balanced. The inverter's output voltage is

$$\begin{aligned} V_{sd}^* &= \left(K_p + K_i \frac{1}{s}\right) (i_{sd}^* - i_{sd}) - \omega_e \sigma L_s i_{sq}^*, \\ V_{sq}^* &= \left(K_p + K_i \frac{1}{s}\right) (i_{sq}^* - i_{sq}) + \omega_e \sigma L_s i_{sd}^* + \omega_e \frac{L_m}{L_r} \varphi_{rd}. \end{aligned} \quad (1)$$

3. The Field Oriented Control

The flux component (d-axis component) of the stator current, i_{ds} , is aligned in the direction of rotor flux, and the torque component of the stator current, i_{qs} , is aligned in the direction perpendicular to it to achieve field orientation along the rotor flux. The slip frequency necessary to acquire indirect field orientation is given by

$$\omega_{sl} = \omega_e - P\omega_r = a_5 \frac{i_{qs}}{\varphi_{dr}}, \quad (2)$$

where

$$a_5 = \frac{R_r L_m}{L_r}.$$

Decoupling of torque and flux is assured in field-oriented control, and it can be controlled. The indirect field orientation control, however, is extremely parameter sensitive owing to the existence of the rotor time constant (R_r/L_r) in equation (23). Erratic parameter variations, external load disturbances, and nonlinear dynamics all have a negative impact on the drive system's control performance.

4. Estimation of Speed

It is better to avoid using a speed sensor because of its price, size of the drive, reliability, and immunity to noise. So, designing and implementing shaft sensorless adjustable speed drive have become an emerging research topic. The speed data required in the presented control technique are estimated using the algorithm described in this section. The speed of the motor is determined by the difference between the slip speed and the synchronous speed. Stator flux components are being used to estimate synchronous speed because they have greater accuracy than rotor flux components.

The speed of the rotor is determined by synchronous frequency or slip frequency. The proposed speed estimation scheme anticipates the synchronous frequency, and it is assumed that the slip frequency is a command.

Figure 1(a) shows the components of the rotor flux vector in the stationary reference frame, and from this, the electrical angle of the rotor flux vector is given by

$$\theta_{\varphi_r} = \tan^{-1} \frac{\varphi_{\beta r}}{\varphi_{\alpha r}}. \quad (3)$$

The instantaneous angular frequency is given by

$$\omega_e = \dot{\theta}_{\varphi_r} = \frac{\varphi_{\alpha r} \dot{\varphi}_{\beta r} - \varphi_{\beta r} \dot{\varphi}_{\alpha r}}{\varphi_{\alpha r}^2 + \varphi_{\beta r}^2}. \quad (4)$$

Figure 1(b) shows the components of the stator flux vector in the stationary reference frame, and from this, the electrical angle of the stator flux vector is given by

$$\theta_{\varphi_s} = \tan^{-1} \left(\frac{\varphi_{\beta s}}{\varphi_{\alpha s}} \right). \quad (5)$$

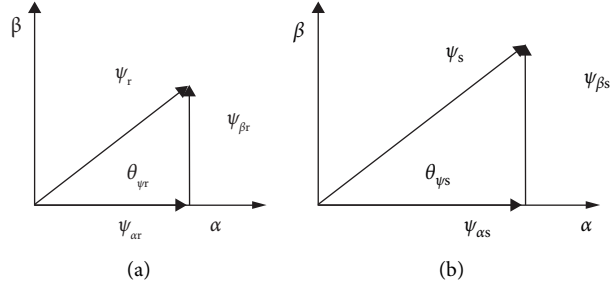


FIGURE 1: Phasor diagram for rotor and stator flux components.

The instantaneous angular frequency is given by the derivative of this rotor flux angle, which is as follows:

$$\omega_e = \dot{\theta}_{\psi_r} = \frac{\varphi_{\alpha s} \dot{\varphi}_{\beta s} - \varphi_{\beta s} \dot{\varphi}_{\alpha s}}{\varphi_{\alpha s}^2 + \varphi_{\beta s}^2}. \quad (6)$$

Figure 2 shows a block diagram of the speed estimation method in conjunction with the sensorless speed control scheme.

The derivation helps to design modeling of the induction motor using Matlab Simulink, and it is used for control purposes. The simulation-based models of induction motors with PI control strategies are discussed. In the analytical summary, the induction motor model is provided in an arbitrary reference frame and analyzed in detail. Because vector-controlled drives must be understood and designed using a dynamic model of the machine under control, we derive the conditions for achieving indirect vector control. The speed estimate algorithm is thoroughly explored to deploy the sensorless technique in the current drive system. A brief overview of the multilevel inverter and its type was also discussed, as well as a brief explanation of the cascaded H-bridge inverter and its switching patterns.

5. Design of the Sliding Mode Controller

The derivations of sliding mode surface gain and relevant control laws to determine the speed tracking property are presented in this section. A variable sliding mode control structure is primarily an adaptive nonlinear control that provides stable performance in the face of parameter changes and load torque disturbances. It can be used on either a linear or nonlinear system. The drive reaction is forced to track or slide along a specified trajectory or benchmark model in sliding mode control, despite system parameter variation and load disturbance, using a switching control algorithm. The control DSP identifies the actual trajectory's departure from the reference trajectory and adjusts the switching strategy to restore tracking (Figure 3).

The merits of sliding mode control are system functions similar to a reduced-order system, which is adaptable to parameter variations, implications, and abnormalities, and the time required for convergence is confined. The demerits of sliding mode control are chattering at a high frequency. Because of inertia, the actuator cannot always respond at that speed, and due to irregular input, the structure's cost is

considerable. The design of sliding mode control is divided into two stages. The first is the selection of stable hyperplanes in the state/error space on which movement should be governed, referred to as the switching function, and the identified sliding surface is then made appealing by using the suitable control law design in the second step.

An induction motor's mechanical equation is expressed as

$$J\omega_m^* + B\omega_m + T_L = T_e. \quad (7)$$

Here, J is the inertia constant, and B is the viscous friction coefficient of the induction motor; T_L is the external load. ω_m is the rotor mechanical speed in angular frequency, which is proportional to the electrical speed of the rotor $\omega_m = 2\pi\omega_p$ where p is the number of poles and T_e is the produced torque of an induction motor. Substituting (8) in equation (34), the mechanical equation becomes

$$\omega_m^* + a\omega_m + f = bi_{qs}, \quad (8)$$

where

$$\begin{aligned} a &= \frac{B}{J}, \\ b &= \frac{K_T}{J}, \\ f &= \frac{T_L}{J}. \end{aligned} \quad (9)$$

The mechanical equation with uncertainties is

$$\omega_m^* = -(a + \Delta a)\omega_m - (f + \Delta f) + (b + \Delta b)i_{qs}, \quad (10)$$

where Δa , Δb , and Δf indicate the uncertainties of the terms a , b , and f , respectively, it should be emphasized that these uncertainties are unknown, and thus determining the upper bound with perfection is tough. The tracking speed error is given by

$$e(t) = \omega_m(t) - \omega_m^*(t). \quad (11)$$

Here, ω_m^* is the speed command of the rotor.

Taking the time derivative of the above equation produced,

$$\dot{e}(t) = \dot{\omega}_m - \dot{\omega}_m^* = -ae(t) + u(t) + d(t). \quad (12)$$

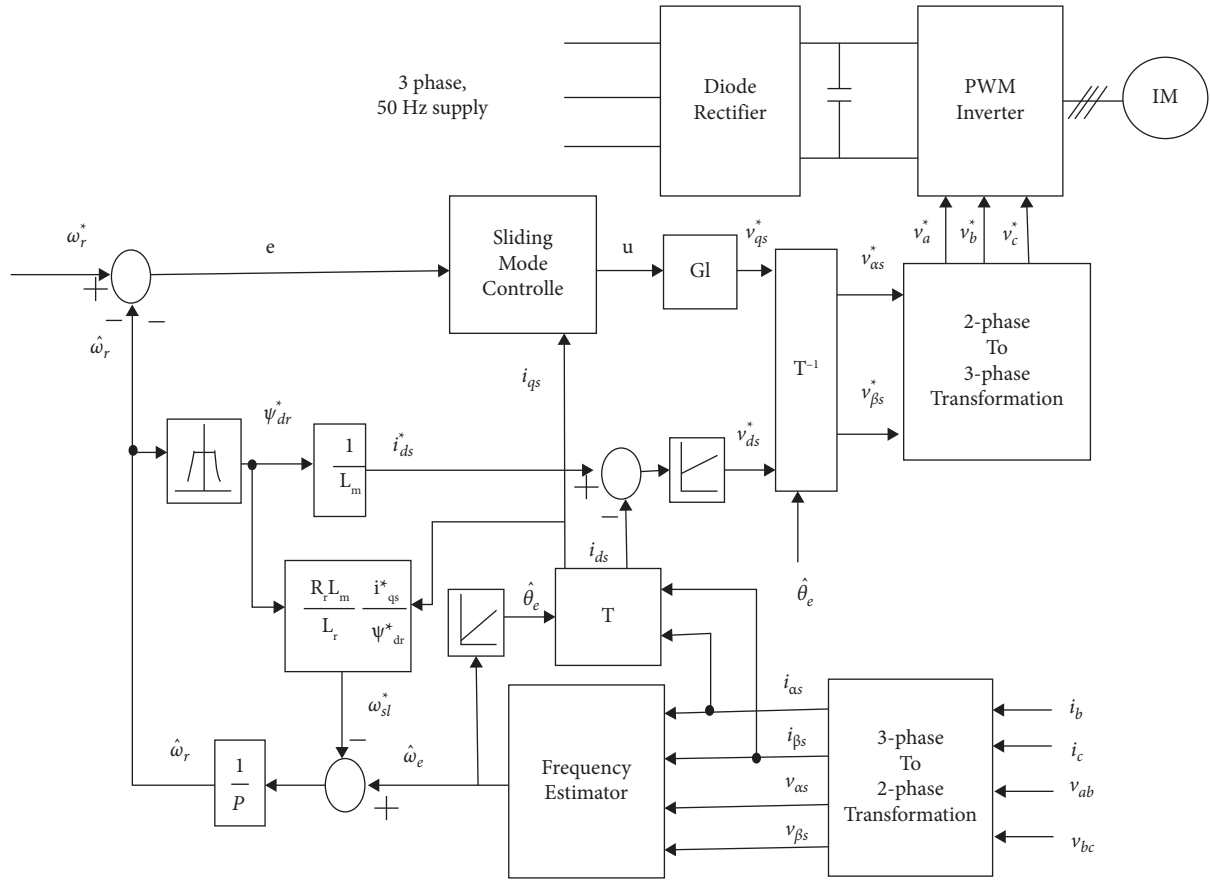


FIGURE 2: Sensorless speed control scheme for induction motor drive.

Here, the terms listed as follows have been gathered in the signal $u(t)$:

$$u(t) = bi_{qs}^*(t) - a\omega_m^*(t) - f(t) - \omega_m^*(t). \quad (13)$$

The signal $d(t)$ has been compiled with the uncertainty terms

$$d(t) = -\Delta a\omega_m(t) - \Delta f(t) + \Delta bi_{qs}(t). \quad (14)$$

To compensate for the system's uncertainties, a sliding adaptive control strategy is proposed. In sliding control theory, the switching gain must be built in order to achieve the sliding condition. An appropriate sliding gain needs to be chosen to compensate for the uncertainties in order to achieve this requirement. When choosing the sliding gain vector, an upper bound of parameter fluctuations, unmodeled dynamics, noise magnitudes, and other factors should be known, but these bounds are typically unknown or impossible to compute in practice. Setting the sliding gain to a high enough value could be a solution, but this technique could result in an extremely high control signal and considerably more activity control is required to meet the control aim. One technique to tackle this challenge is to estimate the gain and update it with an adaptation law to achieve the sliding condition.

The sliding variable $S(t)$ is defined with an integral component as

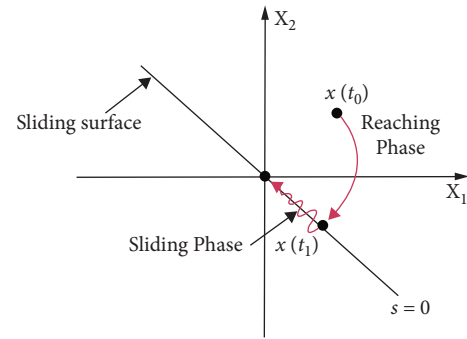


FIGURE 3: Sliding surface.

$$S(t) = e(t) + \int_0^t (a + k)e(\tau) d\tau. \quad (15)$$

Here, k is a constant gain and a is a previously defined parameter in equation (36).

The sliding surface $S(t) = 0$ (5.10).

$$u(t) = -ke(t) - \hat{\beta}(t)\gamma \text{sgn}(S). \quad (16)$$

Here, β is the estimated switching gain, γ is a positive constant, S is the sliding variable defined in equation (42), and $\text{sgn}(s)$ is the signum function. The switching gain β is adjusted according to the updating law, which is as follows:

$$\widehat{\beta} = \gamma|S|\widehat{\beta}(0) = 0. \quad (17)$$

The error signal is compared to the constant value and reference gain value. With the available value, the comparative function is created and analyzed. As per the theory, the obtained output is compared to the suitable control law and set to zero. The output is made to slide to the determined and designed slide surface when the condition is met.

The simulation provides the simulation-based design of sliding mode control to the induction motor with all supporting gain values. To lessen chattering, a limit layer of width θ is presented on both sides of the sliding line. As a result, the control gain inside the limit layer is reduced, resulting in a smooth control sign. Then, the control law of the equation $i_{qs}^* = -K \cdot \text{sgn}(S)$ modifies to the following equation:

$$i_{qs}^* = -K \cdot \text{sgn}\left(\frac{S}{\theta}\right),$$

where $\text{sat}\frac{S}{\theta} = \frac{S}{\theta}$ if $|S| \leq \theta$,

$\text{sgn}(S)$ if $|S| > \theta$.

(18)

To reduce this chattering, the sliding mode controller with a boundary layer as given by the following equation is

$$i_{qs}^* = \left\{ \frac{-\widehat{G} - \lambda \dot{e} + \ddot{w}r^*}{\widehat{b}} \right\} - K \text{sat}\left(\frac{S}{\theta}\right). \quad (19)$$

The outline and application of a sliding mode controller for induction motor control are shown. The sliding mode control hypothesis is quickly demonstrated, and the control law is inferred. The controller gain and bandwidth are dictated by several facts such as load variations, different rotor resistance, and so on. To lessen the chattering impact, the control law is altered, and the job summary is so presented (Figure 4).

6. Simulation Results and Discussion

The induction motor is a vertical, single-stage, top suction, free surface pump of a nonstandard machine as per IS325; the odd rating is to mitigate the torque requirement. The ratings of the motor are presented in Table 1.

The motor is mainly used in the core cooling of the nuclear plant, where the liquid sodium is used as a coolant, and the motor is operated at different speeds which are controlled by the drive mechanism. The design calculation for a 7-level cascaded H-Bridge inverter involves the determination of V_{dc} and I_{dc} . For the cascade bridge, a seven-level inverter is given in (Figure 5.). The line voltage and the line current of the inverter are $V_1 = 3150$ V and $I_1 = 804$ A, respectively. From this, the phase voltage is derived as $V_p = 607$ V. The $V_{dc} = 1206$ V, which is 15% more than the phase voltage, and $I_{dc} = 1206$ A, which is 15 percent more than the phase current. The sim module shows the arrangement of the IGBT cascaded H- bridge 7-level inverter

design for the drive system. Each bridge has the value of $V_{dc} = 909.32$ V and $I_{dc} = 1206$ A.

The single-phase seven-level inverter output is shown in Figure 6, and the filtered output is shown in Figure 7; the three-phase seven-level inverter output phase voltage fed to an induction motor is shown in Figure 8.

Figure 9 depicts the stator currents in three phases, while Figure 10 depicts the speed variation. The speed rises until it reaches 590 rpm. The voltage and current are FFT-analyzed, and the corresponding spectrums are shown in Figures 11 and 12, respectively. The magnitude of the fundamental voltage for a seven-level inverter-fed induction motor drive is 234.4 Volts, as can be seen. Total harmonic distortion is 3.51 percent, with a fundamental current magnitude of 91.15 Amperes. There is a 1.01 percent total harmonic distortion.

The THD generated by the seven-level inverter with the drive is found to be minimal. The simulation results for voltage, current, speed, and spectrum are shown. This drive system can be employed in industries that demand minimal harmonic output from variable-speed drives. The flux and speed control subsystem is shown in Figure 13 where PI tuning is used to control the speed.

The subsystem provides the control logic for park and clack transformation of the induction motor which provides the theta of the motor (Figure 14).

The inference of the waveform shows the presence of high peak current during starting of the PI tuning method, which is a main drawback in the system and is to be rectified. The current waveform is shown in Figure 15.

This section uses simulation examples to investigate the performance of the adaptive sliding-mode control in the aspect of speed regulation. Figure 16 shows the rotor speed tracking reference. The rotor speed tracks the reference (1500), where it provides smooth speed control.

The Simulink describes the SMC control for the nominal speed of the motor (Figure 17).

The waveform shown in Figure 18 proves that the SMC is robust irrespective of speed variation. When the reference is changed to the nominal speed of the motor, the rotor speed tracks it, which provides the elimination of high peak current while starting and smooth control.

The characteristics of the motor show that the time taken for the SMC control is 56 minutes which, when compared with existing system performance, the time taken is less, which proves that speed is smoothly controlled and, in turn, increases the entire system performance (Figure 19). Hence, the high peak current problem is rectified, and the objective of work is satisfied. Figures 20(a), 20(b) and Figure 21 show the HMI and SCADA screen of the VFD drive panel which gives a detailed description of the system configuration and status of the individual system implemented. The abnormalities are identified easily from the control center. The faculty areas can be separated from the live supply lines. The equipment protection is ensured by taking a quick decision based on the parameters displayed in the panel.

The snapshot provides the information of the drive system in the common control panel (CCP), which shows that the motor is in a running state (Figure 21). The figure is a

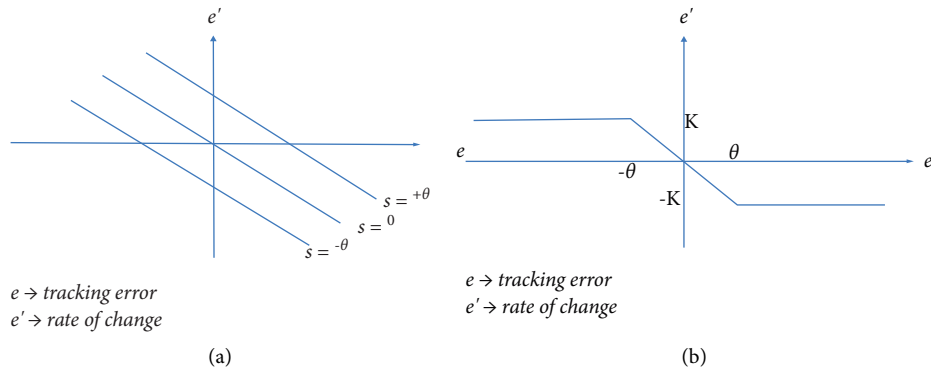


FIGURE 4: Sliding mode principle with the boundary layer.

TABLE 1: Ratings of the induction motor.

Sl.No.	Parameters	Values
1.	Voltage	415 V
2.	Star/delta	Star
3.	Pole	10
4.	Rated current	40 A
5.	Nominal speed	590 rpm
6.	Per phase stator resistance	0.0117 Ω
7.	Per phase rotor resistance	0.0234 Ω

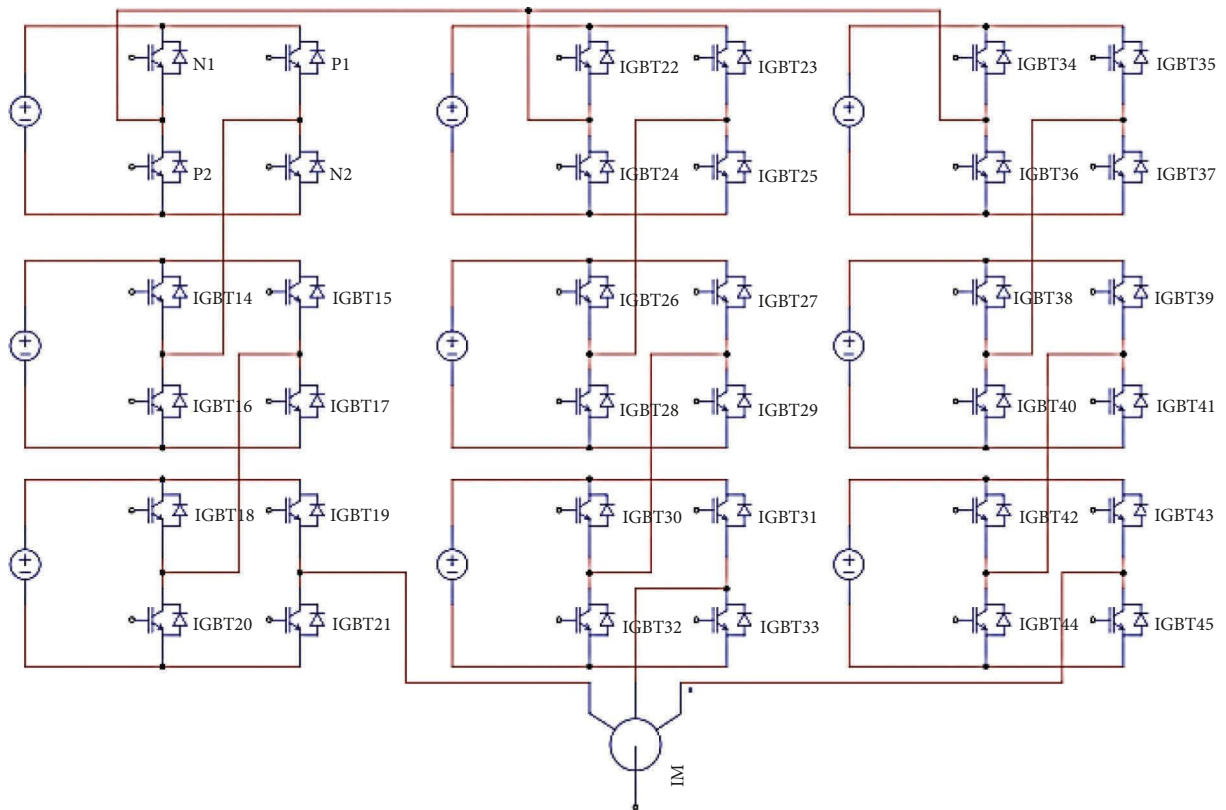


FIGURE 5: Cascaded H-bridge of seven-level inverter fed induction motor drive.

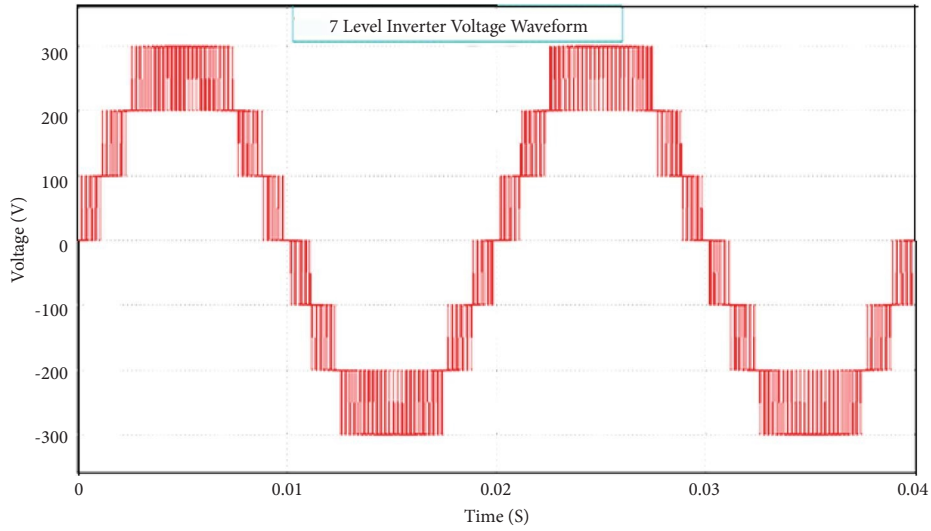


FIGURE 6: The output voltage waveform of a single-phase seven-level inverter.

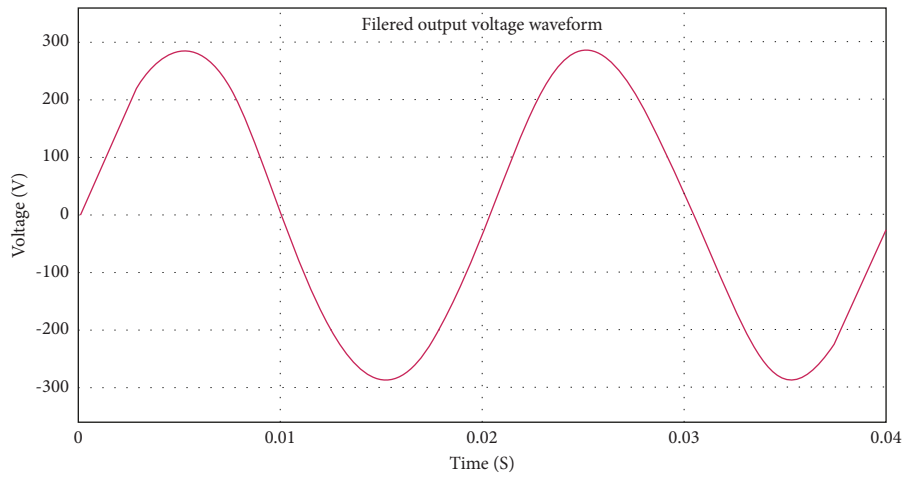


FIGURE 7: The output voltage waveform of a single phase seven-level inverter with a filter.

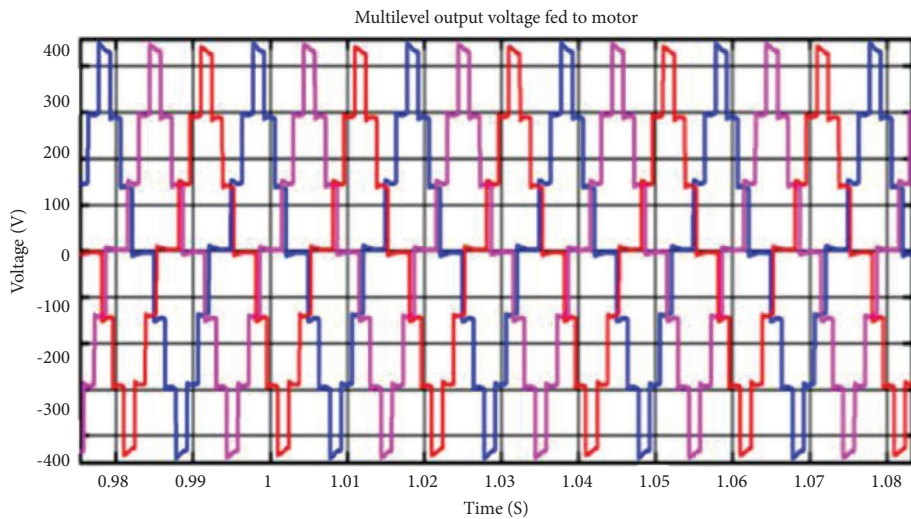


FIGURE 8: The output waveform of the seven-level inverter is fed to the motor with a filter.

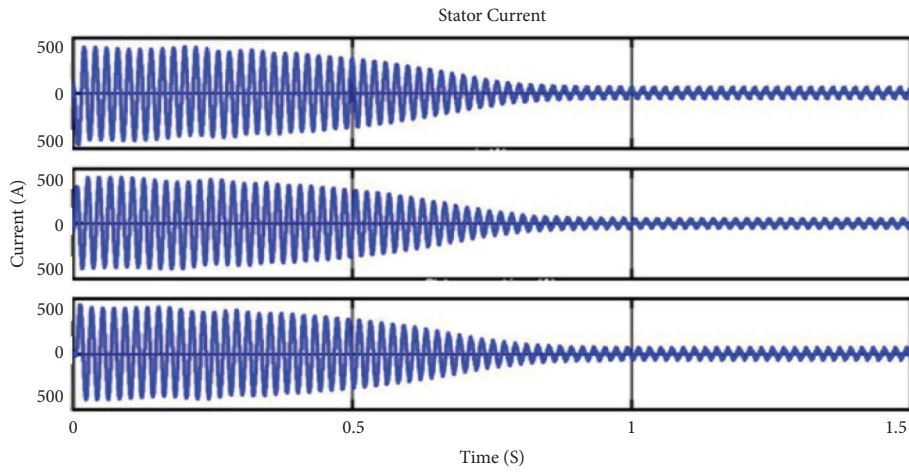


FIGURE 9: Three-phase stator current.

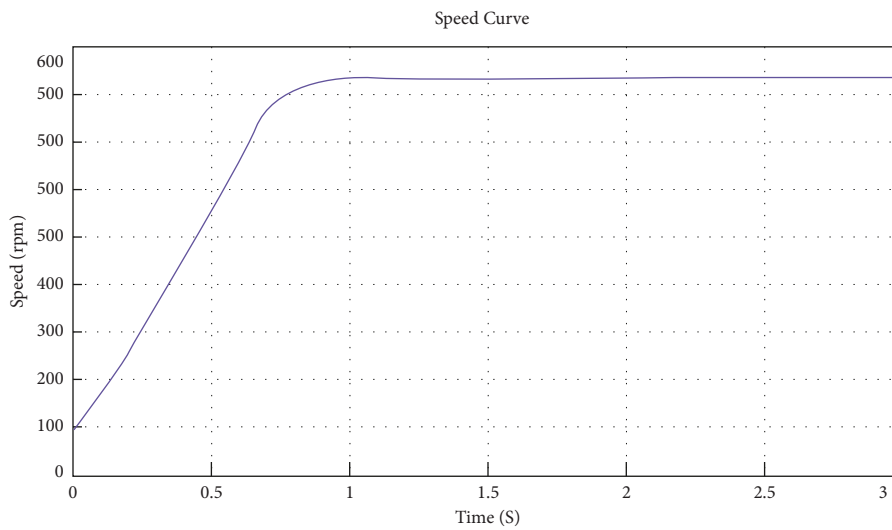


FIGURE 10: Speed vs time.

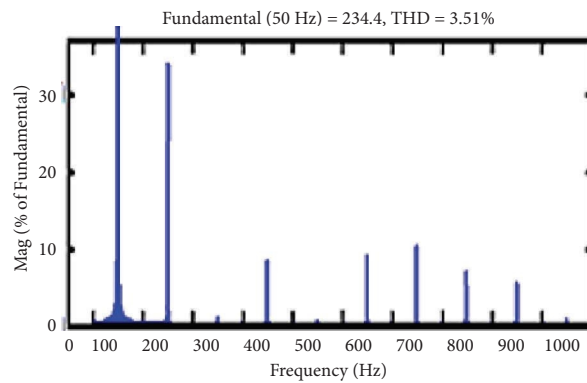


FIGURE 11: FFT analysis of voltage.

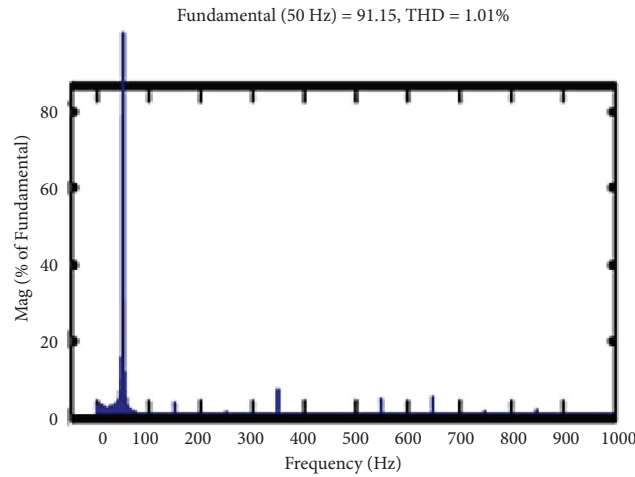


FIGURE 12: FFT analysis of current.

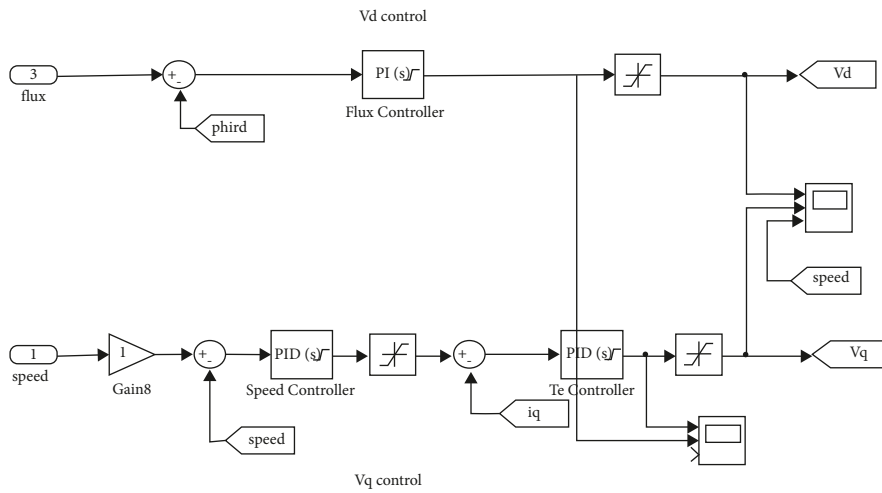


FIGURE 13: The subsystem of flux and speed control.

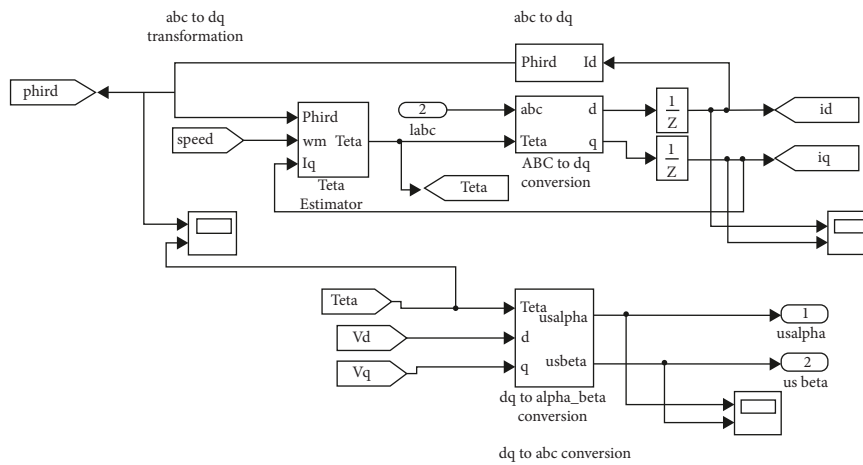


FIGURE 14: The subsystem of abc to dq transformation.

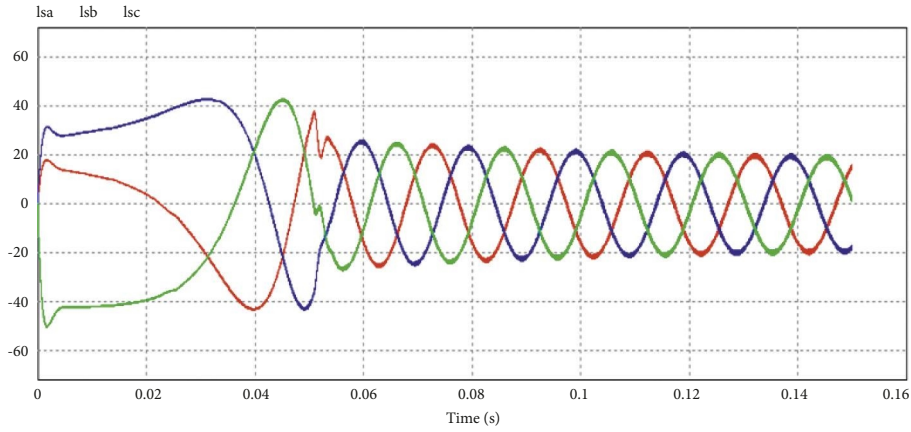


FIGURE 15: The current waveform of the motor.

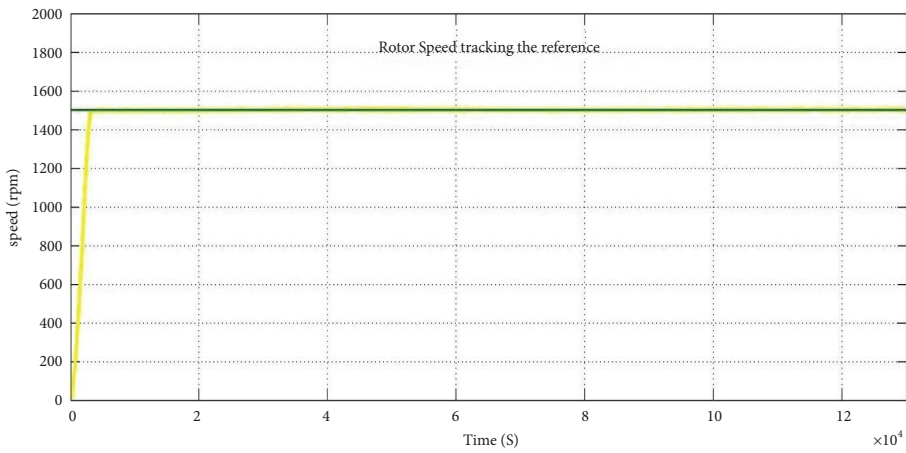


FIGURE 16: Rotor speed tracking waveform.

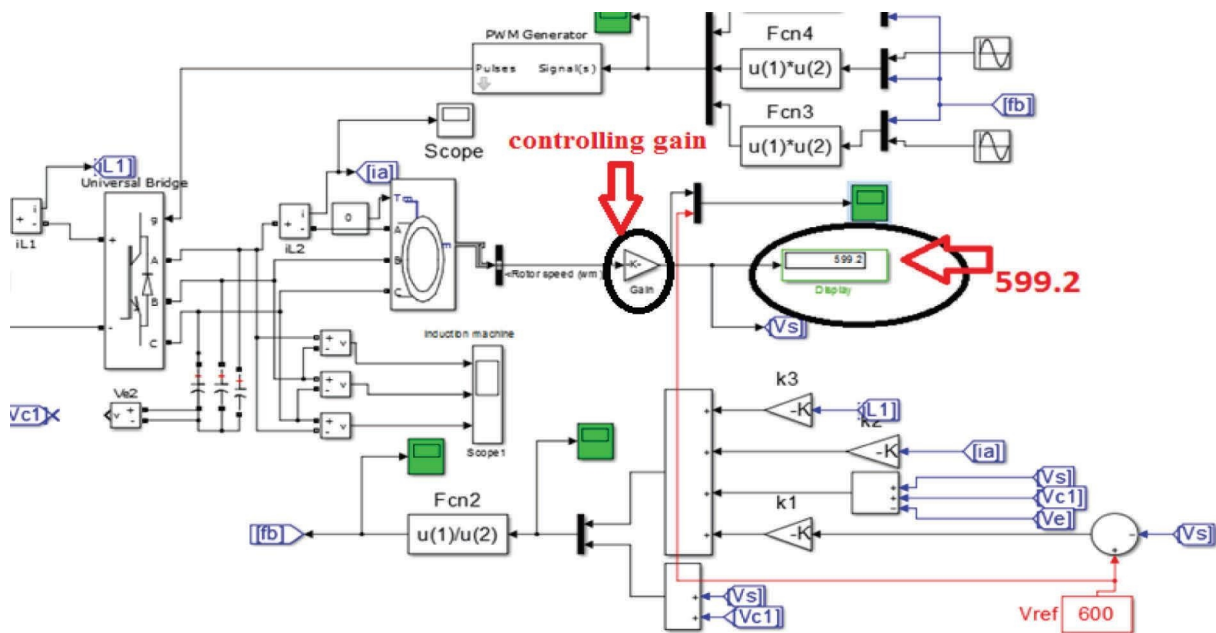


FIGURE 17: Simulink for SMC control for nominal speed of the motor.

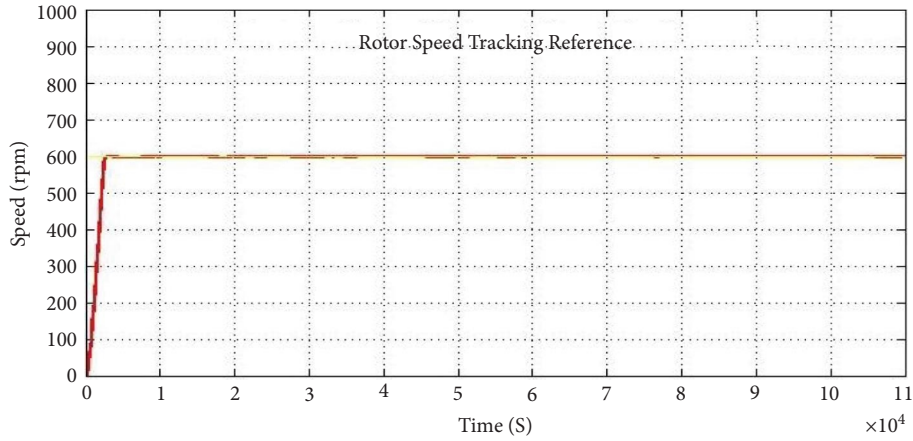
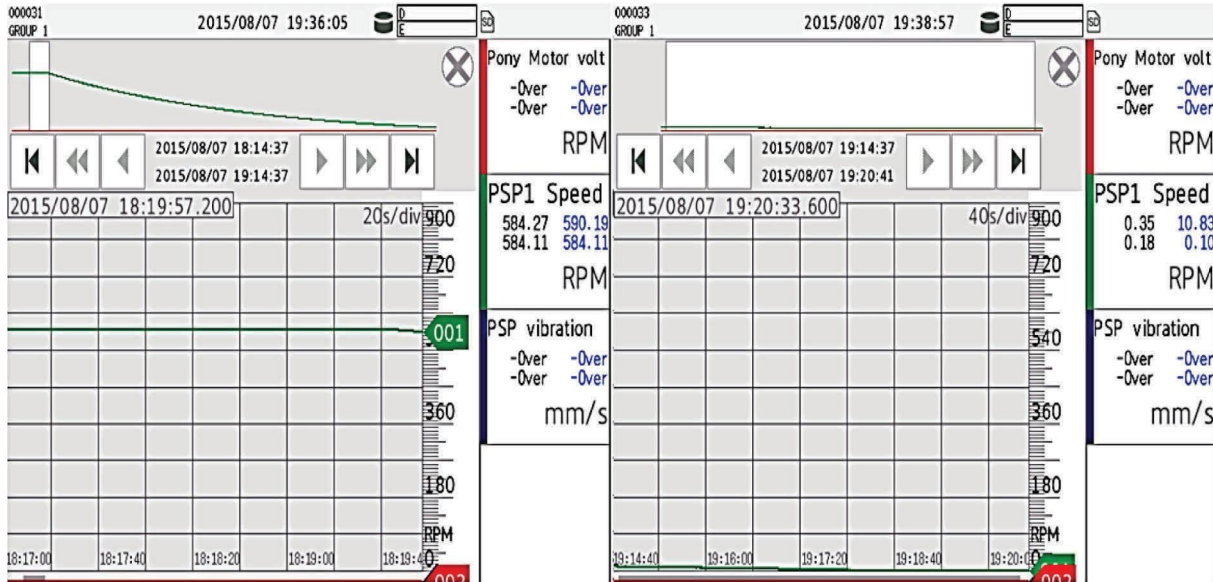


FIGURE 18: Rotor speed tracking the reference (600) of the nominal speed of the motor.



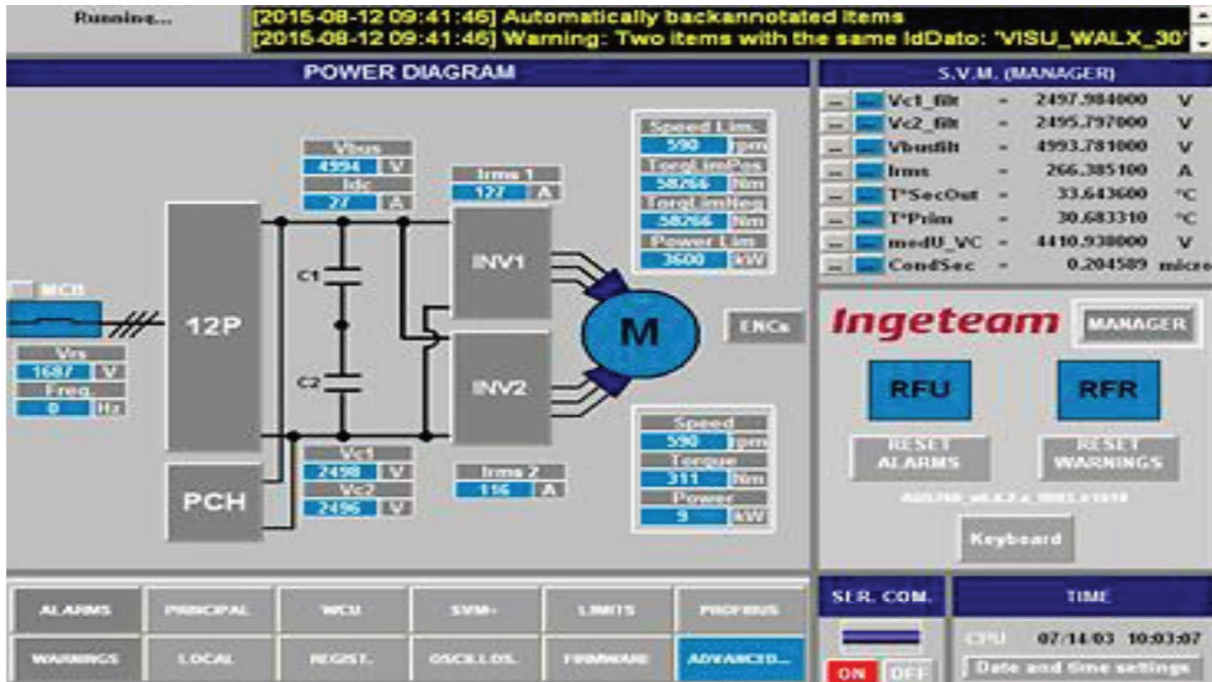
- Motor coast down time from 590RPM to Zero RPM is 56 Minutes

FIGURE 19: Characteristics of the motor with PI and SMC.

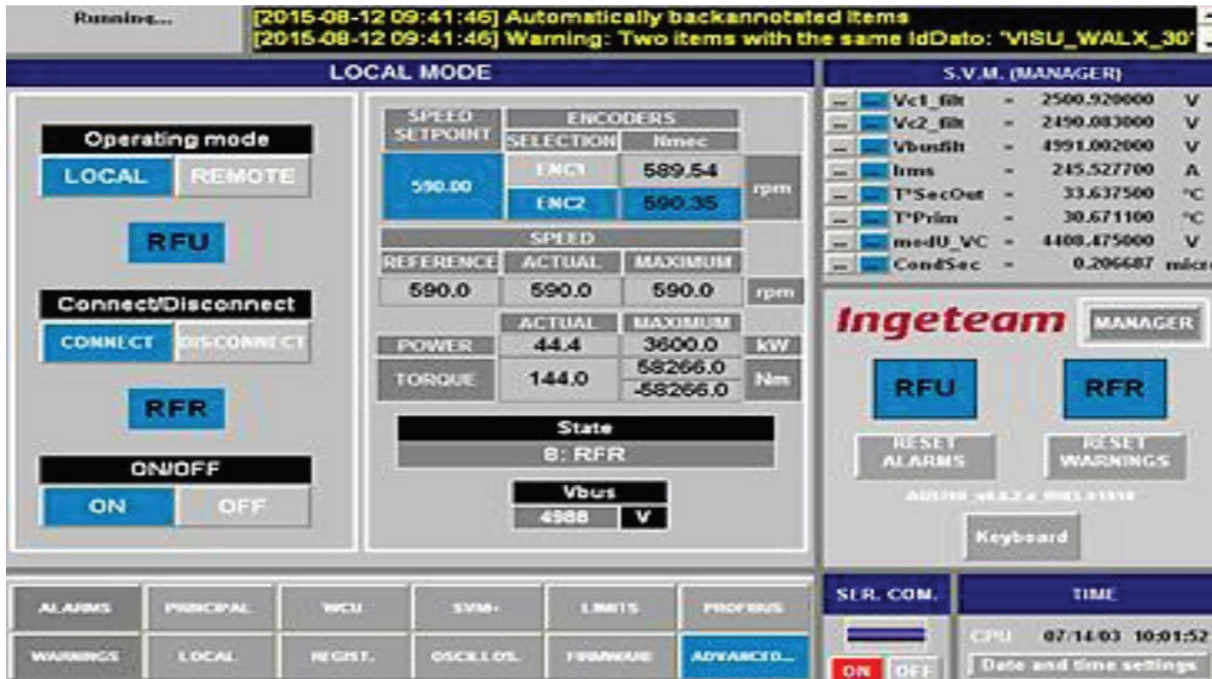
complete pictorial representation of the system from supply to drive. The power flow at any instant can be visualized.

The snapshot shown in Figure 22 provides information about the voltage, power, and current values and also gives an

indication about the working of the drive system. The functioning of the drive is identified from this screen. The fault in the cooling system, converter, controller, supply, and motor can be observed clearly.



(a)



(b)

FIGURE 20: HMI screen of the VFD panel in the power plant.

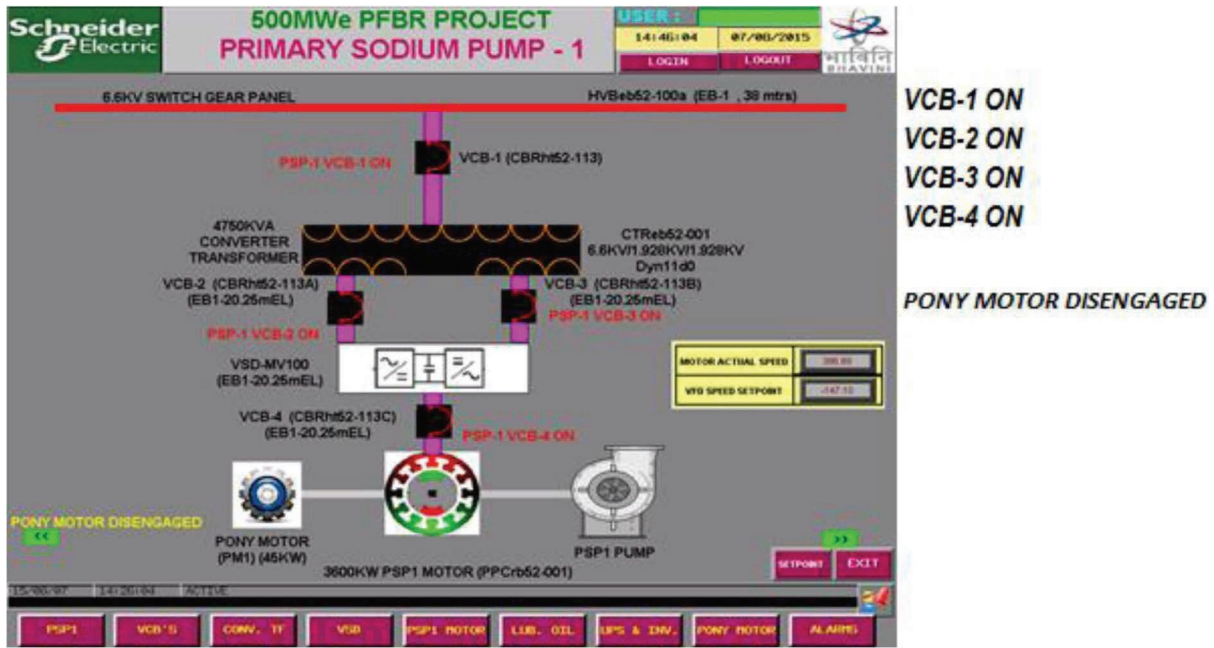


FIGURE 21: VFD running state screen conditions in the common control panel (CCP).

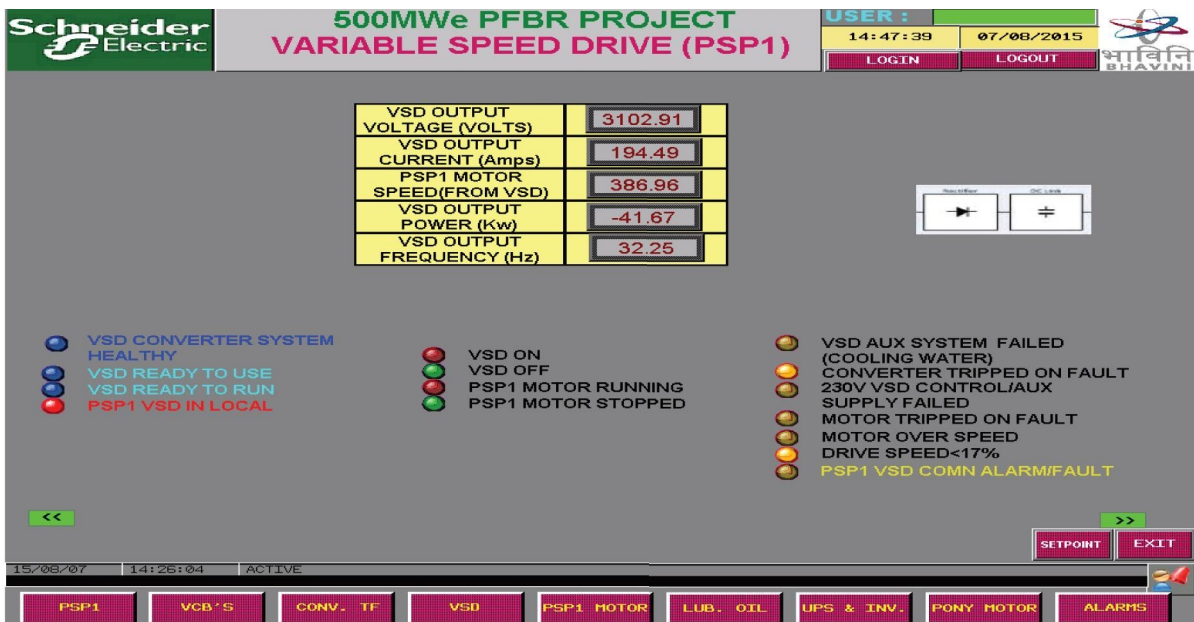


FIGURE 22: Drive output in SCADA.

7. Conclusion

With progressive technology such as multilevel inverters, problems such as high peak current during motor starting, heating effect, and mismatch of the switching pattern of the existing system were rectified and improved. The dynamic performance of the induction motor drive with an indirect vector controller has been improved with less settling time and zero overshoot by implementing sliding mode control which outperforms traditional PI control. The resiliency of

the sliding mode control has been demonstrated during sudden changes in load. The proposed control technique tracks the speed effectively though the load torque, and the parameters are ambiguous. The calculated speed contains ripples due to the discrepancy between current and speed sampling timings. However, the drive system’s speed response is acceptable when the predicted speed is used in the control technique. A 2nd order sliding mode controller could be used in the future to reduce the chattering and parameter variation effects. This controller can be enhanced with fuzzy

logic principles to make it more robust and reliable, allowing it to be used in future drive designs for high-rating motors with critical applications in upcoming power plant units.

Abbreviations

DTC:	Direct self-control
ANN:	Artificial neural networks
SMC:	Sliding mode controller
HMI:	Human-machine interface
SCADA:	Supervisory control and data acquisition
VFD:	Variable frequency drive
CCP:	Common control panel
THD:	Total harmonic distortion
FFT:	Fast fourier transform
PWM:	Pulse width modulation
MLI:	Multilevel inverter

Data Availability

The data used to support the findings of this study are available from the corresponding author upon request.

Conflicts of Interest

The authors declare that they have no conflicts of interest.

Acknowledgments

The authors are thankful to the Deanship of Scientific Research at Najran University for funding this work under the Research Groups Funding Program (NU/RG/SERC/11/6).

References

- [1] R. Bharti, M. Kumar, and B. M. Prasad, "V/F control of three phase induction motor," in *Proceedings of the International Conference on Vision towards Emerging Trends in Communication and Networking (ViTECoN)*, Vellore, India, May 2019.
- [2] J. M. Pena and E. V. Diaz, "Implementation of V/f Scalar Control for Speed Regulation of a Three-phase Induction Motor," in *Proceedings of the IEEE ANDESCON*, IEEE, Arequipa, Peru, October 2016.
- [3] A. R. Harsha, S. Pranupa, B. M. Kiran Kumar, S. Nagaraja Rao, and M. S. Indira, "Arduino based V/f drive for a three phase induction motor using single phase supply," in *Proceedings of the 2020 International Conference on Smart Technologies in Computing, Electrical and Electronics (ICSTCEE)*, IEEE, Bengaluru, India, October 2020.
- [4] B. K. Nishad and R. Sharma, "Induction motor control using modified indirect field oriented control," in *Proceedings of the 2018 8th IEEE India International Conference on Power Electronics (IICPE)*, IEEE, Jaipur, India, December 2018.
- [5] H. Xie, F. Wang, W. Zhang, C. Garcia, J. Rodriguez, and R. Kennel, "Predictive field oriented control based on MRAS current estimator for IM drives," in *Proceedings of the 2020 IEEE 9th International Power Electronics and Motion Control Conference (IPEMC2020-ECCE Asia)*, IEEE, Nanjing, China, November 2020.
- [6] A. Paladugu and B. H. Chowdhury, "Sensorless control of inverter-fed induction motor drives," *Electric Power Systems Research*, vol. 77, pp. 619–629, 2007.
- [7] Z. Zhang and A. M. Bazzi, "Robust sensorless scalar control of induction motor drives with torque capability enhancement at low speeds," in *Proceedings 2019 IEEE International Electric Machines & Drives Conference (IEMDC)*, IEEE, San Diego, CA, USA, May 2019.
- [8] V. J. Stil, K. Miklosevic, Z. Spoljaric, and G. Kurtovic, "Induction motor sensorless and closed loop torque control in frequency converters," in *Proceedings of the 2018 International Conference on Smart Systems and Technologies (SST)*, IEEE, Osijek, Croatia, October 2018.
- [9] X. Cui, B. Li, Z. Kou, and Y. Qiao, "Measurement and control system for variable-frequency speed regulating of motor based on PLC and HMI," in *Proceedings of the IEEE 8th Joint International Information Technology and Artificial Intelligence Conference (ITAIC)*, IEEE, Chongqing, China, May 2019.
- [10] J. P. Wang, X. L. Meng, S. L. Zhang, and Y. K. Zhu, "Adaptive sliding mode control for an unmanned mini vehicle," in *Proceedings of the 2020 5th International Conference on Mechanical, Control and Computer Engineering (ICMCCE)*, IEEE, Harbin, China, December 2020.
- [11] Z. Li, X. Li, and B. Cui, "Cloud neural algorithm based load frequency control in interconnected power system," in *Proceedings of the 2020 24th International Conference on Automation and Computing (ICAC)*, IEEE, Newcastle Upon Tyne, UK, September 2018.
- [12] T. Long, E. Li, Y. Hu et al., "A vibration control method for hybrid-structured flexible manipulator based on sliding mode control and reinforcement learning," *IEEE Transactions on Neural Networks and Learning Systems*, vol. 32, no. 2, pp. 841–852, 2021.
- [13] S. S. Kumar Singh, Arkdev, and M. K. Sarkar, "Load frequency control: higher order sliding mode observer based integral higher order sliding mode controller with stochastic perturbation," in *Proceedings of the 2018 2nd International Conference on Power, Energy and Environment: Towards Smart Technology (ICEPE)*, IEEE, Shillong, India, June 2018.
- [14] M. Yang, B. Xiaowei, T. Yue, and J. Yuanwei, "Design of sliding mode controller for frequency control in an isolated wind-diesel hybrid system," in *Proceedings of the 2013 25th Chinese Control and Decision Conference (CCDC)*, IEEE, Guiyang, China, May 2013.
- [15] J. Robles, F. Sotelo, and J. Chavez, "Robust nonsingular terminal sliding mode control with constant frequency for DC/DC boost converters," in *Proceedings of the 2020 IEEE 21st Workshop on Control and Modeling for Power Electronics (COMPEL)*, IEEE, Aalborg, Denmark, November 2020.
- [16] R. R. Vasu, S. G. Fernandez, and K. Vijayakumar, "Enhanced space vector modulated scalar control of induction motor," *Indonesian Journal of Electrical Engineering and Computer Science*, vol. 21, no. 2, pp. 707–713, 2021.
- [17] A. Fatima, T. Almas, M. K. A. Biabani, and M. Imran, "Sliding mode control of induction motor used in traction," in *Proceedings of the 2016 International Conference on Electrical, Electronics, and Optimization Techniques (ICEEOT)*, IEEE, Chennai, India, March 2016.

- [18] P. Parida, *A Sliding Mode Controller for Induction Motor Drives*” *Dissertation*, National Institute of Technology, Rourkela, Orissa, 2009.
- [19] R. Sreejith and B. Singh, “Sensorless predictive current control of PMSM EV drive using DSOGI-FLL based sliding mode observer,” *IEEE Transactions on Industrial Electronics*, vol. 68, no. 7, pp. 5537–5547, 2021.
- [20] H. Dan, P. Zeng, W. Xiong, M. Wen, M. Su, and M. Rivera, “Model predictive control-based direct torque control for matrix converter-fed induction motor with reduced torque ripple,” *CES Transactions on Electrical Machines and Systems*, vol. 5, no. 2, pp. 90–99, 2021.
- [21] M. Stender, O. Wallscheid, and J. Böcker, “Accurate torque control for induction motors by utilizing a globally optimized flux observer,” *IEEE Transactions on Power Electronics*, vol. 36, no. 11, pp. 13261–13274, 2021.

Research Article

A Grid-Connected Solar PV/Wind Turbine Based Hybrid Energy System Using ANFIS Controller for Hybrid Series Active Power Filter to Improve the Power Quality

Pazhanimuthu Cholanuthu,¹ Baranilingesan Irusappan,¹
Suresh Kalichikadu Paramasivam ,² Senthil Kumar Ramu ,² Suresh Muthusamy ,³
Hitesh Panchal,⁴ Ramakrishna S S Nuvvula ,⁵ Polamarasetty P Kumar,⁵
and Baseem Khan ⁶

¹Department of Electrical and Electronics Engineering, KPR Institute of Engineering and Technology, Coimbatore, Tamil Nadu, India

²Department of Electrical and Electronics Engineering, Sri Krishna College of Technology, Coimbatore, Tamil Nadu, India

³Department of Electronics and Communication Engineering, Kongu Engineering College, Perundurai, Erode, Tamil Nadu, India

⁴Department of Mechanical Engineering, Government Engineering College, Patan, Gujarat, India

⁵Department of Electrical and Electronics Engineering, GMR Institute of Technology, Rajam 530049, India

⁶Department of Electrical and Computer Engineering, Hawassa University, Hawassa, Ethiopia

Correspondence should be addressed to Baseem Khan; baseem_khan04@yahoo.com

Received 16 June 2022; Revised 12 July 2022; Accepted 20 September 2022; Published 14 November 2022

Academic Editor: Ravi Samikannu

Copyright © 2022 Pazhanimuthu Cholanuthu et al. This is an open access article distributed under the Creative Commons Attribution License, which permits unrestricted use, distribution, and reproduction in any medium, provided the original work is properly cited.

The current needs of more nonlinear loads and the frequent usage of single-phase loads in three-phase system drastically create power quality issues in the grid-connected system. As a consequence, it creates an undesirable power quality issue (PQI) in the form of a change in the nature of voltage and current magnitude and waveforms in the power system. The voltage-related PQI leads to a huge disturbance in the system when compared with the current-related PQI. The hybrid series active power filter provides grids with the required voltage in series and suppresses the voltage-related harmonics caused by grid-connected nonlinear loads. The present work deals with an adaptive neurofuzzy inference system controller for the generation of a reference voltage signal that uses a reduced active filter rating. The simulation study was done in the MATLAB 2020b/Simulink environment and the experimental effectiveness of the proposed ANFIS controller was compared with that of a conventional controller. In the grid-connected system, this system prevents voltage quality problems such as voltage sag, flickering, voltage swell, neutral currents, and reactive power. The renewable energy sources interfaced into the DC-link minimize short and long voltage challenges so that they improve the overall performance of the system. In accordance with IEEE standard 519-1992, a prototype model was proved to demonstrate that the power delivery system works effectively under different conditions and reduces the total harmonic distortion by approximately 30%, which is less than the 5% acceptable limit.

1. Introduction

The major usage of nonlinear loads like electronic ballasts, SMPS, rectifiers, inverters, battery chargers, single-phase diode bridge rectifiers, power converter-fed drives, arc welding, furnaces, uninterrupted power supply, adjustable-

speed drive, diode bridge rectifier, thyristor converter, and consumer electronics is producing an unnecessary power quality (PQ) disturbance in the grid-connected system [1–3]. In addition to fluctuations, voltage dips, oscillatory transients, momentary interruptions, harmonic resonance, harmonics, and other issues related to PQ, these loads also

cause significant power budget blowouts. Similarly, single-phase load usage in a three-phase system generates unbalanced current and neutral current in the system, generating inefficient voltage regulation, extreme neutral current, excessive reactive power, and load unbalancing [4,5] formalized paraphrase. An increase in harmonics in the power system has several negative effects, including additional heating, amplifying harmonics due to banks of power factor correction capacitors, reducing transmission system efficiency, distribution transformers' overheating and defective electronic equipment, incorrect operation of circuit breakers, creating errors in measuring equipment, and communication and control signal interference. Poor power quality leads to production loss in industries, life-threatening consequences in hospitals, loss of critical communication in airports, and so on [6–8]. In a country, poor power quality causes a loss in overall productivity, which will badly affect its economy. Numerous studies have been conducted on the solutions to PQ problems such as passive filters (PF), active filters (AF), hybrid filters (HF), and custom power devices. Harmonic-related problems in the electrical power supply can be resolved simply, moderately, and reasonably with a PF [7–10]. However, PFs have shortcomings such as their size, complexity in filter design, resonance, and tuning problems. When compared with passive approaches, active filtering approaches for PQ enhancement have proven to be more effective because of their quicker response time, smaller size, and superior performance in recent years. Furthermore, active filtering automatically adjusts to changes in network characteristics, reducing the possibility of resonance between the filter and the network impedance [11–15]. A problem with AFs is that they produce high-frequency noise when high currents are switched on and off rapidly, which can cause electromagnetic interference in a power system distribution. A hybrid power filter (HPF) is formed by combining the operations of PFs and an active power filter (APF), and it alleviates the problems associated with the individual operation of active and passive filtering [11,13,16–20].

There are many controllers proposed for HSAPF in the literature, but they are limited to certain difficulties. Traditional controllers have some difficulties compensating for long-term system issues [21–23]. To achieve system performance improvements, neural networks and fuzzy logic are combined as a controller. To generate harmonic compensating voltage, an Adaptive Neurofuzzy Inference System (ANFIS) implemented controller is used. Calculations of reference current are to be carried out continuously as the load on the system changes from moment to moment. It is proposed to implement an ANFIS-based digital processor that generates the gating signals for thyristors in the adaptive shunt passive filter, as well as PWM signals for switching devices in the SAPF [24–26]. The modified p-q controller is the main controller to tune the parameters of active and reactive power. This can be done through ANFIS to achieve voltage profile improvement in the system. In order to compensate for the harmonic and the reactive power requirements of the nonlinear load, it produces the appropriate compensation signals for the active filter [27–31]. It

also adjusts the passive filter component values. Using tap-changing transformers or uninterruptible power supplies as traditional methods for suppressing voltage variations has the disadvantage of being bulky, expensive, and slow enough to allow voltage sag effects at the load side to be eliminated. Due to its high controllability and reliability, the Hybrid Series Active Power Filter (HSAPF) uses a voltage source inverter (VSI) as an active filter in series and in parallel with a shunt high-pass filter. The problem of long-term interruptions or block-outs in the supply system is eliminated by incorporating renewable energy sources (RES) into the DC-link. The system improves performance and lowers the THD level below 5% as required by IEEE standard [32–36]. The purpose of this study is to propose an HSAPF to address power quality issues associated with voltage in grid-connected systems with the integration of renewable energy sources (RES). Thus, in this research, the HSAPF is proposed as a compensatory measure for power quality issues in RES integrated grid-connected systems.

2. System Description

2.1. Configuration of SAPF. The SAPF injects harmonic voltages to or from the source voltage as the voltage waveform is transmitted across the nonlinear load. During fundamental component operation, the device presents zero resistance. However, for harmonic component operation, it appears as a resistance with a high impedance. LC filters containing one or more single-tuned elements with or without a high-pass filter make up shunt passive filters. The SAPF with a shunt PF called HSAPF operates as a high impedance harmonic isolator. This is done by injecting a controlled harmonic voltage source between the nonlinear load and the source as shown in Figure 1. The result is that all load current harmonics except those at fundamental frequency are restricted to the passive filter. The load current harmonics are reduced by separating the source from the load.

Grid harmonic currents are not compensated, so instead they act as high impedance currents for loads. Thus, the passive filter can be located on the customer side of the system so that harmonic currents from the power system will not be consumed. In this case, there is no harmonic resonance, and the supply does not have a harmonic flow. HSAPF incorporates the features of a passive high-pass filter, thereby bypassing all upper order harmonics, while SAPF compensates for low order harmonics in the supply voltage.

2.2. The Proposed System Description. It is proposed that photovoltaic and wind energy systems use common DC-link combined with shunt passive filters while nonlinear loads are linked to standard voltage and current harmonic sources. SAPFs reduce the harmonic components of voltage waveforms by injecting voltage components into series with the supply voltage. It is a way to prevent voltage imbalances, voltage sags, and swells resulting from load fluctuations.

The two major RES are integrated into the system in two places, namely, the main source and, secondly, a source for

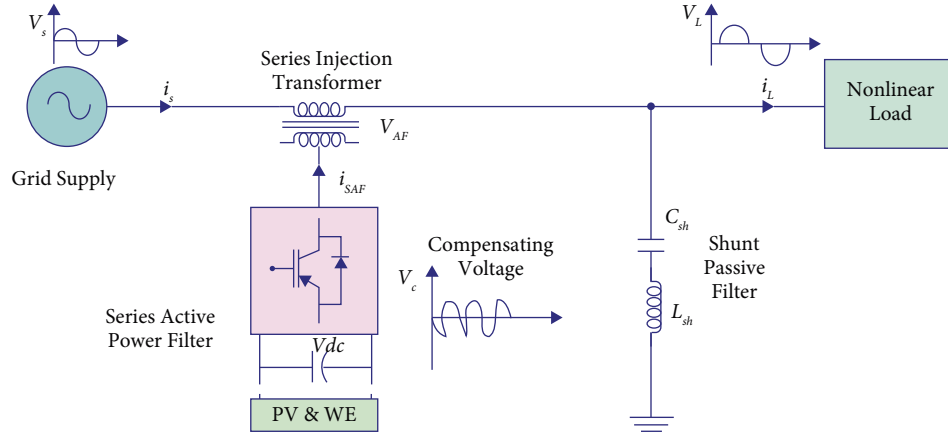


FIGURE 1: Basic configuration of Hybrid Series Active Power Filter.

compensation of long power interruptions through the DC-link. Boosting the low voltage output voltage of the PV panels is achieved by connecting the solar array to a DC-DC boost converter. Several methods for tracking maximum power points (MPPT) have been discussed in the literature, among which incremental conductance (IC) and perturbation and observation (P&O) are commonly employed. Here, the P&O model is used as it utilizes a simple feedback model and fewer parameters compared to the IC, which spends more time tracking maximum power. This algorithm is used to achieve the optimal solar panel output power from the solar energy source. A solar battery bank stores excess power generated by the panels, and the charge controller converts this energy into AC power.

A system that produces wind power is made up of a multipole synchronous generator attached to an adjustable-speed wind turbine. With the help of the rectifier, the output of a three-phase voltage is transformed into a DC voltage. Despite the deviation in the rectified DC voltage, the rectifier's output is combined with a DC-DC buck-boost converter to maintain a constant DC voltage. The output voltage of the rectifier is kept constant even when rectified DC voltage varies because its output is coupled to a DC-DC buck-boost converter. The maximum power of the converter was measured successfully with an MPPT technique by determining the ratio of efficiency to turbine speed.

With a series injection transformer, SAPF injects the compensating voltage in parallel with the voltage supply. Figure 2 illustrates the DC-link voltage generation process using photovoltaic (PV) and wind energy (WE) photovoltaic systems. SAPF is an inverter that uses a VSI made up of transistors and DC-link capacitors, and its compensation is largely influenced by the amount of energy available in the DC-link. This allows a reference value to be set for the DC-link capacitor voltage. A change in the load situation can result in a change in the power balance between the load and the source. SAPF will be able to compensate for variations in real power by using DC-link interfaced RES. This is achieved by injecting the harmonic compensating voltage through an injection transformer in series with the power supply voltage. Through the integration of renewable energy sources into the DC-link, the HSAPF can ensure consistent

supply over the long term. The availability of RES in the DC-link in the system causes different kinds of operation to occur in the system, as shown in Table 1.

3. Design Parameters

The inductor (L_s) power and the capacitor C supplied current (i_s) accumulated in the inductor are expressed in terms of voltage across inductor as

$$xV_L = L_s \times \frac{di_s}{dt}. \quad (1)$$

The boost converter's inductor value is determined from the following expression:

$$L = \frac{V_{in} \times D \times T}{\Delta I}, \quad (2)$$

where D , V_{in} , ΔI , T are the duty cycle, input voltage, inductor ripple current, and time period, respectively.

As a result of the converter, the average output voltage equals

$$V_{out} = \frac{V_{in}}{1-D}. \quad (3)$$

To maximize wind energy output, a buck-boost converter is connected to PMSG through MPPT techniques. The maximum output voltage of V_m in the line-line voltage of rms value is expressed as

$$V_{rms} = \frac{\sqrt{3}V_m}{\sqrt{2}}. \quad (4)$$

When the buck-boost converter steps up or down after rectification, the voltage is expressed as

$$V_{dc} = -\frac{D}{1-D} \times V_{dcrx}. \quad (5)$$

The SAPF is designed to restore a certain amount of power when the system supply sags. For a 3.120 kVA load, the following sizing may be recommended. This is in order to reduce 65% voltage sag, while simultaneously compensating the harmonics in the source current and maintaining power factor.

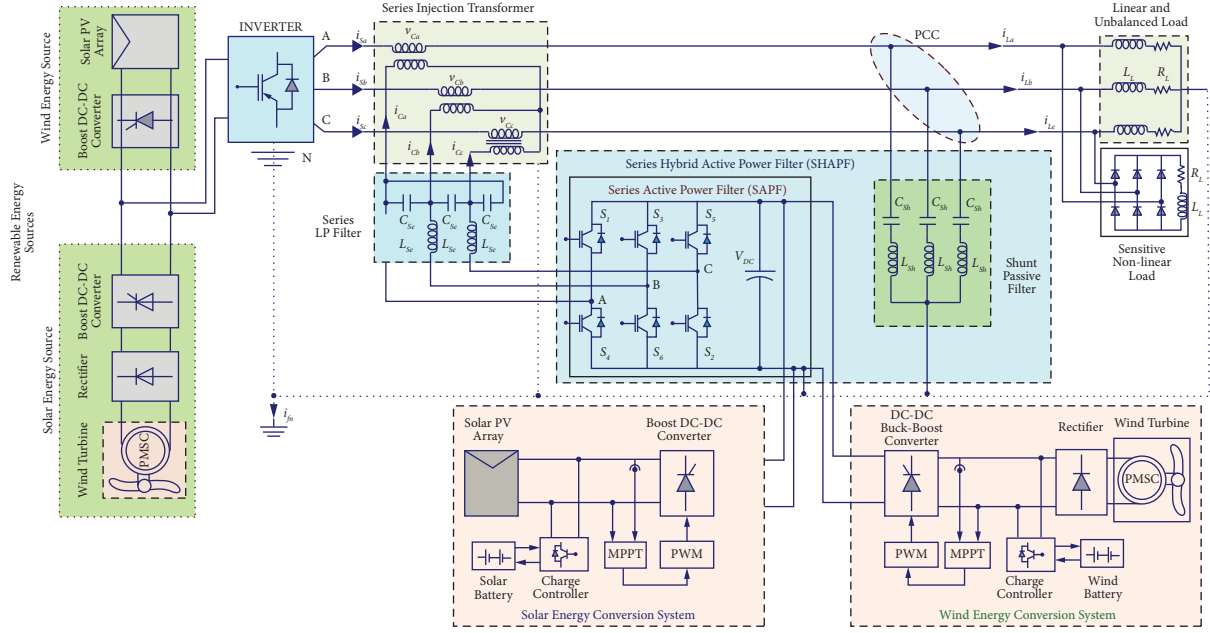


FIGURE 2: Topology of the proposed grid-integrated hybrid system.

TABLE 1: Operating modes of the proposed system.

Mode	Available source	Voltage condition	Power	Operation of energy sources in DC-link
Mode 1	PS = 1 PW = 0 PBS = 0 PBW = 0	$VBS \leq VBS, \text{Min}$ $VBW \leq VBW, \text{Min}$ or $VS = 0$	$PS \geq PL$ and $PW < PL$ or $PW = 0$	The SAPF utilizes solar energy to compensate for harmonics, reactive power, and share load demand when solar power is superior to load demand.
Mode 2	PS = 1 PBS = 1 PW = 0 PBW = 0	$VBS \geq VBS, \text{Min}$ $VBW \leq VBW, \text{Min}$ or $VS = 0$	$PS \geq PO$ and $PW < PL$ or $PW = 0$	Having a fully charged battery and a solar array at once that can supply power to both the DC-link and the load at once, the SAPF is able to run at maximum efficiency. During solar battery charging, constant voltage is switched off to prevent self-discharge.
Mode 3	PS = 0 PW = 0 PBW = 0 PBS = 1	$VBS \geq VBS, \text{Min}$ $VBW \leq VBW, \text{Min}$ or $VS = 0$	$PS < PL$ or $PS = 0$ and $PW < PL$ Or $PW = 0$	Power is supplied to the SAPF-PV load and DC-link when the battery is fully charged.
Mode 4	PS = 0 PBS = 0 PBW = 0 PW = 1	$VBS \leq VBS, \text{Min}$ $VBW \leq VBW, \text{Min}$ or $VS = 0$	$PS < PL$ or $PS = 0$ and $PW \geq PL$	SAPF-WE compensates for harmonics and reactive power when generating wind energy exceeds load demand, as well as sharing load demands when the solar and wind batteries are not fully charged.
Mode 5	PS = 0 PBS = 0 PW = 1 PBW = 1	$VBS < VBS, \text{Min}$ $VBW \geq VBW, \text{Min}$ or $VS = 0$	$PS < PL$ or $PS = 0$ and $PW = 0$	As a result of fully charging the wind battery, the SAPF-WE can operate simultaneously on both DC-link and load power from the wind turbine. To prevent self-discharge, continuous voltage charging is switched off for the wind battery.
Mode 6	PS = 0 PW = 0 PBS = 0 PBW = 1	$VBS < VBS, \text{Min}$ $VBW \geq VBW, \text{Min}$ or $VS = 0$	$PS < PL$ or $PS = 0$ and $PW < PL$ or $PW = 0$	Power is provided to SAPF-WE's load and DC-link by a fully charged wind battery.

Note: PS is solar power, PW is wind power, PBS is power in solar battery, PBW is power in wind battery, VBW is voltage in wind battery, VBS is voltage in solar battery, VS is source voltage, and PL is load power.

The SAPF should have the ability for long time voltage compensation, so that backup supply is accordingly designed as $DC_{\text{source}} = 3.120 \times 65\% = 1875V A$.

The converter nominal voltage is expressed as $V_{\text{Conv}} = 1875V A / 7.825A_{\text{rms}} = 239.6V_{\text{rms}}$.

The converter has the ability of transfer the rms load current and therefore the rating of converter is expressed as $I_{Conv} = I_L = 1875VA/239.6V_{rms} = 7.825A_{rms}$.

The SAPF is controlled as VSC and the DC voltage is derived as

$$v_{dc} = (i_{Ca}S_A + i_{Cb}S_B + i_{Cc}S_C)/C_{dc}. \quad (6)$$

The value of $S_1 - S_6$ is represented as converter switches and AC three-phase line voltages are v_{Ca} , v_{Cb} , and v_{Cc} expressed as

$$\begin{aligned} e_a &= v_{dc}(S_1 - S_2), \\ e_b &= v_{dc}(S_2 - S_3), \\ e_c &= v_{dc}(S_3 - S_1). \end{aligned} \quad (7)$$

The output of SAPF in volt-current equations can be expressed as

$$v_a = r_f i_{Ca} + L_f p i_{Ca} + e_a - r_f i_{Cb} - L_f p i_{Cb}, \quad (8)$$

$$v_b = r_f i_{Cb} + L_f p i_{Cb} + e_a - r_f i_{Cc} - L_f p i_{Cc}, \quad (9)$$

where r_f and L_f are value of SAPF resistance and inductance.

The SAPF compensating current is expressed as $i_{Ca} + i_{Cb} + i_{Cc} = 0$.

The current derivatives of the SAPF are obtained from the following equations:

$$p i_{Ca} = \frac{\{(v_b - e_b) + 2(v_a - e_a) - 3r_f i_{Ca}\}}{3L_f}, \quad (10)$$

$$p i_{Cb} = \frac{\{(v_b - e_b) + (v_a - e_a) - 3r_f i_{Ca}\}}{3L_f}. \quad (11)$$

The SAPF eliminates source current distortions, and only the harmonic component of load voltage is injected. Hence, the line-line fundamental component of voltage (V_{LL}) is expressed as

$$V_{LL} = \left(\frac{\sqrt{6}}{\pi}\right) V_{dc} = 0.779V_{dc}. \quad (12)$$

Here, the calculated DC-link voltage is V_{dc} .

The DC-link value is approximated to 600 V, P is power of 0.76 kVA, and T is energy storing time. Therefore, the DC-link capacitance value can be calculated as

$$C_{dc} = \frac{P \times T}{(1/2) \times V_{dc}^2} = \frac{760 \times 200 \times 10^{-3}}{(1/2) \times 600^2} = 1176\mu F \approx 2200\mu F. \quad (13)$$

Thus, the DC-link capacitance value of 2200 μF is considered to be appropriate for proper voltage compensation.

4. ANFIS Controller for HSAPF

HSAPF controls the inverter by computing the reference voltage waveform for every phase, maintaining continuous DC voltage and inverter signals generation. Figure 3 demonstrates the ANFIS control scheme for the proposed HSAPF configuration. With this circuit, the reference voltage generator creates the appropriate reference voltage for the load and compensates for reactive power and harmonics generated by it. A constant DC voltage is maintained across the capacitor with this circuit.

4.1. Architecture of ANFIS Controller. ANFISs combine fuzzy approaches with neural networks (NNs) that can adapt to achieve the required performance. Integrating the characteristics of the rules, fuzzy set topology, and control system structure into an adaptive system is challenging. Due to the lack of standard techniques for turning human knowledge into rules, FLC is an essential component of the fuzzy inference system (FIS). Hence, input and output membership functions have been selected by trial and error based on the size, type, and parameters. As well, the system is limited in its adaptability due to the range of variables that are difficult to adjust. The membership functions should be tuned and the rule base should be simplified to the fewest essential rules as possible. It is proposed that the ANFIS method be used to overcome the complexity described above. NN and fuzzy qualitative approaches are combined in this method. In contrast to standard fuzzy logic, this system is trainable without the need for a lot of expert knowledge. This results in a reduced rule base.

Figure 3 shows a typical ANFIS structure with a circle indicating a fixed node and a square indicating an adaptive node. Input and output nodes are present in this structure, along with hidden layers. Acts as models and rules are contained within these layers. The MATLAB/ANFIS editor is used to generate it after the initial data from the PI controller is obtained. Observers and moderators can easily understand and modify such a feedforward multilayer system, eliminating the disadvantage. In order to simplify things, let us assume that the FIS has two inputs and one output. The Takagi-Sugeno model is based on two inputs (x and y) and an output (z) and employs a fuzzy system model in ANFIS. This system is further tuned using an error propagation-based method. The error backpropagation learning algorithm implemented on a multilayer feedforward neural network can be trained to capture the mapping implicitly.

Using the error backpropagation algorithm, the error value of instantaneous real power and reactive power is calculated by

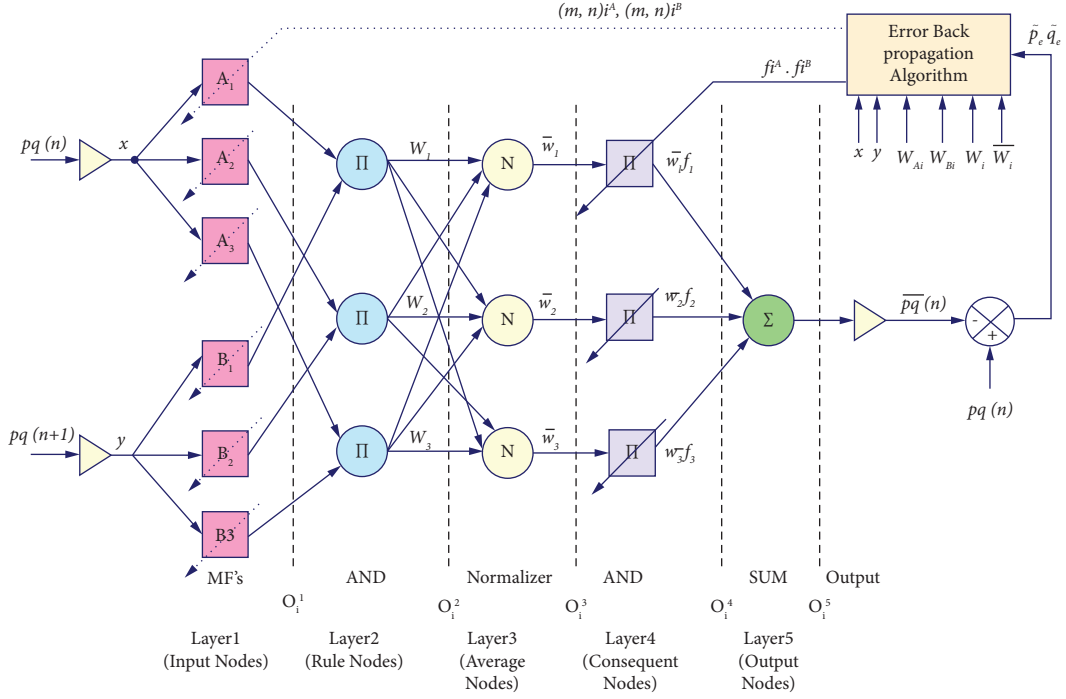


FIGURE 3: Schematic architecture of ANFIS controller.

$$\tilde{p} = p(n) - \bar{p}(n), \quad (14)$$

$$\tilde{q} = q(n) - \bar{q}(n),$$

$$\begin{aligned} f_1 &= p_1x + q_1y + r_1, \\ f_2 &= p_2x + q_2y + r_2, \\ f_3 &= p_3x + q_3y + r_3, \end{aligned} \quad (15)$$

$$f = \frac{W_1f_1 + W_2f_2 + W_3f_3}{W_1 + W_2 + W_3} = \bar{W}_1f_1 + \bar{W}_2f_2 + \bar{W}_3f_3, \quad (16)$$

where p and q are two inputs and \tilde{p} and \tilde{q} are two outputs. It is possible to build up fuzzy logic rules and decide input-output membership functions using the ANFIS, a structure that can be trained using neural learning training examples. Expert knowledge can be integrated into the ANFIS as well. The IF-THEN rules of first-order constitute the basis of the connection structure. Normally, each rule takes an input variable and a constant term as its output. An IF-THEN rule set is with three fuzzy IF-THEN statements for a first-order Sugeno fuzzy model.

5. Reference Voltage Signal Estimation

For three-phase power systems with or without neutrals, instantaneous values can be used to establish the p-q theory. It covers both transient and steady state waveforms in addition to the standard voltage and current waveforms. A p-q theory is a method for computing the current and voltage components of a three-phase input voltage, based on an arithmetic transformation known as Clark's transformation,

which describes how the a-b-c coordinates translate to the α - β -0 reference frame.

Calculating the SAPF instantaneous reference voltages requires a modified p-q theory. According to modified p-q theory, the source voltages are shifted by 90° when calculating instantaneous reactive power. Using LPFs and inverse transformations instead of the conventional AC components, the DC components are removed from the reference voltage before determining the compensation reference voltage.

As shown in Figure 4, the control is mainly aimed at calculating a three-phase reference compensation voltage such as v_{Ca}^* , v_{Cb}^* , and v_{Cc}^* , respectively, to compensate for distortions in the supply phase voltage such as v_{Sa} , v_{Sb} , and v_{Sc} , respectively, at the load terminals by injecting compensating voltages such as v_{Ca} , v_{Cb} , and v_{Cc} correspondingly so as to achieve full sinusoidal at PCC.

The preferred voltages at the load terminals are the supply voltage plus the injected SAPF voltage. Phase-locked loops (PLL), which synchronize with the supply voltage, are used to compensate for the distortion of the supply voltage. Voltage measurements on three phases are sensed and placed into the PLL to generate unit vectors of two quadratures ($\sin \omega t$, $\cos \omega t$). The sensed voltages from the supplies are being fed into the PLL, which is then multiplied by a suitable gain value. PLLs with discrete three-phase modes provide a frequency of 50 Hz at 50 milliseconds.

The α - β -0 reference frame voltage and current are the characteristics of the three phase supply voltages v_a , v_b , and v_0 and the three phase source currents i_a , i_b , and i_0 . This filter reclaims a portion of the real power from the essential voltage component by removing the harmonic

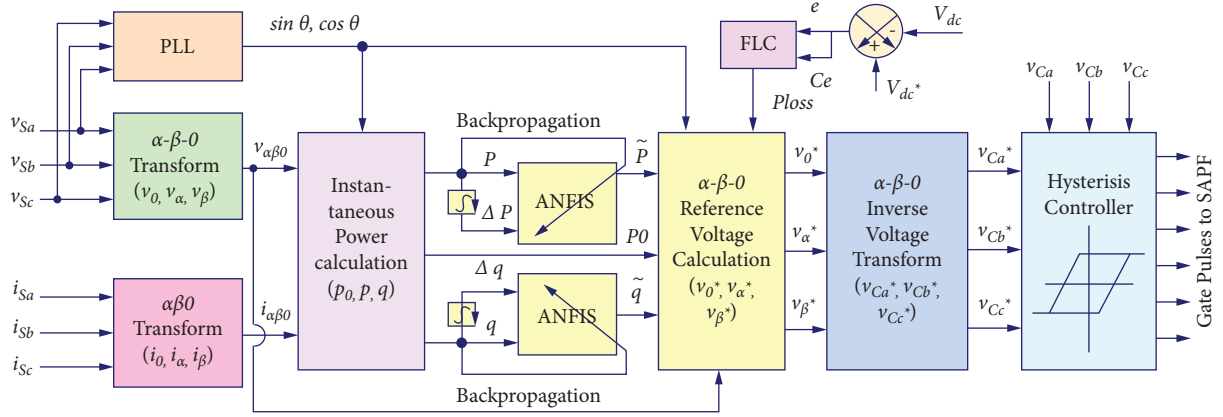


FIGURE 4: ANFIS-based controller for reference voltage signal generation.

components of the voltage supply. This filter regains a portion of the real power that is expressed as

$$\begin{bmatrix} v_0 \\ v_\alpha \\ v_\beta \end{bmatrix} = \frac{\sqrt{2}}{\sqrt{3}} \begin{bmatrix} \frac{1}{\sqrt{2}} & \frac{1}{\sqrt{2}} & \frac{1}{\sqrt{2}} \\ 1 & -\frac{1}{\sqrt{2}} & -\frac{1}{\sqrt{2}} \\ 0 & \frac{\sqrt{3}}{2} & -\frac{\sqrt{3}}{2} \end{bmatrix} \begin{bmatrix} v_{sa} \\ v_{sb} \\ v_{sc} \end{bmatrix}, \quad (17)$$

$$\begin{bmatrix} i_0 \\ i_\alpha \\ i_\beta \end{bmatrix} = \frac{\sqrt{2}}{\sqrt{3}} \begin{bmatrix} \frac{1}{\sqrt{2}} & \frac{1}{\sqrt{2}} & \frac{1}{\sqrt{2}} \\ 1 & -\frac{1}{\sqrt{2}} & -\frac{1}{\sqrt{2}} \\ 0 & \frac{\sqrt{3}}{2} & -\frac{\sqrt{3}}{2} \end{bmatrix} \begin{bmatrix} i_{sa} \\ i_{sb} \\ i_{sc} \end{bmatrix}. \quad (18)$$

The compensating voltage such as V_{Ca}^* , V_{Cb}^* , and V_{C0}^* , respectively, in α - β -0 reference frame is expressed as

$$\begin{bmatrix} v_{ca}^* \\ v_{cb}^* \\ v_{c0}^* \end{bmatrix} = \frac{1}{v_\alpha^2 + v_\beta^2} \begin{bmatrix} v_\alpha & v_\beta & 0 \\ v_\beta & -v_\alpha & 0 \\ 0 & 0 & v_{\alpha\beta} \end{bmatrix} \begin{bmatrix} \tilde{p} \\ \tilde{p} \\ p_0 \end{bmatrix}, \quad (19)$$

where \tilde{p} and \tilde{q} are called essential components and \tilde{p} and \tilde{q} are called the alternating or varying element. Multiplying the compensating voltage V_{Ca}^* , V_{Cb}^* , V_{C0}^* in the a - b - c reference frame with the expression is used to calculate the reference voltages v_{Ca}^* , v_{Cb}^* , and v_{Cc}^* in the reference frame as

$$\begin{bmatrix} v_{ca}^* \\ v_{cb}^* \\ v_{cc}^* \end{bmatrix} = \frac{\sqrt{2}}{\sqrt{3}} \begin{bmatrix} \frac{1}{\sqrt{2}} & 1 & 0 \\ \frac{1}{\sqrt{2}} & -\frac{1}{\sqrt{2}} & \frac{\sqrt{3}}{2} \\ \frac{1}{\sqrt{2}} & -\frac{1}{\sqrt{2}} & -\frac{\sqrt{3}}{2} \end{bmatrix} \begin{bmatrix} v_{ca}^* \\ v_{cb}^* \\ v_{c0}^* \end{bmatrix}. \quad (20)$$

Source voltages are the sum of the load voltages produced by the SAPF, and compensation voltage is represented by

$$\begin{bmatrix} v_{La} \\ v_{Lb} \\ v_{Lc} \end{bmatrix} = \begin{bmatrix} v_{Sa} \\ v_{Sb} \\ v_{Sc} \end{bmatrix} + \begin{bmatrix} v_{Ca} \\ v_{Cb} \\ v_{Cc} \end{bmatrix}. \quad (21)$$

Implementation of a modified p-q theory for a full ANFIS-based control system supports the proposed HRES-HSAPF system. Figure 5 showcases the entire system architecture of the proposed controller based HRES-HSAPF.

6. Simulation Results and Discussion

An implementation of the ANFIS-based modified PQ theory is investigated in this section to control the HSAPF DC-links through RES interfaces, and the effectiveness of this control scheme is estimated under different cases through MATLAB/Simulink. Simulation studies include three different test cases: voltage and load balanced, voltage balanced and unbalanced load, and voltage unbalanced and unbalanced load. Table 2 summarizes the simulation parameters for the RES-HSAPF system.

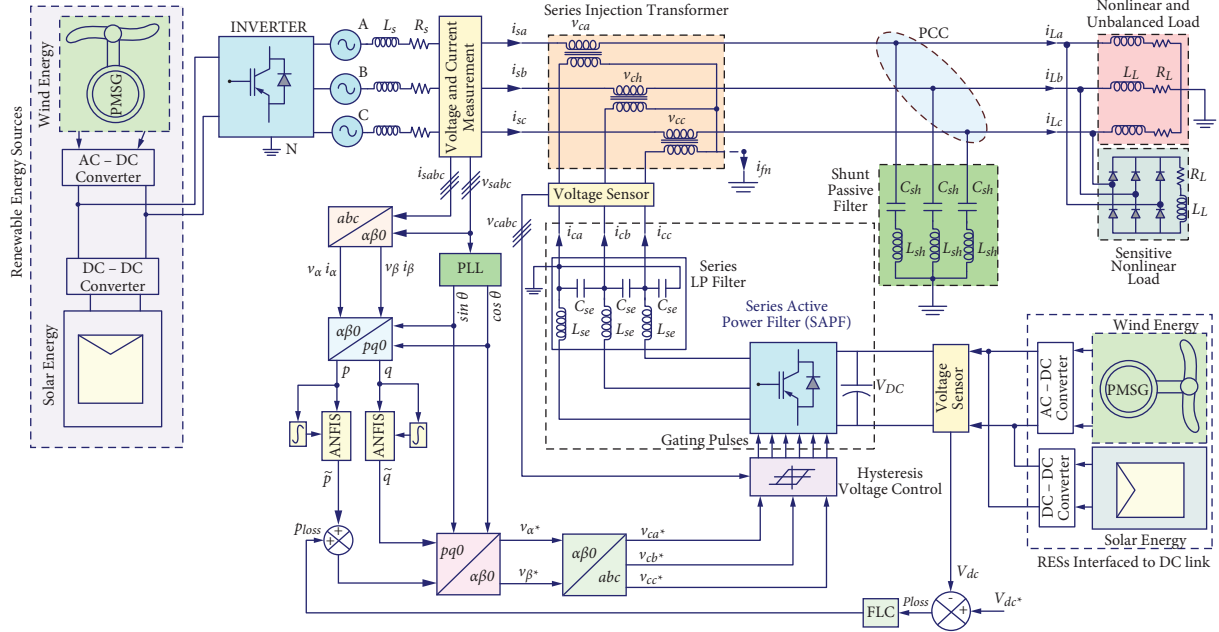


FIGURE 5: Overall control structure of the proposed ANFIS-based system.

TABLE 2: Simulation parameters of the proposed system.

Component	Parameter	Variable	Value
Source	Operating voltage	V_{ph}	240 V
	Frequency	f	50 Hz
Passive filter	LC value	C_{Se}, L_{Se}	34 μ F, 12.5 mH
	Number of cells	N_{cell}	6 \times 10
PV module	Nominal voltage	V_{nom}	12 V
	Maximum power	P_{mmp}	230 W
	Maximum voltage	V_{mmp}	35.5 V
	Maximum current	I_{mmp}	6.7 a
Wind generator	Rated power	P_w	1.20 kW
	Maximum power	P_m	1.50 kW
	Rated speed	ω_s	720 r/m
	Frequency	f	50 Hz
	Voltage	V_{ph}	240 V
DC-link	Voltage	V_{DC}	700 V
	Capacitor	C_{DC}	2200 μ F
SAPF	Filter	L_s, C_s	20 mH, 80 μ F
	Switching frequency	f_s	10 kHz
Series injection transformer	Controlling voltage	$T_{I1}, T_{I2}, \text{ and } T_{I3}$	100 VA and 1:1100 V
	Proportional gain	K_p	6
	Integral gain	K_i	5.5
PI controller	Nominal voltage	V_{Bat}	2 \times 12 V
	Capacity	P_B	2 \times 500 ah
Nonlinear load	Three-phase rectifier	R_L, L_L	10 W, 3 mH
	RL load	R'_L, L'_L	12 W, 75 mH

As shown in Figure 6(a), the test Case 1 is initially considered voltage balanced with a balanced load and is performed for a variety of system voltage and load conditions. The proposed control structure is evaluated by applying a variety of voltage disturbances to the system. The voltage applied to the system has not changed over the period of 0 to 0.04 sec. The system is then subjected to a 25%

swell in voltage between 0.04 and 0.1 sec, followed by no voltage from 0.14 to 0.14 sec. As shown in Figure 6(a), a voltage sag of 75% occurs during the same time period. No voltage injection is required from SAPF for the period from 0 to 0.04 sec. During the 0.04 to 0.1 seconds' period, a 25% voltage swell is detected. The controller compensates for it by applying a negative voltage. In other words, the SAPF injects

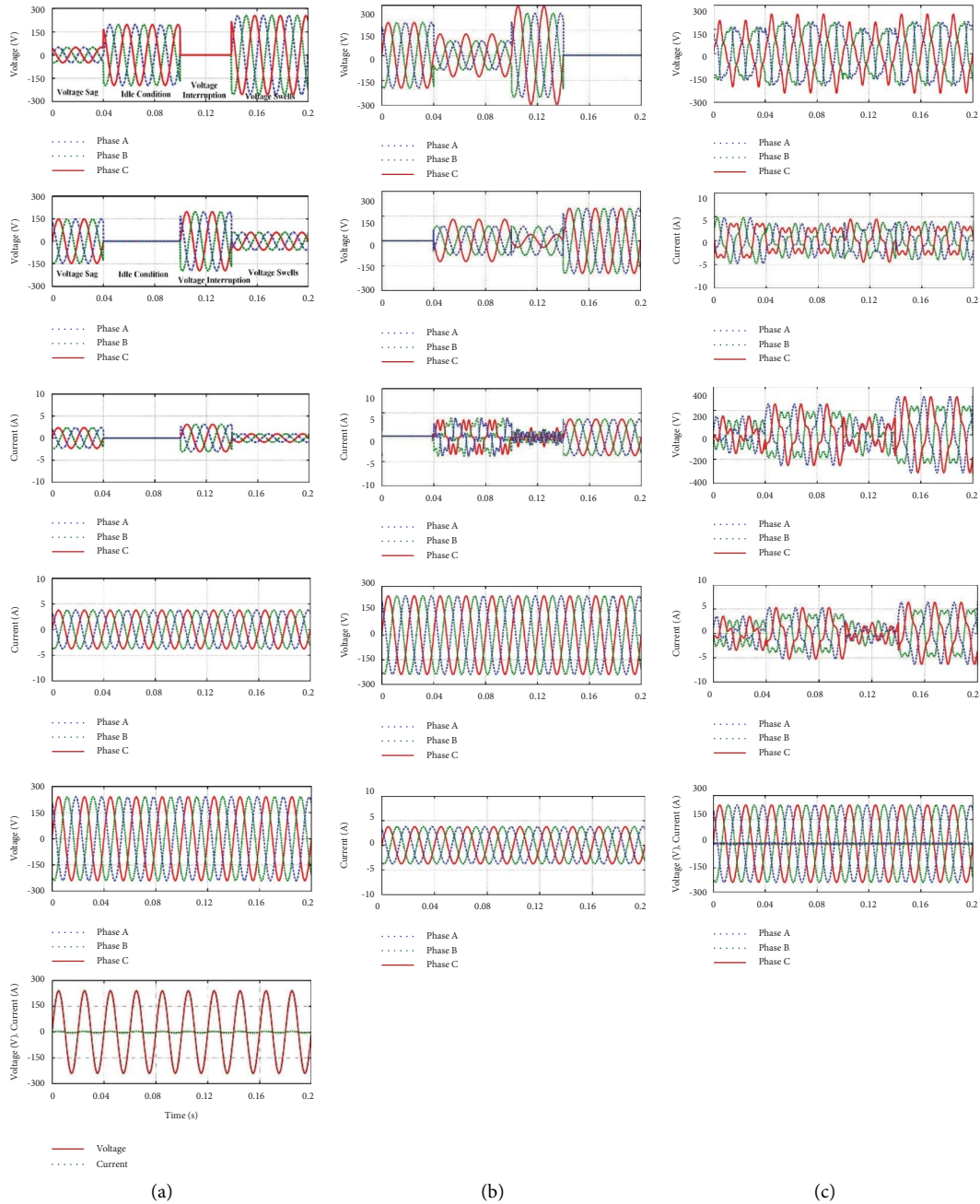


FIGURE 6: Different test cases considered for the performance analysis of the proposed controller. (a) Test Case 1. (b) Test Case 2. (c) Test Case 3.

25% of the actual 60 V through the SIT. The system voltage is interrupted for 0.1 to 0.14 sec, so compensating for the interruption requires the total nominal voltage. The SAPF injects $240 V_{rms}$ in series with the system at the rated system voltage. In this instance, the voltage sag occurs from 0.14 to 0.2 sec, only 25% of the nominal voltage is available, and the controller detects the remaining of 75% shortage. As a result of the switching operation of the HC, the SAPF generates the required voltage and supplies it to the SIT. A load voltage measurement is made after SAPF has performed the compensation. The modified p-q theory control scheme is

applied to compensate for voltage sags, swells, and interruptions present in the system.

The test Case 2, depicted in Figure 6(b), is carried out for various system voltage and load conditions and is considered voltage balanced with an unbalanced load. Tests are performed on a single-phase load connected between two phases in this case to determine whether the load voltages are unbalanced. The controller sets the reference compensating voltage for the HC using the measured voltage prior to compensation. The voltage and current injected through the SAPF are determined by properly identifying voltage imbalances and phase angle jumps. This is to compensate for unbalanced voltage and phase angle

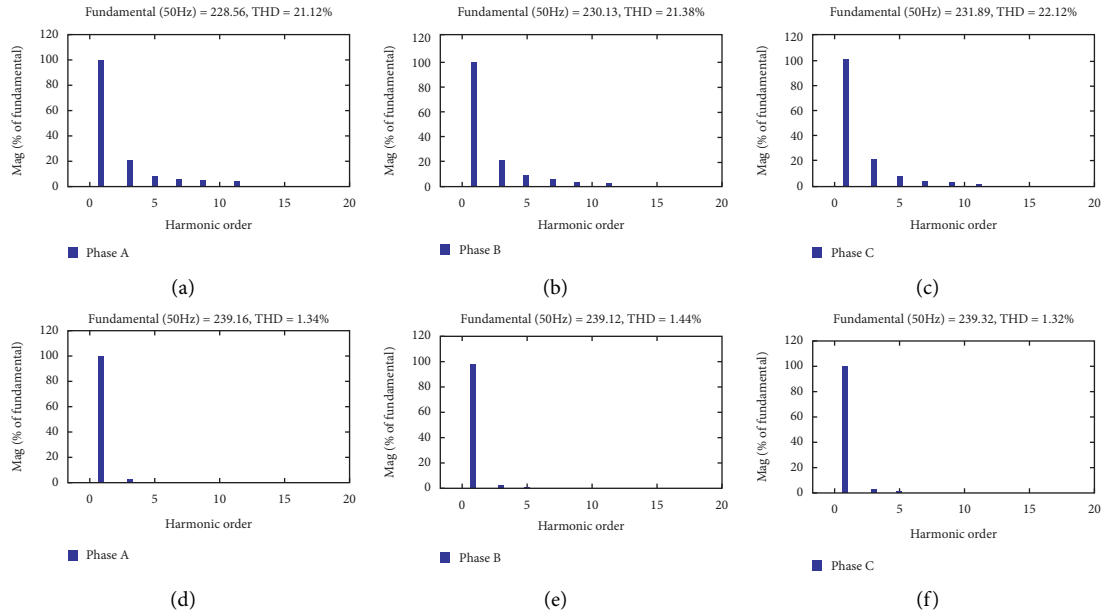


FIGURE 7: THD level of source current before and after compensation of the proposed controller.

jumps. A gate pulse is also generated for the SAPF via this controller. The SAPF produces the required compensating voltage based on the gate signals received. It applies the compensating voltage to the system through SIT.

Likewise, in Test Case 3, as shown in Figure 6(c), voltage unbalanced with unbalanced load is performed for various system voltage and load conditions. Under unbalanced voltages and unbalanced loads, the system performance is evaluated in test Case 3. It is assumed that the load and the system voltage are unbalanced in this test case. To verify this case, the system voltage should be generated with 5th and 7th order harmonics and the load should be operated as a single-phase unbalanced load. As the voltage imbalances between supply and load, accurate measurements of the voltages are sent to the controller. The p-q model based on ANFIS calculates the required voltage for compensation, and it is applied to the hysteresis controller to generate the necessary gating signal. The ANFIS-based modified p-q theory control scheme applied to SAPF eliminates voltage sag, voltage swell, and interruption by inserting a consistent compensating voltage in series with the supply voltage at phase angles of 0° and 180° with the purpose of decreasing voltage sag and swell. The proposed controller effectively compensates neutral currents because before compensation they have a significant number of harmonics.

In Figure 7, THD levels for three-phase source currents with the ANFIS controller before and after compensation are shown. In this case, the THD levels for three-phase source currents before and after compensating with the ANFIS controller are considered. As a result of the ANFIS controller, THD values are reduced to less than 2% after compensation.

7. Experimental Results and Discussion

A prototype of the proposed system is developed with simulated users for the evaluation of its performance: 240 Vrms, 50 Hz, three-phase, and four-wire system. To

implement the control circuit, an STM32F407VGT6 is employed, which operates at 168 MHz. The floating-point unit also has the capability of processing all single-precision data types and commands of an ARM processor. The DSP and memory protection units improve application security by implementing a complete set of DSP instructions. At the PCC, the analog to digital converter acquires and interfaces voltages and source currents. Currently, the controller program calculates reference voltage signals and then compares them with carrier waves to produce gate pulses.

Three voltages and three currents are obtained with the help of six 12 bit ADC channels based on mathematical calculations of sampled data. In order to generate PWM voltage source inverters, you need to calculate and compare gate pulses required for generating reference signals and carrier waves. In order to implement the PWM VSI, six IGBTs from ST Microelectronics are used, and the IR2130 is used as a three-phase bridge driver. The controller generates six gate pulses using optical isolation before the controller connects to the IR2130, and the VSI used had a kVA rating of 1.2 kVA with a turn ratio of 1 : 1.

A set of measurements were conducted with 120 mH source inductor, 20 mH filter inductor, an $80 \mu\text{F}$ filter capacitor, and a 2200 F DC-link capacitor. The inductance and load resistance were 75 mH and 8 Ohms, respectively. IGBT inverters switch at 10 kHz. Load current and voltage are measured using AC-link voltage sensors and DC-link capacitor voltage sensors. The signal conditioning circuit of an analog to digital converter amplifies and presents the offset needed to complete the conversion. An experimental setup that tests both current and voltage harmonics generation by the SHAPF control scheme is represented in Figure 8.

A balanced sinusoidal system voltage and a balanced load are considered to evaluate the proposed controller performance. At the same time, the act of varying the voltage in the system is intended to manage voltage sags, surges, and



FIGURE 8: The proposed system experimental setup.

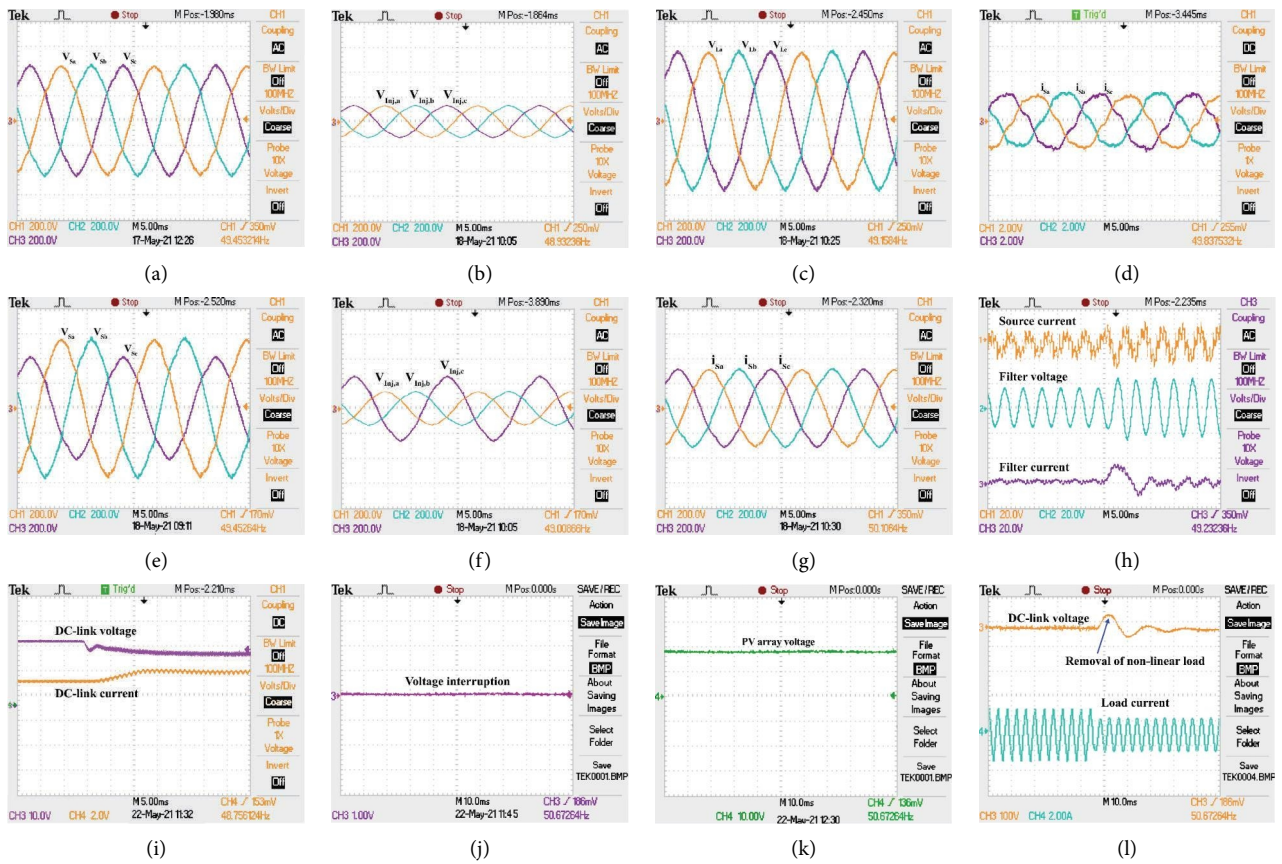


FIGURE 9: Different test cases considered for the performance analysis of the proposed controller.

interruptions. Figure 9 shows the load voltage sag and required compensation voltage of the SAPF controller generated by generating the reference signal. Figure 9 shows the measured source current and load voltage after the compensation carried out by SAPF. Results prove the effectiveness of the controller's compensation in accurately detecting the variation of the load voltage and source current and generating the correct compensating voltages.

As shown in Figure 9, the proposed system was tested with an unbalanced voltage as well as an unbalanced load. The tests should include the single-phase loads in a three-phase system simultaneously as well as the nonlinear loads

at random. The measured source current and voltage before compensation have distorted and oscillatory waveforms are depicted in Figure 9. Sensors can sense unbalanced and oscillatory waves, which generate the correct gate pulse in terms of compensating current and voltage waveforms.

The proposed controller is tested under unbalanced load conditions, the voltage THD values of phase A of 2.53, phase B of 2.71, and phase C of 2.63%, respectively. Furthermore, THD current values for phase A, B, and C are 3.12, 3.23, and 3.26%, respectively, and experimental THD values for the proposed system are shown in Figure 10.

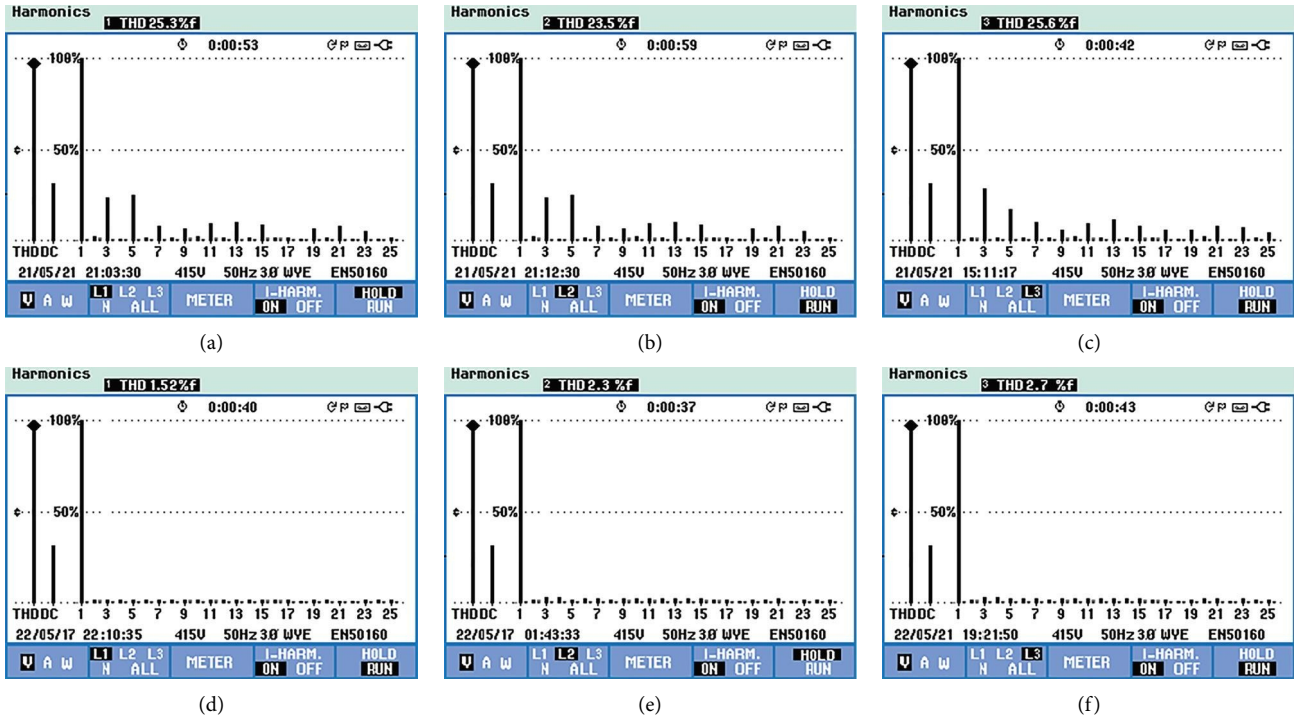


FIGURE 10: Performance measure of THD value under balanced source voltage and unbalanced load.

TABLE 3: Simulation and experimental comparison of the proposed ANFIS-based controller.

Test cases	%THD levels in phase	Simulation results				Experimental results			
		RES-HSAPF with PI		HRES-HSAPF with ANFIS		HRES-HSAPF with PI		HRES-HSAPF with ANFIS	
		Voltages (V)	Currents (A)	Voltages (V)	Currents (V)	Voltages (A)	Currents (A)	Voltages (V)	Currents (A)
Case 1	A	2.95	3.32	1.12	2.52	3.85	4.32	1.72	2.82
	B	2.72	3.41	1.18	2.68	3.81	4.22	1.68	2.98
	C	2.87	3.62	1.14	2.74	3.82	4.71	1.80	2.98
Case 2	A	3.72	4.89	2.12	2.85	4.82	4.93	2.53	3.12
	B	3.62	4.78	2.35	2.78	4.72	4.91	2.71	3.23
	C	3.84	4.82	2.31	2.91	4.80	4.89	2.63	3.26
Case 3	A	4.12	5.23	3.12	3.32	5.23	6.12	3.12	3.85
	B	4.31	5.11	2.89	3.12	5.45	6.11	2.89	3.79
	C	4.23	5.32	2.92	3.35	5.43	6.23	2.92	3.83

Simulations and experimental studies validate the modified p-q theory based on HRES-HSAPF and ANFIS with various test cases. In the proposed system, voltage and current disturbance can be mitigated to a large extent, and its performance can be compared with that of the PI controller. The proposed RES-HSAPF system implemented with the ANFIS controller significantly improves system performance and shows a significant reduction in the THD level from the test results presented in Table 3. In comparison to PI controllers and without HSAPF, the newly developed controller improves the performance of the system.

8. Conclusion

A grid-integrated renewable energy system with a hybrid series active power filter system implemented with an ANFIS controller connected to nonlinear or sensitive loads is presented. In the ANFIS-based modified p-q theory, the ANFIS controller addressed the system parameters and compensated for harmonics, voltage imbalances, and short-term and long-term voltage disturbances in the system. In order to make use of solar and wind power, the HSAPF has been designed to interface to the grid using RES. According

to IEEE standard 519–1992, under balanced and unbalanced supply situations, the system compensates for system voltage unbalance, slight and huge voltage interruptions, and harmonics. Among the various tests, the measured THD has always been within the acceptable limit. The current THD level of the system ranges from 30% to 36% without HSAPF implementation. With HSAPF devices installed with PI controllers, the voltage THD is reduced from 20% to 25% and from 3.5 to 3.7%. In addition, this offers lower current and voltage THDs ranging from 2.5% to 2.9% and 1.3% to 1.5%, respectively. The proposed system, in comparison to a conventional controller, reduced the THD values from 30% to 20%. It has been shown to be quite effective without the use of controllers. Moreover, simulations and experiments concluded that the system is able to effectively mitigate voltage-based distortions, short-term and long-term voltage interruptions, and neutral current and improve the system power factor. The system provided consistent active and reactive power, which increased system reliability based on load demand. In order to reduce the use of energy from the utility grid, RES share their energy with the utility grid. This decreases the amount of electricity used from that grid. It is best suited for small- and medium-sized companies to reduce their panel tariffs and eliminate the need for UPS and power quality conditioners.

Data Availability

The data can be obtained from the corresponding author upon request.

Conflicts of Interest

The authors declare that they have no conflicts of interest.

References

- [1] M. C. Mira, Z. Zhang, A. Knott, and M. A. E. Andersen, "Analysis, design, modeling, and control of an interleaved-boost full-bridge three-port converter for hybrid renewable energy systems," *IEEE Transactions on Power Electronics*, vol. 32, no. 2, pp. 1138–1155, 2017.
- [2] A. Kannan, V. Kumar, T. Chandrasekar, and B. J. Rabi, "A review of power quality standards, electrical software tools, issues and solutions," in *Proceedings of the International Conference on Renewable Energy and Sustainable Energy*, Coimbatore, India, 2013.
- [3] S. Li, W. Qi, S. C. Tan, and S. Y. Hui, "Integration of an active filter and a single-phase AC/DC converter with reduced capacitance requirement and component count," *IEEE Transactions on Power Electronics*, vol. 31, no. 6, pp. 4121–4137, 2016.
- [4] S. Devassy and B. Singh, "Control of a solar photovoltaic integrated universal active power filter based on a discrete adaptive filter," *IEEE Transactions on Industrial Informatics*, vol. 14, no. 7, pp. 3003–3012, 2018.
- [5] S. K. Chauhan, M. C. Shah, R. R. Tiwari, and P. N. Tekwani, "Analysis, design and digital implementation of a shunt active power filter with different schemes of reference current generation," *IET Power Electronics*, vol. 7, no. 3, pp. 627–639, 2014.
- [6] X. Wang, S. Yuvarajan, and L. Fan, "MPPT control for a PMSG-based grid-tied wind generation system," in *Proceedings of the North American Power Symposium*, Arlington, TX, USA, 2010.
- [7] J. Philip, C. Jain, K. Kant et al., "Control and implementation of a standalone solar photovoltaic hybrid system," *IEEE Transactions on Industry Applications*, vol. 52, no. 4, pp. 3472–3479, 2016.
- [8] D. Li, K. Yang, Z. Q. Zhu, and Y. Qin, "A novel series power quality controller with reduced passive power filter," *IEEE Transactions on Industrial Electronics*, vol. 64, no. 1, pp. 773–784, 2017.
- [9] O. Prakash Mahela and A. Gafoor Shaik, "Topological aspects of power quality improvement techniques: a comprehensive overview," *Renewable and Sustainable Energy Reviews*, vol. 58, pp. 1129–1142, 2016.
- [10] D. Li, T. Wang, W. Pan, X. Ding, and J. Gong, "A comprehensive review of improving power quality using active power filters," *Electric Power Systems Research*, vol. 199, Article ID 107389, 2021.
- [11] S. D. Swain, P. K. Ray, and K. B. Mohanty, "Improvement of power quality using a robust hybrid series active power filter," *IEEE Transactions on Power Electronics*, vol. 32, no. 5, pp. 3490–3498, 2017.
- [12] A. K. Mishra, P. K. Ray, R. K. Mallick, A. Mohanty, and S. R. Das, "Adaptive fuzzy controlled hybrid shunt active power filter for power quality enhancement," *Neural Computing & Applications*, vol. 33, no. 5, pp. 1435–1452, 2021.
- [13] A. Javadi, A. Hamadi, L. Woodward, and K. Al-Haddad, "Experimental investigation on a hybrid series active power compensator to improve power quality of typical households," *IEEE Transactions on Industrial Electronics*, vol. 63, no. 8, pp. 1–4859, 2016.
- [14] L. F. J. Meloni, F. L. Tofoli, Á. J. J. Rezek, and E. R. Ribeiro, "Modeling and experimental validation of a single-phase series active power filter for harmonic voltage reduction," *IEEE Access*, vol. 7, pp. 151971–151984, 2019.
- [15] S. D. Swain, P. K. Ray, and K. B. Mohanty, "Design of passive power filter for hybrid series active power filter using estimation, detection and classification method," *International Journal of Emerging Electric Power Systems*, vol. 17, no. 3, pp. 363–375, 2016.
- [16] KP. Suresh and S. Ramesh, "Grid-interconnected solar photovoltaic system for power quality improvement using extended reference signal generation strategy," *Journal of Testing and Evaluation*, vol. 49, no. 1, Article ID 20180924, 2019.
- [17] M. Antchev, V. Gourgoulitsov, and H. Antchev, "Study of the operation of the output filter of a single-phase series active power filter," *International Journal of Power Electronics and Drive Systems*, vol. 12, no. 1, p. 304, 2021.
- [18] M. A. Mulla, R. Chudamani, and A. Chowdhury, "A novel control method for series hybrid active power filter working under unbalanced supply conditions," *International Journal of Electrical Power & Energy Systems*, vol. 64, pp. 328–339, 2015.
- [19] R. A. Modesto, S. A. Oliveira da Silva, and A. A. Júnior, "Power quality improvement using a dual unified power quality conditioner/uninterruptible power supply in three-phase four-wire systems," *IET Power Electronics*, vol. 8, no. 9, pp. 1595–1605, 2015.
- [20] C. Pazhanimuthu and S. Ramesh, "Grid integration of renewable energy sources (RES) for power quality improvement using adaptive fuzzy logic controller based series hybrid active

- power filter (SHAPF),” *Journal of Intelligent and Fuzzy Systems*, vol. 35, no. 1, pp. 749–766, 2018.
- [21] A. T. Hoang, V. V. Pham, and X. P. Nguyen, “Integrating renewable sources into energy system for smart city as a sagacious strategy towards clean and sustainable process,” *Journal of Cleaner Production*, vol. 305, Article ID 127161, 2021.
- [22] P. Chawla and M. Lalwani, “Analysis and simulation of reactive power theory for harmonic elimination using shunt active power filter,” *International Journal of Intelligence and Sustainable Computing*, vol. 1, no. 2, pp. 181–193, 2021.
- [23] M. P. Behera and P. K. Ray, “Reactive power and harmonic compensation in a grid-connected photovoltaic system using fuzzy logic controller,” *International Journal of Emerging Electric Power Systems*, vol. 22, no. 2, pp. 161–175, 2021.
- [24] R. Nirmala and S. Venkatesan, “Inverter current control for reactive power compensation in solar grid system using Self-Tuned Fuzzy Logic Controller,” *Automatika*, vol. 63, no. 1, pp. 102–121, 2022.
- [25] M. T. Benchouia, I. Ghadbane, A. Golea, K. Srairi, and M. E. H. Benbouzid, “Implementation of adaptive fuzzy logic and PI controllers to regulate the DC bus voltage of shunt active power filter,” *Applied Soft Computing*, vol. 28, pp. 125–131, 2015.
- [26] C. Pazhanimuthu, I. Baranilingesan, and A. Karthick, “An improved control algorithm for series hybrid active power filter based on SOGI-PLL under dynamic load conditions,” *Solid State Communications*, vol. 333, Article ID 114357, 2021.
- [27] B. Boukezata, A. Chaoui, J. P. Gaubert, and M. Hachemi, “Power quality improvement by an active power filter in grid-connected photovoltaic systems with optimized direct power control strategy,” *Electric Power Components and Systems*, vol. 44, no. 18, pp. 2036–2047, 2016.
- [28] S. Kasa, P. Ramanathan, S. Ramasamy, and D. P. Kothari, “Effective grid interfaced renewable sources with power quality improvement using dynamic active power filter,” *International Journal of Electrical Power & Energy Systems*, vol. 82, pp. 150–160, 2016.
- [29] A. Verma and B. Singh, “AFF-SOGI-DRC control of renewable energy based grid interactive charging station for EV with power quality improvement,” *IEEE Transactions on Industry Applications*, vol. 57, no. 1, pp. 588–597, 2021.
- [30] M. Golla, K. Chandrasekaran, and S. P. Simon, “PV integrated universal active power filter for power quality enhancement and effective power management,” *Energy for Sustainable Development*, vol. 61, pp. 104–117, 2021.
- [31] P. A. Ostergaard, N. Duic, Y. Noorollahi, H. Mikulcic, and S. Kalogirou, “Sustainable development using renewable energy technology,” *Renewable Energy*, vol. 146, pp. 2430–2437, 2020.
- [32] I. Worighi, A. Maach, A. Hafid, O. Hegazy, and J. Van Mierlo, “Integrating renewable energy in smart grid system: architecture, virtualization and analysis,” *Sustainable Energy, Grids and Networks*, vol. 18, Article ID 100226, 2019.
- [33] S. Impram, S. Varbak Nese, and B. Oral, “Challenges of renewable energy penetration on power system flexibility: a survey,” *Energy Strategy Reviews*, vol. 31, Article ID 100539, 2020.
- [34] M. A. Hannan, S. Y. Tan, A. Q. Al-Shetwi, K. P. Jern, and R. A. Begum, “Optimized controller for renewable energy sources integration into microgrid: functions, constraints and suggestions,” *Journal of Cleaner Production*, vol. 256, Article ID 120419, 2020.
- [35] R. Logesh, S. V, and L. R, “Resources, configurations, and soft computing techniques for power management and control of PV/wind hybrid system,” *Renewable and Sustainable Energy Reviews*, vol. 69, pp. 129–143, 2017.
- [36] G. Das, M. De, and K. K. Mandal, “Multi-objective optimization of hybrid renewable energy system by using novel autonomic soft computing techniques,” *Computers & Electrical Engineering*, vol. 94, Article ID 107350, 2021.

Research Article

Prophetic Energy Assessment with Smart Implements in Hydroelectricity Entities Using Artificial Intelligence Algorithm

Abdullah Saleh Alqahtani,¹ Pravin R. Kshirsagar ,² Hariprasath Manoharan ,³
Praveen Kumar Balachandran ,⁴ C. K. Yogesh,⁵ and Shitharth Selvarajan ⁶

¹Department of Self-Development Skills, CFY Deanship, King Saud University, Riyadh, Saudi Arabia

²Department of Artificial Intelligence, G.H Raison College of Engineering, Nagpur, India

³Department of Electronics and Communication Engineering, Panimalar Engineering College, Poonamallee, Chennai, India

⁴Department of Electrical and Electronics Engineering, Vardhaman College of Engineering, Hyderabad, India

⁵School of Computer Science and Engineering, VIT Chennai Campus, Chennai, India

⁶Department of Computer Science and Engineering, Kebri Dehar University, Kebri Dehar, Ethiopia

Correspondence should be addressed to Shitharth Selvarajan; shitharths@kdu.edu.et

Received 15 August 2022; Accepted 13 September 2022; Published 7 October 2022

Academic Editor: Albert Alexander Stonier

Copyright © 2022 Abdullah Saleh Alqahtani et al. This is an open access article distributed under the Creative Commons Attribution License, which permits unrestricted use, distribution, and reproduction in any medium, provided the original work is properly cited.

An encouraging development is the quick expansion of renewable energy extraction. Harnessing renewable energy is economically feasible at the current rate of technological advancement. Traditional energy sources, such as coal, petroleum, and hydrocarbons, which have negative effects on the environment, are coming under more social and financial pressure. Companies need more solar and wind power because this calls for a well-balanced mix of renewable resources and a higher proportion of alternative energy sources. Sustainable energy can be captured using a variety of techniques. Massive scale and small-sized are the two most prevalent techniques. No renewable energy source possesses an inherent property that restricts how it may be managed or how it can be planned to produce electricity. A number of factors have contributed to a growth in the use of alternative sources, one of which is to mitigate the effects of rising temperatures. To improve the ability to estimate renewable energy, various modeling approaches have been created. This region might use an HRES to give many sources with the inclusion of different energy sources. The inventiveness of solar and wind power and the brilliant ability of neural networks to handle complex time-series data signals have both aided in the prediction of sustainable energy. Therefore, this research will examine the numerous information models in order to determine which proposed models can provide accurate projections of renewable energy output, such as sunlight, wind, or pumped storage. In the fields of sustainable energy predictions, a number of machine learning methods, such as multilayer perceptions MLP, RNN CNN, and LSTM designs, are frequently utilized. This form of modeling uses historical data to predict potential values and can predict short-term patterns in solar and wind generation.

1. Introduction

It has been realized that extensive fossil fuel use would speed up the depletion of fossil fuel supplies while harming the ecosystem. Global warming and increased health consequences will be the consequence of these effects. Adding to the two renewable energy sources, coal power and energy production are the speediest energy sources today. Alternative sources are any kind of energy that can be harvested in nature and is renewable or nonpolluting [1–4]. It may be

found in a number of different forms, including sun's electricity, solar energy, electricity, geothermal heat, waves, tide, and hydroelectricity. The sustainable use of renewable has lately received significant attention, which has caused much research to examine the subject. The biggest obstacle renewable energy faces in the foreseeable future are finding enough supplies of electricity. Renewable energy is found in the present or future energy infrastructure by integrating renewable resources [5]. With sustainable energy, critical concerns such as increased supply dependability and

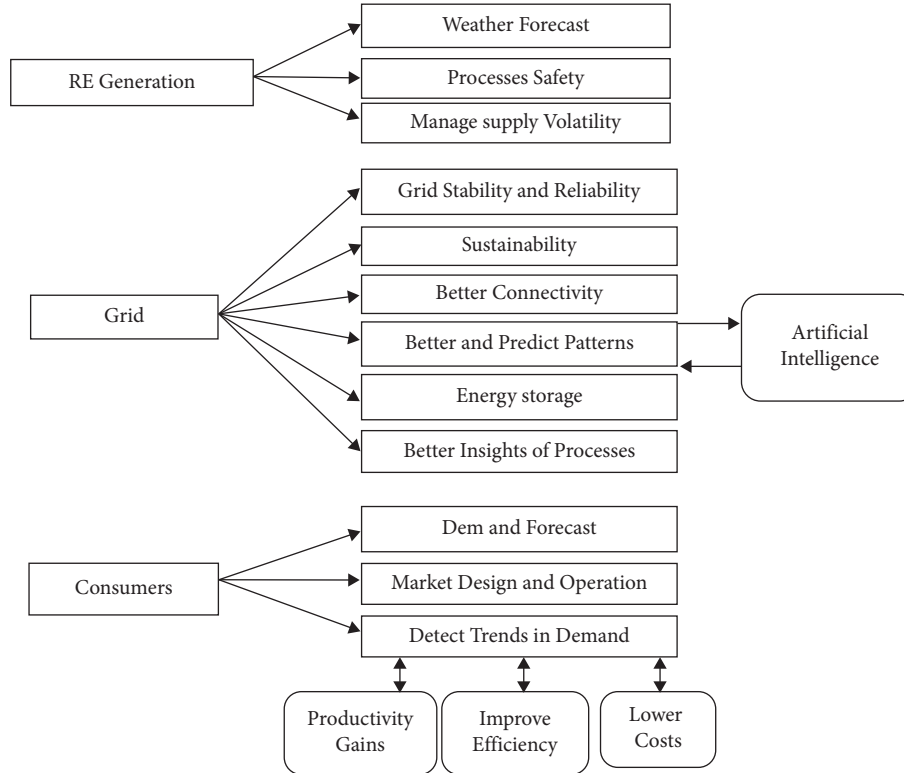


FIGURE 1: Integration of energy systems with artificial intelligence.

addressing localized power shortages will just be available to be addressed. This renewable energy production is discontinuous and chaotic because of the enormous unpredictability and inconsistent and randomized characteristics of renewable energy. Even yet, the accuracy of renewable energy statistics has yet to be mastered. Improved power efficiency is made possible by high-intensity management. The power development process, administration, and regulation are all heavily reliant on power forecasting technologies. The use of renewable energy is on the rise; therefore, it is crucial to create systems to store green energy. Many studies show different robot algorithms were used to renewable energy forecasts [2]. Effective renewable energy forecasts are offered by document models. More importantly, artificially intelligent models were developed to enhance renewable energy forecasting accuracy. Electricity forecasts of varying time periods, such as milliseconds, days, weekdays, and months, were implemented to meet different forecasting objectives [6]. While evaluating device models' generalization ability, prediction effectiveness is always used to determine their overall effectiveness.

Machine learning has long been used in areas such as those dealing with data-driven issues. This diverse group of multidisciplinary tools, including analytics, arithmetic, artificial neural networks, information gathering, and optimization, are artificial intelligence methods. Artificially intelligent methods strive to discover connections amongst incoming data and produce data by looking for relationships that may or may not exist using mathematical formats. The final machine learning algorithms are developed by using the

whole dataset, and after senior managers may feed forecasted input data into the trained models to get results that are within a desired range [3]. The information which was before is critical to computer science, and it may boost machine learning's performance by enhancing the results. Learning algorithm, unsupervised classification, and supervised learning are the primary techniques that machine learning technology employs. Supervised leverages labeled training data during the monitored period. Training process is when you use data for training that has not even been labeled to classify new data by specific criteria, which allows the system to understand. Figure 1 indicates the integration model.

Since groupings usually rely on grouping criteria, the number of nodes varies. Augmentation learning refers to the process of gaining input from the environment to create greater anticipated rewards. Many methodologies were highlighted and techniques were suggested by the use of three fundamental learning concepts [6]. In addition, several types of research are produced from renewable generation forecasting via the use of a single AI framework [4]. Unfortunately, it is challenging to enhance prediction power that used a simple device model owing to the varied datasets, time stages, predictions ranges, parameters and measurement and management [7–12]. Hence, several researchers have created artificially intelligent algorithms or total renewable energy forecasting prediction techniques in order to enhance forecasting accuracy. In the information systems discipline, support-vector algorithms and underground techniques have become highly common recent.

1.1. State-of-the-Art Models. Many existing models that predict the amount of energy supplied in the system is monitored where the study [10] evaluates convolution neural networks for sustainable energy predictions. The prediction techniques were classified into four classifications profound faith network, vehicle stack, profound recurring machine learning, and others. Furthermore, a wide range of data pretests and postmethods were used to enhance the accuracy of the prediction. Studies [11, 12] analyzed adaptive intelligence power and dependability predicting systems. Forms of energy include solar, hydroelectric, and windy in this research. In very many instances, the advantage of neural networks in power and dependability forecasts was shown. [13] showed that the material on solar energy forecasting was evaluated utilizing AI algorithms, equipment, pattern recognition, and hybrid approaches, respectively. The analysis points out that even the information on solar photovoltaic reliance can be estimated using arithmetical weather forecasts with features and intelligent systems to accomplish a prolonged solar energy prognostication, great memory channels, convolutionary neural connections, and recurring artificial neural. In [14], installations are examined and categorization of power generation computer methods. Authors found that hybrid methods are better in the implementation of energy technologies than standard machine algorithms. A study [15] researched smart home energy management model predictions, including energy dispatched, supercapacitors, climate policy and marketplaces, dependability, and optimum reserves infrastructure constraints. This study was helpful for the electricity industry by presenting current trends and predicting advances to power distribution management and implementation. A study [16] evaluates the applicability of SVM in the predictions of renewable, and suggested the predictions of the SVM, outperform the other forecasts as far as the correctness of the predictions was concerned. The scientists also showed that composite vector holder methods may provide better prediction outcomes than a simple support—vector system [17]. The research showed that usage of artificial intelligence and support-vector generator is effective in solar power. The article points out that seasons change has led to high predictions of solar energy mistakes. Since ultraviolet irradiance is a major solar power source.

In [18], the SVR is a version of SVR that has finally been condensed to a nonlinear issue and it is more highly scalable than SVR or ANN conventional. In combination with wavelet processing, ANN can forecast wind production over timescales of up to 24 hours. Its same SVR simplest ways can be employed, and with a cancroids remote technique, in order to find and choose pieces of data with similar raw numbers for the predicted template strand. A study [19] indicated that when this whole existent dataset contains is entered into SVR, the significance of each component in the ramp prediction will be evaluated to minimize the chosen number. The method is known as unidirectional analysis and has been shown to provide superior performance similar to Pearson correlations, Gray causative link, and network-based assessment [20]. All four methods have been used in a Simulation. Approaches including RF can provide extremely

high accuracy in the prediction of renewable power, allowing a simple evaluation of features significance.

1.2. Proposed Methodology. To examine the effect of applied optimization in the energy management systems of different devices a transportation vehicle is introduced where decisions are taken automatically with best control practices [21]. The vehicle is tested with two different energy cases, low and high, where a learning model uses previous data set for identification cases thus a line of energy intersection is present. Further, a home management system using AI procedures is incorporated with a specialized metering scheme that is operated under automated mode [22]. But if the metering scheme is introduced then a local management terminal must be designed for transmitting the information to different consumers. Even the above-mentioned case studies are analyzed by several researchers in Morocco where energy-efficient operation is achieved only if AI is incorporated. All the existing models [21–36] focuses only on different renewable energy sources to forecast various behavior of appliances in real-time environmental conditions. But most of the procedures that are present in existing methodologies are not introduced with high-end monitoring devices and even the analytical framework is not framed. Moreover, several drawbacks such as high error conditions, improper training and testing data, absence of conventional power plants reduce the efficiency of existing methods. But some researchers have formulated a real-time working principle using different AI algorithms but at the same time, the mathematical model is not implemented in a closed loop condition for solving various forecast problems. Hence, the proposed method identifies the gap that is present in the existing method and provides a working methodology using an effective energy management system.

The projected model is incorporated to monitor the amount of energy that is supplied to each appliance and minimized the energy in such a way where the same working efficiency is guaranteed. For increasing the efficiency of the proposed technique an AI algorithm is implemented where the presence of renewable energy sources is identified and controlled. In addition, if the amount of energy falls below a certain limit, then it will be identified using an error detection procedure and it is also framed in analytical form. Moreover, the proposed method ensures a precise energy monitoring system that manages the energy by storing all the monitored values in a separate cloud management system.

2. Objectives

The major objective of the proposed work that is used in real-time implementations for monitoring all the complexities that are present in different environmental conditions is framed using the analytical model where the minimization objective functions are as follows:

- (i) Incorporating an AI model for minimizing the energy of appliances with proper utilization of energy resources
- (ii) To minimize the time complexity series in the prediction of external data that provides reliable forecast behavior
- (iii) To reduce the amount of errors that are present in prediction process using preprocessing and feature extraction procedures

3. Evaluation Metrics: An Analytical Model

During the practice session, errors are computed from the actual performance to the goal and the parameters are then adjusted in all stages it until error achieves a satisfactory limit [26]. The background propagating method utilizes various cost functions to measure prediction performance including correlations and error correction between target and predicted value. The major uncertain indicators used to evaluate the quality of the system networks are RMSE or CV-RMSE, MBE, or NMBE, MAE or MAPE (R2). Comparing the error variance of the average worth (y_k) and the calculated value (x_k) with both the number of measurements N is provided via RMSE and CV-RMSE and it can be determined as follows:

$$\text{RMSE} = \sqrt{\frac{\sum_{k=1}^N (y_k - x_k)^2}{N}}. \quad (1)$$

$$\text{CV - RMSE} = \frac{\text{RMSE}}{x} \times 100\%. \quad (2)$$

MBE measures the average point error that indicates the general performance of the predicted result with respect to the linear function of the sample. Positive figures imply bad forecasting, whereas low signs reflect a computer judgment. NMBE is the normalized of the MBE index to measure the outcomes of MBE, thereby creating a global gap here between estimated worth and the relevant buffer:

$$\text{MBE} = \frac{1}{N} \sum_{k=1}^N (y_i - x_k). \quad (3)$$

$$\text{NMBE} = \frac{\text{MBE}}{x} \times 100\%. \quad (4)$$

The measurement of accuracy rate is indeed MAE and MAPE, whereby MAE is the measurement of the amount of error between its predicted values as well as the associated observed, and the MAPE is stated as follows:

$$\text{MAE} = \frac{1}{N} \sum_{k=1}^N |(y_k - x_k)|. \quad (5)$$

$$\text{MAPE} = \frac{1}{N} \sum_{k=1}^N \frac{|(y_k - x_k)|}{x_k} \times 100\%. \quad (6)$$

R^2 , defined as a regression line, is a mathematical measure of the variation which is limited among 0 and 1. The

quantity tends to be 1 and the estimates are closely linked to the measurements obtained. The following is described in R2.

$$R^2 = 1 - \frac{\sum_{k=1}^N (y_k - x_i)^2}{\sum_{k=1}^N (y_i - \bar{x}_i)^2}. \quad (7)$$

All equations that are represented in Equations (1)–(7) represent the integration of a closed loop function where error measurements are made. Therefore, the combined Equation on objective function is framed using Equation (8) is mentioned as follows:

$$\text{obj}_i = \min \sum_{i=1}^n \text{MBE, RMSE, } E_i, t_i, \quad (8)$$

where MBE, RMSE describes the error functions; E_i indicates the energy of appliances, and t_i denotes the time complexity functions.

3.1. Integration of AI with RES. In both energy industries, AI is much required since it works with huge amounts of measurements and ever more sophisticated technologies. Specifically, via improved surveillance, operation, management, and preservation of the wind industry and timely systems operation and management, the RE market may be encouraged by AI [23]. The combination of RE with power sources relates to the following important AI technologies such as RE generating in light of intermittent renewable unpredictability and supply volatility, presence of adequate and dependability; personnel security, effective predictive forecasting, and weather predictions. efficient macroeconomic and grid storage procedures. Figure 2 illustrates the relationships suggested by AI as well as its application. Important uses in the RE industry include smart matching demand-supply, intelligence caching, centralized control network, and intelligence micronetworks. Even now the increasing use of RE gives the existing societies a huge chance to reduce carbon emissions and the shortage of resources, there is a danger to the position of the RE sector's electricity leadership in its intermittent nature [3].

The prospect of not deploying conventional power stations, such as energy sources, inhabits in the AI, reliant as to whether the RE is entirely reliant, that will provide an accurate RE energy supply prediction to react to normal variations, adjust operational processes as the initiatives are not directly impacted and react appropriately to existing customers requirements as supposed. The performance of RE should be improved via the automating of procedures, which include a significant usage of AI. The ultimate goal for RE grids is to maximize the volatilities and associated uncertainties costs of feed from producing capacity [23]. AI is used to predict energy consumption for smoother peak adaptation. It is also essential to manage energy producers and consumers from decentralized production environments, which will need grid electricity whenever their output is below their requirements, and then when they create more than they use the energy extra is returned to the grid. This would require continual energy flow amongst buyers and

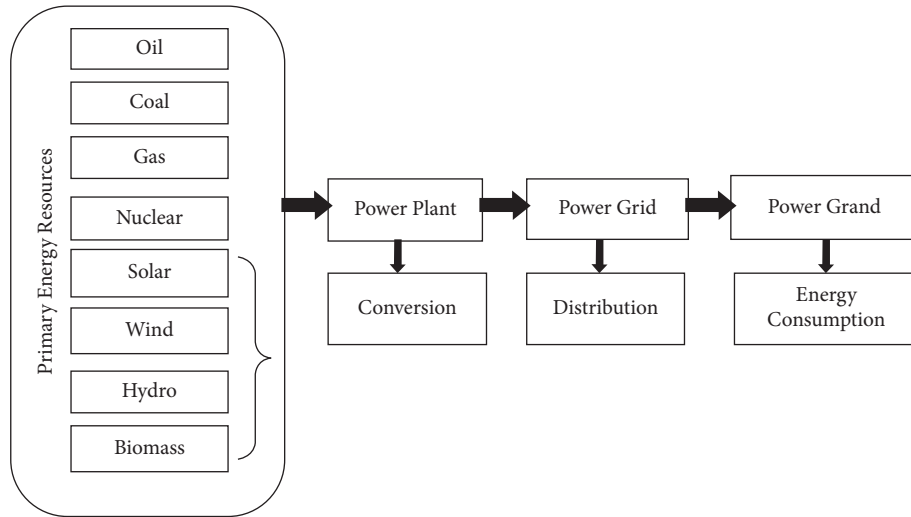


FIGURE 2: Energy generation forecast model.

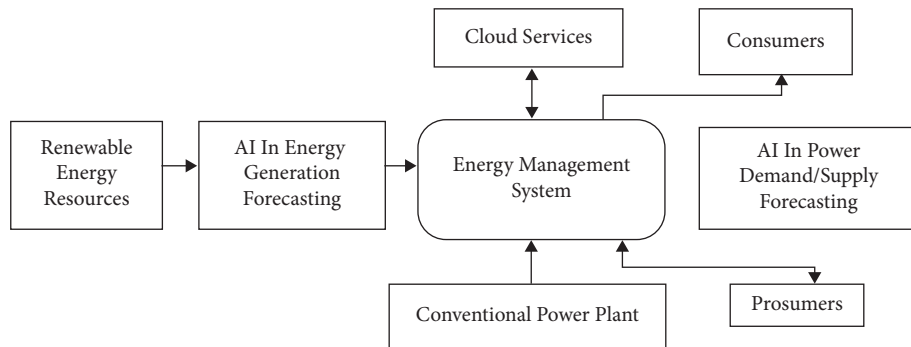


FIGURE 3: Centralized control center for AI in RES.

producers. The centralized control networks AI will proactively prevent power shortages by identifying early problems and assist minimize the time required for maintenance. In order to be successful in these areas, it should contain statistical alerts, report, usage of subscriber and browser interfaces, restoration of backup's servers in unforeseen situations, authenticating password security enabling users at various points, etc. The use of AI in RE is essential because of the huge quantity of data that growing connectivity across grids are created. Consolidated intelligence functions in relation to the infrastructure required to manage the controlled locations. This exponentially increasing data may be managed by AI and provided techniques for addressing RE variations based on experience and predictions [23]. All of this will enable the RE successfully connect to the electricity system and utilize the capacity among those sources, regardless of their unpredictability. Various properties have the varying capability for energy, new versions, and age. In guaranteeing its performance, they must be connected and pushed to almost the same commonality. The performance should really be confirmed by the fluctuating market circumstances that rarely a centralized smart unit need to react and adapt to new circumstances (Figure 3).

3.2. Advanced Technologies. Artificially intelligent methods have been used in the generating and demand sectors for effective energy administration. AI techniques may be used, either in a hold as well as generator solar and wind power, depending on the type of barriers and needs [33]. Figure 4 shows the areas when machine learning may be used to prevent electricity, anticipate demand and monitor photovoltaic systems, and also used to increase performance. The main uses of AI techniques in HRES are the prediction of sustainable energy release. The prediction of energy output is a critical problem for renewable resources and machine training plays an essential role as a method for predicting electricity production. In this regard, using historical information, renewable power energy may be forecast. The precise details of the forecast are difficult since the source of this energy depends on the surroundings [24]. This research is used to forecast renewable energy production by CNN. Stating clearly the placement, construction, and magnitude of sustainable plants. The optimum size of renewable power plants in HRES is a difficult issue. The placement of the power plant and other characteristics depends on various weather, land, and availability, and expenditure considerations. In addition, the operation of sustainable energy facilities, unlike fossil fuels, requires space [34]. Therefore, it is

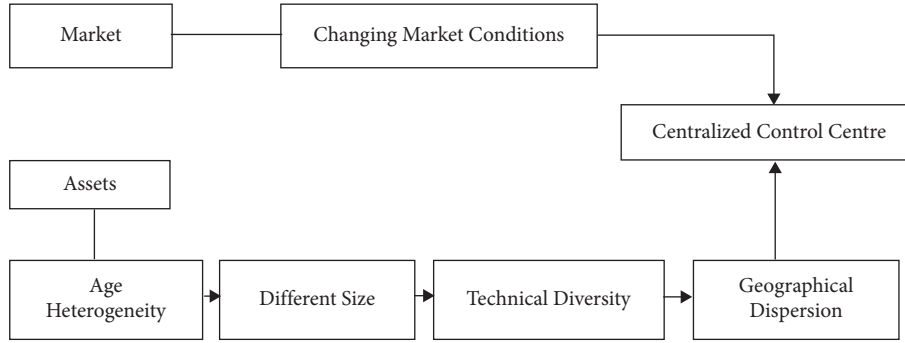


FIGURE 4: Advanced technologies in hybrid-renewable-energy system (HRES).

important to determine the number and quality, for example, meteorological information, dampness, temperatures, wind velocity, radioactivity, etc. Artificial intelligence methods are capable of supporting this judgment call.

The new power production Smart Grid (SG) is a system that optimizes all the grid segments from generation to transportation and energy storage. Stakeholders want the grid to be managed by rapidly expanding the electricity grid and continuously improving its intelligent, economical and productive, and successful [24]. Offering answers to energy distribution negative issues, such as requirement balance, failure detection, verifiable and permanent way, and governance, grid and regulation database administration. The forecast of electricity generation guarantees supply dependability and thus the supply-chain management must be bathmats. Since external actors have distinct features in HRES, predicting electricity consumption is a challenging job. Methods of AI can sort out the correct estimate for electricity consumption in the country, along with manufacturing and distribution of sustainable energy. Reinforcement learning expands its capacity to upgrade the finding of resources. It may be utilized to promote various areas of forms of energy phones, battery, catalyzed, and crystal findings. AI methods may thus be utilized to create substances for sustainable energy sources [24]. In yet another important and interesting field also, AI is utilized, such as reverse design, in which the characteristics of the component are accorded to the Artificial intelligence system and the components derived from them are found.

4. Methodology

Two components form part of the overall electricity forecasting method. First, the data collection and interpretation are discussed. Second, for data or information, artificially intelligent methods are presented. The primary aim of this research is to provide document models which can correctly forecast wind and solar energy. The most essential element of the sustainable energy forecast is the collection and analysis of data. For the correct energy prediction, the data should be sent through into the data packet, including standardization, undesirable/false data outsource, data grouping, and data inferential statistics [24]. The first 2 are not used for all data instructional

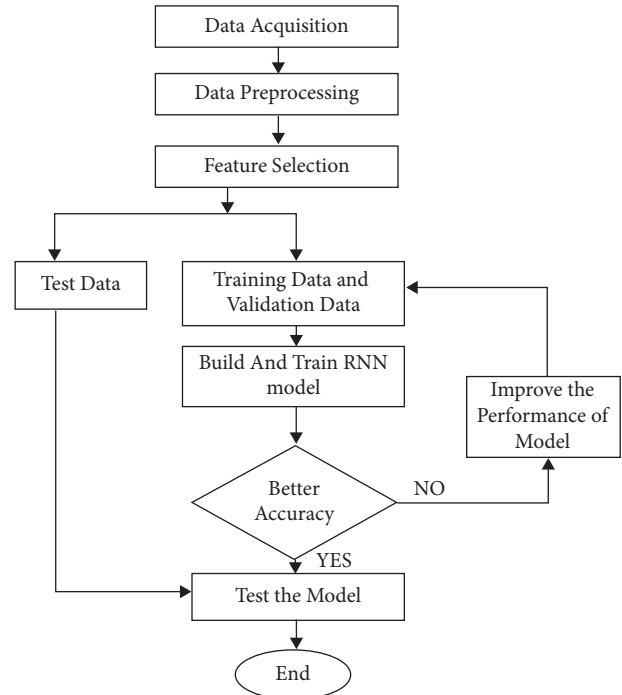


FIGURE 5: Schematic block of the AI-based training and prediction stages.

strategies and are primarily popular from before the data. Nevertheless, database clustering is needed to generate a training data. Furthermore, empirical pearson correlation offers insight into the delays used by the prediction models. Various renewable energy input variables regarding the training modeling and evaluation of particular predictions of renewable radiation, renewable and hydroelectricity [30]. Solar power prediction requires no more than nine factors, such as altitude, latitude/length, time (containing month by year and), median air temperature, median air currents, wind velocity and mean dampness in air.

The forecast would be average sun radiation. Similarly, the forecast of wind power requires wind speed/direction at specified place and temperatures. Figure 5 summarizes the approach that is based on the Machine Intelligence (AI) paradigm. The application of AI on renewable databases to future predicted values consists of 3 main phases:

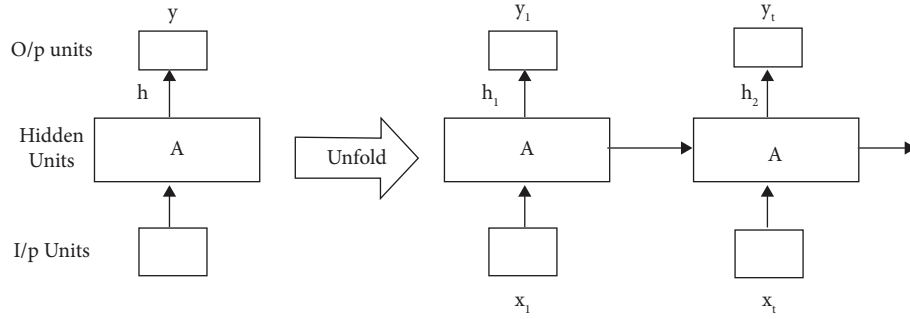


FIGURE 6: Illustration of RNN with unit performance.

- (i) Collecting power sources and surroundings data.
- (ii) Standardizing and preprocessing input information to extract characteristics.
- (iii) Develop the optimization technique, evaluate the correctness of the examples for the development and verify the was before model using patterns of verification. The developed AI algorithm is then utilized to predict energy output via testing dataset.

Neural networking methods which have the capacity to learn, store and create connections between non-linear information have included most outstanding data mining algorithms [31]. The sensors can monitor data with predictable styles, but not equivalent to one another and. Algorithms have fault resistant and better able to approximate any linear combination. They, therefore, are in a position to handle fragmented, noisy, quadratic, and quasi-data set [23].

4.1. RNN Model. The RNN is a separate kind of ANN with looped that may sense knowledge in training sets. It may exchange characteristics between neurons in various layers to create sequencing cycling in the networks to anticipate better outcomes. The looping design of RNN enables them to anticipate the time series and to process data before the output is produced [25]. Thus, the RNN model may have reminiscence and utilize preliminary data that will impact its value towards future predictions [26]. The feedback loops in the networks update the model or assist to recall future trends. It is one of the latest ANN methods that can predict time series in power generation. As the program can store everything information in memory, it is an appropriate and productive method to solar or wind generation forecast, such as time series analysis [18]. Figure 6 shows the basic architecture of an RNN unit inside which block 'A' uses the input model to produce h_t as well as predicted values. The chevron in block 'A' indicates the ongoing use of information within the block. Once the configuration is unwrapped, certain side effects seem to be a cause, as illustrated in Figure 6. The deployment of the Recurrent neural network, like with other methods, has three successive stages, namely retraining, training, and verification. The hidden layer displays network effectiveness and regulates time steps first from input data series to the predicted outputs. To show the RNN unit functionality in step t time,

let $x [x_1, x_2, \dots, x_t]$ be taken into account as the integration time, h_t as the hidden layer, and y_t as the predicted output. The cable network process from raw material to finished product is shown as follows.

The hidden state is expressed as follows:

$$h_t = f(h_{t-1}, x_t). \quad (9)$$

Also, the repeated previous hidden h_t is changed by altering input text by adding a dimension n . W_{xh} to the combination of previous state h_{t-1} and the weighted W_{hh} . By the transmission periodic function, the total of the weightings is then engaged as follows:

$$h_t = f(W_{hh} \cdot h_{t-1} + W_{xh} \cdot x_t). \quad (10)$$

The output is calculated by changing the previous hidden h_t by the concealed weighted to the output. Therefore, the equation can be written as follows:

$$y_t = f(W_{hy}, h_t). \quad (11)$$

The measurement result is compared with the goal such that error coastal areas are generated and then weighed up at all levels until an acceptable value is achieved.

5. Results and Discussion

Best accuracy measures are described and evaluated. In all, 40 kinds of prediction accuracy measures were collected in this research and it is simulated to verify its performance using MATLAB under five different case studies:

- Case study 1: Measurements of Forecasting Accuracy
- Case study 2: Observation of MAPE Values in Energy Prediction
- Case study 3: Calculation of R^2 Values in the Energy Prediction
- Case study 4: Comparison of R^2 and Training Time for the Selected Algorithms
- Case study 5: Comparison of MAE and RMSE for the Selected Algorithms

5.1. Case Study 1. Table 1 and Figure 7 include prediction accuracy measures used in more than 8 researches. The three most commonly used measures are the absolute mean error

TABLE 1: Measurements of forecasting accuracy.

Sources of energy measurement	Solar	Wind	Hydro-power	Biomass
RMSE	37	33	1	5
MAE	18	27	1	4
MAPE	13	24	0	2
R^2	7	9	1	4

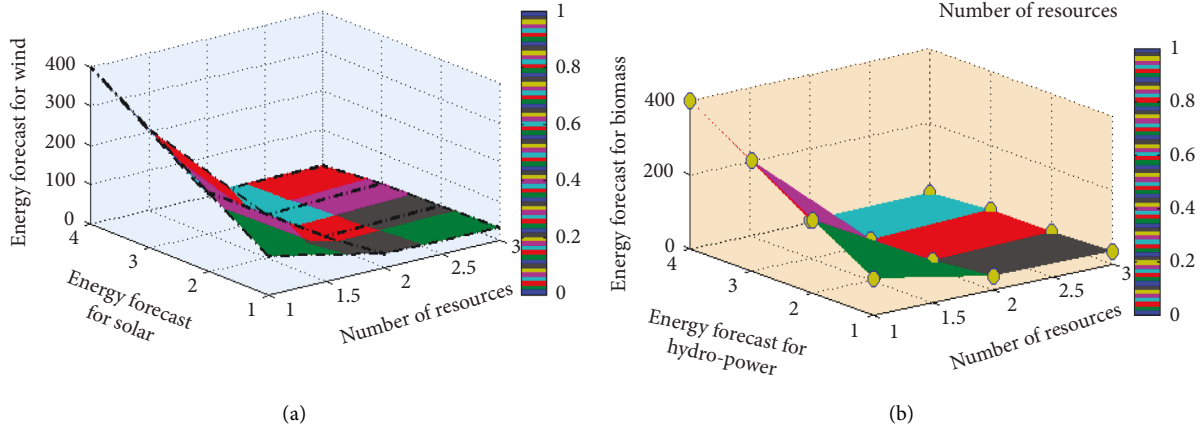


FIGURE 7: Accuracy of forecast. (a) Solar vs wind. (b) Hydro-power vs biomass.

(MAE), the absolute mean percentage error (MAPE) and the square root mean (RMSE). In varied units, renewable energy may be expressed, and renewable energy values vary a lot for various research. MAPE is given here to show prediction accuracy to prevent the effects of measures and quantities of sustainable power.

5.2. Case Study 2. A total of 36 gathered studies utilize MAPE to evaluate predictive accuracy in Table 2 and Figure 8. In general, in each research, several models were presented. Table 2, therefore, displays the best results in each research. MAPE scores below 10% indicate extremely accurate forecasts. The predictive accuracy of the gathered studies is thus excellent in terms of MAPE. Furthermore, the determination coefficient (R^2) is also another measure given for investigation in this research. The adjusted R^2 indicates the percentage of the variation in the dependent variable that may be explained by other factors.

5.3. Case Study 3. Table 3 and Figure 9 show 22 research gathered using R^2 as a sustainable energy prediction measure. The majority of R^2 values are greater than 0.8.

5.4. Case Study 4. At the conclusion of the optimization, Table 4 and Figure 10 show the optimum parameters and chosen values. In all, RNN offers more versatility than the other different methods. Nonetheless, the characteristics of SVM, RT, and RF seem more common than RNN. The freedom with which parameters are selected is both good and bad.

In terms of the capacity to capture the whole phenomena under evaluation, the best results were shown by RNN, followed immediately by RF and SVM.

5.5. Case Study 5. Table 5 and Figure 11 explain that R^2 values of SVM, RF, and RNN may seem comparable and different viewpoints may be shown in terms of evaluating MAE and RMSE. RNN provides an MAE 21% smaller than RF, 36% smaller than SVM and 60% smaller than RT. If the effectiveness is evaluated with regard to the MW of power, the variations between both the models become apparent. RNNs are more complicated than SVM, RT and RF, however, the accuracy of the model has priority above time and complexity provided the needs and restrictions of the use case are recognized.

5.5.1. Verve Robustness. This scenario examines the energy characteristics that are represented in terms of robustness by using best iteration conditions. Since the proposed method is used for minimizing the amount of energy in the case of different appliances, there is a possibility that the energy devices will become robust as the AI procedure is incorporated. The above-mentioned robustness will be present in real-time conditions as complexity in terms of time is much higher for every home appliance and as a result, strong optimization procedure is needed. In addition, the projected method frames the analytical model using closed-loop format thus reducing the robustness of energy appliances even at large operating conditions. The examined characteristics are simulated and compared with the existing model, as shown in Figure 12.

TABLE 2: MAPE values in energy prediction.

Sources of energy	Average MAPE (%)
Solar	9.019863
Wind	6.885576
Hydro-power	4.894
Biomass	2.6951

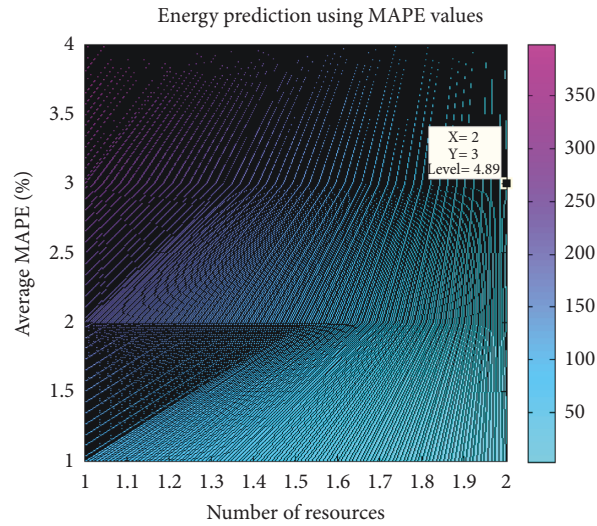


FIGURE 8: MAPE values in energy prediction.

TABLE 3: R^2 values in the energy prediction.

Sources of energy	Average R^2
Solar	0.9352
Wind	0.97527
Hydro-power	0.83
Biomass	0.9548

TABLE 4: Comparison of R^2 for the selected algorithms.

Algorithms	R^2
SVM	0.9738
RT	0.7814
RF	0.9648
RNN	0.9977

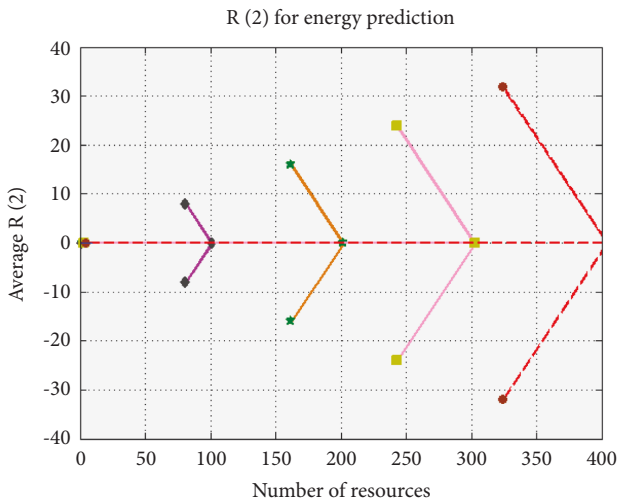


FIGURE 9: R^2 values in the energy prediction.

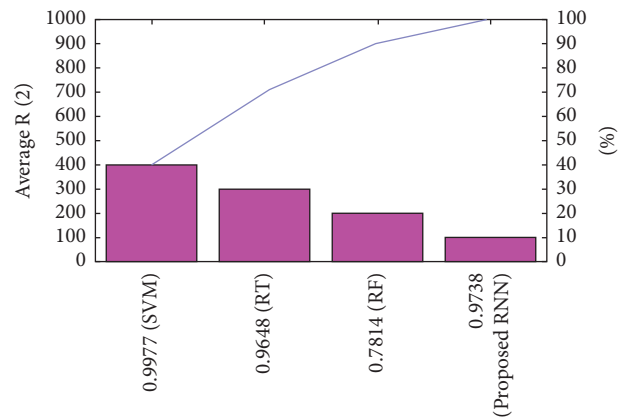


FIGURE 10: Comparison of R^2 for the selected algorithms.

In Figure 12, it is observed that the number of appliances is varied from 1 to 30 and for each change robustness is measured. From the comparison, it is much clear that the proposed method reduces the robustness of all appliances in real-time

conditions whereas the existing method increases the value of robustness to a certain extent. This can be proved with 15 different appliances as the proposed method crosses the robustness line without any marginal limit but in the next case with 16 appliances after reducing the number of renewable sources the projected method provides low robust conditions.

TABLE 5: Comparison of MAE and RMSE for the selected algorithms.

Algorithms	MAE	RMSE
SVM	983.87	1387.85
RT	1679.89	2318.87
RF	708.87	1188.93
RNN	684.10	862.85

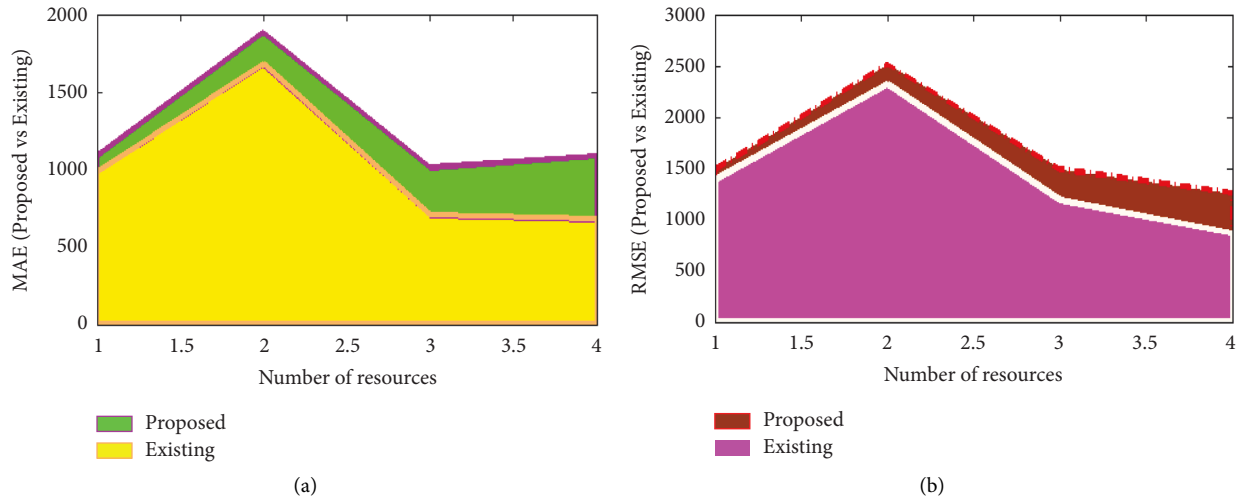


FIGURE 11: Comparison plot for the selected algorithms. (a) MAE. (b) RMSE.

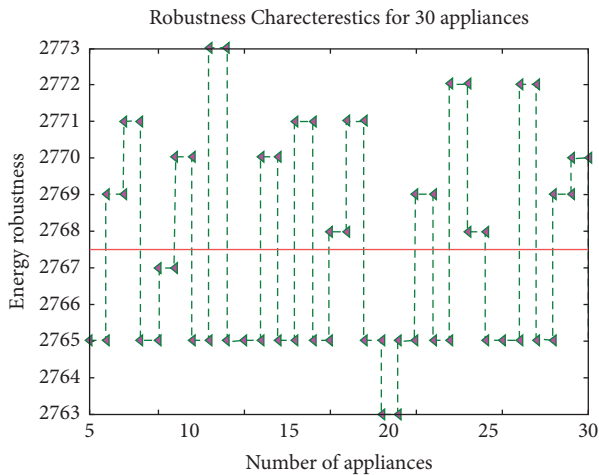


FIGURE 12: Comparison of robustness characteristics.

But in the existing method [21] if the number of appliances is increasing then robustness of all installed appliances increases in such a way thus energy management is not guaranteed as renewable sources are increased in the system.

6. Conclusions

The problem of sustainable power is growing because of current climatic changes and melting concerns. Accurate estimation of renewable energy is thus essential and a lot

of associated research has been carried out. Furthermore, the complexities of different environmental circumstances in systems for renewable resulting in inadequate use of closed mathematics formats to represent systems for bioenergy. Applications of AI have thus become common in the forecasts of sustainable power. In current history, this research has examined and evaluated artificial energy intelligent systems in energy forecasts from elements of intelligent machines, renewable resources, condition characterized methods, variable selection procedures and forecast performance-based assessment. Some potential future study paths in the clean energy forecast for artificially intelligent models were listed as follows. First of all, it can be noted that the majority of renewable energy projections in artificial intelligence technologies have concentrated on solar and wind energy forecasts. Therefore, other dispatchable projections, such as hydropower, hydroelectric power, wave action, pressurized water, and geothermal, may be viable areas for future study rather than forecasts of renewable. Furthermore, artificially intelligent and hybrid approaches may provide promising methods to predict sustainable power. Second, data before techniques affect simulation model forecasting accuracy in sustainable energy forecasts. This problem, however, has not yet received much attention. The study of data preparation methods and ML algorithms in sustainable energy forecasts may thus be a different path for additional investigation. Finally, the choice of criteria affects the effectiveness of machine intelligence algorithms in renewable power forecasts.

6.1. Policy Implications. The energy management system can be applied in all industries for managing different devices in the network by building a forecast application where all users can able to check the number of resources that are present at a certain time interval. Even the projected method using AI can be applied for choosing proper decision in emergency conditions about different energies that need to be supplied at appropriate time periods.

Data Availability

The data that support the findings of this study are available from the corresponding author, upon reasonable request.

Conflicts of Interest

The authors declare that they have no conflicts of interest.

References

- [1] J. Huertas-Tato, R. Aler, I. M. Galván, F. J. Rodríguez-Benítez, C. Arbizu-Barrera, and D. Pozo-Vázquez, "A short-term solar radiation forecasting system for the Iberian Peninsula. Part 2 Model blending approaches based on machine learning," *Solar Energy*, vol. 195, pp. 685–696, 2020.
- [2] Y.-J. Ma and M.-Y. Zhai, "A dual-step integrated machine learning model for 24h-ahead wind energy generation prediction based on actual measurement data and environmental factors," *Applied Sciences*, vol. 9, no. 10, Article ID 2125, 2019.
- [3] K. Irshad, A. Almalawi, K. Habib et al., "Experimental study of a thermoelectric air duct dehumidification system for tropical climate," *Heat Transfer Engineering*, vol. 42, no. 13-14, pp. 1159–1171, 2021.
- [4] D. Srpak, L. Havaš, S. Skok, and B. Polajžer, "Reducing wind power forecast error based on machine learning algorithms and producers merging," in *Proceedings of the 2019 IEEE International Conference on Environment and Electrical Engineering and 2019 IEEE Industrial and Commercial Power Systems Europe*, Genoa, Italy, June 2019.
- [5] P. R. Kshirsagar, H. Manoharan, H. A. Alterazi, N. Alhebaishi, O. B. J. Rabie, and S. Shitharth, "Construal attacks on wireless data storage applications and unraveling using machine learning algorithm," *Journal of Sensors*, vol. 2022, Article ID 8457116, 13 pages, 2022.
- [6] K. Irshad, A. I. Khan, S. A. Irfan, Md M. Alam, A. Almalawi, and Md H. Zahir, "Utilizing artificial neural network for prediction of occupants thermal comfort: a case study of a test room fitted with a thermoelectric air-conditioning system," *IEEE Access*, vol. 8, pp. 99709–99728, 2020.
- [7] S. Mujeeb, N. Javaid, H. Gul, N. Daoood, S. Shabbir, and A Arif, "Wind power forecasting based on efficient deep convolution neural networks," in *Proceedings of the 3PGCIC Conference*, Antwerp, Belgium, November 2019.
- [8] E. C. Eze and C. R. Chatwin, "Enhanced recurrent neural network for short-term wind farm power output prediction," *Journal of Applied Sciences*, vol. 5, pp. 28–35, 2019.
- [9] H. A. Alterazi and P. R. Kshirsagar, "Hariprasath Manoharan, Shitharth selvarajan, nawaf alhebaishi, gautam sri-vastava, jerry chun-wei lin, "prevention of cyber security with the internet of things using particle swarm optimization", " *Sensors*, vol. 2022, Article ID 22166117, 2022.
- [10] H. Z. Wang, Z. X. Lei, X. Zhang, B. Zhou, and J. Peng, "A review of deep learning for renewable energy forecasting," *Energy Conversion and Management*, vol. 198, Article ID 111799, 2019.
- [11] J. Ferrero Bermejo, J. F. Gómez Fernández, F. Olivencia Polo, and A. Crespo Márquez, "A review of the use of artificial neural network models for energy and reliability prediction. a study of the solar PV, hydraulic and wind energy sources," *Applied Sciences*, vol. 9, Article ID 1844, 2019.
- [12] S. Shitharth, "Gouse baig mohammad, K.sangeetha, 'predicting epidemic outbreaks using IoT, artificial intelligence and cloud', the fusion of internet of things, artificial intelligence, and cloud computing in health care," *Internet of Things*, vol. 1, no. Issue 1, pp. 197–222, 2021.
- [13] A. Mellit, A. Massi Pavan, E. Ogliairi, S. Leva, and V. Lughi, "Advanced methods for photovoltaic output power forecasting: a review," *Applied Sciences*, vol. 10, no. 2, p. 487, 2020.
- [14] A. Mosavi, M. Salimi, S. Faizollahzadeh Ardabili, T. Rabczuk, S. Shamshirband, and A. R. Varkonyi-Koczy, "State of the art of machine learning models in energy systems, a systematic review," *Energies*, vol. 12, no. 7, 2019.
- [15] A. Ahmed and M. Khalid, "A review on the selected applications of forecasting models in renewable power systems," *Renewable and Sustainable Energy Reviews*, vol. 100, pp. 9–21, 2019.
- [16] A. Zendeheboudi, M. A. Baseer, and R. Saidur, "Application of support vector machine models for forecasting solar and wind energy resources: a review," *Journal of Cleaner Production*, vol. 199, pp. 272–285, 2018.
- [17] U. K. Das, K. S. Tey, M. Seyedmahmoudian et al., "Forecasting of photovoltaic power generation and model optimization: a review," *Renewable and Sustainable Energy Reviews*, vol. 81, pp. 912–928, 2018.
- [18] Z. Zhu, D. Zhou, and Z. Fan, "Short term forecast of wind power generation based on SVM with pattern matching," in *Proceedings of the 2016 IEEE International Energy Conference*, Leuven, 2016.
- [19] A. Torres-Barran, A. Alonso, and J. R. Dorronsoro, "Regression tree ensembles for wind energy and solar radiation prediction," *Neurocomputing*, vol. 326-327, pp. 151–160, 2019.
- [20] S. Akojwar and P. Kshirsagar, "A novel probabilistic-PSO based learning algorithm for optimization of neural networks for benchmark problems," *WSEAS Transactions on Electronics*, vol. 7, pp. 79–84, 2016.
- [21] Y. Liu, G. Liu, Y. Wu, W. He, Y. Zhang, and Z. Chen, "Reinforcement-learning-based decision and control for autonomous vehicle at two-way single-lane unsignalized intersection," *Electronics (Switzerland)*, vol. 11, no. 8, Article ID 1203, 2022.
- [22] Y. Ma, X. Chen, L. Wang, and J. Yang, "Study on smart home energy management system based on artificial intelligence," *Journal of Sensors*, vol. 2021, Article ID 9101453, 9 pages, 2021.
- [23] N. Islam, K. Irshad, Md H. Zahir, and S. Islam, "Numerical and experimental study on the performance of a Photovoltaic Trombe wall system with Venetian blinds," *Energy*, vol. 218, Article ID 119542, 2021.
- [24] M. A. Ramli, S. Twaha, K. Ishaque, and Y. A. Al-Turki, "A review on maximum power point tracking for photovoltaic systems with and without shading conditions," *Renewable and Sustainable Energy Reviews*, vol. 67, pp. 144–159, 2017.
- [25] S. K. Prashanth, S. Shitharth, B. Praveen Kumar, V. Subedha, and K. Sangeetha, "Optimal feature selection based on evolutionary algorithm for intrusion detection," *SN Computer Science*, vol. 3, no. 6, p. 439, 2022.

- [26] S. Selvarajan, H. Manoharan, T. Hasanin et al., *Biomedical Signals for Healthcare Using Hadoop Infrastructure with Artificial Intelligence and Fuzzy Logic Interpretation* Applied Sciences, Iserlohn, Berlin, 2022.
- [27] I Ameenuddin, S Sayed, I Kashif et al., “Machine learning-based modeling of thermoelectric materials and air-cooling system developed for a humid environment,” *Materials Express*, vol. 11, no. 2, pp. 153–165, 2021.
- [28] H. Manoharan, Y. Teekaraman, P. R. Kshirsagar, S. Sundaramurthy, and A. Manoharan, “Examining the effect of aquaculture using sensor-based technology with machine learning algorithm,” *Aquaculture Research*, vol. 51, no. 11, pp. 4748–4758, 2020.
- [29] A. Visvizi and M. D. Lytras, *Smart Cities: Issues and Challenges: Mapping Political, Social and Economic Risks and Threats*, Elsevier, Amsterdam, The Netherlands, 2019.
- [30] S. N. Qasem, S. Samadianfard, H. S. Nahand, A. Mosavi, S. Shamshirband, and K. W. Chau, “Estimating daily dew point temperature using machine learning algorithms,” *Water*, vol. 11, no. 3, p. 582, 2019.
- [31] M. Gouse Baig, S. Shitharth, and P. Dileep, “Classification of normal and anomalous activities in a network by cascading C4.5 decision tree and K-means clustering algorithms,” in *Social Network Analysis, Theory and Applications* Wiley Online Library, Scrivener Publishing, Hoboken, New Jersey, U.S, 2022.
- [32] S. G. Akojwar and P. R. Kshirsagar, “Performance evolution of optimization techniques for mathematical benchmark functions,” *International Journal of Computers*, vol. 1, pp. 231–236, 2016.
- [33] K. Irshad, “Performance improvement of thermoelectric air cooler system by using variable-pulse current for building applications,” *Sustainability*, vol. 13, Article ID 9682, 2021.
- [34] M. Padmaja, S. Shitharth, K. Prasuna, A. Chaturvedi, P. R. Kshirsagar, and A. Vani, ‘*Growth of Artificial Intelligence to Challenge Security in IoT Application*’, *Wireless Personal Communications*, Springer, Berlin Germany, 2021.
- [35] K. Nam, S. Hwangbo, and C. Yoo, “A deep learning-based forecasting model for renewable energy scenarios to guide sustainable energy policy: a case study of Korea,” *Renewable and Sustainable Energy Reviews*, vol. 122, Article ID 109725, 2020.
- [36] A. Rochd, A. Benazzouz, I. Ait Abdelmoula et al., “Design and implementation of an AI-based and IoT-enabled home energy management system: a case study in benguerir—Morocco,” *Energy Reports*, vol. 7, pp. 699–719, 2021.

Research Article

An Innovative Solution for Battery Draining in 5G Devices Using Alternate Routing Model

M. Sivasubramanian,¹ J. Vignesh,² V. Senthil kumar,³ S. Sumathi,⁴ R. Sathish,⁵ Kumar Parasuraman,⁶ B Santhosh Kumar,⁷ M Kathirvelu,⁸ Leena Bojaraj,⁹ Srihari K ,¹⁰ and Negasi Tsegay Sbhat ¹¹

¹Department of Computer Science, JP College of Arts and Science, Agarakattu, Tenkasi 627852, Tamilnadu, India

²Department of Information Technology, Malla Reddy Institute of Technology and Science, Hyderabad, Telangana 500100, India

³Department of Computer Science and Engineering, Malla Reddy Institute of Technology & Science, Secunderabad, Telangana 500100, India

⁴Department of Artificial Intelligence and Data Science, Sri Eshwar College of Engineering, Coimbatore, Tamilnadu, India

⁵Department of AI & DS, Kgisl Institute of Technology, Coimbatore, Tamilnadu, India

⁶Centre for Information Technology and Engineering, Manonmaniam Sundaranar University, Tirunelveli 627 012, Tamilnadu, India

⁷Guru Nanak Institute of Technology, Hyderabad, Telangana, India

⁸Department of ECE, KPR Institute of Engineering and Technology, Coimbatore 641407, Tamil Nadu, India

⁹Department of ECE, KGISL Institute of Technology, Coimbatore, Tamilnadu, India

¹⁰SNS College of Technology, Coimbatore, Tamilnadu, India

¹¹Department of Chemical Engineering, College of Biological and Chemical Engineering, Addis Ababa Science and Technology University, Addis Ababa, Ethiopia

Correspondence should be addressed to Srihari K; harionto@gmail.com and Negasi Tsegay Sbhat; negasi.tsegay@aastustudent.edu.et

Received 8 August 2022; Revised 10 September 2022; Accepted 14 September 2022; Published 29 September 2022

Academic Editor: Ravi Samikannu

Copyright © 2022 M. Sivasubramanian et al. This is an open access article distributed under the Creative Commons Attribution License, which permits unrestricted use, distribution, and reproduction in any medium, provided the original work is properly cited.

When the electrolyte is layered, excessively large and prolonged charging and exhaust currents lead to the random tendency of reactions in different parts of the electrodes. This was leading to mechanical stresses and the warming of the plates of the battery. The presence of nitric and acetic acid contaminants in the electrolyte improves the oxidation of the deeper layers of positive electrodes. Because lead dioxide has a larger volume than lead, electrodes expand and curve. Positive electrodes are subject to war and growth. The negative electrode curve is mainly caused by the nearby distracted positive people. The adjustment of the distracted electrodes can only be carried out by removing the battery. The lack of sulfate and fully charged electrodes are subject to correction because they are soft and easy to adjust. The main contribution of this proposed work is to provide an innovative solution to resolve the battery draining issues in 5G devices with the help of an alternate routing model. The proposed model will provide an idea that is used to slice distracted electrodes washed with water and placed between soft, hard boards. Generally, on the top board, a load is installed, which increases the edges of the electrodes. Electrodes are banned directly or through the amplitude of a top or hammer to avoid the destruction of the active layer; hence, the draining of the battery was reduced.

1. Introduction

The number of users is increasing with these smart 5G network devices because it is easier to access modern networks like 2 G,

3 G, and 4 G and social networking sites like Facebook and WhatsApp. Due to this, the usage of smart 5G network devices is increasing [1]. But there is a problem with that. That is, most people have complained that my 5G network devices go dry

immediately and do not charge; we have used it ourselves [2,3]. After a few hours of continuous use, it starts beeping “battery low,” and immediately we go to the charger. This is a regular occurrence. This low battery problem occurs, if it is caused by frequent charging or is it caused by overnight charging. It is widely believed that the life of the battery will decrease due to this [4,5]. Generally, users of smart 5G network devices do not use them for more than two years. By then they sell it to purchase new 5G network devices [6]. So, they do not know about the battery damage. But experts say that due to frequent charging, the lithium batteries in the 5G network devices are damaged and thus the charge does not hold [7]. Frequent charging like this is sure to damage lithium-ion batteries. But it's not because it takes too long to charge, because smart5G network devices are designed to handle a lot of charges [8]. The main cause of battery damage is that our batteries are designed to charge quickly. This causes the batteries to heat up and thus damage them. Smart5G network devices should always be kept at temperatures below 35 degrees Celsius [9,10]. There is a way to extend the life of our smart 5G network device batteries. It means that using some chargers that are patient charging types will not damage the battery and increase its life. Smart 5G network devices today come with advanced features and amenities. The variety of applications in smart 5G network devices makes the users very attractive [11]. But as the applications increase, the 5G network devices' battery life becomes a concern. Users may want to fully utilize apps, but at the same time, they need to worry about battery life [12]. It is not convenient to recharge the 5G network devices every time. So, improving the battery life of smart 5G network devices is a concern for developers, manufacturers, and users [13]. You may wonder why you need to worry about battery power when you have a charger or power bank at home. Answer: repeated charging will degrade your battery performance. This will drain your battery life. So, care needs to be taken to conserve battery power [14].

If the distracted electrodes are not dangerous to nearby negative electrodes, we are allowed to limit measures to prevent a short circuit. For this, an additional splitter is placed on the accumulated side of the distracted electrode. Such electrodes are replaced during the next battery repair. With significant and progressive casting, it is necessary to replace all the positive electrodes in the battery with new ones [15]. Replace only the distracting electrodes with new ones. The main source of harmful contaminants in the electrolyte during the operation is to get water. Therefore, it should be used to get the first place to be filtered or equal to the entry of harmful contaminants in the electrolyte. To remove the iron, the batteries are discharged, removed with contaminated electrolyte slag, and washed with filtered water. After washing, the batteries are filled with 1.04–1.06 g/cm³ density and will be charged until the voltage and density of the electrolyte are changed [16]. The solution is then removed from the batteries, replaced with 1.20 g/cm³ instead of the new electrolyte, and the batteries are discharged to 1.8 V. At the end of the discharge, the electrolyte is checked for iron content. With favorable analysis, the batteries are normal. In the event of an adverse analysis, the treatment cycle is

repeated. To eliminate manganese pollution, the batteries are discharged. The electrolyte is new and the batteries are normally charged. If the pollution is new, a single electrolyte change is sufficient. Copper is not removed from batteries with electrolytes [17]. To remove it, the batteries must be charged. When charging, the copper is converted to negative electrodes, which are replaced after charging. Therefore, it is advisable to make such an alternative if the old replacement nonnegative electrodes are in the stockpile. In accumulations with opaque tanks, you can check the number of scissors using a square made of acid-resistant material [18]. A separator is removed from the middle of the accumulation, lifting several separators nearby, and reduced to the space between the electrodes until a square has interacted. Then the angle is rotated 90° and rises to communicate with the lower edge of the electrodes. The distance to the lower edge of the electrodes from the slag surface is equal to the difference in the variation of the measurements at the upper end of the square and 10 mm [19–22]. If the square does not spin or rotate with difficulty, the slag can be communicated with or near electrodes. The working principle of the proposed system is concentrated on identifying the electrolyte leaks on the equipment, cleaning the electrolyte, and recycling the remaining electrolyte.

The main contribution of this proposed method is focused on the following:

- (i) The improvisation and utilization of the battery life cycle and its concentration on the improvement of electrolytes.
- (ii) The battery power and the used loader components and their selection and utilization are monitored, and effectiveness is calculated and measured.
- (iii) Also, the proposed method concentrates on managing the charging and outdoor components and their resource utilization.

2. Literature Review

Smart 5G network devices consume more power than voice notifications. So, turning off the vibration alert will save battery charge. Dimming the screen display can go a long way toward saving power. Higher brightness consumes more power whenever we turn on our display [1]. It's best to use an auto-brightness setting that automatically adjusts screen brightness while conserving battery. The lower the brightness, the higher the batteries' charge. Reducing screen time-out times can reduce power consumption [2]. Our 5G network devices lose charge in standby mode. So once the screen is off, it will save the battery from being used anymore. We do not always remember to lock the 5G network devices once we use it. Reducing screen time during that time will save battery. If you are not using the 5G network devices for a long time while attending a meeting or any other important activity, it is useful to switch it off. However, turning on the 5G network devices may use more power [3].

Turning it off for a few hours will save more battery power than sleep mode. You need to know the type of battery used in your 5G network devices for proper charging.

There are two types of batteries commonly used in smart 5G network devices, namely lithium-ion (Li-Ion) and nickel-based batteries (nickel-metal-hydrate (NiMH) and nickel-cadmium (NiCd)) [4]. Nickel-based batteries should only be charged when there is no power supply. Repeated charging reduces battery life. They should not be charged when there is a good amount of electricity. Li-ion batteries have a long cycle life. They have to charge frequently to maintain the original capacity [8]. So, find your battery type for proper charging, and then follow the proper charging strategy. While using the 5G network devices we can open many applications. But often we do not worry about closing them later. So even if we are not using it, it will consume battery power in the background, so closing unused apps actually reduces power consumption [10].

A GPS system allows you to track your location. It consumes a lot of battery power. When enabled, many apps use GPS to track their location and waste battery power. So, it is better to turn off GPS when not needed to save power. Constantly searching for signals consumes energy [11]. So always turn off these services when you do not need them. Otherwise, it drains the battery's power. A lot of energy is spent searching for signals, especially when you are in an area with poor network reception. Therefore, it is better to keep the 5G network devices in airplane mode in such places. Use these services only when necessary [12]. Too many notifications from various apps can consume too much power. To disable notifications for a specific app, go to app info and uncheck the option to show notifications. It can reduce energy consumption through applications. Smart 5G network devices can heat up and discharge more battery power when kept at high temperatures [13]. So, maintaining a cool temperature will help bring out the optimum performance of your battery, so avoid exposing your 5G network devices to high temperatures. Keep away from direct sunlight or any other hot places. Avoid exposing your 5G network devices to excessive heat [14].

3. Proposed Model

When charging and recharging, gases are released from all batteries and storage batteries, excluding gas-tightly sealed batteries. It is the result of water electrolysis in the recharge current. The resulting gases are hydrogen and oxygen. When they are released into the environment, the amount of hydrogen concentration in the air may exceed 4%. To avoid improper charging and/or excessive gas evolution, the type of charger, its class, and its properties must be matched to the battery type according to the manufacturer's instructions. If the testing gas emission is less than the installation of this quality, the requirements for the calculation of ventilation will not be accepted during the standard battery test. If the test gas emission values are higher than those of this quality, the ventilation requirements will be tightened. Types of batteries are shown in Figure 1. A battery (secondary cell, rechargeable cell, and single cell) is a chemical current source with the ability to restore electricity tariff after an interruption.

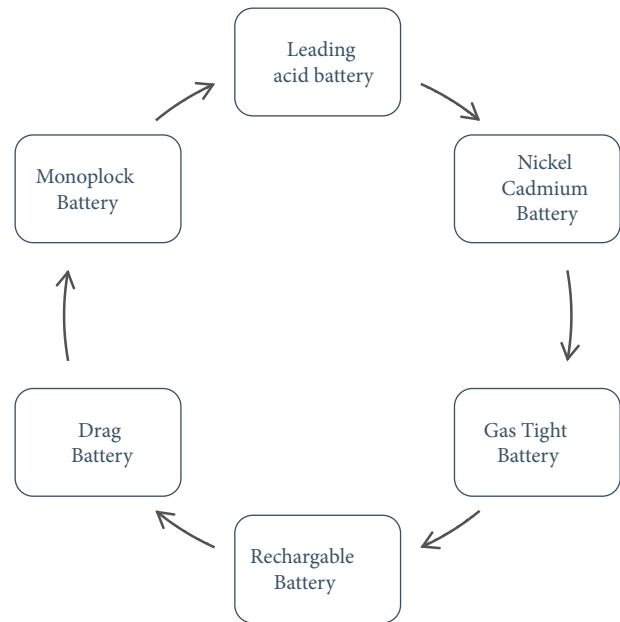


FIGURE 1: Different types of batteries.

- (i) Leading acid battery: It's a rechargeable battery based on the aquatic solution of sulfuric acid, which contains lead dioxide and negative electrodes leading the lead.
- (ii) Nickel cadmium battery: it is an alkaline electrolyte battery that contains cadmium in nickel oxide and negative electrodes.
- (iii) Gas-tight battery: the battery is sealed and does not discharge gas or liquid during operation under the limited charge and temperature conditions specified by the manufacturer. Battery protection devices can be installed to prevent dangerous high internal stresses
- (iv) Rechargeable battery: two or more batteries are combined together and used as an electrical source.
- (v) Drag battery: A rechargeable battery designed to supply electric vehicles with the energy saved.
- (vi) Monoplock Battery: A battery with many separate but electricity-attached chemical current sources, each containing electrodes, an electrolyte, tracks or connectors, and, separators.

When the charging equipment is stopped, it can be considered that the excretion from the batteries has been completed within 1 hour after turning off the charging current. However, after this time, safety precautions must be followed by the battery shock when the gas is installed in the batteries or when the vehicle is in operation. Some gases can be released during maintenance due to regeneration braking. Battery 5G networks, plates, boxes, and boxes must have adequate mechanical strength, resist the chemical effects of electrolytes, and protect against the effects of leakage or electrolyte leakage. This proposed model is shown in the following Figure 2:

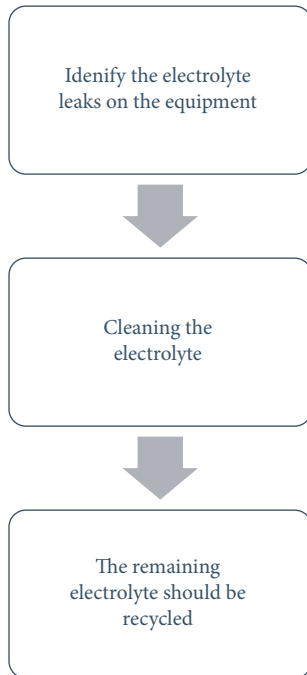


FIGURE 2: Proposed model approach for draining.

- (i) Precautions should be taken against electrolyte leaks on the equipment/accessories above the battery.
- (ii) Nothing should be banned from cleaning the electrolyte or water spilled on the battery tray.
- (iii) After maintenance, the remaining electrolyte should be recycled according to local rules.

When working with any battery, its batteries are interconnected by pipes for a gas exhaust system or water top-up system, and precautions should be taken to reduce the spread of eruptions between the current leak or battery batteries. The following security measures must be taken from the proposed model shown in Figure 3:

- (i) Reduce the risk of the current leak; for this purpose, the pipe system must match the energy of the circuit.
- (ii) Reduce the risk of spreading current leaks and eruptions by reducing the number of batteries in circuits attached by a pipe system.
- (iii) Maximum batteries attached to the pipe of the pipes in a row are not greater than the size specified by the manufacturer of the system.

A centralized gas exhaust system is used to discharge gases from the battery. In most cases, this system is related to the centralized water topping system. There are no products, testing, or standards for batteries with centralized gas exhaust systems using hydrogen exhaust systems or gas collecting hats and pipes. Nevertheless, it is recommended to comply with the requirements of the grade regarding the ventilation of a 5G network or vehicle when charging batteries. With a centralized flue gas system, the cavity must be located outside the battery box and protect the flames from

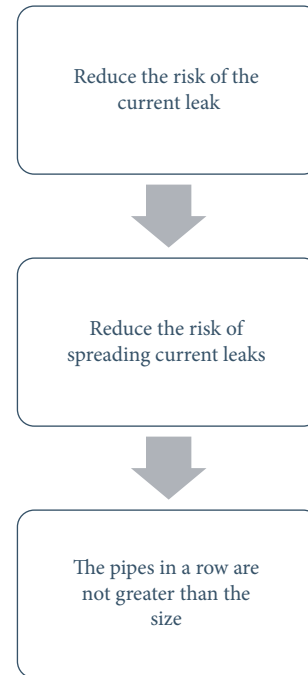


FIGURE 3: Proposed model approach for draining.

the possibility of an eruption caused by the flame sources near the vents. When charging, if a separate windmill is connected to a compulsory ventilation system, it releases all the evolved gases outside the charging zone.

- (i) Step 1: the batteries in the power plants are operated by the power workshop, and the sub-plants are operated by the subpower service.
- (ii) Step 2: the maintenance of the battery should be assigned to a specialist battery expert or specially trained electrician. Accepting the battery after installation and repair, its function and maintenance must be managed by the person in charge of the power station or network company's electrical equipment.
- (iii) Step 3: when running battery systems, ensure the required voltage level in DC buses in their long-term, reliable activity and in normal and emergency conditions.
- (iv) Step 4: before running the newly fitted or retired battery, the battery capacity should be verified for 10 hours of exhaust current, the quality and density of the electrolyte, the voltage of the batteries, and the battery's relation to the ground at the end of the charge and the excretion.
- (v) Step 5: batteries should be constantly charged. Charging installation should provide voltage confirmation in battery tires with $\pm 1-2\%$ deviation. Additional battery packs that are not constantly used in the process must have a separate charging device.
- (vi) Step 6: all battery packages should be fully charged to prevent the sulfation of the electrodes, and the battery charges should be balanced.

- (vii) Step 7: to determine the real battery capacity (within nominal efficiency), the control discharges must be carried out in accordance with the SEC.
- (viii) Step 8: after the battery emergency discharge at the power station, the capacity of 90% of its normality should not be carried out for more than 8 hours.
- (ix) Step 9: control batteries are planned to monitor the status of the battery. Control batteries must be replaced annually, and their number is set by the energy company's chief engineer, depending on the battery status, but not less than 10% of the batteries in the battery.
- (x) Step 10: the electrolyte density is normalized at a temperature of 20°C. Therefore, since the density of the electrolyte is measured at a different temperature from 20°C, the formula must be densely reduced to 20°C
 R_{20} is the density of electrolyte at a temperature of 20°C, G/CM3;
 where,
 R_T -temperature t ,
 electrolyte density in G/CM3;
 the coefficient of the density of the electrolyte with a temperature change of 0, 0007-1°C;
 T -electrolyte temperature, °C.
- (xi) Step 11: the battery of the 5G network should be kept clean. The ground spilled electrolyte should be removed immediately with dry sawdust. After that, soak the floor in the soda ash solution and then wipe it with water.
- (xii) Step 12: battery tanks, busbar insulators, insulators under the tanks, wardrobe their insulators, and wrap the shelf plastic coatings with a cloth, first moistened with water or soda solution, and then dry.
- (xiii) Step 13: the temperature in the battery 5G network should be maintained at less than +10. In auxiliary power plants that do not have staff on duty, temperature decrease is allowed up to 5 C. Sudden temperature changes in the battery's 5G network are not allowed, thereby not causing moisture condensation, and reducing the battery's insulation resistance.
- (xiv) Step 14: it is important to monitor the status of the acid-resistant sketch of walls, ventilation pipes, metal structures, and shelves. All defective places should be colored.
- (xv) Step 15: technical petroleum jelly lubrication of nonpainted compounds should be renewed from time to time.
- (xvi) Step 16: the network equipment in the battery 5G network should be closed. In the summer, the network equipment is allowed to be open during

the fees, if the outdoor air is not dusty, and if there are no other 5G networks above the entrance of the chemical plants or above the ground.

- (xvii) Step 17: in the wooden pots, the top edges of the lead lining should not touch the tank. If the contact is found, the edges of the lining must be bent to prevent the drops of the electrolyte from entering the cortex by destroying the tree of the tank.
- (xviii) Step 18: to reduce the evaporation of the electrolyte of open-type batteries, the cardboard should be used to absorb the electrolyte. Care should be taken not to stretch beyond the inner edges of the tank.

Even at the same battery current, even at the optimal battery charging voltage, it is not sufficient to maintain all batteries fully charged due to the differences in the self-exclusion of individual batteries. To bring all SK-type batteries to a fully charged state and prevent the sulfation of the electrodes, the standard-level value of the electrolyte density in all batteries should be set at 1.2–1.21 g/cm³. Batteries running in standard charging mode are not used under normal conditions. If the charging device is fails or disconnected, they are only discharged during emergencies or control discharges. Controlled discharges are made to determine the real capacity of the battery and are carried out in 10- or 3-hour exhaust modes. At thermal power plants, the control of batteries should be carried out once every 1 to 2 years. In the hydroelectric stations and substations, the required amount of discharges must be made. In cases where the number of batteries is not adequate to provide voltage on the tires at the end of the discharge within the specified limits, a portion of the main batteries is allowed to be discharged.

4. Results and Discussion

The proposed alternate routing model (ARM) was compared with the existing Trust-Based Co-Operative Cross-Layer Routing (TCCR), Dynamic Energy Scheduling and Routing (DESR), efficient routing and performance amelioration (ERPA), and integrated structured cabling system (ISCS). The entire proposed simulation routing model and other existing routing models are carried out and executed using NS 3 simulator, and a high computing processor system has been used in this experiment. The percentage of accuracy achieved in this proposed work ranges between 96% and 98% higher than other existing routing protocols and scheduling algorithms.

4.1. Battery Life Cycle. The battery is covered with a lid so that electrolysis and evaporation materials are freely removed from the battery in the atmosphere. The rechargeable battery, in which batteries are covered but there is a valve that removes gas if the internal pressure is exceeded. This was shown in the following Table 1.

TABLE 1: Management of battery life cycle.

No of inputs	TCCR	DESR	ERPA	ISCS	ARM
100	71.31	74.58	68.66	89.47	95.22
200	71.64	76.08	69.25	91.34	96.23
300	72.98	77.19	70.23	92.17	96.39
400	74.12	77.57	71.44	93.08	97.35
500	75.17	78.58	72.58	94.00	96.92
600	75.88	79.51	73.69	95.33	98.12
700	77.18	80.51	74.39	96.41	98.28

4.2. Electrolyte Management. A liquid or solid material with mobile ions that provide ionic conductivity. The gas evolution from water electrolysis in the battery electrolyte is called gas emissions. The electrolyte used in lead-acid batteries is an aquatic solution of sulfuric acid. The electrolyte used in nickel-cadmium and nickel-metal hydride batteries is the water solution of potassium hydroxide. To prepare the electrolyte, use only distilled or dehydrated water. Battery auxiliary equipment, racks, or products used for rails, and battery components must be resistant to or protected from the chemical effects of electrolyte. In the case of splashing electrolyte, it is necessary to remove the fluid with an absorbed substance, preferably one that is neutral. This was shown in Table 2.

4.3. Battery Power. The process of receiving electrical energy from a battery or rechargeable battery from the outer circuit results in chemical changes in the battery, resulting in the electrical energy's chemical power. This is shown and discussed in Table 3.

4.4. Loader Component (High Charge). Continuous charging leads to temperature increase and loss in efficiency of the battery. When installing the temperature control system, it is necessary to prevent any risk from flame sources, leakage current, and electrolyte leaks. This is shown and discussed in Table 4.

4.5. Outdoor Battery Equipment. Equipment installed in the battery to maintain or monitor battery function. The centralized water filling system, the electrolyte compound system, the battery control system, the centralized gas exhaust system, the battery connectors (plug connectors/connections), and the temperature control systems are the important components of outdoor equipment. This is shown and discussed in Table 5.

4.6. Charging Components. It is a closed space or area designed for charging batteries. The 5G network can also be used for battery care. Designed and fitted the outer part for charging batteries. The bat can also be used for maintenance. Maintenance devices such as funnels, hydrometers, and thermometers should be isolated separately for lead-acid and nickel-cadmium batteries and should not be used for any other purpose. This is shown and discussed in Table 6.

TABLE 2: Management of electrolyte.

No of inputs	TCCR	DESR	ERPA	ISCS	ARM
100	69.01	72.28	72.06	82.21	94.31
200	69.34	73.78	72.65	84.08	95.35
300	70.68	74.89	73.63	84.91	95.48
400	71.82	75.27	74.84	85.82	96.44
500	72.87	76.28	75.98	86.74	96.01
600	73.58	77.21	77.09	88.07	97.25
700	74.88	78.21	77.79	88.94	97.36

TABLE 3: Management of battery power.

No of inputs	TCCR	DESR	ERPA	ISCS	ARM
100	72.06	93.29	66.14	87.24	96.00
200	70.43	91.55	64.56	85.82	94.71
300	69.95	89.21	62.36	84.56	93.70
400	68.66	88.40	60.73	82.57	92.81
500	66.55	86.11	59.59	80.10	92.44
600	65.06	84.18	57.39	78.66	91.40
700	63.25	82.45	56.24	76.94	90.63

TABLE 4: Management of loader component.

No of inputs	TCCR	DESR	ERPA	ISCS	ARM
100	70.27	64.54	64.50	73.77	94.05
200	71.90	66.28	66.08	75.19	95.34
300	72.38	68.62	68.28	76.45	96.35
400	73.67	69.43	69.91	78.44	97.24
500	75.78	71.72	71.05	80.91	97.61
600	77.27	73.65	73.25	82.35	98.65
700	79.08	75.38	74.40	84.07	99.42

TABLE 5: Management of outdoor battery equipment.

No of inputs	TCCR	DESR	ERPA	ISCS	ARM
100	68.89	65.01	62.15	70.58	94.21
200	68.78	65.03	61.98	70.31	93.71
300	68.76	65.91	62.71	70.61	93.83
400	71.86	68.74	66.05	74.12	97.06
500	73.06	70.06	66.78	75.44	97.44
600	73.67	70.89	67.67	75.98	98.01
700	74.08	71.29	67.75	76.28	97.71

TABLE 6: Management of charging components.

No of inputs	TCCR	DESR	ERPA	ISCS	ARM
100	74.85	75.89	54.98	65.40	92.07
200	76.52	77.02	57.91	66.66	94.54
300	78.47	77.37	59.45	68.55	95.34
400	80.46	79.32	61.48	69.75	96.54
500	83.04	80.09	62.38	61.31	97.18
600	85.03	80.47	64.35	73.06	98.44
700	87.05	81.60	65.82	73.99	99.44

5. Discussion

Mainly, the overall working principle of the proposed system is concentrated on identifying the electrolyte leaks on the equipment, cleaning the electrolyte, and recycling the remaining electrolyte. The percentage of accuracy achieved in this proposed work has been improvised over other existing routing protocols and scheduling algorithms. The proposed method gives a clear idea of how we obtain a better battery life cycle and also about the utilization and selection of battery power and electrolyte. Also, it shows that we achieved 98 percent accuracy in the allocation of loads and selection of outdoor components, which is higher than other existing routing mechanisms.

6. Conclusion

Before the start of the discharge, the exhaust date of the electrolyte in each battery, the voltage, and the temperature in the density and control batteries are recorded. Measurement results must be compared to the results of the measurements of the previous digits. For the most accurate assessment of the battery status, it is necessary to carry out all the control discharges of this battery in the same mode. The measurement data must be entered. If the average temperature of the electrolyte varies from 20°C during the discharge, the actual capacity obtained should be reduced to 20°C according to the formula. The resistance of the charged battery is measured by the insulation monitoring device in the DC buses or with a voltmeter with an internal resistance of at least 50 kOHM. If there are signs of a short circuit, the batteries in the glass tank should be carefully examined by a small translucent lamp. The batteries in hard rubber and wooden pots are studied from the top. In batteries running under standard charging with increased voltage, the growth of fluffy leading trees may develop on the negative electrodes, which causes a short circuit. If the growths are found on the upper edges of the electrodes, they should be disconnected with a piece of glass or other acidic materials. It is recommended to make small movements of the separators to prevent and remove a growth in other parts of the electrodes. In future enhancements by performing several deep learning algorithms and artificial intelligence concepts the improvisation on the battery usage can be improved[23].

Data Availability

The datasets used and/or analyzed during the current study are available from the corresponding author upon reasonable request.

Conflicts of Interest

The authors declare that they have no conflicts of interest.

References

- [1] M. Panchal, R. Upadhyay, and P. Vyavahare, "Trust-based cooperative cross-layer routing protocol for industrial wireless sensor networks," <https://www.ijcna.org/Manuscripts/IJCNA-2022-O-25.pdf>.
- [2] G. Manoharan and A. Sumathi, "Efficient routing and performance amelioration using Hybrid Diffusion Clustering Scheme in heterogeneous wireless sensor network," *International Journal of Communication Systems*, vol. 35, no. 15, Article ID e5281, 2022.
- [3] J. Logeshwaran, M. Ramkumar, T. Kiruthiga, and R. Sharanpravin, "The role of integrated structured cabling system (ISCS) for reliable bandwidth optimization in high-speed communication network," *ICTACT Journal on Communication Technology*, vol. 13, no. 01, pp. 2635–2639, 2022.
- [4] N. Islam, M. I. Hossain, and A. Rahman, "A comprehensive analysis of quality of service (QoS) in ZigBee network through mobile and fixed node," *Journal of Computer and Communications*, vol. 10, no. 03, pp. 86–99, 2022.
- [5] M. Alqahtania, M. J. Scottb, and M. Hub, "Dynamic energy scheduling and routing of a large fleet of electric vehicles using multi-agent reinforcement learning," *Computers & Industrial Engineering*, vol. 169, 2022.
- [6] I. Ioannou, C. Christophorou, V. Vassiliou, and A. Pitsillides, "A novel Distributed AI framework with ML for D2D communication in 5G/6G networks," *Computer Networks*, vol. 211, Article ID 108987, 2022.
- [7] Y. Wang, R. Xu, C. Zhou, X. Kang, and Z. Chen, "Digital twin and cloud-side-end collaboration for intelligent battery management system," *Journal of Manufacturing Systems*, vol. 62, pp. 124–134, 2022.
- [8] H. Pourrahmani, A. Yavarinasab, R. Zahedi, A. Gharehghani, M. H. Mohammadi, and P. Bastani, "The applications of Internet of Things in the automotive industry: a review of the batteries," *Internet of Things*, vol. 19, Article ID 100579, 2022.
- [9] M. Momeni, H. Soleimani, S. Shahparvari, and B. Afshar-Nadjafi, "Coordinated routing system for fire detection by patrolling trucks with drones," *International Journal of Disaster Risk Reduction*, vol. 73, Article ID 102859, 2022.
- [10] J. Logeshwaran and S. Karthick, "A smart design of a multi-dimensional antenna to enhance the maximum signal clutch to the allowable standards in 5G communication networks," *ICTACT Journal on Microelectronics*, vol. 8, no. 1, pp. 1269–1274, 2022, April.
- [11] G. Tsaramirsis, A. Kantaros, I. Al-Darraj et al., "A modern approach towards an industry 4.0 model: from driving technologies to management," *Journal of Sensors*, vol. 2022, Article ID 5023011, 18 pages, 2022.
- [12] P. Das, S. Ghosh, S. Chatterjee, and S. De, "A low cost outdoor air pollution monitoring device with power controlled built-in PM sensor," *IEEE Sensors Journal*, vol. 22, no. 13, pp. 13682–13695, 2022.
- [13] S. A. H. Mohsan, M. A. Khan, F. Noor, I. Ullah, and M. H. Alsharif, "Towards the unmanned aerial vehicles (UAVs): a comprehensive review," *Drones*, vol. 6, no. 6, p. 147, 2022.
- [14] A. Gupta, A. V. H. Vardhan, S. Tanwar, N. Kumar, and A. Singh, "Performance Analysis at different millimetre wave frequencies for indoor shopping complex and outdoor UAV applications towards 5G," *Microprocessors and Microsystems*, vol. 90, Article ID 104506, 2022.
- [15] L. M. Alkwai, A. N. Mohammed Aledaily, S. Almansour, S. D. Alotaibi, K. Yadav, and V. Lingamuthu, "Vampire attack mitigation and network performance improvement using probabilistic fuzzy chain set with authentication routing protocol and hybrid clustering-based optimization in wireless

- sensor network,” *Mathematical Problems in Engineering*, vol. 2022, Article ID 4948190, 11 pages, 2022.
- [16] M. Alqahtani, M. J. Scott, and M. Hu, “Dynamic energy scheduling and routing of a large fleet of electric vehicles using multi-agent reinforcement learning,” *Computers & Industrial Engineering*, vol. 169, Article ID 108180, 2022.
- [17] A. Gupta and S. K. Gupta, “A survey on green unmanned aerial vehicles-based fog computing: challenges and future perspective,” *Transactions on Emerging Telecommunications Technologies*, Article ID e4603.
- [18] M. Sutharasan and J. Logeshwaran, “Design intelligence data gathering and incident response model for data security using honey pot system,” *International Journal for Research & Development in Technology*, vol. 5, no. 5, pp. 310–314, 2016.
- [19] N. Chandnani and C. N. Khairnar, “An analysis of architecture, framework, security and challenging aspects for data aggregation and routing techniques in iot wsns,” *Theoretical Computer Science*, vol. 929, 2022.
- [20] M. Suriya and M. G. Sumithra, “Overview of spectrum sharing and dynamic spectrum allocation schemes in cognitive radio networks,” *8th International Conference on Advanced Computing and Communication Systems (ICACCS)*, vol. 1, pp. 934–937, 2022, March.
- [21] H. Anandakumar and R. Arulmurugan, “A graphic model, simulators and formal evaluation of protocols for wireless communication,” in *Proceedings of the 2019 Third International Conference on I-SMAC (IoT in Social, Mobile, Analytics and Cloud)(I-SMAC)*, Piscataway, NJ, USA, 2019.
- [22] N. Thiyagarajan and N. Shanmugasundaram, “An investigation on energy consumption in wireless sensor network,” *8th International Conference on Advanced Computing and Communication Systems (ICACCS)*, vol. 1, pp. 1359–1364, 2022.
- [23] S. Dalal, B. Seth, V. Jaglan et al., “An adaptive traffic routing approach toward load balancing and congestion control in Cloud-MANET ad hoc networks,” *Soft Computing*, vol. 26, no. 11, pp. 5377–5388, 2022.

Research Article

Environmental Fault Diagnosis of Solar Panels Using Solar Thermal Images in Multiple Convolutional Neural Networks

Tamilselvi Selvaraj,¹ Ramasubbu Rengaraj,¹ GiriRajanbabu Venkatakrishnan,¹ Soundharia Ganesan Soundararajan,¹ Karuppiah Natarajan,² Praveen Kumar Balachandran ,² Prince Winston David,³ and Shitharth Selvarajan ⁴

¹Department of Electrical and Electronics Engineering, Sri Sivasubramaniya Nadar College of Engineering, Chennai, Tamil Nadu 603110, India

²Department of Electrical and Electronics Engineering, Vardhaman College of Engineering, Hyderabad, Telangana 501218, India

³Department of Electrical and Electronics Engineering, Kamaraj College of Engineering and Technology, Virudhunagar, Tamil Nadu 626001, India

⁴Department of Computer Science and Engineering, KebriDehar University, Kabridahar, Somali 001, Ethiopia

Correspondence should be addressed to Shitharth Selvarajan; shitharths@kdu.edu.et

Received 1 August 2022; Revised 1 September 2022; Accepted 2 September 2022; Published 22 September 2022

Academic Editor: Albert Alexander Stonier

Copyright © 2022 Tamilselvi Selvaraj et al. This is an open access article distributed under the Creative Commons Attribution License, which permits unrestricted use, distribution, and reproduction in any medium, provided the original work is properly cited.

Every year, each solar panel suffers an efficiency loss of 0.5% to 1%. This degradation of solar panels arises due to environmental and electrical faults. A timely and accurate diagnosis of environmental faults reduces the damage caused by faults on the panel. In recent years, deep learning precisely convolutional neural networks have achieved wonderful results in many applications. This work is focused on finely tuning pretrained models of convolutional neural networks, especially AlexNet, GoogleNet, and SqueezeNet. Based on the performance metrics, SqueezeNet is used for training thermal images of solar panels and for the classification of environmental faults. The results obtained show that SqueezeNet has a significant testing accuracy of 99.74% and F1 score of 0.9818, which make the model successful in identifying environmental faults in solar panels and help users to protect the panels.

1. Introduction

Photovoltaic systems are one of the most distinguished and clean sources of energy which generate power by converting solar energy from the sun into direct current electricity. In 2019, solar power delivered was 2.7% of total worldwide electricity production. The International Energy Agency has stated by 2050, solar power would contribute up to 16% of the world's electric energy production with solar being the largest renewable source of energy. Electric power generated by a 1 KW system of solar panels is roughly around 850 KWh per year. However, each year the solar panels suffer an efficiency loss of 0.5% to 1% resulting in reduced output power generation. This power loss in solar panels arises due to environmental and electrical faults [1].

Environmental faults like shading, soiling, and snowing tend to cause a significant power loss in PV modules. Solar panels are expensive and require proper maintenance throughout the year. Hence, it is necessary that faults in the solar panels are detected and rectified in the preliminary stage [2].

The goal of this research is to detect environmental faults in the solar panels accurately. For this purpose, different convolutional neural networks (CNN), namely, AlexNet, GoogleNet, and SqueezeNet are trained and their performance metrics are obtained. Based on the results, a suitable network is opted for training thermal images of solar panels and for the precise determination of environmental faults in solar panels.

S.K. Firth conducted a survey and found that annually the different faults in photovoltaic systems reduce the power output by 19% [3]. To detect these faults, W. Chine proposed

a feasible solution for the fault classification of photovoltaic system using Artificial Neural Network (ANN) [4]. In this proposed method, a simulation model is introduced for computing a number of parameters like current, voltage, and the number of peaks in the current-voltage (I-V) characteristics of the PV cells. Two ANN architectures are employed for environmental and electrical faults detection in PV systems: the Multilayer Perceptron (MLP) and the Radial basis function (RBF). For the MLP based model, the true and false classification rates achieved are 90.3% and 9.7%, respectively, and for RBF-based model, they are 68.4% and 31.6%, respectively.

C. Mantel developed a machine learning model where electroluminescence images of photovoltaic panels were fed to the model [5]. Two architectures, Support Vector Machine (SVM) and Random Forest Model (RF), were employed. The results obtained from SVM had an accuracy of 0.997 and a recall of 0.274. The RF model had an accuracy of 0.967 and a recall of 0.193. The results demonstrated that SVM had an improvement of about 3% in terms of accuracy compared to the RF model. However, the high accuracy of both the classifiers (SVM and RF) makes them promising for detecting faults in PV modules from electroluminescence images.

Furthermore, Natarajan studied the above model by using thermal images of photovoltaic systems [6]. Based on the fundamentals of thermal image processing, an algorithm is suggested for deriving the characteristics of the solar cells in operation. The images are classified by a classifier tool called SVM, which determines whether the solar modules are faulty or nonfaulty. The results obtained are 97% accurate with the comparison of test and training results. This fault classification technique is used in real time for the large PV system with very less computation time.

Papadomanolaki on his research based on benchmarking different deep learning networks for classification of precise and sharp satellite multispectral data has trained CNN from scratch using huge datasets comprising large number of labeled data samples [7]. Therefore, employing a pretrained deep learning model has been proposed and successfully achieved in this paper.

In addition, C. Szegedy has carried out a detailed study of different CNN architectures, namely, AlexNet, VGG Net, and GoogleNet in the computer vision community, and their versions are made available publicly [8].

Diverse range of works in machine learning community have successfully manifested the generalization power of deep learning networks where large datasets have performed well in regards with classification of other datasets, even from different distinct. Motivated by these results, we apply pretrained models of AlexNet, GoogleNet, and SqueezeNet on a large-scale image classification dataset for fault classification in PV arrays [9–11].

The following paper comprises various sections elaborating in detail about environmental fault diagnosis of solar panels using CNN. Section 2 describes about the various environmental faults in solar panels while the Section 3 discusses about the identification of these faults. In Section 4, the mechanism of deep learning and different neural

networks are elaborated followed by the explanation of confusion matrix algorithm in Section 5. Section 6 displays the corresponding experimental results for environmental fault diagnosis of solar panels using various CNN architectures.

2. Environmental Faults in Solar Panels

Solar panels are operated in the open air, making them vulnerable to environmental conditions [12]. Under these conditions, the PV module may fail to operate efficiently due to the following effects:

- (i) Shading effect: shading can arise from direct shadows or temporary shadows. Direct shadows cause serious impact on the performance of the solar panel. Temporary shadows are caused due to shades of buildings, trees, snow, etc. Shading effect is classified into two types such as partial shading and fully shading. Partial shading leads to reduced current and voltage and the output power is dropped to half the nominal value while full shading leads to no output power extraction as shading of at least 1/36 of the cell reduces the output power by 75% [13].
- (ii) Soiling effect: the aggregation of dust particles like sand, cement, mud, and leaves etc., on solar panel's surface is called soiling. The various factors causing soiling and power loss are climatic conditions, tilt angle, and liquid used for cleaning solar panels [14].
- (iii) Snowing effect: when a thick layer of snow is deposited on a solar panel, solar cells find it difficult to absorb solar radiation, and this affects the output power very badly. This affects more worse when the snow remains on the panel for a longer period of time [15].
- (iv) Temperature rise: solar panels are temperature-sensitive. A temperature rise above the optimum temperature 35°C degrades the output power of the solar panel and causes excess heat emission, highly affecting the open circuit voltage of the solar panel.

3. Identification of Environmental Faults

The following section describes about the various stages involved in the identification of environmental faults in solar panels such as capturing and processing the thermal images of the solar panels, detecting hotspots in the images, and identifying those faults.

3.1. Thermography. Environmental faults like the temperature rise in solar panels and shading effects cannot be perceived by human eyes. In such cases, the solar panel fault can be detected by the principle of thermography. Each object having a temperature above the absolute zero point (0 Kelvin) emanates infrared radiation, which is directly proportional to its intrinsic temperature [16,17]. A thermal imager when placed at a distance of 1 m from the solar panel,

the imager perceives the infrared radiation from the solar panel and determines the surface temperature of the panel. The imager converts the infrared radiation into electrical signals and displays these signals with varying temperature in different colors [18,19].

3.2. Thermal Image Processing. Thermal image processing helps to enhance the characteristics of the image data. The image processing method used in this research captures the accurate hotspot area of the panel, and the contrast level of the image is adjusted for better training of faults in neural networks. In Figure 1, the actual thermal image of the panel is displayed, whereas in Figure 2, the contrast level of the panel is adjusted high using thermal image processing software.

3.3. Hotspot Phenomenon. Hotspots are high temperature zones affecting a particular section of a solar panel, thereby reducing the localized efficiency and lowering the output power of the solar panel [20]. The hotspot phenomenon primarily occurs due to shading and dust accumulation on the panel. These preliminary damages in the solar panel can be detected using thermal images. In Figure 3, the black box shows the hotspot of the panel indicating the abnormal working condition of the solar panel. The remaining blue portion and faded yellow-green portion indicates the normal functioning of the solar panel.

3.4. Fault Detection and Identification. Fault detection checks for any abnormal working condition in the solar panel. In this research, the faults are determined based on the location of the hotspot in the thermal image [21].

4. Convolutional Neural Network

Deep learning is a crucial fragment of machine learning where multiple layers of nodes perform complex operations like abstraction and representation, which perceive images, sound, and text. Figure 4 represents the functioning of deep learning network in a flowchart.

Convolutional neural networks (CNNs) are a subset of deep neural networks which are designed to operate on visual imagery [22, 23]. The properties and features of the input images are extracted and are encoded by the CNN architecture resulting in the reduction of parameters in large quantities compared to normal neural networks.

4.1. Types OF CNN.

- (i) AlexNet: Alex Krizhevsky designed AlexNet (AN) in 2012. This network consists of eight layers where the first five layers are convolutional layers succeeded by max-pooling layers and the last three layers are fully connected layers. For better training performance, AN prefers ReLu activation function over sigmoid and tanh [24].
- (ii) GoogleNet: Google developed the GoogleNet (GN) architecture. This network consists of nine inception modules where in the twenty-two layers, four

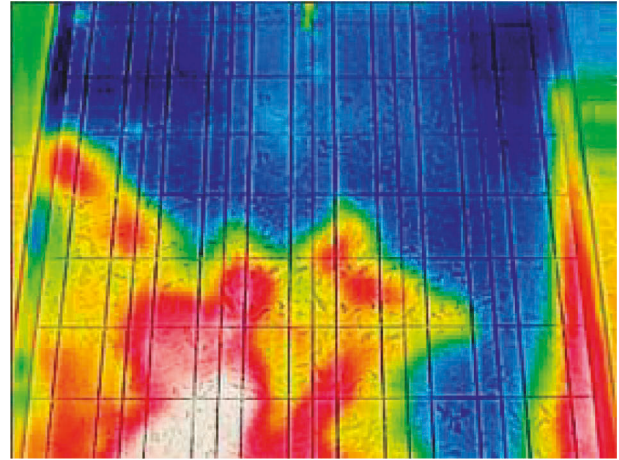


FIGURE 1: Thermal image of a solar panel with fault.

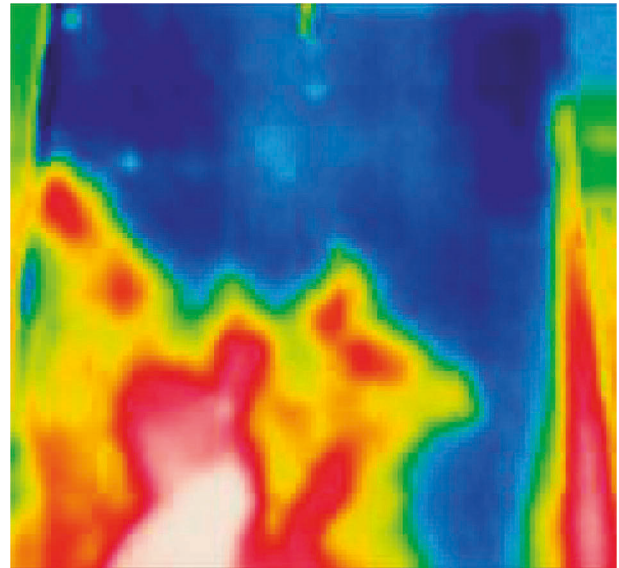


FIGURE 2: Thermal image of the faulty solar panel with the contrast level adjusted high.

are convolutional layers and max-pooling layers, three layers are for average pooling followed by a section of five fully connected layers and three softmax layers [25].

- (iii) SqueezeNet: SqueezeNet (SN) was developed by DeepScale in 2016 and has accuracy with 50x less parameter. This network contains eighteen layers which begins with a single convolution layer followed by eight fire modules and ends with a convolutional layer. Different activation functions like ReLu, tanh, and sigmoid can be used where ReLu provides a good boost in the performance [26].

5. Parameters for Determination of the Suitable Network

Confusion matrix is a predictive analysis method used for describing the performance of the classification model in deep learning [27]. The rows in the confusion matrix depict

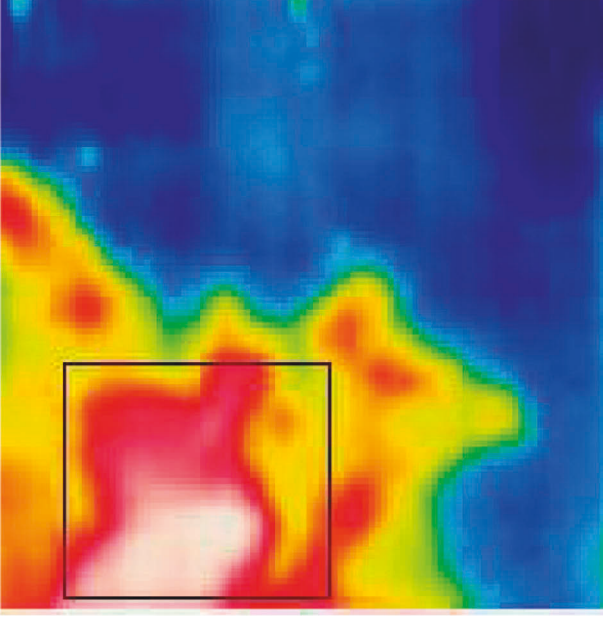


FIGURE 3: Hotspot location in the solar panel.

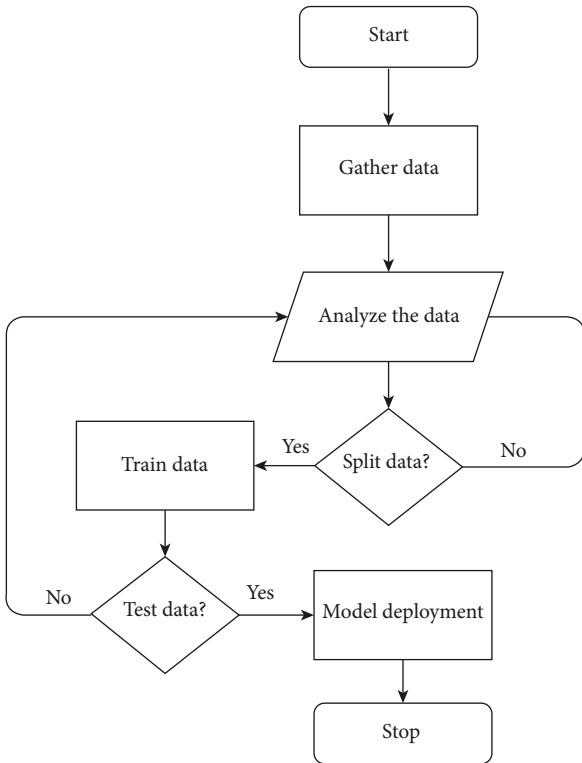


FIGURE 4: Flowchart representation of deep learning algorithm.

the true class, whereas the columns depict the predicted class. The confusion matrix reports true positive, false positive, true negative, and false negative. Furthermore, it helps to calculate statistical measures like accuracy, specificity, sensitivity, precision, and F1 score.

True positive (TP): the output class matches with the true class. **True negative (TN):** the output class is not predicted for other classes except the true class. **False positive (FP):** the output class is predicted as the true class when it is not. **False**

negative (FN): the output class is not predicted as the true class when it is. Figure 5 shows the true positive, false positive, true negative, and false negative of a confusion matrix.

5.1. Statistical Measures. **Accuracy:** accuracy is the ability to detect the target class and the output class correctly, that is, to numerate the fraction of true positive and true negative in all the evaluated classes.

$$\text{Accuracy} = \frac{(TP + TN)}{(TP + TN + FP + FN)} \quad (1)$$

Specificity: specificity refers to the ability to determine the target class correctly by the predicted class, that is, to calculate the proportion of true positive.

$$\text{Specificity} = \frac{TN}{(TN + FP)} \quad (2)$$

Sensitivity: sensitivity refers to the ability to determine the proportion of true negative, that is, the fraction of true positive classes in all the positive assessments.

$$\text{Sensitivity} = \frac{TP}{(TP + FN)} \quad (3)$$

Precision: precision is defined as the fraction of positive predictions in all the predicted positive classes.

$$\text{Precision} = \frac{TP}{(TP + FP)} \quad (4)$$

F1 score: F1 score is the harmonic mean of precision and sensitivity and is a better measure than accuracy. A high value of F1 score determines that the neural network has better performance on positive classes.

$$F1\text{score} = 2 * \left[\frac{(\text{Precision} \times \text{Sensitivity})}{(\text{Precision} + \text{Sensitivity})} \right] \quad (5)$$

Compared to accuracy performance metrics, statistical measures like precision, sensitivity, specificity, and F1 score provide better insights into the prediction accuracy of neural networks.

6. Experimental Results

The following sections discuss in detail about data collection and clustering of environmental faults in solar panels and provide a comparative analysis of the trained and tested fault images in various neural networks. Figure 6 represents the various steps involved in the collection of fault images from solar panels.

6.1. Data Collection and Clustering. A total of 1197 real images of solar panels for different fault conditions were captured. For training of various neural networks, the images were further divided in the percent ratio of 70 and 30 for training and testing of solar panel images. Table 1 shows the number of images for each training class of real images. The total numbers of images for testing and training are 313 and 884, respectively.

		True Class	
		Positive	Negative
Predicted Class	Positive	TP	FP
	Negative	FN	TN

FIGURE 5: Confusion matrix.

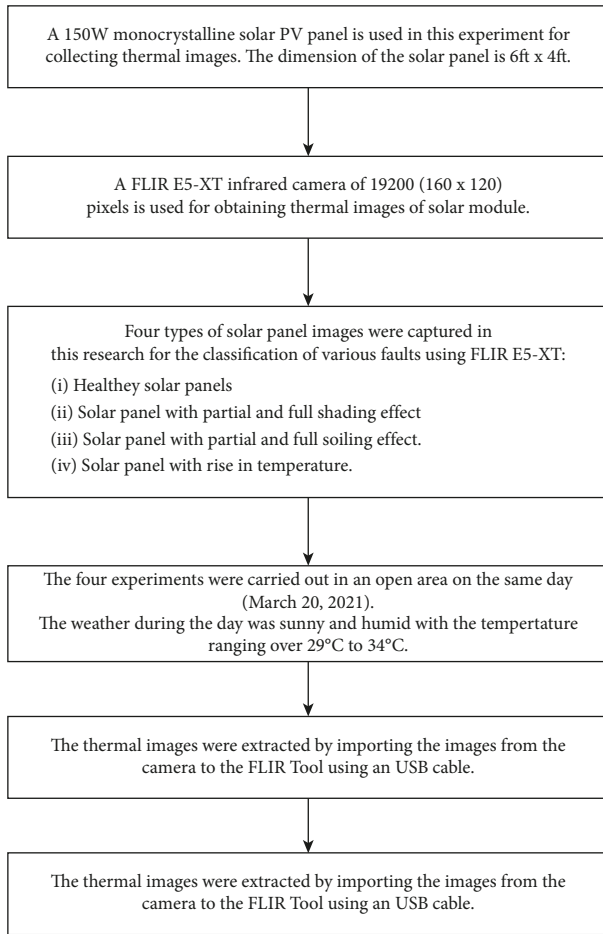


FIGURE 6: Methodology for data collection and clustering.

Similarly, a total of 872 thermal images for various faults were captured from the infrared camera and divided in the percent ratio of 70 and 30 for training and testing, respectively. This clustering of images helps in proper and efficient training of neural networks. Table 2 shows the number of images for each training class of thermal images. The total numbers of images for testing and training are 272 and 610, respectively.

6.2. Neural Network Analysis. Real images collected are trained in Deep Network Designer application in MATLAB software for various pretrained networks: SN, AN, and GN.

TABLE 1: Number of real images used in each training class.

S. no.	Training class	Image count
1	Normal panel	156
2	Partially cement covered	157
3	Fully cement covered	120
4	Partially snow covered	144
5	Fully snow covered	163
6	Mud covered	144

TABLE 2: Number of thermal images used in each training class.

S. no.	Training class	Image count
1	Normal panel	100
2	Partially shaded	100
3	Fully shaded	108
4	Partially soil covered	102
5	Completely soil covered	100
6	Temperature rise	100

For the proper fitting of the trained model, training options are set as shown in Table 3.

The execution environment employed for training is CPU. Table 4 shows the intermediate results obtained from the training of real images in SN, AN, and GN. Figures 7–9 show the training progress of the various pretrained networks where the blue and red lines specify the training accuracy and loss while the black dotted line specifies the validation accuracy and loss of the trained model.

From the following figures, it can be seen that the dataset is finely trained by AN as it attains a training accuracy of 99.8% and 100% at epochs 2 and 3 at a faster rate of 14 min 47 s while SN takes a time of 21 min 15 s to train and attains a training accuracy of only 91.9% and 100% at corresponding epochs 2 and 3. Compared to the other two neural networks, GN takes a longer time of 23 min 31 s to reach a training accuracy of 92.48% and 99.15% at epochs 2 and 3, respectively. Hence, AN is more suitable for training solar panels for the fault classification of solar panels due to better training accuracy and shorter training time followed by SN next.

A set of 100 images are selected from the testing images. The confusion matrix for these samples is plotted, and corresponding statistical measures such as accuracy, sensitivity, specificity, precision, and F1 score are calculated for SN, AN, and GN are given in the following. Figures 10–12 are the confusion matrices of SN, AN, and GN while Figures 13–15 are the statistical measures of SN, AN, and GN.

Figures 16–18 show the solar panel faults classified by various neural networks along with their testing accuracy for twenty testing images.

Table 5 shows the average of testing accuracy, specificity, sensitivity, precision and F1 score. For the selection of an appropriate neural network for fault to provide better acuity in prediction accuracy, it is necessary for the various statistical parameters such as testing accuracy, specificity, sensitivity and precision to complement each other and provide a good F1 score. From the three neural networks

TABLE 3: training options employed for the pretrained networks.

S. no.	Training option	Value
1	Solver	*SGDM
2	Maximum epochs	3
3	Mini batch size	8
4	Max number of iterations	231
5	Base learning rate	0.0001

*Stochastic gradient descent with momentum.

TABLE 4: intermediate results for SqueezeNet, AlexNet, and GoogleNet.

Type of network	Epoch	Iteration	Time elapsed (hh:mm:ss)	Validation accuracy	Training accuracy	Validation loss	Training loss
SqueezeNet	1	1	00:00:26	17.3585	18.95	3.3108	3.2987
	2	75	00:07:07	92.376	91.9345	0.1751	0.06371
	3	155	00:14:10	100	100	0.0436	0.00668
	3 (end)	231	00:20:44	100	100	0.0267	0.01164
AlexNet	1	1	00:00:18	13.5849	12.5	3.7124	4.5314
	2	75	00:04:11	94.5783	99.875	0.00021	4.575e-05
	3	155	00:09:35	100	100	6.9009e-05	2.644e-05
	3 (end)	231	00:14:16	100	100	9.0214e-05	0.0008
GoogleNet	1	1	00:00:28	18.4905	19.3834	2.63963	3.1751
	2	75	00:08:07	96.9811	92.4764	0.13759	0.0445
	3	155	00:14:50	100	99.1528	0.02365	0.005
	3 (end)	231	00:23:00	100	100	0.0124	0.0026

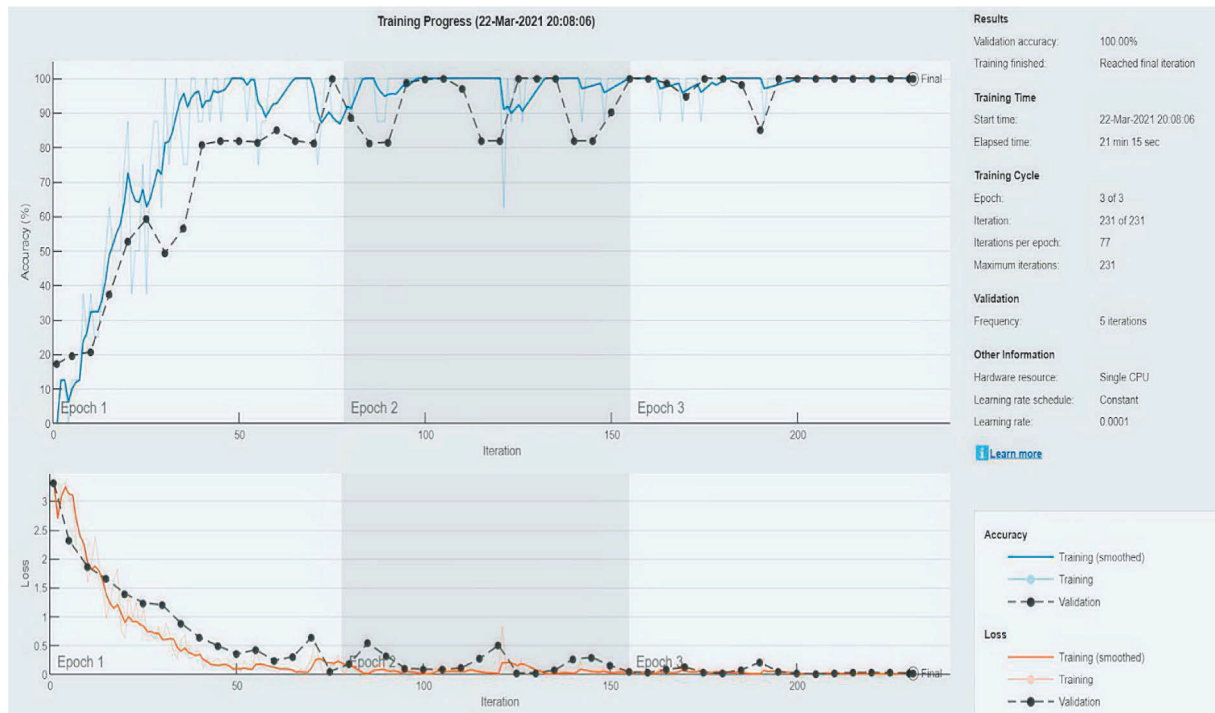


FIGURE 7: Training progress of finely tuned SqueezeNet.

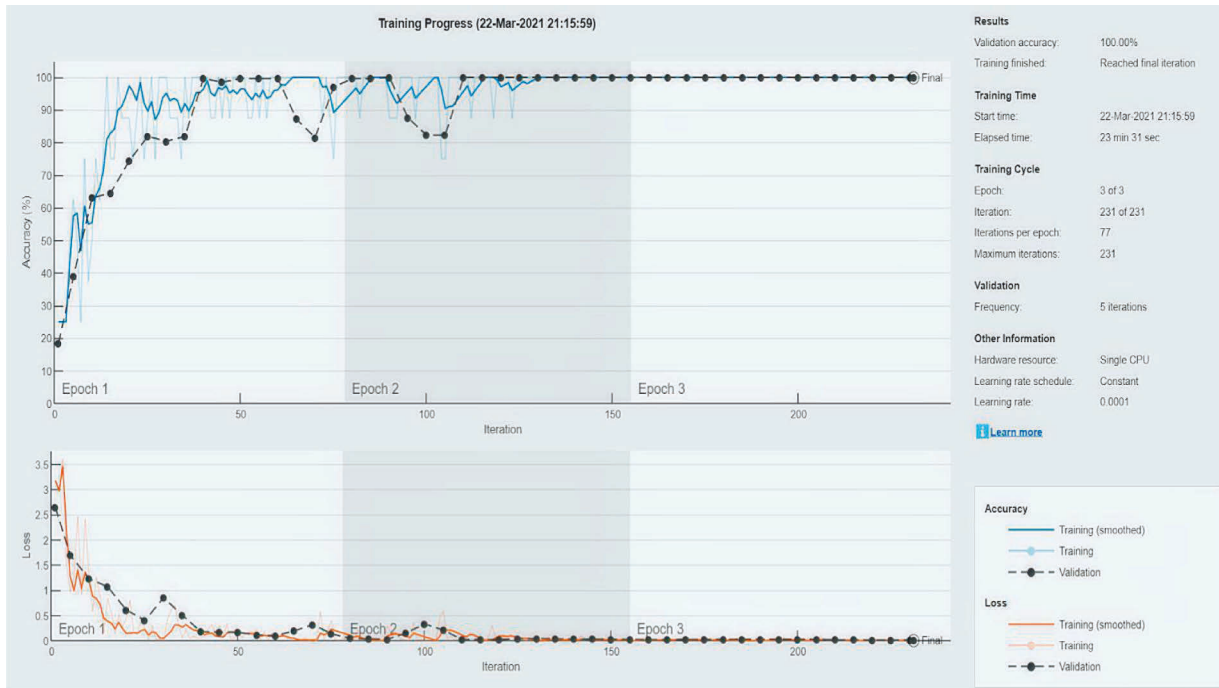


FIGURE 8: Training progress of finely tuned AlexNet.

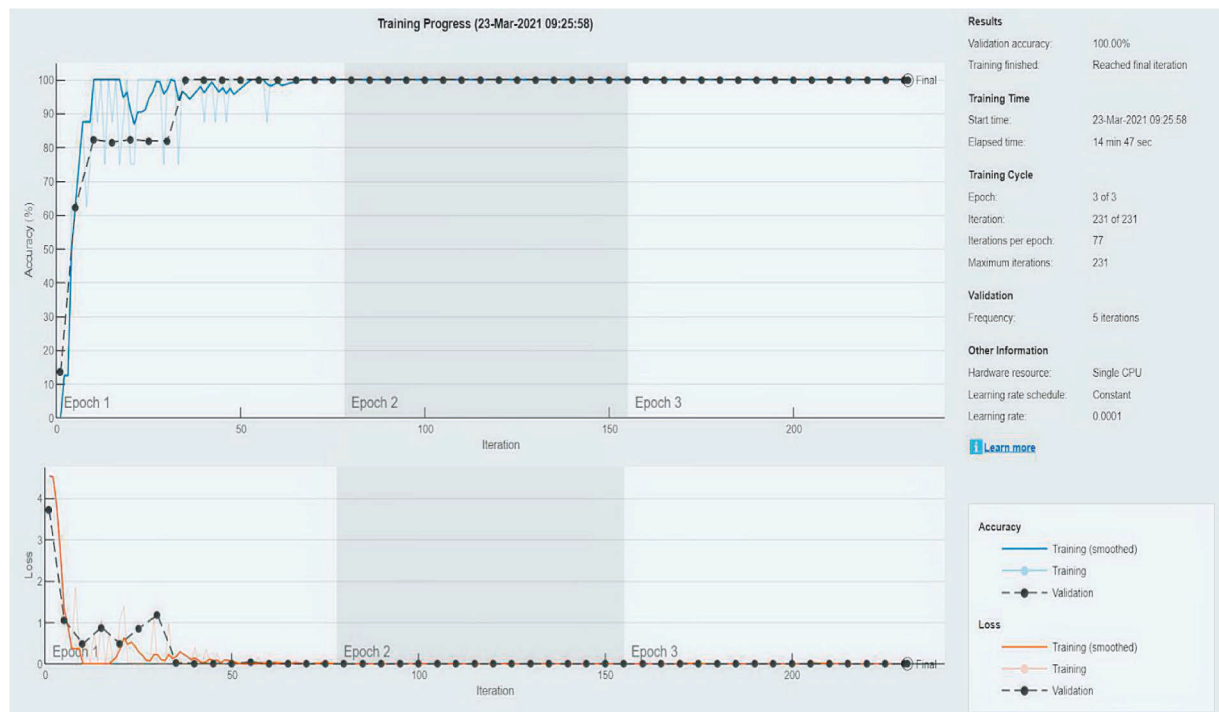


FIGURE 9: Training progress of finely tuned GoogleNet.

tested, SN provides a remarkable testing accuracy of 99.815% and a F1 score of 0.992. On the other hand, AN despite having better training accuracy, the testing accuracy of the network is 94.975 and F1 score is 0.9559 which is comparatively low compared to the other two networks as GN

itself provides a testing accuracy of 92.285% and F1 score of 0.9832. Similarly, the order of specificity, sensitivity and precision results were obtained higher for SN as the corresponding values were 0.9978, 0.9907 and 0.9936 and the lowest values were obtained for AN as the values were

Confusion Matrix

Output Class	Fully Cement covered	7 7.0%	0 0.0%	0 0.0%	0 0.0%	0 0.0%	0 0.0%	100% 0.0%
	Fully Snow covered	0 0.0%	25 25.0%	0 0.0%	0 0.0%	0 0.0%	0 0.0%	100% 0.0%
	Mud Covered	0 0.0%	0 0.0%	18 18.0%	0 0.0%	0 0.0%	0 0.0%	100% 0.0%
	Normal Panel	0 0.0%	0 0.0%	0 0.0%	23 23.0%	0 0.0%	0 0.0%	100% 0.0%
	Partially Cement Covered	0 0.0%	0 0.0%	0 0.0%	0 0.0%	9 9.0%	0 0.0%	100% 0.0%
	Partially Snow Covered	0 0.0%	1 1.0%	0 0.0%	0 0.0%	0 0.0%	17 17.0%	94.4% 5.6%
		100% 0.0%	96.2% 3.8%	100% 0.0%	100% 0.0%	100% 0.0%	100% 0.0%	99.0% 1.0%
	Fully Cement covered	Fully Snow covered	Mud Covered	Normal Panel	Partially Cement Covered	Partially Snow Covered		
	Target Class							

FIGURE 10: Confusion matrix for SqueezeNet.

Confusion Matrix

Output Class	Fully Cement covered	6 6.1%	0 0.0%	0 0.0%	0 0.0%	0 0.0%	0 0.0%	100% 0.0%
	Fully Snow covered	0 0.0%	24 24.2%	0 0.0%	0 0.0%	0 0.0%	0 0.0%	100% 0.0%
	Mud Covered	0 0.0%	0 0.0%	18 18.2%	0 0.0%	0 0.0%	0 0.0%	100% 0.0%
	Normal Panel	0 0.0%	0 0.0%	0 0.0%	20 20.2%	0 0.0%	0 0.0%	100% 0.0%
	Partially Cement Covered	1 1.0%	0 0.0%	0 0.0%	0 0.0%	9 9.1%	0 0.0%	90.0% 10.0%
	Partially Snow Covered	0 0.0%	2 2.0%	0 0.0%	2 2.0%	0 0.0%	17 17.2%	81.0% 19.0%
		85.7% 14.3%	92.3% 7.7%	100% 0.0%	90.9% 9.1%	100% 0.0%	100% 0.0%	94.9% 5.1%
	Fully Cement covered	Fully Snow covered	Mud Covered	Normal Panel	Partially Cement Covered	Partially Snow Covered		
	Target Class							

FIGURE 11: Confusion matrix for AlexNet.

0.9897, 0.9515 and 0.9664. For GN, specificity, sensitivity and precision results were 0.9977, 0.975 and 0.9936. It can be seen that the specificity and precision of SN and GN are nearly equal. However, the F1 score and sensitivity of SN has an edge over GN.

Table 6 represents the comparative results of different neural networks based on the number of layers, the number

of images which can be processed, and their image size. Furthermore, SN requires a low memory size of 4.6 MB with 18 layers that can process a total of 1.24 million images. GN with a memory size of 27 MB can process up to 7 million images in 22 layers. AN can process up to 61 million images, and it requires a memory size of 227 MB and has only 8 layers.

Confusion Matrix

Output Class	Fully Cement covered	7 7.1%	0 0.0%	0 0.0%	0 0.0%	0 0.0%	0 0.0%	100% 0.0%
	Fully Snow covered	0 0.0%	25 25.3%	0 0.0%	0 0.0%	0 0.0%	0 0.0%	100% 0.0%
	Mud Covered	0 0.0%	0 0.0%	18 18.2%	0 0.0%	0 0.0%	0 0.0%	100% 0.0%
	Normal Panel	0 0.0%	0 0.0%	0 0.0%	20 20.2%	0 0.0%	0 0.0%	100% 0.0%
	Partially Cement Covered	0 0.0%	0 0.0%	0 0.0%	0 0.0%	9 9.1%	0 0.0%	100% 0.0%
	Partially Snow Covered	0 0.0%	1 1.0%	0 0.0%	2 2.0%	0 0.0%	17 17.2%	85.0% 15.0%
		100% 0.0%	96.2% 3.8%	100% 0.0%	90.9% 9.1%	100% 0.0%	100% 0.0%	97.0% 3.0%
	Fully Cement covered	Fully Snow covered	Mud Covered	Normal Panel	Partially Cement Covered	Partially Snow Covered		
	Target Class							

FIGURE 12: Confusion matrix for GoogleNet.

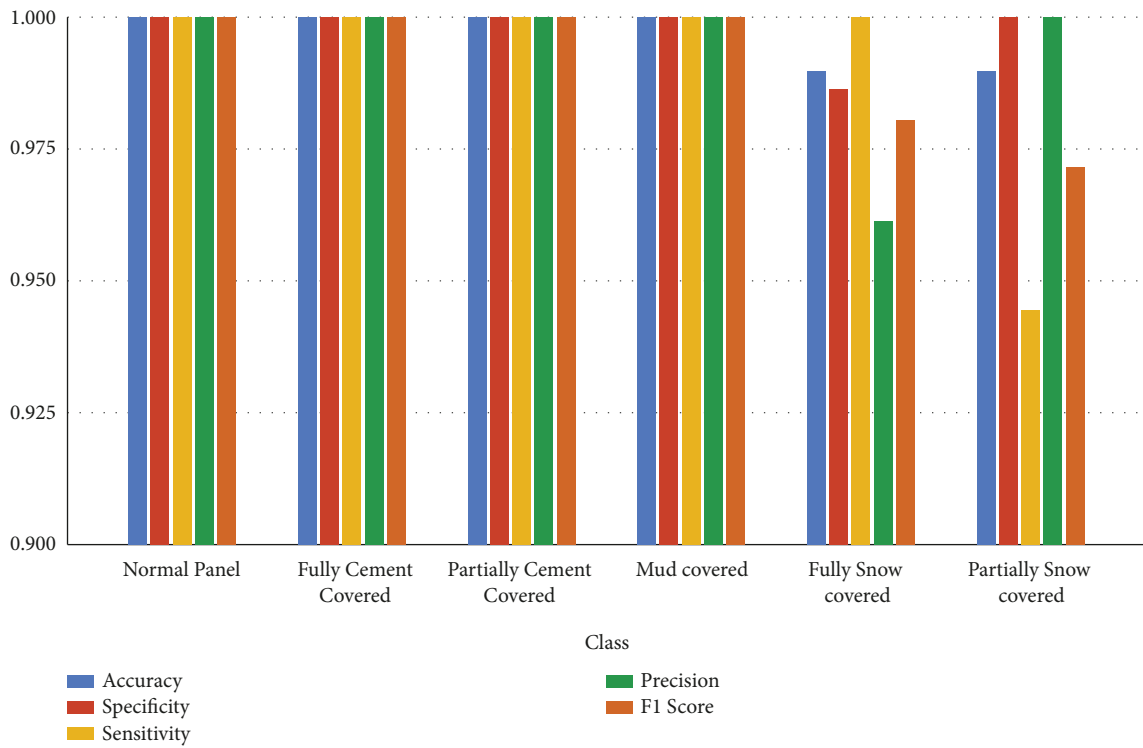


FIGURE 13: Statistical measures for SqueezeNet.

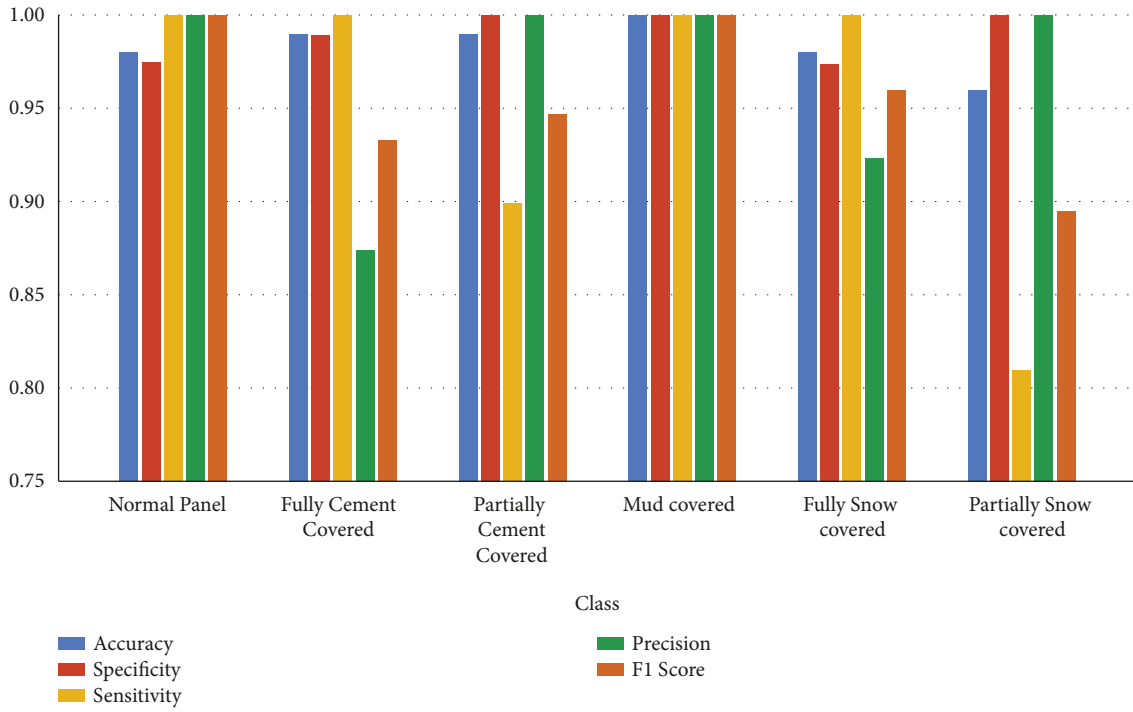


FIGURE 14: Statistical measures for AlexNet.

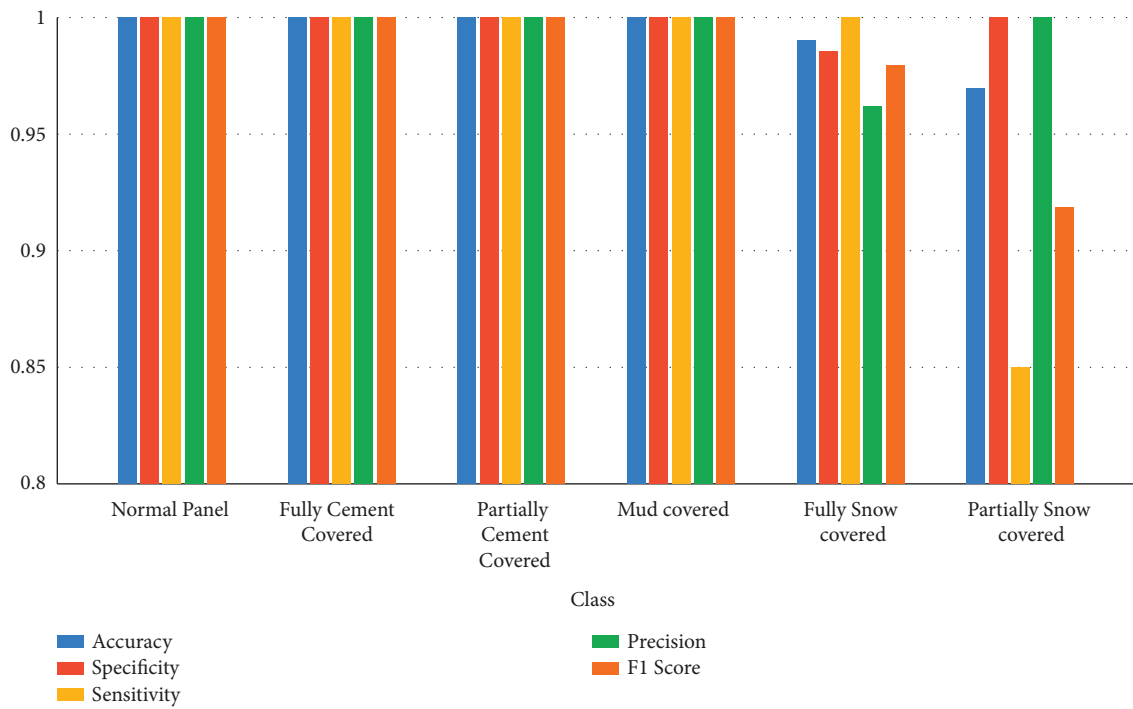


FIGURE 15: Statistical measure for GoogleNet.

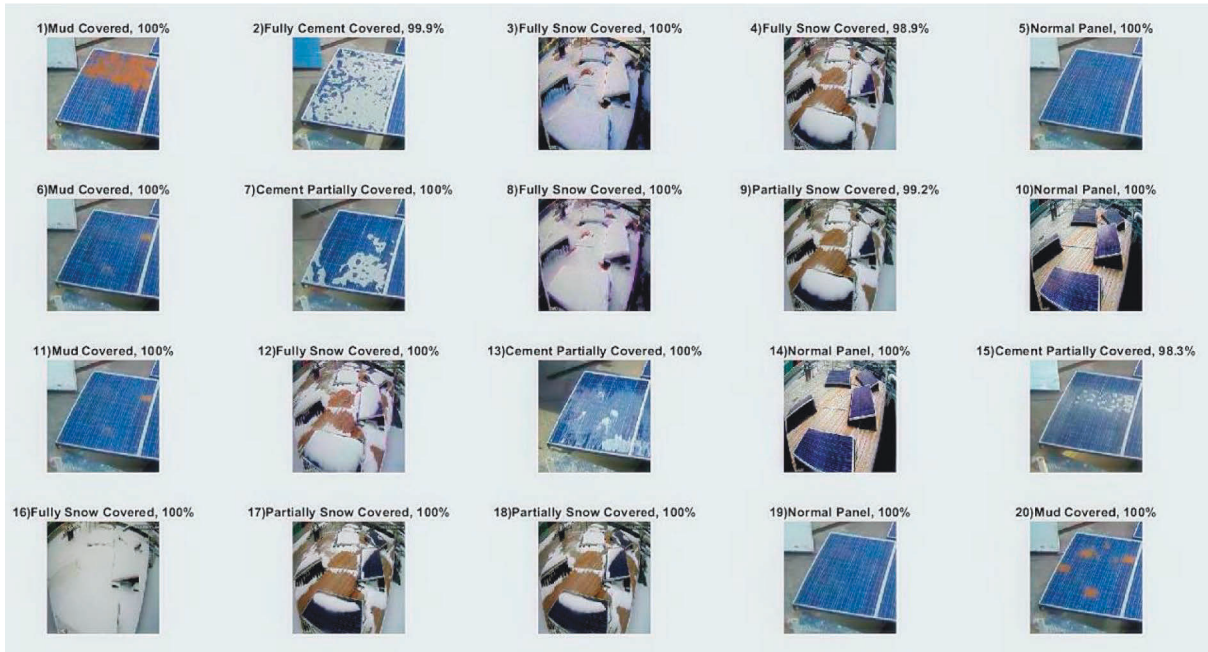


FIGURE 16: Fault classified by SqueezeNet with testing accuracy.

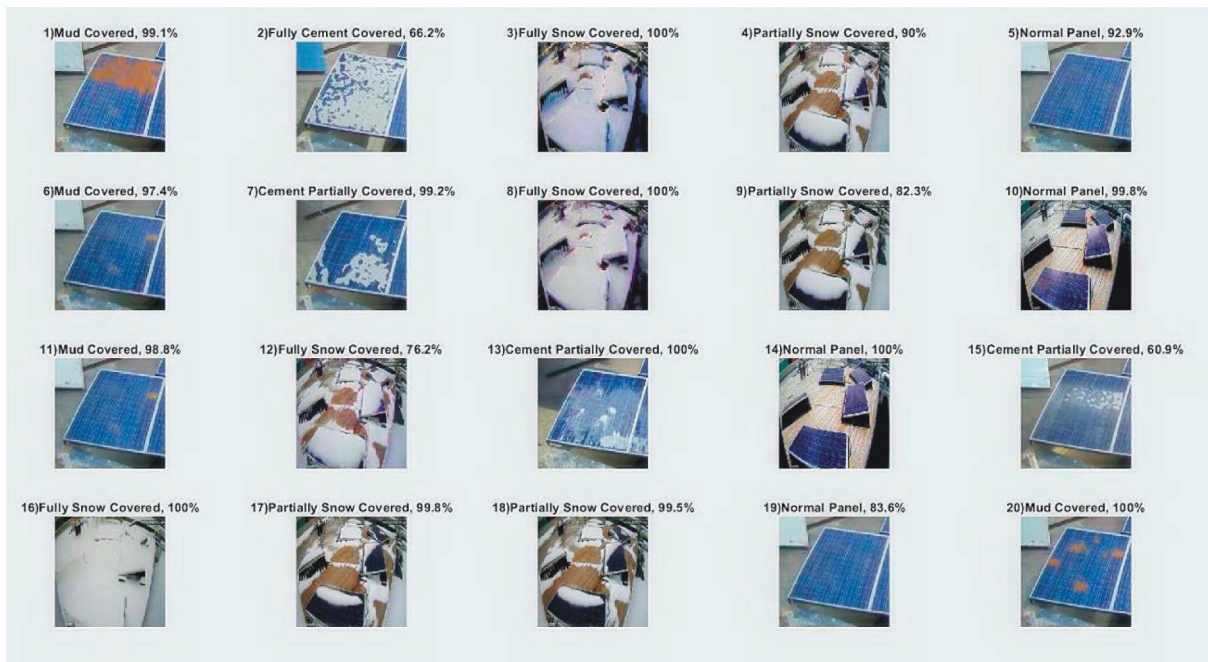


FIGURE 17: Fault classified by AlexNet with testing accuracy.

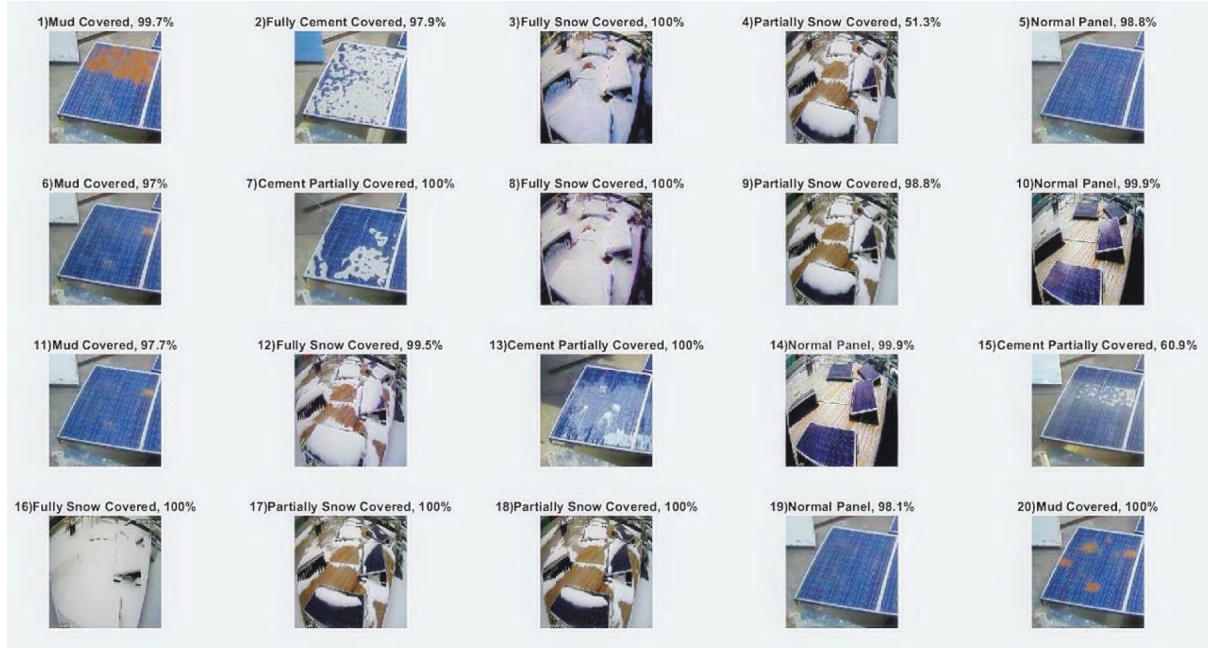


FIGURE 18: Fault classified by GoogleNet with testing accuracy.

TABLE 5: Comparative measures of SN, GN, and AN.

Network type	Testing accuracy of image	Accuracy of prediction	Specificity	Sensitivity	Precision	F1 score
SN	99.82	0.997	0.998	0.991	0.994	0.992
AN	92.29	0.983	0.990	0.952	0.966	0.956
GN	94.98	0.993	0.998	0.98	0.994	0.983

TABLE 6: Parameters of various neural networks.

Network Type	Memory size (MB)	Image Size	Image capacity (Million)	Layers count
SN	4.6	227 × 227	1.24	18
AN	227	227 × 227	61	8
GN	27	224 × 224	7	22

Based on factors such as testing and training accuracy, statistical measures, training time, and memory requirement, it can be seen that SN is efficient for the fault classification of solar PV panels with precision. Hence, a set of thermal images were trained in SN. Figure 19 shows the training progress of thermal images of solar panels with faults. Table 7 indicates that the time required for training and validating 610 images is 11 min 53 s where the training accuracy attains a training accuracy of 99.861 and 100 at the end of epochs 2 and 3, respectively. Figures 20 and 21 present the classification of PV faults in SN for real and thermal images.

The confusion matrices obtained for a sample of hundred real and thermal images are shown in Figures 22 and 23. From the confusion matrices, it can be seen that for real images, the desired class matches with the output class giving 100% accuracy while the confusion matrix for thermal images gives an accuracy of 98%. Table 8 presents the statistical measures of thermal images trained in SN

where the neural network trained has an F1 score of 0.9818.

Table 9 depicts that the testing accuracy of thermal images is 99.74% as the testing accuracy of each image tested is above 0.95 while for real images the testing accuracy is comparatively low, that is, 94.42%. However, the prediction accuracy of real images by the pretrained SN is far better as the accuracy is 100% while for thermal images the accuracy is 98%. The decrease in the prediction accuracy of thermal images is due to the hotspots in the panels, which may arise due to the temperature rise in addition to the actual fault in the panel.

7. Limitations and Scope for Future Work

For efficient training of neural networks, a large number of thermal images of solar panels are required. This also increases the training time which may extend from 1 hour to 2.5 hours and requires a better execution environment, most

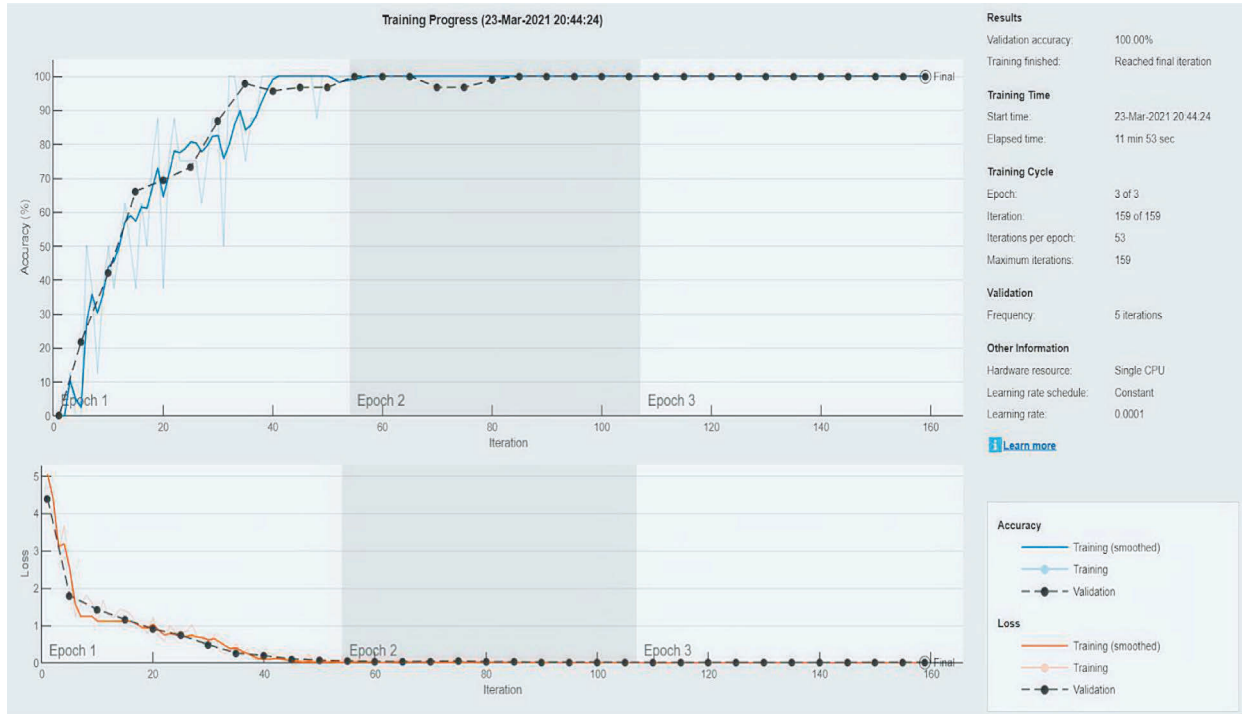


FIGURE 19: Training progress of SqueezeNet for fault classification of thermal images of solar panels.

TABLE 7: Intermediate results of thermal images trained in SN.

Epoch	Iteration	Time elapsed (hh:mm:ss)	Validation accuracy	Training accuracy	Validation loss	Training loss
1	1	00:00:10	0	0	4.5739	5.0128
2	54	00:04:56	99.861	97.698	0.0675	0.1597
3	105	00:08:29	100	100	0.00236	0.0011
3	159	00:11:18	100	100	0.00054	0.00085

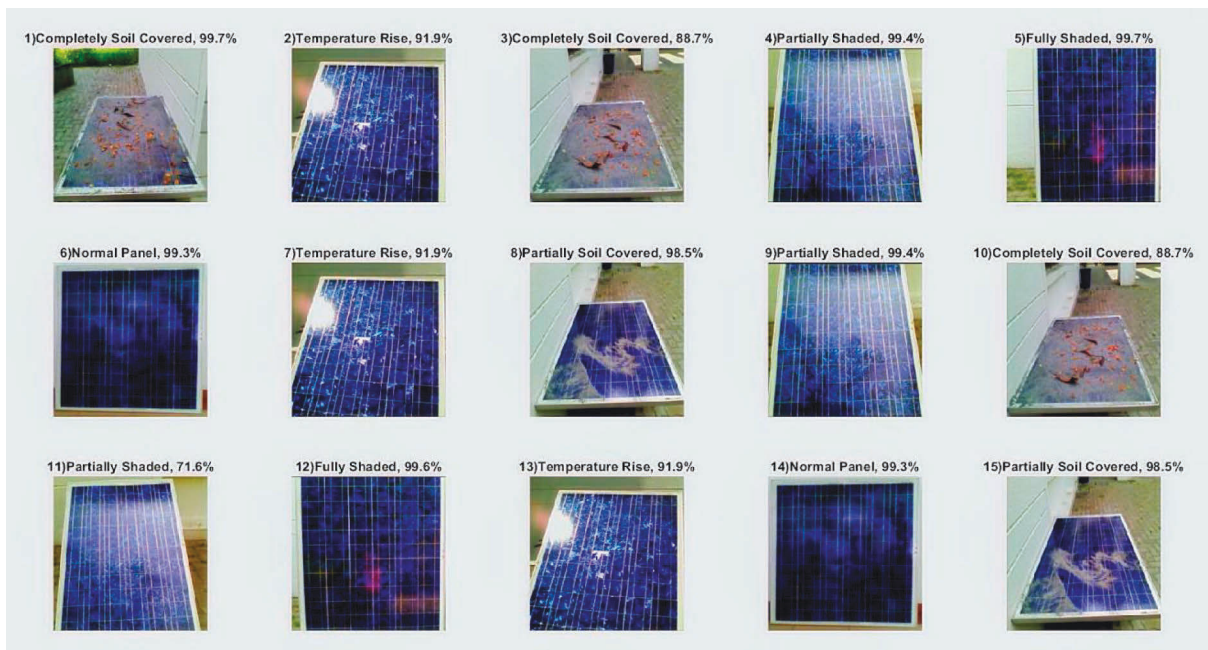


FIGURE 20: Fault classified by SqueezeNet for real images of solar panels.

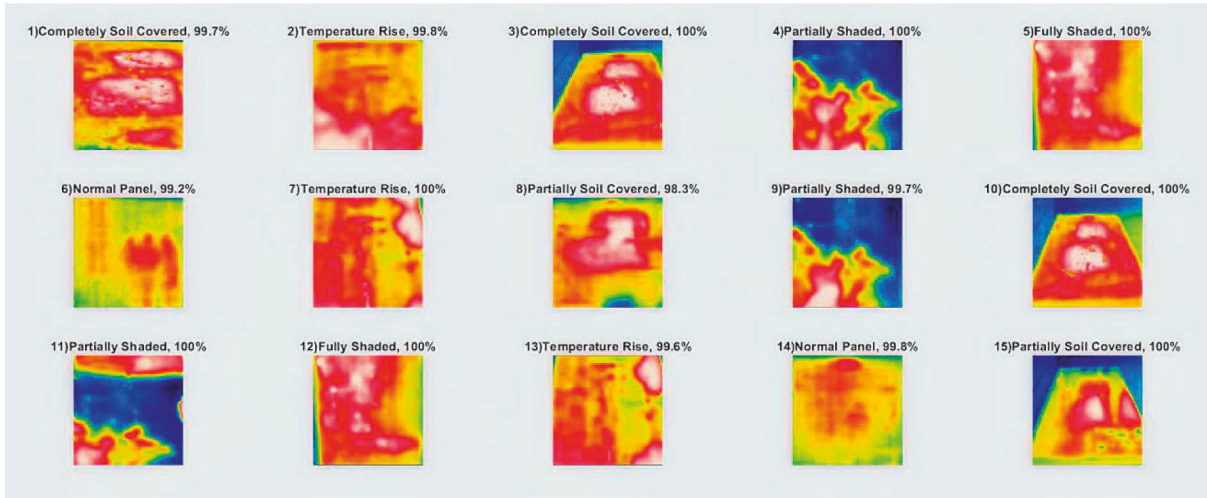


FIGURE 21: Fault classified by SN for thermal images of solar panels.

Confusion Matrix

Output Class	Completely Soil Covered	16 16.0%	0 0.0%	0 0.0%	0 0.0%	0 0.0%	0 0.0%	100% 0.0%
	Fully Shaded	0 0.0%	10 10.0%	0 0.0%	0 0.0%	0 0.0%	0 0.0%	100% 0.0%
	Normal Panel	0 0.0%	0 0.0%	32 32.0%	0 0.0%	0 0.0%	0 0.0%	100% 0.0%
	Partially Shaded	0 0.0%	0 0.0%	0 0.0%	12 12.0%	0 0.0%	0 0.0%	100% 0.0%
	Partially Soil Covered	0 0.0%	0 0.0%	0 0.0%	0 0.0%	18 18.0%	0 0.0%	100% 0.0%
	Temperature Rise	0 0.0%	0 0.0%	0 0.0%	0 0.0%	0 0.0%	12 12.0%	100% 0.0%
		100% 0.0%	100% 0.0%	100% 0.0%	100% 0.0%	100% 0.0%	100% 0.0%	100% 0.0%
	Completely Soil Covered	Fully Shaded	Normal Panel	Partially Shaded	Partially Soil Covered	Temperature Rise		

FIGURE 22: Confusion matrix for real images with fault in solar panels.

preferably Graphical Processing Unit instead of CPU. In the future, the average testing accuracy of SN for thermal images can be increased by altering the number of layers in the neural network. Also, a mobile application can be created

that executes the SN model for automatic classification of faults in solar panels, so users with scarce or no knowledge can employ the application to detect faults in solar panels effectively.

Confusion Matrix

Output Class	Completely Soil Covered	16 16.0%	0 0.0%	0 0.0%	0 0.0%	0 0.0%	0 0.0%	100% 0.0%
	Fully Shaded	0 0.0%	10 10.0%	0 0.0%	0 0.0%	0 0.0%	0 0.0%	100% 0.0%
	Normal Panel	0 0.0%	0 0.0%	30 30.0%	0 0.0%	0 0.0%	0 0.0%	100% 0.0%
	Partially Shaded	0 0.0%	0 0.0%	0 0.0%	12 12.0%	0 0.0%	0 0.0%	100% 0.0%
	Partially Soil Covered	0 0.0%	0 0.0%	0 0.0%	0 0.0%	18 18.0%	0 0.0%	100% 0.0%
	Temperature Rise	0 0.0%	0 0.0%	2 2.0%	0 0.0%	0 0.0%	12 12.0%	85.7% 14.3%
		100% 0.0%	100% 0.0%	93.8% 6.3%	100% 0.0%	100% 0.0%	100% 0.0%	98.0% 2.0%
	Completely Soil Covered	Fully Shaded	Normal Panel	Partially Shaded	Partially Soil Covered	Temperature Rise		
	Target Class							

FIGURE 23: Confusion matrix for thermal images with fault.

TABLE 8: Statistics of thermal images in SN.

Class	Accuracy	Specificity	Sensitivity	Precision	F1 score
Normal panel	0.98	0.971	1	0.938	0.968
Completely soil covered	1	1	1	1	1
Partially soil covered	1	1	1	1	1
Temperature rise	0.98	1	0.857	1	0.923
Fully shaded	1	1	1	1	1
Partially shaded	1	1	1	1	1
Average	0.993	0.995	0.976	0.990	0.982

TABLE 9: Prediction and testing accuracy of real and thermal images.

Parameter	Prediction accuracy (%)	Testing accuracy of image (%)
Real image	100	94.42
Thermal image	98	99.74

8. Conclusion

This research proposed a deep learning technique by comparing CNN pretrained models and fine-tuning them for the diagnosis of environmental faults in solar panels. The insight of this research focused on comparing the performance of AlexNet, GoogleNet, and SqueezeNet with

different performance metrics and finding a suitable model for fault classification. The three models used in this research were capable of classifying five faults in solar panels from the productive class, in which the SqueezeNet model comprising 18 layers reached a testing accuracy of 99.815%. On the other hand, AlexNet despite its significant training accuracy obtained the lowest performance testing accuracy of 94.975% compared to the other architecture. Hence, the SqueezeNet model was used for training thermal images of solar panels which provided a testing accuracy of 99.74% and F1 score of 0.9818. The proposed method looks forward to make a significant contribution to the solar industry.

Data Availability

No data were used to support this study.

Conflicts of Interest

The authors declare that they have no conflicts of interest.

References

- [1] P. Jenitha and A. Immanuel Selvakumar, "Fault detection in PV systems," *Applied Solar Energy*, vol. 53, no. 3, pp. 229–237, 2017.
- [2] S. Das and M. B. AbhikHazra, "Metaheuristic optimization based fault diagnosis strategy for solar photovoltaic systems under non-uniform irradiance," *Renewable Energy*, vol. 118, pp. 452–467, 2018.
- [3] S. K. Firth, K. J. Lomas, and S. J. Rees, "A simple model of PV system performance and its use in fault detection," *Solar Energy*, vol. 84, no. 4, pp. 624–635, 2010.
- [4] W. Chine, A. Mellit, V. Lughi, A. Malek, G. Sulligoi, and A. Massi Pavan, "A novel fault diagnosis technique for photovoltaic systems based on artificial neural networks," *Renewable Energy*, vol. 90, pp. 501–512, 2016.
- [5] C. Mantel, "Machine learning prediction of defect types for electroluminescence images of photovoltaic panels," in *Proceedings of the SPIE-Optics and Photonics*, San Diego, CA, USA, 2019.
- [6] K. Natarajan, P. Kumar Bala, and V. Sampath, "Fault detection of solar PV system using SVM and thermal image processing," *International Journal of Renewable Energy Resources*, vol. 10, pp. 967–977, 2020.
- [7] M. V. Papadomanolaki and K. Karantzalos, "Benchmarking deep learning frameworks for the classification of very high-resolution satellite multispectral data," *ISPRS*, vol. 3, pp. 83–88, 2016.
- [8] C. Szegedy, W. Liu, Y. Jia et al., "Going deeper with convolutions," in *Proceedings of the IEEE Conference Computer Vision and Pattern Recognition (CVPR)*, Boston, MA, USA, 2015.
- [9] A. Mellit, G. M. Tina, and S. A. Kalogirou, "Fault detection and diagnosis methods for photovoltaic systems: a review," *Renewable and Sustainable Energy Reviews*, vol. 91, pp. 1–17, 2018.
- [10] K. Simonyan and A. Zisserman, "Very deep convolutional networks for large-scale image recognition," 2014, <https://arxiv.org/abs/1409.1556>.
- [11] Y. Sun, J. Xu, H. Qiang, C. Chen, and G. Lin, "Adaptive sliding mode control of maglev system based on RBF neural network minimum parameter learning method," *Measurement*, vol. 141, pp. 217–226, 2019.
- [12] M. K. Alam, F. Khan, J. Johnson, and J. Flicker, "A comprehensive review of catastrophic faults in PV arrays: types, detection, and mitigation techniques," *IEEE Journal of Photovoltaics*, vol. 5, no. 3, pp. 982–997, 2015.
- [13] A. K. Tripathi and C. S. N. Murthy, "Effect of shading on PV panel technology," in *Proceedings of the 2017 International Conference on Energy, Communication, Data Analytics and Soft Computing (ICECDS)*, pp. 2075–2078, Chennai, India, 2017.
- [14] M. Dhimish, V. Holmes, M. Dales, and B. Mehrdadi, "The effect of micro cracks on photovoltaic output power: case study based on real time long term data measurements," *Micro & Nano Letters*, vol. 12, 2017.
- [15] M. A. Ramli, E. Prasetyono, R. W. Wicaksana, N. A. Windarko, K. Sedraoui, and Y. A. Al-Turki, "On the investigation of photovoltaic output power reduction due to dust accumulation and weather conditions," *Renewable Energy*, vol. 99, pp. 836–844, 2016.
- [16] W. Yongqing, G. Zongqing, W. Shuonan, and H. Ping, "The temperature measurement technology of infrared thermal imaging and its applications review," in *Proceedings of the 2017 13th IEEE International Conference on Electronic Measurement & Instruments (ICEMI)*, Yangzhou, China, 2016.
- [17] F. f. Song, X. He, P. Lai, and R. wang, "The Study of infrared radiation thermal imaging technology for temperature testing," in *Proceedings of the 2012 13th International Conference on Electronic Packaging Technology & High Density Packaging*, Guilin, China, 2012.
- [18] J. A. Tsanakas, L. Ha, and C. Buerhop, "Faults and infrared thermographic diagnosis in operating c-Si photovoltaic modules: a review of research and future challenges," *Renewable and Sustainable Energy Reviews*, vol. 62, pp. 695–709, 2016.
- [19] T. Takashima, J. Yamaguchi, K. Otani, T. Oozeki, K. Kato, and M. Ishida, "Experimental studies of fault location in PV module strings," *Solar Energy Materials and Solar Cells*, vol. 93, no. 6-7, pp. 1079–1082, 2009.
- [20] C. A. Belhadj, I. H. Banat, and M. Deriche, "A detailed analysis of photovoltaic panel hot spot phenomena based on the bishop model," in *Proceedings of the 2017 14th International Multi-Conference on Systems, Signals & Devices (SSD)*, Marrakech, Morocco, 2017.
- [21] K. Itako, N. Iiduka, T. Kudoh, and K. Koh, "Proposition of novel real time hot-spot detection method for PV generation system," in *Proceedings of the: 2017 IEEE International Conference on Smart Grid and Smart Cities (ICSGSC)*, Singapore, 2017.
- [22] S. Albawi, T. A. Mohammed, and S. Al-Zawi, *Understanding of a Convolutional Neural Network*, pp. 1–6, Springer, Berlin, Germany, 2017.
- [23] S. S. Roy, A. Mallik, R. Gulati, M. S. Obaidat, and P. V. Krishna, *A Deep Learning Based Artificial Neural Network Approach for Intrusion Detection*, pp. 44–53, Springer, Berlin, Germany, 2017.
- [24] L. Xiao, Q. Yan, and S. Deng, "Scene classification with improved AlexNet model," in *Proceedings of the 12th International Conference on Intelligent Systems and Knowledge Engineering (ISKE)*, pp. 1–6, Nanjing, China, 2017.
- [25] S. Aswathy and D. Mishra, "Deep googlenet features for visual object tracking," in *Proceedings of the IEEE 13th International Conference on Industrial and Information Systems (ICIIS)*, Rupnagar, India, 2018.
- [26] Y. Liu, Z. Li, X. Chen, G. Gong, and H. Lu, "Improving the accuracy of SqueezeNet with negligible extra computational cost," in *Proceedings of the 2020 International Conference on High Performance Big Data and Intelligent Systems (HPBD&IS)*, Shenzhen, China, pp. 1–6, 2020.
- [27] R. Chauhan, K. K. Ghanshala, and R. C. Joshi, "Convolutional neural network (CNN) for image detection and recognition," in *Proceedings of the 2018 First International Conference on Secure Cyber Computing and Communication (ICSCCC)*, Jalandhar, India, 2018.

Review Article

A Review on Potential Opportunities to Preheat the Batteries Using a Finned Solar Air Energizer to Enhance Power Quality and Thermal Management in Low-Temperature Surroundings

P. K. Dhal,¹ J. Uma,² Piyush Gaur,³ D. Prasad,⁴ Melvin Victor Depoures ,⁵ A. Rajkumar,⁶ M. Ramesh ,⁷ Praveen Bhai Patel ,⁸ and Habtewolde Ababu Birhanu ⁹

¹Department of Electrical and Electronics Engineering, Vel Tech Rangarajan Dr Sagunthala R&D Institute of Science and Technology, Chennai 600062, Tamil Nadu, India

²Department of Electrical and Electronics Engineering, M.Kumarasamy College of Engineering, Karur 639113, Tamil Nadu, India

³Mechanical Engineering Cluster, School of Engineering, University of Petroleum and Energy Studies, Bidholi Campus Via Premnagar, Dehradun 248007, Uttarakhand, India

⁴Department of Electrical and Electronics Engineering, Sona College of Technology, Salem 636005, Tamil Nadu, India

⁵Department of Thermal Engineering, Saveetha School of Engineering, Saveetha Institute of Medical and Technical Sciences, Chennai 602105, Tamil Nadu, India

⁶Department of Electrical and Electronics Engineering, K. Ramakrishnan College of Technology, Tiruchirappalli 621112, Tamil Nadu, India

⁷Department of Electrical and Electronics Engineering, Vaageswari College of Engineering, Karimnagar 505527, Telangana, India

⁸Department of Chemical Engineering, University Institute of Engineering and Technology C S J M University, Kanpur 208024, Uttar Pradesh, India

⁹Faculty of Mechanical Engineering, Arba Minch Institute of Technology Arba Minch University, PO Box 21, Arba Minch, Ethiopia

Correspondence should be addressed to Melvin Victor Depoures; melvin.mech02@gmail.com and Habtewolde Ababu Birhanu; habtewold.ababu@amu.edu.et

Received 9 June 2022; Accepted 10 August 2022; Published 16 September 2022

Academic Editor: Ravi Samikannu

Copyright © 2022 P. K. Dhal et al. This is an open access article distributed under the Creative Commons Attribution License, which permits unrestricted use, distribution, and reproduction in any medium, provided the original work is properly cited.

This research study's objective is to provide a comprehensive analysis of the efforts that have been made to improve the power quality and thermal management of batteries that are operating at low temperatures. These improvements have been made by combining the utilization of conventional solar air energizer (SAE) ducts with the application of a variety of different configurations of longitudinal fins. These expanded surfaces can be found on the absorber or bottom plate surface, and they are placed in a variety of positions along the airflow channel. It does this by increasing the surface area of the typical SAH and making the flow more turbulent, both of which contribute to the improvement in performance. Several studies have been carried out to enhance the thermal efficiency of clear SAE ducts by making use of experimental fins. An effort has been made to establish the Nusselt number and the friction factor by making use of the correlations that the researchers have provided. This was performed so that the performance of various configurations of finned SAEs could be compared to one another.

1. Introduction

The global expansion of industry raises the demand for thermal energy and depletes fossil resources. Solar energy has been identified by experts as a viable option for creating

energy from an unlimited resource. Flat plate solar air energizers (SAEs) are utilized for the drying of agricultural (pepper, coffee, tea, grapes, Chilies, etc.) and industrial items (curing of concrete blocks, drying of paints, etc.). They are also utilized to improve the efficiency of desalination and

heat pump systems. In addition, they are utilized for space heating applications and hot air requirements up to 120°C at low temperatures [1–4]. SAEs have a basic structure, less manufacturing, and maintenance complexity, and lower initial investment and maintenance expenses [5]. Even though SAEs have their own merits, the thermal performance of the flat plate SAE is low (40 to 45 percent) due to the low heat transfer coefficient produced by the thermo-physical properties of air.

To boost the thermal performance of conventional SAEs, researchers have utilized a variety of methods to increase the heat transfer coefficient between the air and absorber plate. The formulation of the laminar sublayer is one of the major primary factors that decrease the convection heat transfer rate. In previous research [6, 7], artificially rough wires are added to the absorber plate to disrupt the laminar sublayer formulation. In addition, the rate of heat transmission is increased by affixing V-grooves [8, 9], corrugations [10, 11], turbulators, and baffles [12, 13] to the absorber plate and generating local turbulence. In addition, the packed bed, wire meshes, and energy storage materials are attached to the absorber plate to increase its efficiency during periods of low sunlight [14–18]. The CFD-based analysis of SAEs is performed to analyze and gain a deeper understanding of heat transfer phenomena. Pashchenko conducted a CFD-based analysis for SAE using ANSYS-FLUENT and concluded that the optimal efficiency occurs at an inclination angle of 60 degrees between the absorption surface and the Earth [19]. Moreover, he discovered that using an L-shaped fin on SAE with a pitch of 30 mm and Re of 1500 improves its thermodynamic performance [20]. Using MATLAB tools, the finned and roughened SAE designs are examined, and the design configurations are optimized based on energy and exergy efficiency [21, 22].

There are numerous published reviews on the implications of various roughness design settings on the performance of SAEs [23, 24]. Singh and Dhiman [25] analyzed the various design configurations of double-pass SAEs and concluded that hot air recycling improves thermal performance. Alam et al [26] conducted a comprehensive analysis of the application of turbulators and evaluated the performance of SAE ducts with various forms of baffles, ribs, and barriers. From a review of the relevant literature, it can be determined that the attachment of fins increases the heat transfer surface area, local turbulence, and the convective heat transfer rate. As far as the author is aware, no systematic studies have been conducted on this design configuration, and additional improvisation techniques are not mentioned to heat the batteries under low-temperature operating conditions. The thermal performance of finned SAEs is compared on the basis of the Nusselt number and friction factor [27–30] in this study, which reviews the various configurations and designs of finned SAEs. From the aforementioned literature survey, it can be inferred that various review articles have been presented about SAH thermal enhancement strategies. As far as the authors know, no one has reviewed extended surface (fin) SAHs put longitudinally in the duct.

1.1. Thermal Efficiency. The real usefulness of SAH can be determined by taking into account the amount of energy that

enters the collector in the form of radiation as well as the pace at which energy is lost to the surrounding environment. It is determined by making use of the Duffie and Beckman relation and taking into account the fact that the entire absorber plate is kept at an average fluid temperature of T_f and an ambient temperature of T_a .

$$Qu = F_R A_C [I(\tau\alpha) - U_L(T_f - T_a)]. \quad (1)$$

The answer to the previous equation, T_f is given by

$$T_f = \frac{T_i + T_o}{2}. \quad (2)$$

The amount of useable energy that is gathered by the SAH can be calculated by taking into account the enthalpy difference that exists between the air that enters and leaves the device.

$$Qu = mC_p(T_o - T_i). \quad (3)$$

From equations (1) and (3), the heat removal factor FR is expressed as

$$F_R = \frac{mC_p(T_o - T_i)}{A_C [I(\tau\alpha) - U_L(T_f - T_a)]}. \quad (4)$$

Using the Hottel-Whillier-Bliss equation and taking into account the overall loss coefficient U_L and the heat removal factor FR, one may determine the level of thermal efficiency that solar collectors possess. It is represented by

$$\eta_{th} = \frac{Qu}{IA_C} = F_R \left[I(\tau\alpha) - U_L \left(\frac{T_f - T_a}{I} \right) \right]. \quad (5)$$

The heat removal factor FR can be evaluated using the relation as follows:

$$F_R = \frac{mC_p}{U_L A_c} \left[1 - \exp \left(\frac{U_L A_p F'}{mC_p} \right) \right]. \quad (6)$$

1.2. Effective Thermal Efficiency. The actual performance of the system can be determined by looking at the effective thermal efficiency of the SAH. It evaluated everything by taking into account the pumping power consumption that was used to propel the air inside the channel, the efficiency of the blower, the efficiency of the motor, the efficiency of the transmission, and the efficiency of the power plant.

Calculating the effective thermal efficiency is possible by applying the relation that is as follows:

$$\eta_{ETE} = \frac{Qu}{IA_C} - \frac{P_m}{IA_C (\eta_B \eta_m \eta_T \eta_P)}. \quad (7)$$

2. Solar Air Energizer with Smooth and Fin Absorber Plates

The rate of heat transfer and SAE pipeline pressure drop are critical factors to be considered for the selection of the system for heating applications. Figure 1(a) shows a basic

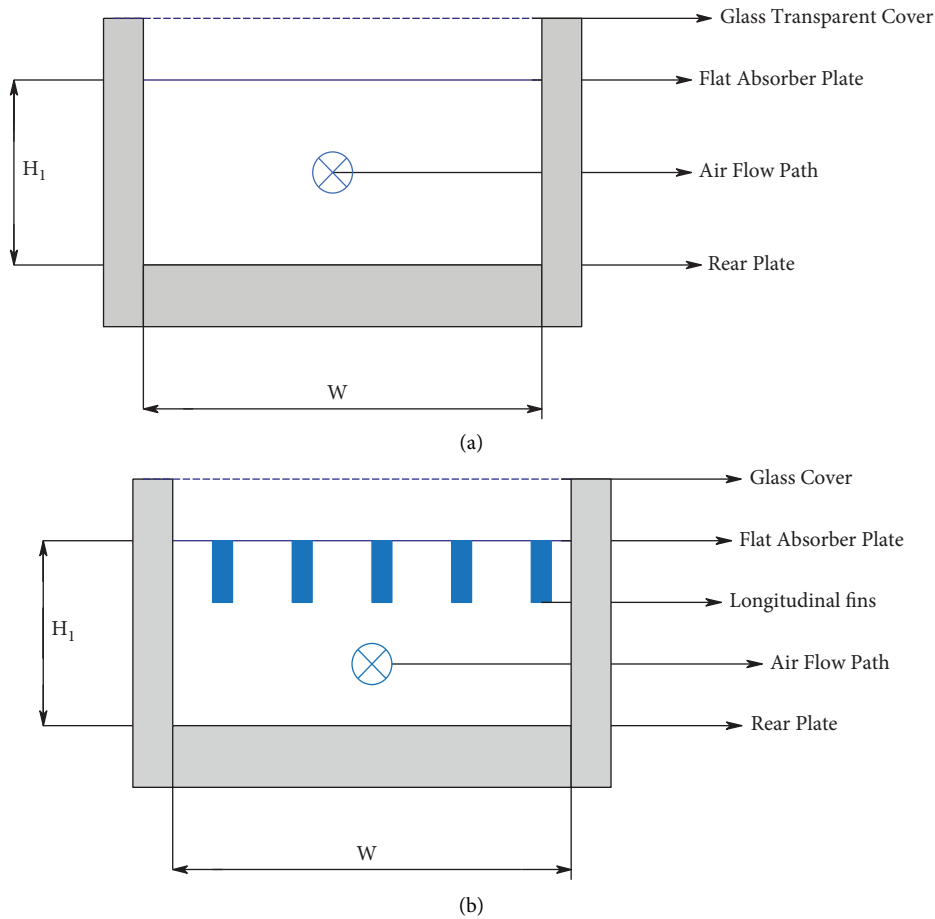


FIGURE 1: (a) Conventional smooth absorber plate solar air energizer. (b) Solar air energizer with a longitudinal fin plate absorber.

smooth plate SAE consisting of thin-walled bottom and glass-covered blackened absorber plates. There are longitudinal fins attached to the absorber surface of the heater shown in Figure 1(b).

3. Configurations of Fins and Flow Path Arrangements Utilized for the Heating Process

3.1. Longitudinal Fin-Integrated Solitary Pass Rectangular Solar Air Energizer. Garg et al. [31], who placed longitudinal fins on an absorber plate, were the first to observe the effect of rectangular fins on SAE. Using their mathematical model of steady state, they investigated the effect of fins on the efficiency of SAE. They evaluated three distinct types of SAE, including the Type-I conventional solar duct with an absorber plate as depicted in Figure 1(a). In Type-II SAEs with expanded surfaces, Figure 1(b) shows that Type-II SAEs are positioned across the absorber surface. The Type-III SAE was equipped with a V-grooved absorber plate. All SAE outputs and performance were analyzed using a single glass cover. The effect of the number of fins (n) on the outlet air temperature and thermal performance of a finned SAE was investigated by using three different rates of flows (m) in three different configurations. Garg et al. [32] analyzed three

different designs of SAEs. They configured the Type-I SAE as illustrated in Figure 2(a). This comprises a double glass cover, and fins are put on the absorber plate to increase the turbulence of the flow. In addition, they adjusted the design by repositioning the fins on the backplate and assessed the resulting effect ((Figure 2(b)). As seen in Figures, Type-III SAE is created by combining both designs and incorporating fins into both SAE plates (Figure 2(c)). Following analytical and experimental processes, a comparison is performed between SAEs. Then, the effects of the fin density (n), mass flow rate (m), fin length (L), and height of the SAE duct (H) on the SAE performance were examined and compared to the performance of a conventional SAE under identical operating conditions.

The researchers Garg et al. and Karim and Hawaladar [33, 34] investigated the configuration of the expanded surface on the solar air energizer duct, which can be seen in Figure 3. They designed an SAE in which the height of the fin is proportional to the depth of the cavity. As a direct consequence of this, the absorber plates and back plates are connected by fins, which results in the formation of individual flow cells. The efficiency of the SAE and the temperature at its exit are investigated by making adjustments to the mass flow rate and the number of fins. Additionally, the impact that the SAE depth has on the organization's overall performance is investigated. After that, the researchers

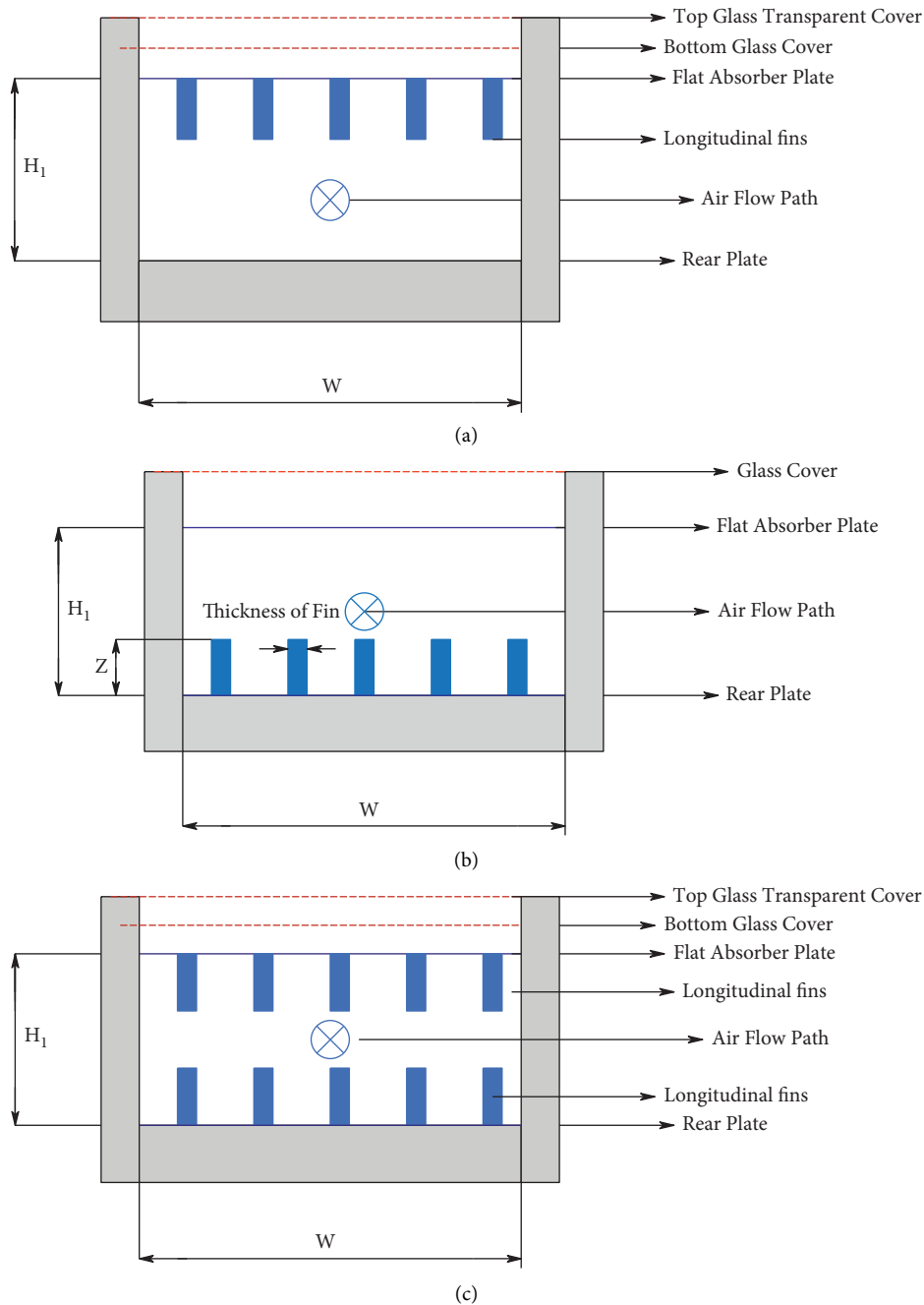


FIGURE 2: (a) Fin solar air energizer with twin transparent sheets and the fin-integrated absorber surface [32]. (b) Fin solar air energizer with solitary glass sheets (fins at both the sheets) [32]. (c) Fin solar air energizer with finned bottom and glass sheet covered finned absorber plates [32].

investigated how a smooth plate and a V-groove SAE performed in single-pass and double-pass operation modes, respectively.

Bahrehmand et al. [35] developed an analytical model to evaluate the thermal performance of rectangular and triangular SAE fins. The SAE configurations are depicted in Figures 4 and 5. During the analysis, the effect of a suspended thin metal sheet on the airflow channel, the design configuration of the fins, the Reynolds number, the depth, and the length of the duct are examined.

At lower Reynolds numbers (4000), it is established that the SAE without fins integrated with thin metal sheets operates

better. In addition, for higher Reynolds numbers (>4000), the thin metal sheet solar air energizer with triangle fins is more efficient. For practicing engineers to design the SAE, they also report the critical values of design and operating circumstances, such as Re of 13500, depth of 0.095 m, and length of 2 m.

3.2. Semicircular Fin-Integrated Solitary Pass Rectangular Solar Air Energizer. Chabane et al [36] conducted an experiment to determine the effect of semicylindrical fins distributed longitudinally across the absorber plate, as depicted in Figure 6. The analysis was conducted under

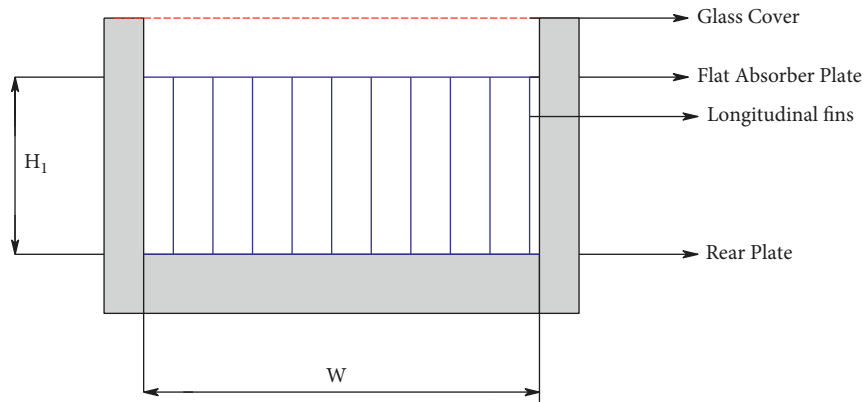


FIGURE 3: Fin solar air energizer with single glass cover investigated by the authors in [33, 34].

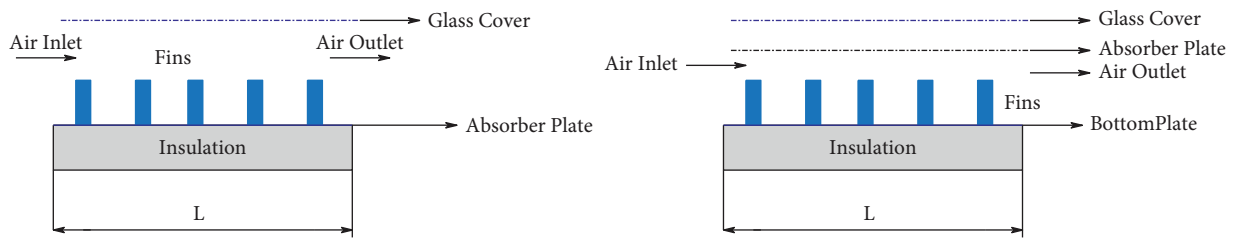


FIGURE 4: Solar air energizer with the extended surface (Type-I with only absorber plates and Type-II with absorbers and finned bottom plates) [35].

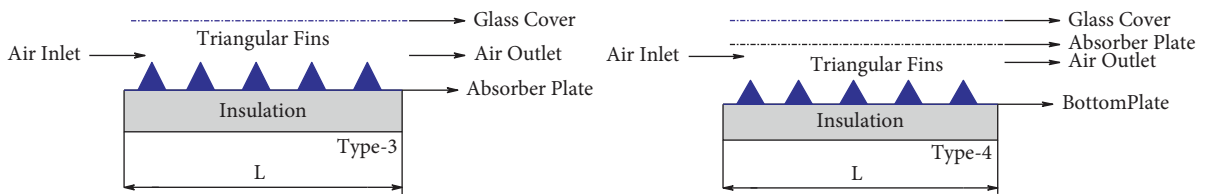


FIGURE 5: Solar air energizer with triangular fins (Type-III without bottom plates and Type-IV with absorbers and bottom plates) investigated by the authors in [35].

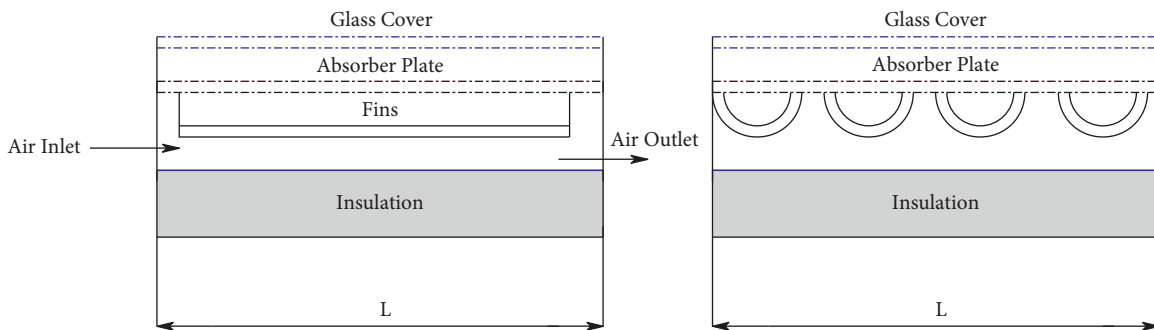


FIGURE 6: Semicircular fin-integrated solitary pass rectangular solar air energizer [36].

actual ambient circumstances with a mass flow rate between 0.012 and 0.016 kg/s. During the experiment, the impact of design and operating circumstances on the output air temperature, Nusselt number, Prandtl number, and heat removal rate is examined. In addition, the scientists determined that the highest increase in the Nusselt number was

99.03 at a mass flow rate of 0.016 kg/s and created a correlation for forecasting the Nusselt number as a function of design and operating parameters.

Chabane et al [37] conducted additional experimental research on the finned SAE (Figure 6). According to reports, the performance of SAE is dependent on solar intensity, inlet

air temperature, and the distance between the absorber plate and the glass cover. At a mass flow rate of 0.016 kg/s, the maximum thermal efficiency of 43.94 percent is attained, according to the researchers.

4. Longitudinal Fin-Integrated Parallel Pass Rectangular Solar Air Energizer

To improve the convective heat transfer coefficient, researchers additionally implemented a double-pass configuration for SAE. Among these double pass flow systems, Yeh et al [38] affixed rectangular fins for additional augmentation, as depicted in Figure 7. Analytically and experimentally, the influence of solar radiation and the flow ratio on mass flow rates between 38 and 78 kg/h is examined. The analysis concludes that thermal efficiency has improved as solar radiation has increased, and it reaches its optimum value at a mass flow ratio (r) of 0.5.

Experimentally, Karim and Hawlader [39] examined the thermal performance of conventional, finned, and V-grooved SAEs working in both single-pass and double-pass modes. The comparison outcomes are depicted in Figure 8. The analysis is conducted in accordance with ASHRAE standards, and the flow rate ranges between 0.01 and 0.06 kg/s m². The results demonstrated that V-corrugated arrangement is more thermally efficient than finned SAE for the range of parameters studied.

Sebaili et al [40] conducted analytical and experimental research on double pass-double glass cover finned and V-corrugated SAEs. The performance evaluation was conducted under actual outdoor situations. Then, they compared the performance of the SAEs as depicted in Figures 9. As shown in Figure 10, throughout the analysis, the mass flow rate is kept between 0.01 and 0.06 kg/s.

Under comparable operational and climatic conditions, they concluded that the V-corrugated SAE and finned SAE achieve their maximum thermohydraulic performance at 0.0125 kg/s and 0.0225 kg/s, respectively. Moreover, the thermal performance of V-corrugated SAEs is 9.3 to 11.9%, which is greater than that of finned SAEs.

In addition, empirical work has been assessed, and reasonable agreement between experimental findings has been established. It has been determined that the V-corrugated SAE performs better than the finned and standard plate SAEs due to less pressure loss and the creation of more turbulence.

5. Longitudinal Fin-Integrated Counter Pass Rectangular Solar Air Energizer

Naphon [41] performed an analytical study on the SAE with fins parallel to the flow path on either side of the collection plate and a double-pass airflow arrangement as depicted in Figure 11. The mass flow rate, number of fins, and fin height are modified by 0.02 to 0.1 kg/s, 45 to 55, and 5 to 8 cm, respectively, during the analysis. Based on the findings, he concluded that an increase in the number of fins, flow rate, and fin height improves thermal efficiency and that these factors have an inverse relationship with entropy generation.

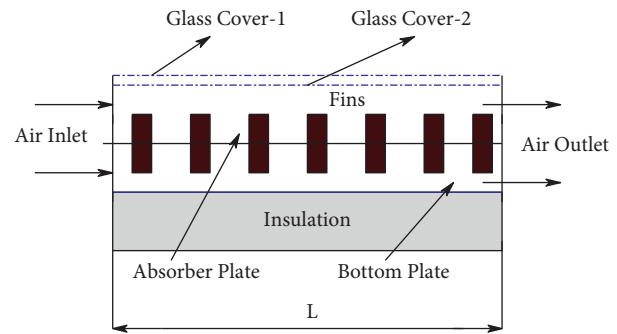


FIGURE 7: Double flow fin solar air energizer with multiple glass covers [38].

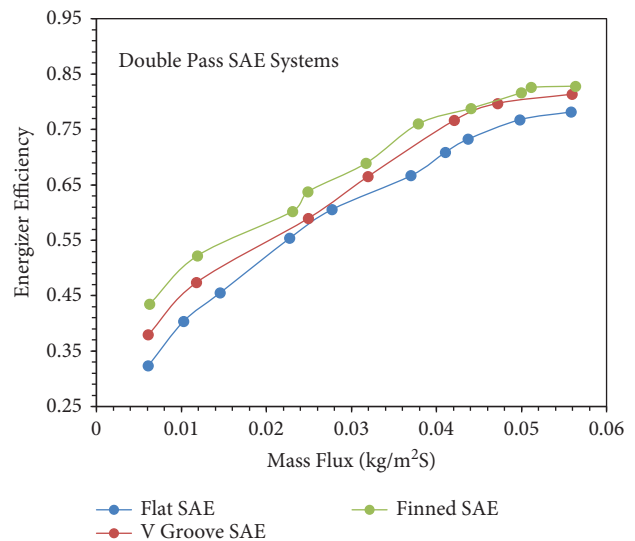


FIGURE 8: Performance assessment of finned SAEs with conventional and inline V-grooved SAEs for dual pass flow conditions [39].

Fudholi et al. [42] explored the performance of double-pass SAEs with fins at the lower path, as depicted in Figure 12. On the basis of the energy and exergy efficiency data, they conducted experimental and theoretical analysis and compared the performance with traditional double-pass SAEs. According to the findings of the investigation, the thermal efficiency of SAEs ranges from 54 to 79 percent, with an outlet temperature of 36.4 to 62.9 degree Celsius. It has been stated that the thermal efficiency improvement is in linear relation with the sun insolation (I) for a fixed quantity flow rate (m). Additionally, the yearly cost and yearly energy gain of the two SAEs have been evaluated and published.

6. Longitudinal Fin-Integrated Repeated Pass Rectangular Solar Air Energizer

Velmurugan and Kalaivanan [43] created mathematical models of the thermal performance of various SAEs. Figure 13(a) depicts a Type-I SAE with a single-pass, double-glass SAE and a smooth absorber plate. In addition, they analyzed the performance of longitudinal finned SAEs with

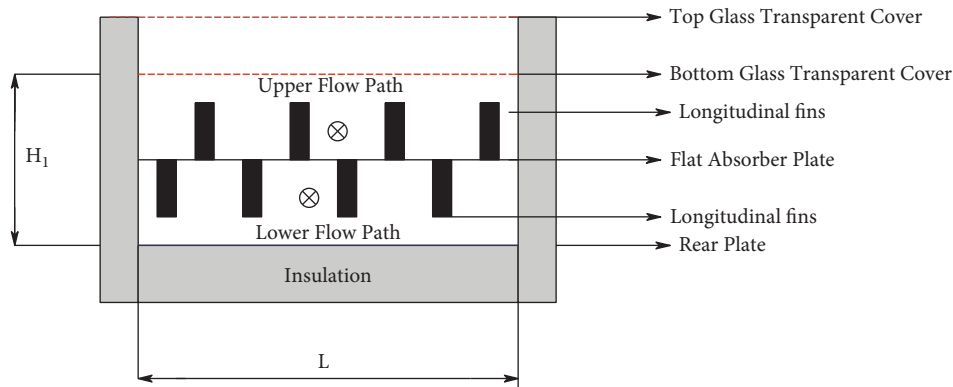


FIGURE 9: Double flow finned solar air energizer [40].

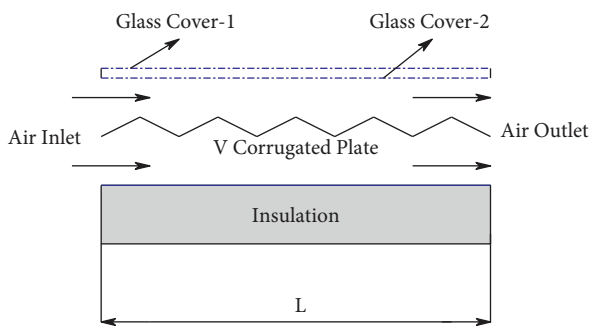


FIGURE 10: Double flow V-corrugated plate solar air energizer [40].

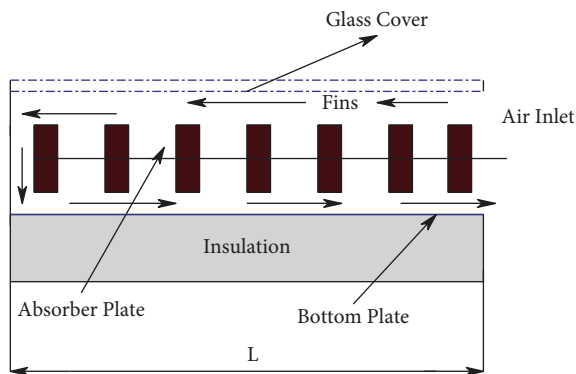


FIGURE 11: Double pass fin solar air energizer arrangement investigated by the authors in [41].

Type-II, double glass double pass and Type-III, double glass triple-pass operation, as depicted in Figures 13(b) and 13(c).

They created a mathematical model for SAEs and used the MATLAB code to solve it. They analyzed the impact of the mass flow rate, inlet air temperature, and solar radiation in the ranges of 0.01 to 0.04 kg/s, 294 to 306 K, and 800 to 1000 W/m². In addition, it is concluded that the triple-pass SAE with fins produces superior performance with a greater value of beneficial heat gain enhancement to a power consumption increment value of 0.1.

SAEs of four different varieties were tested in an indoor experiment by Velmurugan and Kalaivanan [44]. It is divided into four distinct types: Type-I: a single-pass flat plate; Type-II: two passes with roughness rib on the absorber plate;

Type-III: double passes with fins on the glass cover; Type-IV: double passes with wire mesh. Each SAE configuration was examined to determine its first and second law efficiency (Figure 14).

7. Wavy Form Fin-Integrated Solitary Pass Rectangular Solar Air Energizer

A wavy finned absorber plate (SAE) has been studied by Priyam and Chand [45], and the results are displayed in Figure 15. The mass flow rate varied from 0.01 to 0.08 kg/s, while the fin spacing varied from 1 to 5 cm. From the analytical investigation, the influence of these parameters on the thermal efficiency, collector heat removal factor, collector efficiency factor, effective temperature rise, effective efficiency, and pressure drop of the SAE is reported. Additional research was carried out by the authors to examine the influence of the amplitude and wavelength of wavy fins (ranging from 3 cm to 20 cm) on energy and system efficiency [46]. Based on heat transfer correlations, the model was created [47]. Both the parameter and performance evaluation parameters such as energy transfer first law-based efficiency, heat removal factor at SAE, collector efficiency factor, effective rise, and effective rise in temperature have an inverse connection.

8. Performance Characteristic Comparison between Finned Solar Air Energizers

A comparison of heat transfer in terms of the Nusselt number and the friction factor for various types of longitudinal finned SAEs has been made, and the results of this comparison are shown in Figure 16, respectively. This comparison was Figure 17 made based on the correlations that different researchers found while reading the relevant literature. The values of the Nusselt number are shown to be directly proportional to the mass flow rate in Figure 17, and the SAE that was created by Garg et al. [33] has the greatest value of Nu. In addition, the data shown in Figure indicate that the friction factor has an inverse correlation with the mass flow rate (m). According to the findings of Fudholi

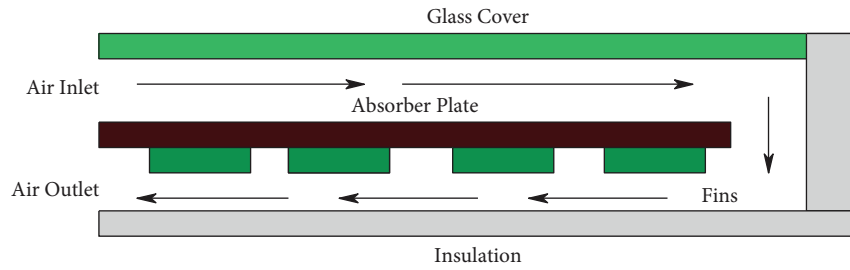


FIGURE 12: Layout of dual pass finned solar air energizer [42].

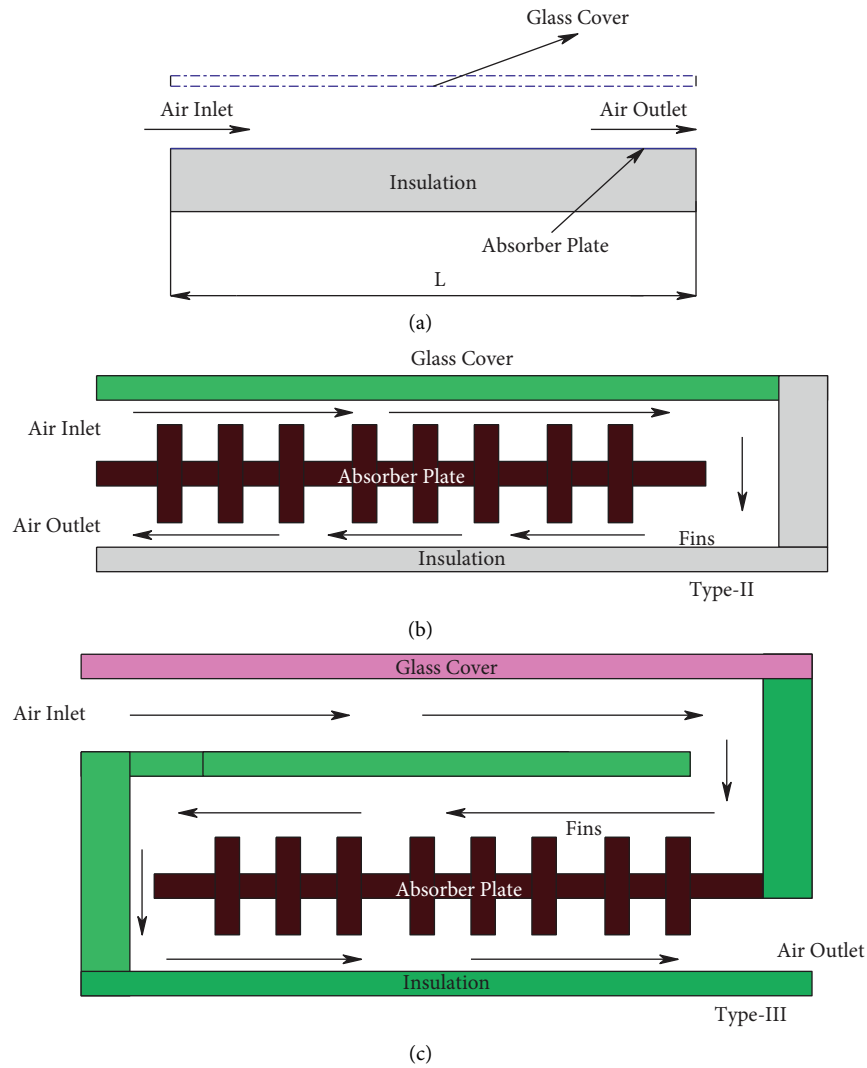


FIGURE 13: (a) Type-I: solitary pass twin glass smooth plate SAEs [43]. (b) Type-II: double pass, double glass [43]. (c) Type-III: multipass, twin glass SAEs with extended surfaces [43].

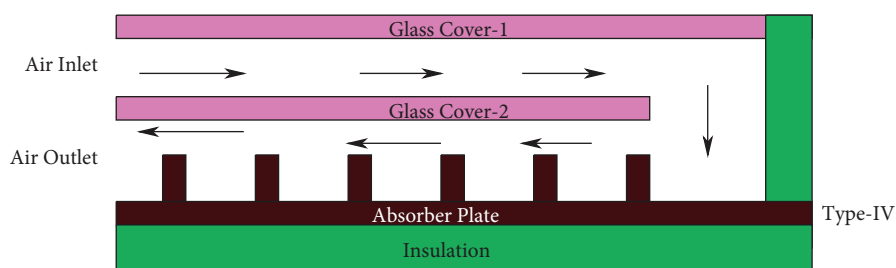


FIGURE 14: Twin pass, twin glass SAEs with extended surfaces (Type-IV) [44].

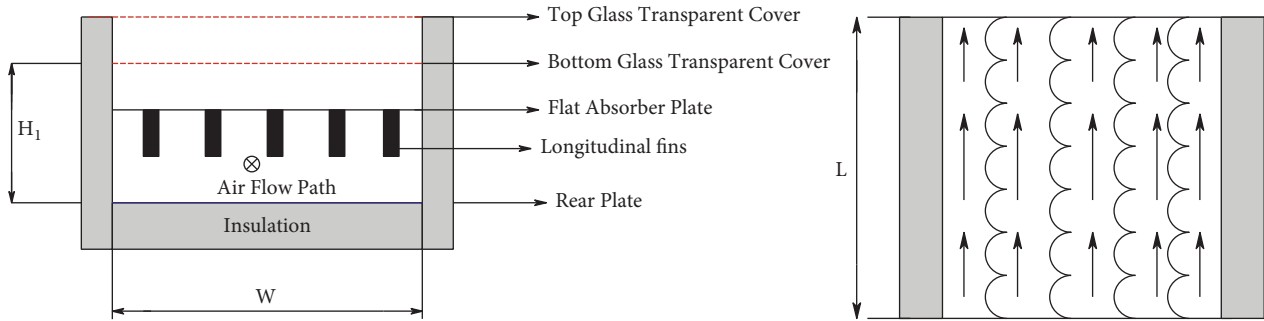


FIGURE 15: Solar air energizer with a wavy finned absorber [45, 46].

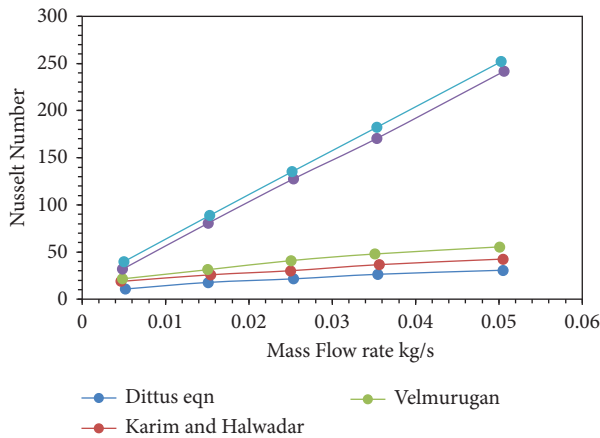


FIGURE 16: Comparison of the Nusselt number reported by various researchers for different types of longitudinal finned SAEs with the Dittus–Boelter equation as reported in [48].

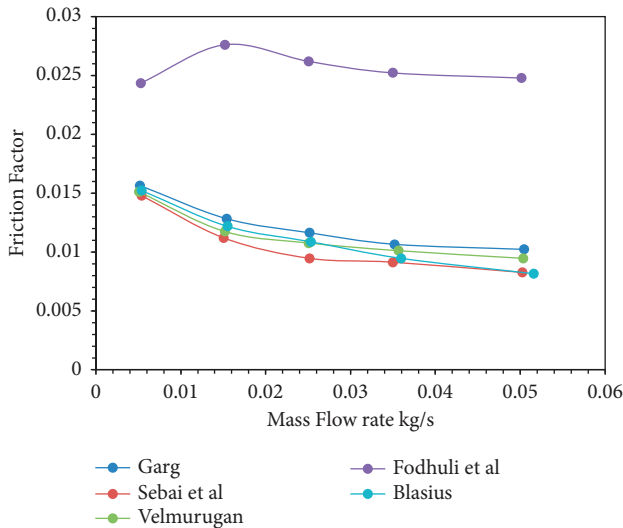


FIGURE 17: Comparison of the friction factor reported by various researchers for different types of longitudinal finned SAEs with the Blasius equation as reported in [48].

et al. [42], the friction factor had the greatest value out of all the factors that were considered.

The solar air heaters can maintain the battery at the required temperature while operating under low-

temperature conditions. The low-cost technology is very useful for the commercialization process.

9. Conclusion

In this article, a thorough review and study of how longitudinal finned SAEs are used were performed. The researchers attached different shapes of fins to the SAE, such as rectangular, triangular, and semicylindrical profiles and then used analytical and experimental studies to figure out what effect these have. From this thorough look at the finned SAEs, the following conclusions have been drawn:

- (i) When compared to the smooth plate solar air energizer, the addition of longitudinal fins increases the solar air energizer’s thermal efficiency in functionally equivalent settings.
- (ii) Fin factors such as the number of fins, fin length, and fin height, operating parameters such as mass flow, and geometrical parameters such as sun intensity and ambient air temperature all have a substantial impact on the performance of SAE.
- (iii) SAE fin density and thermal efficiency are both improved, as is the pressure drop in the airflow channel, as the fin height is increased.
- (iv) Increasing the depth of the ducts has a negative impact on SAE’s thermal efficiency, and increasing the number of glass covers and air passes has a positive impact on SAE’s thermal efficiency.
- (v) The majority of the research studies that have been performed to increase the performance of SAEs have utilized rectangular fins as the primary method of investigation. In addition, there is not a lot of research that looks at how effective SAE fins that are triangular or semicylindrical. As a consequence of this, scientists need to direct their attention toward the development of innovative fin designs that will result in an increase in SAE’s overall performance. It is possible to increase the electrical output quality of low-temperature situations by first heating the cabins and then using batteries in those environments.

Data Availability

The data used to support the findings of this study are included within the article.

Conflicts of Interest

The authors declare that there are no conflicts of interest regarding the publication of this article.

References

- [1] J. A. Duffie, *Solar Engineering of Thermal Processes*, pp. 250–330, John Wiley & Sons, Noida, India, 1991.
- [2] A. Veera Kumar, T. V. Arjunan, D. Seenivasan, R. Venkatramanan, S. Vijayan, and M. M. Matheswaran, “Influence of twisted tape inserts on energy and exergy performance of an evacuated Tube-based solar air collector,” *Solar Energy*, vol. 225, pp. 892–904, 2021.
- [3] V. J. Manoj Praveen, R. Vigneshkumar, N. Karthikeyan, A. Gurumoorathi, R. Vijayakumar, and P. Madhu, “Heat transfer enhancement of air-concrete thermal energy storage system—CFD simulation and experimental validation under transient condition,” *Proceedings of the Institution of Mechanical Engineers-Part E: Journal of Process Mechanical Engineering*, vol. 235, no. 5, pp. 1304–1314, 2021.
- [4] R. K. Prasad and M. K. Sahu, “Investigation on optimal thermohydraulic performance of a solar air heater having arc shaped wire rib roughness on absorber plate,” *International Journal of Thermodynamics*, vol. 19, no. 4, pp. 214–224, 2016.
- [5] M. M. Matheswaran, T. V. Arjunan, S. Muthusamy et al., “A case study on thermo-hydraulic performance of jet plate solar air heater using response surface methodology,” *Case Studies in Thermal Engineering*, vol. 34, Article ID 101983, 2022.
- [6] K. Prasad and S. C. Mullick, “Heat transfer characteristics of a solar air heater used for drying purposes,” *Applied Energy*, vol. 13, no. 2, pp. 83–93, 1983.
- [7] B. N. Prasad and J. S. Saini, “Effect of artificial roughness on heat transfer and friction factor in a solar air heater,” *Solar Energy*, vol. 41, no. 6, pp. 555–560, 1988.
- [8] M. A. Karim and M. N. A. Hawlader, “Performance evaluation of a v-groove solar air collector for drying applications,” *Applied Thermal Engineering*, vol. 26, no. 1, pp. 121–130, 2006.
- [9] T. Liu, W. Lin, W. Gao et al., “A parametric study on the thermal performance of a solar air collector with a v-groove absorber,” *International Journal of Green Energy*, vol. 4, no. 6, pp. 601–622, 2007.
- [10] H. M. Abd, O. R. Alomar, and M. M. M. Salih, “Improving the performance of solar air heater using a new model of V-corrugated absorber plate having perforations jets,” *International Journal of Energy Research*, vol. 46, no. 6, pp. 8130–8144, 2022.
- [11] W. Gao, W. Lin, T. Liu, and C. Xia, “Analytical and experimental studies on the thermal performance of cross-corrugated and flat-plate solar air heaters,” *Applied Energy*, vol. 84, no. 4, pp. 425–441, 2007.
- [12] P. Promvong, “Heat transfer and pressure drop in a channel with multiple 60 V-baffles,” *International Communications in Heat and Mass Transfer*, vol. 37, no. 7, pp. 835–840, 2010.
- [13] R. Kumar, M. Sethi, R. Chauhan, and A. Kumar, “Experimental study of enhancement of heat transfer and pressure drop in a solar air channel with discretized broken V-pattern baffle,” *Renewable Energy*, vol. 101, pp. 856–872, 2017.
- [14] S. A. Sadri, H. Parsa, M. Saffar-Avval, and M. R. Hajmohammadi, “Configuration optimization of the honeycomb core in the latent heat thermal energy storage of a solar air heater: experimental and numerical study,” *International Journal of Energy Research*, vol. 46, no. 5, pp. 5924–5954, 2022.
- [15] L. B. Y. Aldabbagh, F. Egelioglu, and M. İlkan, “Single and double pass solar air heaters with wire mesh as packing bed,” *Energy*, vol. 35, no. 9, pp. 3783–3787, 2010.
- [16] P. Naphon, “Effect of porous media on the performance of the double-pass flat plate solar air heater,” *International Communications in Heat and Mass Transfer*, vol. 32, no. 1–2, pp. 140–150, 2005.
- [17] M. R. I. Ramadan, A. A. El-Sebaei, S. Aboul-Enein, and E. El-Bialy, “Thermal performance of a packed bed double-pass solar air heater,” *Energy*, vol. 32, no. 8, pp. 1524–1535, 2007.
- [18] P. Dhiman, N. S. Thakur, and S. R. Chauhan, “Thermal and thermohydraulic performance of counter and parallel flow packed bed solar air heaters,” *Renewable Energy*, vol. 46, pp. 259–268, 2012.
- [19] D. I. Pashchenko, “CFD modeling of operating processes of a solar air heater in ANSYS Fluent,” *Journal of Engineering Physics and Thermophysics*, vol. 92, no. 1, pp. 73–79, 2019.
- [20] D. I. Pashchenko, “ANSYS fluent CFD modeling of solar air-heater thermoaerodynamics,” *Applied Solar Energy*, vol. 54, no. 1, pp. 32–39, 2018.
- [21] P. T. Saravanakumar, D. Somasundaram, and M. M. Matheswaran, “Thermal and thermo-hydraulic analysis of arc shaped rib roughened solar air heater integrated with fins and baffles,” *Solar Energy*, vol. 180, pp. 360–371, 2019.
- [22] C. Sivakandhan, T. V. Arjunan, and M. M. Matheswaran, “Thermohydraulic performance enhancement of a new hybrid duct solar air heater with inclined rib roughness,” *Renewable Energy*, vol. 147, pp. 2345–2357, 2020.
- [23] M. K. Sahu and R. K. Prasad, “A review of the thermal and hydrodynamic performance of solar air heater with roughened absorber plates,” *Journal of Enhanced Heat Transfer*, vol. 23, no. 1, pp. 47–89, 2016.
- [24] V. Singh Bisht, A. Kumar Patil, and A. Gupta, “Review and performance evaluation of roughened solar air heaters,” *Renewable and Sustainable Energy Reviews*, vol. 81, pp. 954–977, 2018.
- [25] S. Singh and P. Dhiman, “Thermal performance of double pass packed bed solar air heaters—a comprehensive review,” *Renewable and Sustainable Energy Reviews*, vol. 53, pp. 1010–1031, 2016.
- [26] T. Alam, R. P. Saini, and J. S. Saini, “Heat and flow characteristics of air heater ducts provided with turbulators—a review,” *Renewable and Sustainable Energy Reviews*, vol. 31, pp. 289–304, 2014.
- [27] C. D. Ho, H. M. Yeh, T. W. Cheng, T. C. Chen, and R. C. Wang, “The influences of recycle on performance of baffled double-pass flat-plate solar air heaters with internal fins attached,” *Applied Energy*, vol. 86, no. 9, pp. 1470–1478, 2009.
- [28] K. Mohammadi and M. Sabzpooshani, “Comprehensive performance evaluation and parametric studies of single pass solar air heater with fins and baffles attached over the absorber plate,” *Energy*, vol. 57, pp. 741–750, 2013.
- [29] M. Sabzpooshani, K. Mohammadi, and H. Khorasanizadeh, “Exergetic performance evaluation of a single pass baffled solar air heater,” *Energy*, vol. 64, pp. 697–706, 2014.
- [30] H. M. Yeh, C. D. Ho, and C. Y. Lin, “The influence of collector aspect ratio on the collector efficiency of baffled solar air heaters,” *Energy*, vol. 23, no. 1, pp. 11–16, 1998.
- [31] H. P. Garg, G. Datta, and B. Bandyopadhyay, “A study on the effect of enhanced heat transfer area in solar air heaters,” *Energy Conversion and Management*, vol. 23, no. 1, pp. 43–49, 1983.

- [32] H. P. Garg, G. Datta, and A. K. Bhargava, "Performance studies on a finned-air heater," *Energy*, vol. 14, no. 2, pp. 87–92, 1989.
- [33] H. P. Garg, R. Jha, C. Choudhury, and G. Datta, "Theoretical analysis on a new finned type solar air heater," *Energy*, vol. 16, no. 10, pp. 1231–1238, 1991.
- [34] M. A. Karim and M. N. A. Hawlader, "Development of solar air collectors for drying applications," *Energy Conversion and Management*, vol. 45, no. 3, pp. 329–344, 2004.
- [35] D. Bahrehmand, M. Ameri, and M. Gholampour, "Energy and exergy analysis of different solar air collector systems with forced convection," *Renewable Energy*, vol. 83, pp. 1119–1130, 2015.
- [36] F. Chabane, N. Moumami, D. Bensahal, and A. Brima, "Heat transfer coefficient and thermal losses of solar collector and Nusselt number correlation for rectangular solar air heater duct with longitudinal fins hold under the absorber plate," *Applied Solar Energy*, vol. 50, no. 1, pp. 19–26, 2014.
- [37] F. Chabane, D. Kherroubi, A. Arif, N. Moumami, and A. Brima, "Influence of the rectangular baffle on heat transfer and pressure drop in the solar collector," *Energy Sources, Part A: Recovery, Utilization, and Environmental Effects*, pp. 1–17, 2020.
- [38] H. M. Yeh, C. D. Ho, and J. Z. Hou, "Collector efficiency of double-flow solar air heaters with fins attached," *Energy*, vol. 27, no. 8, pp. 715–727, 2002.
- [39] M. A. Karim and M. N. A. Hawlader, "Performance investigation of flat plate, v-corrugated and finned air collectors," *Energy*, vol. 31, no. 4, pp. 452–470, 2006.
- [40] A. A. El-Sebaei, S. Aboul-Enein, M. R. I. Ramadan, S. M. Shalaby, and B. M. Moharram, "Thermal performance investigation of double pass-finned plate solar air heater," *Applied Energy*, vol. 88, no. 5, pp. 1727–1739, 2011.
- [41] P. Naphon, "On the performance and entropy generation of the double-pass solar air heater with longitudinal fins," *Renewable Energy*, vol. 30, no. 9, pp. 1345–1357, 2005.
- [42] A. Fudholi, K. Sopian, M. H. Ruslan, and M. Y. Othman, "Performance and cost benefits analysis of double-pass solar collector with and without fins," *Energy Conversion and Management*, vol. 76, pp. 8–19, 2013.
- [43] P. Velmurugan and R. Kalaivanan, "Thermal performance studies on multi-pass flat-plate solar air heater with longitudinal fins: an analytical approach," *Arabian Journal for Science and Engineering*, vol. 40, no. 4, pp. 1141–1150, 2015.
- [44] P. Velmurugan and R. Kalaivanan, "Energy and exergy analysis of solar air heaters with varied geometries," *Arabian Journal for Science and Engineering*, vol. 40, no. 4, pp. 1173–1186, 2015.
- [45] A. Priyam and P. Chand, "Thermal and thermohydraulic performance of wavy finned absorber solar air heater," *Solar Energy*, vol. 130, pp. 250–259, 2016.
- [46] A. Priyam and P. Chand, "Effect of wavelength and amplitude on the performance of wavy finned absorber solar air heater," *Renewable Energy*, vol. 119, pp. 690–702, 2018.
- [47] D. Junqi, C. Jiangping, C. Zhijiu, Z. Yimin, and Z. Wenfeng, "Heat transfer and pressure drop correlations for the wavy fin and flat tube heat exchangers," *Applied Thermal Engineering*, vol. 27, no. 11–12, pp. 2066–2073, 2007.
- [48] M. K. Sahu and R. K. Prasad, "Thermohydraulic performance analysis of an arc shape wire roughened solar air heater," *Renewable Energy*, vol. 108, pp. 598–614, 2017.

Research Article

Integrating Industrial Appliances for Security Enhancement in Data Point Using SCADA Networks with Learning Algorithm

Alaa O. Khadidos ¹, Adil O. Khadidos ², Hariprasath Manoharan ³,
Khaled H. Alyoubi ¹, Abdulrhman M. Alshareef ¹, and Shitharth Selvarajan ⁴

¹Department of Information Systems, Faculty of Computing and Information Technology, King Abdulaziz University, Jeddah, Saudi Arabia

²Department of Information Technology, Faculty of Computing and Information Technology, King Abdulaziz University, Jeddah, Saudi Arabia

³Department of Electronics and Communication Engineering, Panimalar Engineering College, Poonamallee, Chennai, India

⁴Department of Computer Science, Kebri Dehar University, Kebri Dehar, Ethiopia

Correspondence should be addressed to Shitharth Selvarajan; shitharths@kdu.edu.et

Received 5 August 2022; Accepted 20 August 2022; Published 15 September 2022

Academic Editor: Albert Alexander Stonier

Copyright © 2022 Alaa O. Khadidos et al. This is an open access article distributed under the Creative Commons Attribution License, which permits unrestricted use, distribution, and reproduction in any medium, provided the original work is properly cited.

The process of ensuring automatic operation for industrial appliances using both supervision and control techniques is a challenging task. Therefore, this article focuses on implementing Supervisory Control and Data Acquisition (SCADA) for controlling all industrial appliances. The design process of implementation case is performed using an analytical framework by examining the primary energy sources at the initial state; thus, a smart network is supported. The designed mathematical model is integrated with a learning technique that allocates resources at proper quantities. Further, the complex manual tuning of individual appliances is avoided in the projected method as the input variables are driven in a direct way at reduced loss state. In addition, the data processing state of individual appliances is carried out using central data controller where all parametric values are stored. In case any errors are observed, then SCADA network fixes the error in an automated way, reducing end-to-end delays in all appliances. To validate the effectiveness of the proposed method, five scenarios are examined and simulated where outcomes prove that SCADA network using learning models provides optimal results on an average of 84 percent as compared to the existing models without learning algorithm.

1. Literature Survey

SCADA, which is used for different industrial operations, is implemented under both large and small scale processes. Thus, it is always necessary to analyze the effect of SCADA systems by examining existing models and procedures that are followed to update the current security mechanisms. Therefore, the existing models are analyzed with respect to implementation, data gathering, and security, thus providing a clear analytical model with derivative frameworks. In [1] multiple layers are represented using two different units such as primary and secondary terminal units where a key preservation is made for enhancing security of the network.

Both terminal units use satellite as one mode of communication link with SCADA at intermediate junction. It is necessary that two terminal lines must be connected to the central station which is not processed; thus, as a result, individual monitoring is prepared. In addition to the terminal lines, the transmission stability of SCADA plays a vital role in all industrial operations in case of automated determinations [2]. Therefore, the stability of entire SCADA is initialized using state vectors where a specialized software tool is implemented for gathering information at output units. Even though hardware and software tools are combined, the process of time domain is carried out, which cannot determine complete stability of SCADA networks.

An evaluation model is framed and determined in comparison with multiple methods in case of risk factor determinations [3], where all protocols for managing separate keys are provided. The above-mentioned determinations can be used for enhancing the security of SCADA network, but the complete risk in a particular process cannot be avoided at any point of time.

Some of the techniques are developed for micro grid operations in order to manage energy much effectively in building platform [4]. These kinds of application developments are made using SCADA network where high infrastructure is needed and it is processed even with critical loads. While processing critical loads, some control strategies are designed and it is modified during the implementation stage. The above-mentioned modifications are not processed in real time cases if SCADA is implemented at a particular time period. If any changes are processed after the implementation phase, an effective connection is needed for the transmission network [5]. Thus the connection arrangements are formulated using mathematical representations by converting all connections at the same amount. However, if the same amount for different lines is used, then the critical distance of measurement must also be observed in coupling stage periods which is a difficult management process. To manage complexity conditions, both real and reactive measurements are taken for distribution systems using scheduling operation where a greater number of energy resources are introduced [6]. During this scheduling process, the energy in SCADA network and the cost of implementation are reduced, but in case of distribution level measurements, active voltage measurements can only be made which is observed as a major drawback. If SCADA networks are implemented in distribution systems, then it is essential to check reliability of parametric values using Q -terms [7]. If the raised Q factor is lesser, then the security of the entire SCADA network falls below a certain limit and this measurement is processed for every appliance on an hourly basis. Due to hour-basis measurements, the system fails to explore disturbance time in individual appliances; thus, as a result, more than 50 percent of SCADA units are not handled in a perfect way [8–10].

In order to ensure a proper handling mechanism of all appliances, a multiple variation system is established [11] which monitors all curves if power is varied in SCADA network. Moreover, in real time, it is possible to control additional dissimilarities with voltage and current parameters; thus, multiple variations do not occur if SCADA networks are incorporated. The aforementioned changes in each curve can be established only if different appliances are installed without any external limitations. Hereafter, a medium scale distribution system is introduced with SCADA measurement process and this is termed as the hybrid implementation effect on distinct systems [12]. Since two different combinations are made, SCADA measurements provide appropriate outcomes with perfect estimation in state lines. But then again the hybrid measurement increases the switching complexity of the measurement process; thus, only small scale systems are assimilated and tested. To increase the testing phase with large scale system,

four unique methods are followed by using reactive variable phases [13] in all appliances. Due to reactive variables, estimation of voltage scales is processed using pi-type architecture for SCADA networks. On the other hand, implementation cost of pi-type networks is much higher as it requires curved shape data to be represented in the system. As much failure occurs in implementation of the automated process, more steps are taken in the initialization phase using learning algorithms [14]. The type of learning algorithm that is present in automated process must begin with normal characteristics, and high security state must be provided for proper decision making. As a result of using an appropriate decision-making mechanism, values are created and tested in real time by enabling smart metering systems [15]. All executive measures are carried out in implementation of smart metering systems, but assimilation of hardware and software tools is not processed; thus, decision-making systems are much slower than expected.

A comparative study is made with SCADA networks using support vector machine [16–18] for removing all types of uncertainties in the entire data handling process. In this method, also power curves are represented to solve complexities, but as indicated earlier large scale uncertainties cannot be deciphered using individual SCADA measurements. An integration process of cloud security using SCADA is carried out for industrial application where a greater number of remote units are installed in communication path. Since more units are installed, if any SCADA network fails, then other networks will carry out the entire operation with high security features [19]. However, a bigger number of remote units increase the cost of a communication unit inside the infrastructure medium. To reduce the number of remote units, operations are carried out using allocation of renewable energy sources in the path between two SCADA networks [20], and as a result, the IoT-based operation is flexible by reducing the cost of installations. On the other hand, the IoT operation is carried out using low security open source tool, and this type of SCADA operation requires modernization of the entire network. Thus, after careful comparison, SCADA networks are incorporated in the proposed method by incapacitating the disadvantages of the existing techniques, and a distinctive mathematical model is formulate in Section 2.

1.1. Objectives. In the proposed method, multiple SCADA networks are implemented and used for industrial appliances for ensuring proper operation by identifying parametric changes. Therefore, the primary objectives of the projected method are framed as a minimization problem as follows.

- (i) To integrate a learning technique that extends sustenance to SCADA networks in terms of data segments area of installation.
- (ii) To minimize the energy resource constraint of all appliances, therefore overload capacity cases being avoided.
- (iii) To reduce the amount of loss and delay in terms of data transmission using different state vector, thus increasing the security of operation.

2. SCADA for Industrial Applications: An Analytical Model

The process of implementing SCADA is processed by designing a mathematical model that supports the generation process when a system is located in open or closed loop conditions. In addition, the process of SCADA operation is carried out using a solar panel where the battery is stored for a secondary purpose. As the battery is stored in a regular medium, it is necessary to measure all the industrial appliances that are operated without the presence of primary energy source. The above-mentioned operation is designed using

$$PE_i = \sum_{i=1}^n \frac{I_i * d_i}{a_t}, \quad (1)$$

where I_i indicates the disturbance time period, d_i represents downcast time, and a_t describes the total number of operating appliances.

Equation (1) indicates the time period of operation that is separated using all appliances that are present inside industry and in this case total impaired measurements are observed. However, the SCADA system is highly effective only if individual measurements are taken for separate appliances. Thus an individual determination is made using

$$d_a(i) = \sum_{i=1}^n \frac{I_s(i) * f_i}{a_s(i)}, \quad (2)$$

where I_s represents distinct appliance disturbance time, f_i indicates frequency supplied to appliances, and a_s denotes discrete operating appliances.

In (2) it is necessary to minimize disturbance time period by supplying the necessary amount of frequency to all appliances. In case the disturbance period is much higher, then the loss rate is determined using full scale capacity as follows:

$$\text{loss}_i = \min \sum_{i=1}^n (l_a(i) + l_c(i)) * e_i, \quad (3)$$

where l_a, l_c denotes loss of electricity due to absence of squall and presence of full load appliance capacity and e_i represents expected appliance energy loss.

The major objective function in SCADA is to minimize the energy loss that is present in the entire appliance, but this type of minimization is possible only if the critical distance of appliance is within the boundary limits. Thus the limitations are formulated using

$$\text{dist}_i = \min \sum_{i=1}^n CD(t_1 - t_i) + \delta_i, \quad (4)$$

where CD indicates critical distance of appliances, t_1, t_i represents distance between first and end transmission appliance, and δ_i denotes total life period of appliances.

The second minimization objective is framed using critical distance measurement by considering a reference potential point at the beginning of SCADA connections [21–23]. In addition to variations in critical distance

measurements, the schedule period of storage for all appliances provides great advantage in the entire process as storage points can be shifted from one end to the other. This scheduling process is formulated using

$$S_i = \sum_{i=1}^n E_o(i) * E_c(i), \quad (5)$$

where E_o, E_c represent original and unoccupied energy rates.

In case of delayed SCADA measurements at the output unit, unoccupied energy rate increases and it cannot be controlled. Thus the delay in measurements is minimized using

$$\text{dealy}_i = \min \sum_{i=1}^n (w_i * c) + z_i, \quad (6)$$

where w_i indicates the weight of appliance, c denotes the random measurement function, and z_i represents the period of energy supplied to appliances.

If the delay period is reduced, then data measurements phase is monitored where all changes in data pathways are controlled using SCADA data transmission and reception blocks. The data control phase is formulated using

$$DC_i = \min \sum_{i=1}^n \begin{bmatrix} P_1 & \cdots & P_i \\ \vdots & \ddots & \vdots \\ P_i & \cdots & P_n \end{bmatrix} + \begin{bmatrix} V_1 & \cdots & V_i \\ \vdots & \ddots & \vdots \\ V_i & \cdots & V_n \end{bmatrix} + \Delta t_i, \quad (7)$$

where P_1, P_i, P_n describes control data, V_1, V_i, V_n denotes rapidity data, and Δt_i indicates the change in time period intervals.

All the analytical equations that are framed represent the operation of SCADA in closed condition cases where the objective can be represented in terms of analytical equations using

$$\text{obj}_i = \min \sum_{i=1}^n \text{loss}_i, \text{dist}_i, \text{dealy}_i, DC_i. \quad (8)$$

The multiple objective functions in (8) are termed as the minimization function that represents SCADA parametric values to be much lower than values in operational cases. All the formulated equations are derived using a basic set of formulations from SCADA parametric real and reactive power phase [24–27]. Thus in order to increase the accuracy of SCADA measurements in industrial systems, an optimization algorithm is integrated and it is described in the subsequent section.

3. Optimization Algorithm

One of the major problems in the implementation of SCADA system is that security of data must be enhanced as separate commands are implemented for each appliance. Thus it is necessary to drive SCADA system which is termed as a large factor setup using an optimization algorithm. Hence a learning algorithm is chosen for preprocessing all the necessary data where the appliances in industries are protected without any external intrusion attacks [28, 29]. In addition, SCADA system requires the input data to start

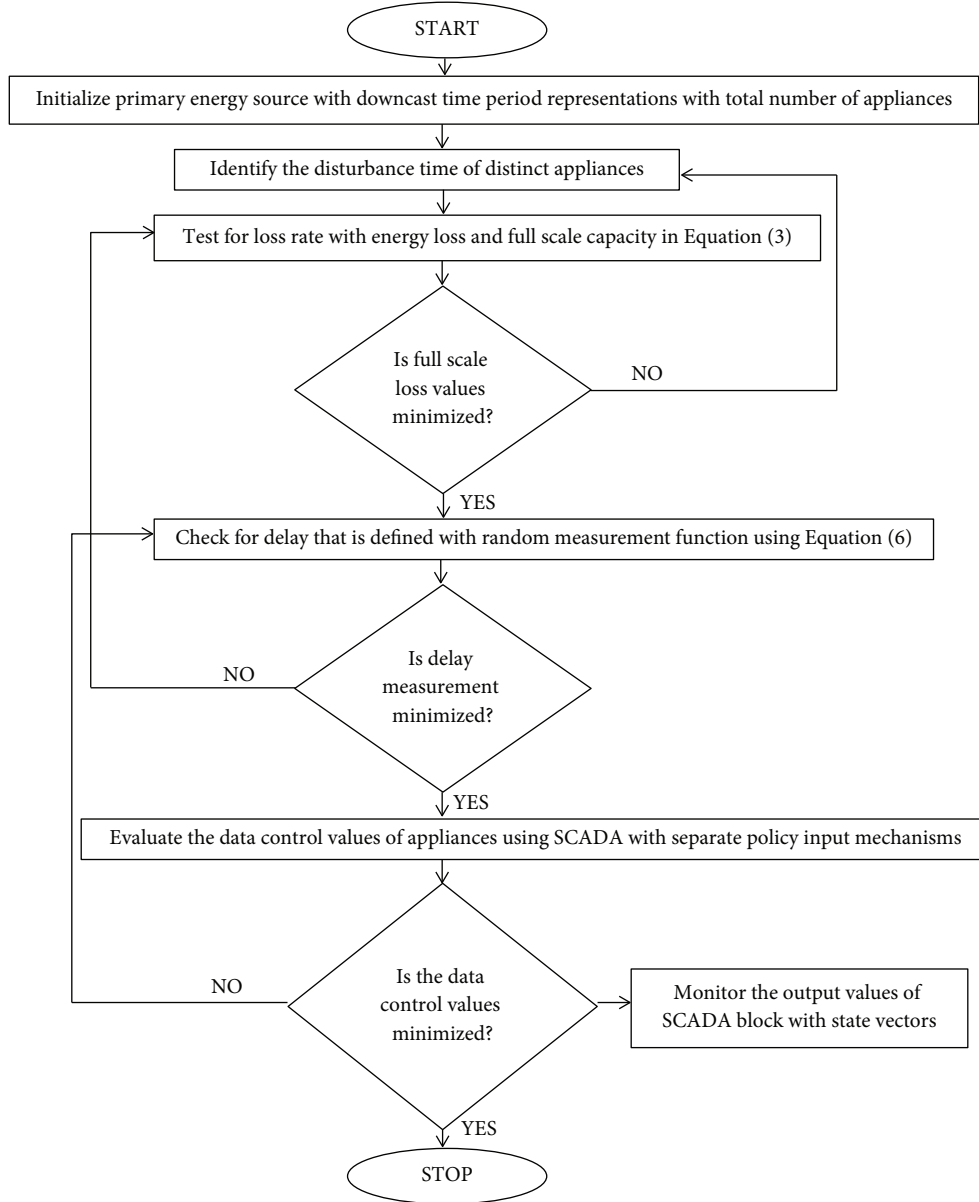


FIGURE 1: Integration flow of the proposed method with learning technique.

from the initial state, thus providing multiple solutions for controlling a particular problem [27, 30, 31]. Since multiple solutions are provided, optimal paths are chosen at the output end for handling distinct alert situations, and one of the major advantages of reinforcement learning algorithm is that all decisions are made in a sequential manner and thus the next state output is determined using previous case problems. Therefore, if reinforcement learning algorithms are applied in real time for SCADA systems, then it is not possible to overcome current problems without solving the existing problem conditions. Even if high complexities are present around SCADA environs, the objective of solving all uncertainties is always assured if behavior learning is processed in the best mode of operation (Figure 1). The optimization process under a particular area is framed using

$$\text{area}_i = \sum_{i=1}^n \alpha_i + (\rho_i * \omega_i), \quad (9)$$

where α_i indicates reduced policy input, ρ_i denotes frequency of SCADA examination, and ω_i describes improvement input policy.

The two procedures that are described in (9) provide great improvement in SCADA feedback process; thus, the entire area is examined using frequency source.

Therefore, the stability of SCADA system in industrial application increases to a certain extent which is measured using

$$\sigma_i = \max \sum_{i=1}^n (q_i(r) - q_i) + w_i, \quad (10)$$

Input: Initialize the primary energy source with disturbance factor and downcast time periods PE_i ($PE \leq i \leq n$), I_i ($I \leq i \leq n$) and state representation values using matrix representation of individual appliances a_i ;
Output: Optimized values for automation of appliances in industrial process using learning model at reduced policy rate and good control rate;
Step 1: At first, the objective function is constructed with the loss factor using $loss_i$;
Step 2: Initialize the frequency of operating appliances with appliance disturbance time that must be followed by certain improvements in policy factor $a_s(i)$ with $0 \leq i \leq 1$, and its individual determination $d_a(i)$ with the indication of full scale capacity values;
Step 3: While ($d_a(i) < N$) do.
 Provide the loss values $loss_i$ in both presence and absence of full scale appliances in a systematic way for computing the total loss in automation process by using equation (3);
 Verify the energy loss values in both previous and current state using distance vector separation $dist_i$ for identifying the critical changes;
 If the critical distance changes are higher, CD_i is not at ($CD_i < N$);
 Modify the transmission appliance values using life period of a particular appliance that is having different energy rates using equations (4) and (5), S_i with $1 \leq i \leq N$ into N number of unoccupied energy states;
 //Delay phase
 Update the delay values $delay_i$ with random measurement function r_i by generating the weight function w_i using supplied energy as shown in equation (6);
 //Data control phase
 Select the control and rapidity scale matrix with changes in time periods Δt_i as defined in equation (7);
 Update the control function state variables using equation (11) with probability values of corresponding state vectors followed by the data segment values and compute the new secured data position σ_i as defined in equation (10);
 The improvements in policy segments in separate areas are updated by using equation (9);
 $area_{new} = area_{old} + 1$;
 End;
Step 4: If ($\sigma_i < 0$) then
 $\sigma_i \leftarrow 0$; //Interchange the existing solution in the current loop with the new solution;
 End if;
Step 5: If ($\sigma_{MAX} [0, 1] < 1$) then
 Reinitialize the appliance values with new segments;
 Obtain the overall best solution;
 End if;
Step 6: If ($I_{max} < N$) //Existing solution is replaced with the new solution
 $\gamma_i = \gamma_{modified}$;
 $I_{min} = N$; //Attain the most feasible solutions for determining the overall best solution;
 Increment the count $area_{new}$ by 1;
 Return the best overall solution;
End;

ALGORITHM 1: Reinforcement Learning Algorithm.

where $q_i(r)$, q_i denotes quality of repeated and nonrepeated data segments in SCADA.

The stability margin defined in (10) must be maximized under the expectation region of separation where the state equation for SCADA using reinforcement learning algorithm for different appliances in industry is described using

$$\gamma_i = \sum_{i=1}^n \begin{bmatrix} \tau_1 & \cdots & \tau_i \\ \vdots & \ddots & \vdots \\ \tau_{i+1} & \cdots & \tau_n \end{bmatrix} * [\partial_1 \dots \partial_i], \quad (11)$$

where $\tau_1 \dots \tau_i \dots \tau_{i+1}$ denotes corresponding state vectors for separate appliances and $\partial_1 \dots \partial_i$ indicates probability of different appliances in industry.

Even though many related networks are installed in supporting industrial applications, SCADA remains a unique network in industrial operation of all appliances. Even for monitoring the usage of high end applications, SCADA network can be modernized in the existing

infrastructure networks [32–34]. Therefore, the major advantage of SCADA industrial appliance is the storage system that is used for detecting all types of problems in connected network. Further, the appliance downtime is much reduced due to proper supply of energy resources which in turn provides a better maintenance period for all operating appliances. In addition, even secondary advantages of SCADA provide appropriate graphical status for all real time environmental verifications.

4. Experimental Verification

The combined model of analytical representations with optimization algorithm is verified using real time experimental cases in order to prove effective automatic operation of several appliances. In this process, the SCADA networks are installed in the industrial appliances with low critical distance which is modified to produce low power drop in the

considered area. Further the full scale capacity of SCADA networks for proposed system is taken as 500 Megawatts supporting the entire appliances in the automated mode of operation. The above-mentioned full scale capacity can also be increased to further extent in case if appliances are added at critical points. But in the proposed method, addition of appliances is avoided as it leads to a raise in instabilities and even a delay in data processing increases. At the initial stage, the process started with random SCADA data error measurement where less than 1 percent of distribution values is provided. However, as appliances are increased, the error rate is varied to nominal phase for about 1.5; thus, the disturbance period is much lesser in case of the proposed method. In addition, the control process in SCADA network provides a valuable pseudo rate using true and measurement values. Moreover, these values are directly integrated in software tool where outcomes are generated using MATLAB at low uncertainty cases. To observe the adeptness of proposed SCADA network in industries, five scenarios are distributed based on analytical design as follows:

- Scenario 1: measurement of primary energy
- Scenario 2: minimization of loss
- Scenario 3: observation of critical distance
- Scenario 4: SCADA data delay
- Scenario 5: data control phase

All the above-mentioned scenarios are simulated and compared with existing models that incorporated different data set. However, the data set used in the proposed method is much similar to the existing cases with a variation of 2 percent with respect to the distribution base. In addition to data base, complete state periods are measured in the system in order to prevent initial delay in control phase of the network. The detailed description of all the aforementioned scenarios is as follows.

4.1. Scenario 1. The amount of primary energy source is a much important measurement to be considered as the appliances operate in a perfect way if the disturbance period is much lesser than the actual operating amount. Also the downcast time period of appliance is considered in this design in order to check the amount of fluctuation during the automated mode of operation. In case fluctuations are much higher than expected, then the frequency of selected appliances will change, thus resulting in low disturbance period. Therefore, a separation is made in the design process by reproducing disturbance, downcast, and frequency values. All these changes are observed in the system for making individual determinations of each appliance, and as a result primary energy sources are established at transmission end. Moreover, the total number of operating appliances is converted to discrete form, thus ensuring less changes in terms of battery operating system. Figure 2 portrays the amount of energy sources for various appliances with disturbance time periods.

From Figure 2, it is observed that the total number of appliances is varied from 10 to 50 and individual disturbance times are measured as 2.33, 2.98, 3.11, 3.36, and 3.42,

respectively. All the disturbance time periods are measured in the average form with respect to changing appliances only. Since more variations are not found with respect to disturbance time, the frequency of appliances is changed in a direct form. Thus the frequency of variations is considered as 60, 89, 103, 116, and 127 kHz, respectively, for a set of appliances that are mentioned earlier. By considering the above-mentioned specifications, energy source determinations are made and it is observed that appliances are operated in automated mode with low primary energy source in the proposed method. This can be proved with 30 different appliances inside the industry where 5.1 watts is allocated for individual operation [11] whereas with same number of appliances the proposed method operates at 50 percent of primary energy source which is equal to 2.05 watts at high effective time periods.

4.2. Scenario 2. In case of the automated operation of appliances, it is necessary that low disturbance period must be assured and if any failure rate occurs in this period, then losses in SCADA network will be determined. Thus this scenario is provided to measure the amount of total loss in the system with full scale operating capacity of appliances. For this type of determinations, two individual values are considered such as summation of original value and full scale capacity which is reproduced using energy loss in the system. Further this reproduction rate must be minimized in such a way that it should be less than 40 percent on an average as compared to appliances that are operated without full scale capacity. If appliances are not operated at full scale capacity, it will directly affect the energy rate of subcomponents, thus leading to manual adjustment in the entire process which in turn should be avoided. Figure 3 illustrates the total loss that is calculated due to high disturbance time periods.

From Figure 3, it is perceived that full load capacity of appliances is varied as 100, 200, 300, 400, and 500, respectively, and even the capacity can be increased to further extent if appliances are added. As the proposed method measures the loss rate for medium scale appliances, the allocated full load capacity is much sufficient for operational cases. During this simulation study, the energy loss of particular appliance is observed to be 2.1, 2.4, 2.8, 3.2, and 3.4 and with this loss the amount of full scale capacity is reproduced. In addition, a comparison plot is provided where the total loss for the proposed method is much lesser and it is lesser than 1, but the existing method provides high variation of loss if appliances are increased. This can be demonstrated with full load capacity of 300 and with energy loss of 2.8 where implementation of SCADA network provides 0.89 as a loss factor. But with the same amount of capacity, the existing method operates at 1.39 loss rate which is much higher in case of individual appliances.

4.3. Scenario 3. The starting and end time periods of SCADA network in all appliances are selected for determining the critical distance points. Additionally, the total life period of individual appliances is used for determining distance measurements with summation cases. Thus when a distance

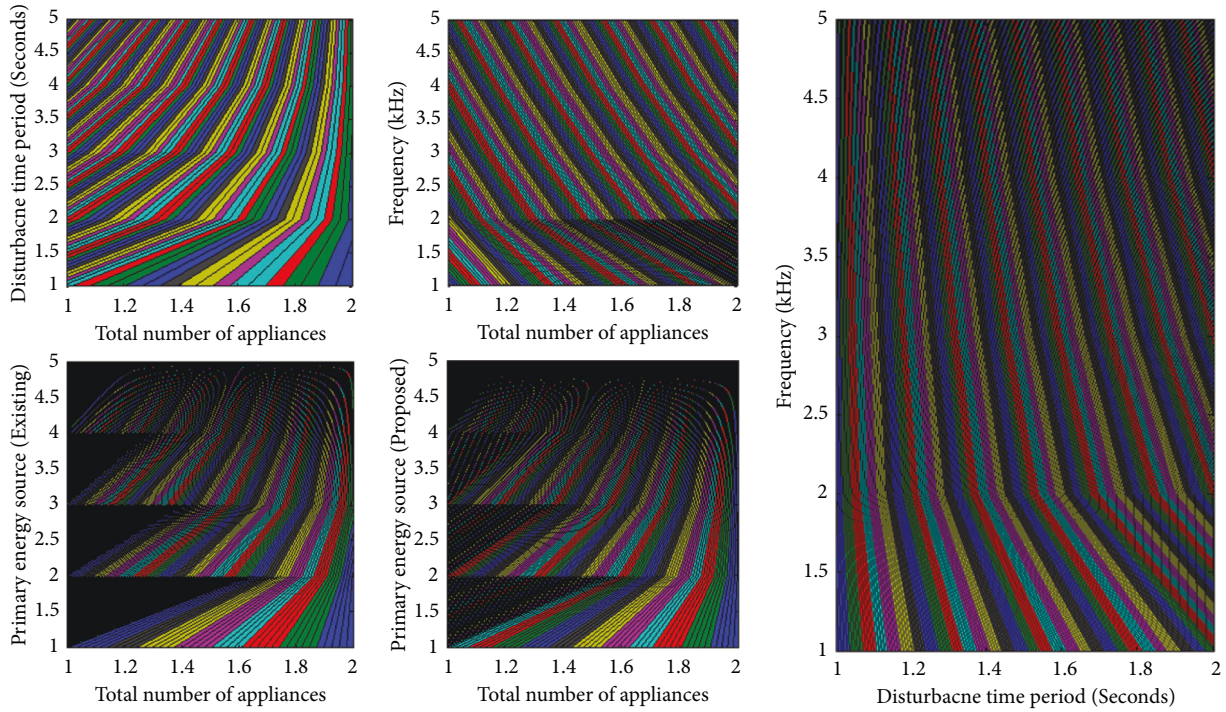


FIGURE 2: Comparison of primary energy source.

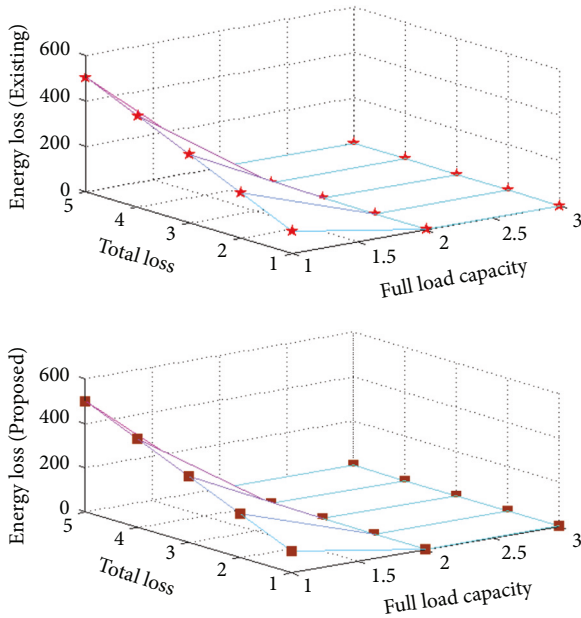


FIGURE 3: Observed energy losses at full load capacity.

point is marked, then the difference between the first point and the end point is termed as critical distance value. This type of determinations is made in such a way that end-to-end appliances are considered without any gap between available industrial space. Since the process is automated using a set of SCADA networks, the critical distance must be minimized as low as possible. In case distance is much larger, then the total life period of appliances will be reduced at great extent. Therefore, to avoid such circumstances, the

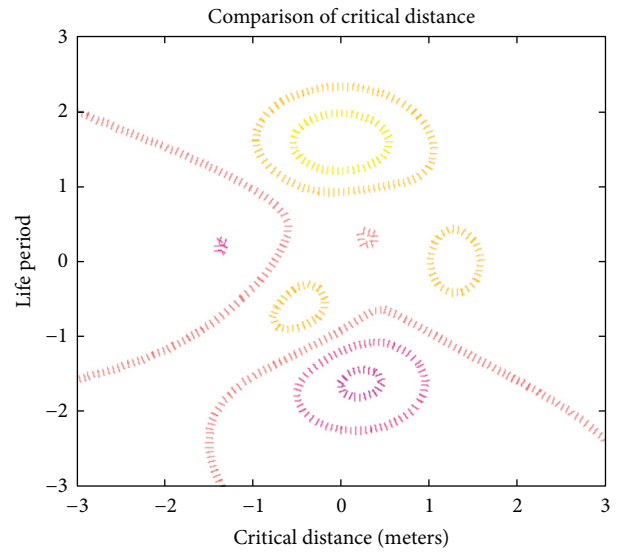


FIGURE 4: Measurement of critical distance.

corresponding distance of appliance and end distance of other appliances which are connected using same communication unit must be minimized. Figure 4 deliberates the simulation plot of critical distance measurements.

From Figure 4, it is pragmatic that difference in terms of critical distance is set as 120, 180, 240, 280, and 360, and this distance is not varied until new appliances are added inside the boundary of SCADA network. The average life time of all appliances inside the industry is gathered from existing data set and it cannot be varied; thus, a total appliance life period is represented in this simulation study. Thus the life period

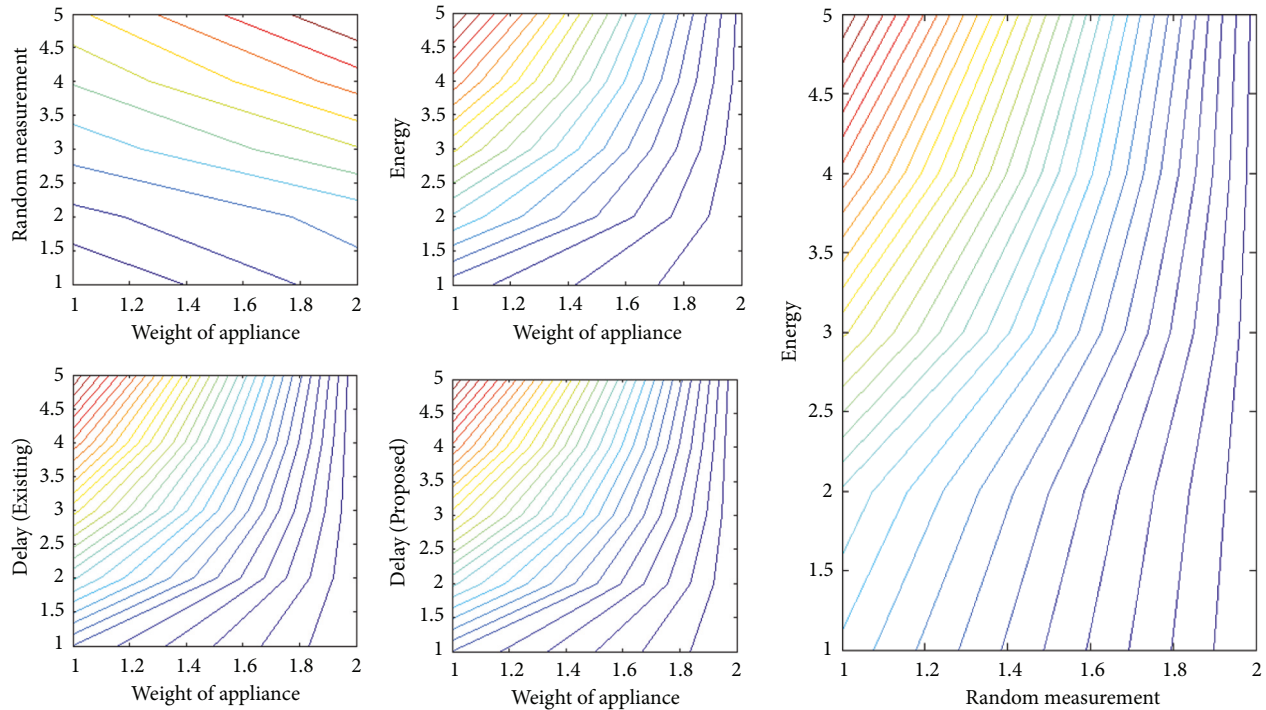


FIGURE 5: Delays in data measurement.

of appliances is set as 1000, 1300, 1600, 1900, and 2100 which exactly matches with critical distance values. By using the above-mentioned specifications, total distance is measured and compared with the existing method that operates under manual distance changing operations. Since the proposed method using SCADA network is operated in automated mode, total distance is minimized for average life time separation. This can be observed with critical distance of 280 meters and life period of 1900 days where the distance of separation in allocation of data is equal to 172 meters, whereas in case of existing method, it is maximized to 502 meters.

4.4. Scenario 4. The SCADA network is incorporated in the industrial system by combining multiple appliances; thus, there is a need to integrate all the data that is present in the entire network. Hence, the delay in processing data must be minimized by considering random measurement function. Moreover, the delay is calculated using weight functions of all appliances that are directly reproduced with measurement values. Further, the data delay phase that is reproduced in the system is summed with total energy supply where it is completely occupied in the SCADA network. However, the unoccupied energy rate is not increased in proposed method as it leads to more delay in entire process. For the input data set, the implemented SCADA network must maintain 0.54 second of delay and this limitation factor cannot be changed even during processing stage. Therefore, all individual appliances that are connected within the industry must reach the control center at correct time periods. Figure 5 provides simulation plot of delay functions with variation in energy rates.

From Figure 5, it is detected that the weight of appliance is varied from 10 to 50 kilograms where random measurements are provided as 25, 30, 45, 60, and 75, respectively. For each variation, the total energy of appliance is taken and a new ingenuity energy loss is considered in a direct way. This type of consideration is usually processed in special case if appliances are operated in an automatic way. Moreover, the weight of total appliances is much higher; thus energy loss can be used in direct cases as 2.1, 2.4, 2.8, 3.2, and 3.4 respectively. By using random measurements, comparisons are made for the delay period calculation where it is much reduced in case of the proposed method as compared to the existing cases. This can be verified in real time by considering 40 kilograms of appliances in an industry where the delay periods are kept within defined limits of 0.4. But in the existing method, the delay period is maximized above limitations and at last phase exact boundary limit is achieved.

4.5. Scenario 5. One of the important processing units is SCADA network data processing that is made using parametric matrix type. Hence in the proposed method, control data are determined from transmission to end user appliances, thus making necessary modifications in the entire data. In addition to control data, another type of measurement matrix is provided which is termed as rapidity data matrix that is used for selecting appropriate rate. Further, these two matrixes are separated from pathways and finally it is summed up and used for initial cases. Once the pathways are separated, then change in time intervals is measured using delta matrix values. Thus total data phase variation in individual appliances is provided and marked as separate cases for large scale automation using SCADA networks. If

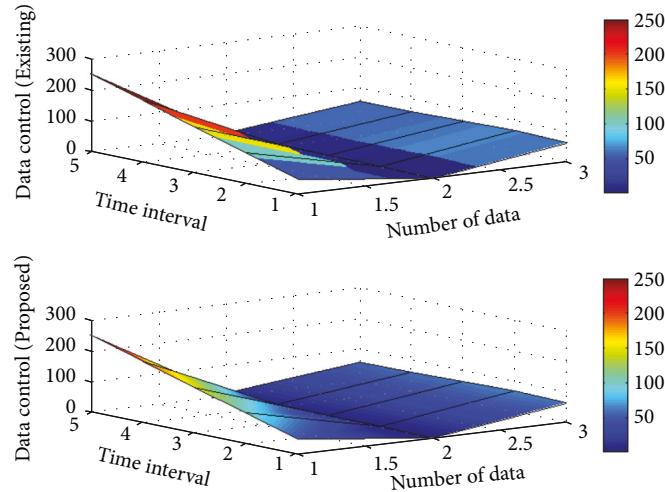


FIGURE 6: Observation of data control phase.

any changes are observed in certain interval for data measurements, then it must be minimized at appropriate phases. Figure 6 illustrates the minimization plot of SCADA data control phase.

From Figure 6 it is observed that the total number of SCADA data is varied in step size of 50 with two second time interval periods. During this data dissimilarity, the entire data that are transferred to control unit must be minimized and it is guaranteed in case of the proposed method as compared to the existing method. For verification, if the number of data is equal to 150 with six second break periods, then the percentage of data control that is achieved in case of SCADA network with the proposed method is 87 percent whereas the existing method controls and secures the central data around 63 percent. Furthermore, complete data control is attained only in case of the proposed method up to 92 percent, but the controlling factor of SCADA network with the existing system without any learning model decreases to 57 percent. Since the data phase is reduced, the proposed method can be applied in real time to all automated industries with high security features.

4.6. Robustness of SCADA. The robustness of SCADA determines the tractability solutions when it is incorporated in any type of medium. Usually SCADA networks operate at different time periods, thus creating multiple delays in a communication channel. However, in case of multiple delays, both data and security of industrial appliances are highly sensitive; thus, network operation must be highly robust against distinct type of scalable parameters. In other terms, robustness is measured using primary energy source where operation of all appliances is started. During this energy source operation, the distance between two different SCADA networks causes low robustness as much better hardware setup is installed. Figure 7 portrays robustness characteristics of SCADA network with changing iteration values.

From Figure 7, it is observed that the best epoch is chosen between 10 and 100 as 20, 40, 60, 80, 100,

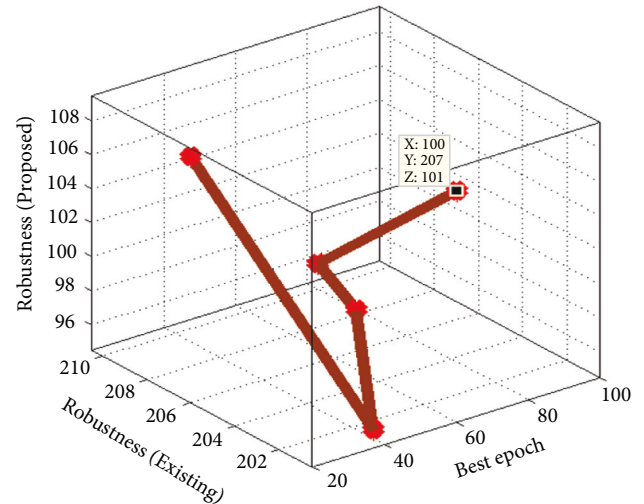


FIGURE 7: Comparison of robustness with the best epoch.

respectively, where for all best iteration values robustness is calculated. In the proposed method, robustness characteristics are simulated by accumulation of primary energy sources and critical distance in SCADA networks; thus high values are achieved. Moreover, in the comparison case study, the proposed method using learning technique performs much better as compared to the existing method [11]. This can be substantiated with the best epoch as 80, and during this period, the robustness of existing model in absence of the learning-based technique is 210 whereas the projected method provides low robustness of 96 due to much reduced primary sources.

5. Conclusions

The process of implementing SCADA networks for processing automated operations in large scale appliances using learning technique is illustrated. Whenever appliances are

introduced in a particular system, then it is necessary to perform automatic operations as some of the parametric values change with immediate effect. In addition, the weight of a particular appliance must be managed in entire industry as all appliances are combined and operated using a common control network (SCADA). Also the resources that are shared by supervisory blocks must be fulfilled to all appliances in small, medium, and large scaling factors. Thus a primary energy source is determined in the proposed method where all the appliances are trained and learned to operate in innocuous mode. Since primary energy sources are measured at initial state, all the appliances are protected by changing the down time of the appliance using frequency shift factors. Therefore, as a result, the difference in loss periods is much reduced where all appliances in industries are operated at low energy rate. This type of minimization process is framed using an analytical representation that turns out as an action point for automatic operational conditions. Moreover, several constraints provided for appliance operation are much reduced and thus high flexibility is provided in projected SCADA network implementation process. In case of data handling process, high security is provided by SCADA network where data of all appliances are transferred only to control center. The analytical model is framed in such a way for integrating multiple objectives such as minimization of delay, critical distance, and energy loss where all the objectives are tested by combining SCADA hardware setup with realization software tool. Furthermore, experimental verifications are carried out by examining five scenarios, and in the comparison study it is comprehended that SCADA network with learning models provides high effectiveness for about 84 percent. In future, the proposed model on SCADA network can be extended for industrial applications using artificial intelligence and machine learning techniques as the cost of installation will be reduced in a suitable way.

Data Availability

The data that support the findings of this study are available from the corresponding author, upon reasonable request.

Conflicts of Interest

The authors declare that they have no conflicts of interest.

Acknowledgments

This project was funded by the Deanship of Scientific Research (DR) at King Abdulaziz University (KAU), Jeddah, Saudi Arabia, under grant no. RG-4-611-43. The authors, therefore, acknowledge with thanks DSR for technical and financial support.

References

- [1] D. Upadhyay, M. Zaman, R. Joshi, and S. Sampalli, "An efficient key management and multi-layered security framework for SCADA systems," *IEEE Transactions on Network and Service Management*, vol. 19, no. 1, pp. 642–660, 2022.
- [2] A. A. Suvorov, A. A. Zaki Diab, A. S. Gusev et al., "Comprehensive validation of transient stability calculations in electric power systems and hardware-software tool for its implementation," *IEEE Access*, vol. 8, pp. 136071–136091, 2020.
- [3] Y. Cherdantseva, P. Burnap, A. Blyth et al., "A review of cyber security risk assessment methods for SCADA systems," *Computers & Security*, vol. 56, pp. 1–27, 2016.
- [4] A. O. Khadidos, H. Manoharan, S. Selvarajan et al., "A class multifacet clustering and fused optimization based classification methodologies for SCADA security," *Energies*, vol. 15, 2022.
- [5] S. Shitharth, K. M. Prasad, K. Sangeetha, P. R. Kshirsagar, T. S. Babu, and H. H. Alhelou, "An enriched RPCO-BCNN mechanisms for attack detection and classification in SCADA systems," *IEEE Access*, vol. 9, pp. 156297–156312, 2021.
- [6] S. Shitharth, N. Satheesh, B. Praveen Kumar, and K. Sangeetha, "IDS detection based on optimization based on WI-CS and GNN algorithm in SCADA network, architectural wireless networks solutions and security issues," *Lecture Notes in Network and Systems*, vol. 196, no. 1, pp. 247–266, 2021.
- [7] S. Shitharth, K. Sangeetha, and G. B. Mohammed, "Enhanced SCADA IDS security by using MSOM hybrid unsupervised algorithm," *International Journal of Web-Based Learning and Teaching Technologies*, vol. 17, no. 2, 2022.
- [8] Z. Lv, S. Lv, H. Feng, and H. Lv, "Clinical characteristics and analysis of risk factors for disease progression of COVID-19: a retrospective cohort study," *International Journal of Biological Sciences*, vol. 17, pp. 1–7, 2021.
- [9] X. Liu, J. Zhao, J. Li, B. Cao, and Z. Lv, "Federated neural architecture search for medical data security," *IEEE Transactions on Industrial Informatics*, vol. 18, no. 8, pp. 5628–5636, 2022.
- [10] B. Cao, J. Zhang, X. Liu et al., "Edge-cloud resource scheduling in space-air-ground integrated networks for internet of vehicles," *IEEE Internet of Things Journal*, vol. 9, no. 8, pp. 5765–5772, 2022.
- [11] D. Astolfi, "Perspectives on scada data analysis methods for multivariate wind turbine power curve modeling," *Machines*, vol. 9, no. 5, p. 100, 2021.
- [12] X. Kong, Y. Chen, T. Xu et al., "A hybrid state estimator based on SCADA and PMU measurements for medium voltage distribution system," *Applied Sciences*, vol. 8, no. 9, p. 1527, 2018.
- [13] H. Kong, M. Lu, L. Que, F. Xu, J. Zhao, and A. Xue, "A new four-step method to identify the parameters of transmission line based on SCADA data," *IET Generation, Transmission & Distribution*, vol. 16, no. 9, pp. 1822–1835, 2022.
- [14] S. Shitharth, M. Shaik, and S. Sirajudeen, "Mining of intrusion attack in SCADA network using clustering and genetically seeded flora based optimal classification algorithm," *Information Security IET*, vol. 14, no. Issue 1, pp. 1–11, 2019.
- [15] J. Temido, J. Sousa, and R. Malheiro, "SCADA and smart metering systems in water companies. A perspective based on the value creation analysis," *Procedia Engineering*, vol. 70, pp. 1629–1638, 2014.
- [16] R. Pandit and A. Kolios, "SCADA data-based support vector machine wind turbine power curve uncertainty estimation and its comparative studies," *Applied Sciences*, vol. 10, no. 23, pp. 8685–8718, 2020.
- [17] M. B. Mollah and S. S. Islam, "Towards IEEE 802.22 based SCADA system for future distributed system," in *Proceedings of the 2012 International Conference on Informatics, Electronics and Vision, ICIEV*, Dhaka, Bangladesh, May, 2012.

- [18] S. Shitharth, Sangeetha, and P. Kumar, "Integrated probability relevancy classification (IPRC) for IDS in SCADA', design framework for wireless network," *Lecture Notes in Network and Systems*, vol. 82, no. 1, pp. 41–64, 2019.
- [19] F. A. Osman, M. Y. M. Hashem, and M. A. R. Eltokhy, "Secured cloud SCADA system implementation for industrial applications," *Multimedia Tools and Applications*, vol. 81, no. 7, pp. 9989–10005, 2022.
- [20] M. O. Qays, M. M. Ahmed, M. A. Parvez Mahmud et al., "Monitoring of renewable energy systems by IoT-aided SCADA system," *Energy Science & Engineering*, vol. 10, no. 6, pp. 1874–1885, 2022.
- [21] H. Cheng, M. Shojafar, M. Alazab, R. Tafazolli, and Y. Liu, "PPVF: privacy-preserving protocol for vehicle feedback in cloud-assisted VANET," *IEEE Transactions on Intelligent Transportation Systems*, vol. 23, no. 7, pp. 9391–9403, 2022.
- [22] J. Chen, Y. Liu, Y. Xiang, and K. Sood, "RPPTD: robust privacy-preserving truth discovery scheme," *IEEE Systems Journal*, vol. 16, no. 3, pp. 4525–4531, 2022.
- [23] F. Liu, G. Zhang, and J. Lu, "Multi-source heterogeneous unsupervised domain adaptation via fuzzy-relation neural networks," *IEEE Transactions on Fuzzy Systems*, vol. 29, no. 11, pp. 3308–3322, 2021.
- [24] D. Li, S. S. Ge, and T. H. Lee, "Fixed-time-synchronized consensus control of multiagent systems," *IEEE Transactions on Control of Network Systems*, vol. 8, no. 1, pp. 89–98, 2021.
- [25] X. Wu, W. Zheng, X. Chen, Y. Zhao, T. Yu, and D. Mu, "Improving high-impact bug report prediction with combination of interactive machine learning and active learning," *Information and Software Technology*, vol. 133, Article ID 106530, 2021.
- [26] M. Zhang, Y. Chen, and W. Susilo, "PPO-CPQ: a privacy-preserving optimization of clinical pathway query for E-healthcare systems," *IEEE Internet of Things Journal*, vol. 7, no. 10, pp. 10660–10672, 2020.
- [27] J. Yan, H. Jiao, W. Pu, C. Shi, J. Dai, and H. Liu, "Radar sensor network resource allocation for fused target tracking: a brief review," *Information Fusion*, vol. 86, pp. 104–115, 2022.
- [28] D. Shitharth and D. Prince Winston, "An enhanced optimization algorithm for intrusion detection in SCADA network," *Journal of Computer Security*, vol. 70, pp. 16–26, 2017.
- [29] D. Shitharth and D. Prince Winston, "A new probabilistic relevancy classification (PRC) based intrusion detection system (IDS) for SCADA network," *Journal of Electrical Engineering*, vol. 16, no. 3, pp. 278–288, 2016.
- [30] W. Zheng and L. Yin, "Characterization inference based on joint-optimization of multi-layer semantics and deep fusion matching network," *PeerJ Computer Science*, vol. 8, p. e908, 2022.
- [31] J. Yu, L. Lu, Y. Chen, Y. Zhu, and L. Kong, "An indirect eavesdropping attack of keystrokes on touch screen through acoustic sensing," *IEEE Transactions on Mobile Computing*, vol. 20, no. 2, pp. 337–351, 2021.
- [32] K. Cao, B. Wang, H. Ding et al., "Improving physical layer security of uplink NOMA via energy harvesting jammers," *IEEE Transactions on Information Forensics and Security*, vol. 16, pp. 786–799, 2021.
- [33] Z. Lv, J. Guo, and H. Lv, "Safety poka yoke in zero-defect manufacturing based on digital twins," *IEEE Transactions on Industrial Informatics*, vol. 1, 2022.
- [34] Z. Lv, L. Qiao, and I. You, "6G-Enabled network in box for internet of connected vehicles," *IEEE Transactions on Intelligent Transportation Systems*, vol. 22, pp. 5275–5282, 2021.

Research Article

Diagnosis of Broken Bars in V/F Control Induction Motor Drive Using Wavelets and EEV Estimation for Electric Vehicle Applications

Senthil Kumar Ramu ¹, Gerald Christopher Raj Irudayaraj,² Gunapriya Devarajan ³, V. Indragandhi,⁴ V. Subramaniaswamy ⁵ and J. Sam Alaric ⁶

¹Department of Electrical and Electronics Engineering, Sri Krishna College of Technology, Coimbatore 641042, India

²Department of Electrical and Electronics Engineering, PSNA College of Engineering and Technology, Dindigul 624622, India

³Department of Electrical and Electronics Engineering, Sri Eshwar College of Engineering, Coimbatore 641202, India

⁴School of Electrical Engineering, Vellore Institute of Technology, Vellore 632014, India

⁵School of Computing, SASTRA Deemed University, Thanjavur 613401, India

⁶Department of Electrical and Computer Engineering, Wollega University, Nekemte, Ethiopia

Correspondence should be addressed to J. Sam Alaric; samalaric@gmail.com

Received 23 July 2022; Accepted 16 August 2022; Published 5 September 2022

Academic Editor: Ravi Samikannu

Copyright © 2022 Senthil Kumar Ramu et al. This is an open access article distributed under the Creative Commons Attribution License, which permits unrestricted use, distribution, and reproduction in any medium, provided the original work is properly cited.

The induction motor (IM) defect diagnosis has been an important field of research in recent years. The development in control circuits for IM has piqued the interest of industrialists and researchers. This paper presents a method for detecting and quantifying broken rotor bar (BRB) faults via wavelets and energy Eigen value (EEV) estimation in voltage/frequency control-fed IM. The fast Fourier transform (FFT) extracts the signal's amplitude and frequency components, while the discrete wavelet transform (DWT) decomposes it. In this paper, the energy estimation for each level of breakdown and the method to overcome the diagnose faults are explained. The EEV of the motor current of the signal determines the fault's severity and provides a better method for identifying the faults. The usage of a single current sensor is a gain of this technology. With a fluctuating load, we can identify the issue and the number of broken bars via online. After processing of DWT, the faulty BRB's stator current signal is suppressed to 91% in amplitude when compared to existing techniques. Simulation and experimental results have proved that the proposed method's stability, durability, and resilience.

1. Introduction

The greatest approach would be to replace traditional internal combustion engine (ICE) automobiles with electric vehicles (EVs), which emit fewer pollution than current ICE vehicles. This is the same as reducing transportation-related air pollution to zero. The electric motor is a key component of an EV's electric powertrain (which includes the drivetrain and the motor). According to comparative research, IM is more suited for use as a traction motor in electric vehicles [1, 2]. In addition, IMs are susceptible to a variety of failures [3, 4]. The BRB defect is one of them [5]. Overloading

working conditions, mechanical cracks, and manufacturing problems can all contribute to it [6]. A broken bar causes a significant rise in currents and pressures in neighboring rotor bars, potentially leading to more damage and even stator problems [3, 7]. As a result, detecting the broken bar fault at an early stage is important. The IM is designed to be a fault-tolerant computer and a more enjoyable solution for EV applications in today's reality.

BRB defects are instigated through a mixture of several loads which are imposed on the rotor by thermal, environmental, electromagnetic, mechanical, and dynamic variables. The BRBs cause speed and torque oscillations, as

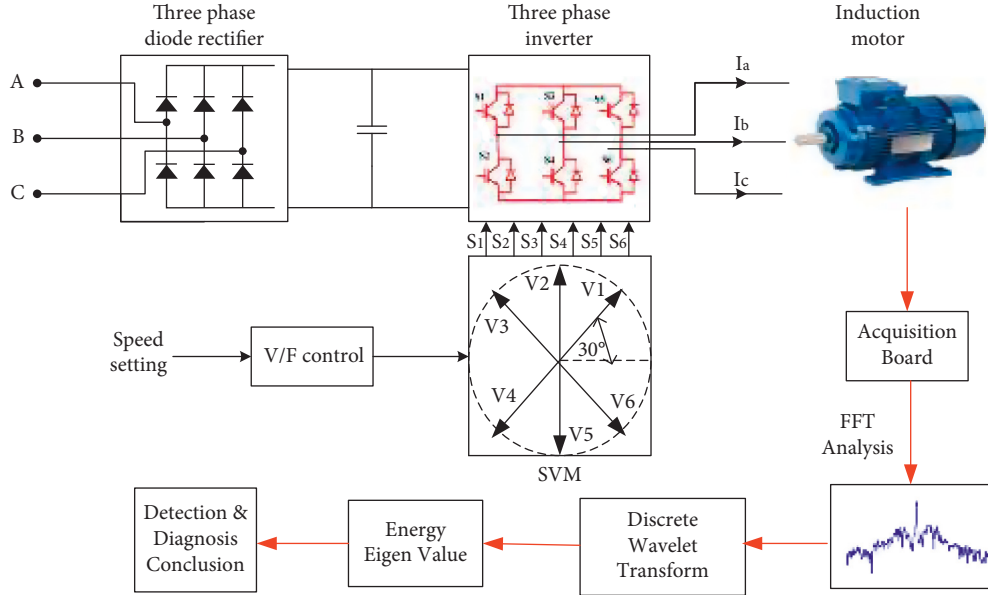


FIGURE 1: Block diagram of DWT and energy EEV estimation-based fault diagnosis.

well as bearing degradation that is incomplete. It can also cause rotor shaft vibrations, bearing problems, and air gap eccentricity. Also, a mixture of stress operating on the rotor causes rotor deficiency. It causes more deviations, which reduces magnitude of torque. As a result, mechanical faults and larger variations occur, which lead to disastrous consequences for the machine. BRB faults do not cause the machine to halt. It can cause extreme mechanical stress to insulation, as well as winding failure, which can result in costly repairs and production losses. With the invention of solid-state inverters, the constant V/F control became widespread [8, 9], and this type of variable speed drive is used by the huge majority of variable speed drives in use today [10]. To gain the best results, IM should function with rated stator flux. This can be accomplished by keeping the voltage constant. To gain the best results, IM should function with rated stator flux [11].

Motor current signature analysis (MCSA) is most often method for fault diagnosis of IM [12, 13]. It is indeed a noninvasive, easy, and effective approach under specific loads. As a consequence, it is in commonplace in industrial settings [14]. Instantaneous power, magnetic flux, torque, and vibrational signals are some of the other indicators used to diagnose rotor problems [15, 16]. In addition, methodologies for distinguishing between broken bar defects and moment loads have engaged a considerable number of scholars in recent years [17, 18]. The intricacy of the system that has to be diagnosed is also a factor. In the diagnostic sector, there are two types of procedures: analytical model-based diagnostic techniques and non-analytical model-based diagnostic methods [19]. The references cover a wide range of failure scenarios as well as the methods for detecting them. According to our investigation and extensive literature evaluation, signal processing is among the most important methodologies used in fault diagnosis.

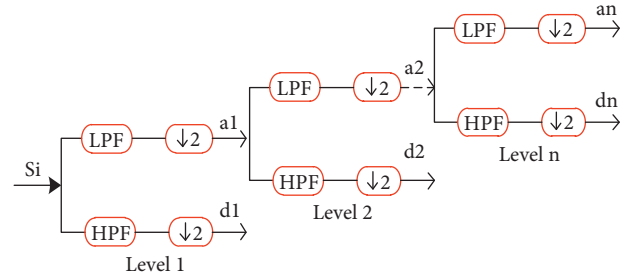


FIGURE 2: Decomposition using DWT.

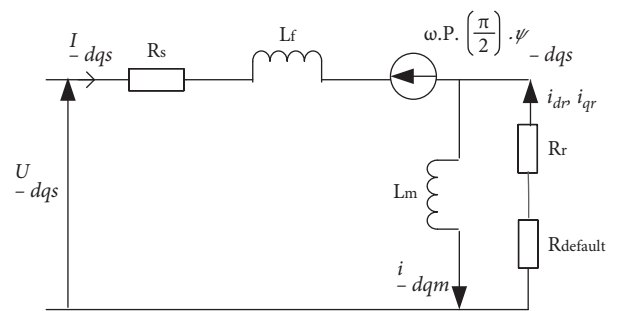


FIGURE 3: Equivalent circuit diagram for BRB fault IM.

The signal processing approach may be separated into two halves, the first of which uses traditional techniques such as FFT [20] and Hilbert analysis [21], and the second of which uses novel techniques such as windowed Fourier transforms and wavelet analysis [22]. Frequency examination of quantifiable variables is currently the important method utilized approach for defect analysis. One of the most significant of these approaches is the FFT. The primary drawback of this technology is that it can only be employed

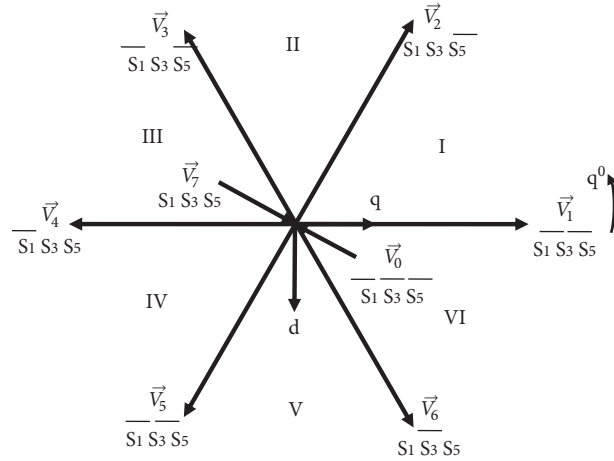


FIGURE 4: Space vector representation of VSI.

TABLE 1: Switching states and space vector representation of VSI.

Type	Switching state	On-state switch	PWM inverter voltage			Space vector
			V_{AN}	V_{BN}	V_{CN}	
Active states	[1 6 2]	S_1, S_6, S_2	V_d	0	0	$\vec{V}_1 = (2/3)V_d e^{j0}$
	[1 3 2]	S_1, S_3, S_2	V_d	V_d	0	$\vec{V}_2 = (2/3)V_d e^{j\pi/3}$
	[4 3 2]	S_4, S_3, S_2	0	V_d	0	$\vec{V}_3 = (2/3)V_d e^{j2\pi/3}$
	[4 3 5]	S_4, S_3, S_5	0	V_d	V_d	$\vec{V}_4 = (2/3)V_d e^{j3\pi/3}$
	[4 6 5]	S_4, S_6, S_5	0	0	V_d	$\vec{V}_5 = (2/3)V_d e^{j4\pi/3}$
	[1 6 5]	S_1, S_6, S_5	V_d	0	V_d	$\vec{V}_6 = (2/3)V_d e^{j5\pi/3}$
Zero states	[1 3 5]	S_1, S_3, S_5	0	0	0	$\vec{V}_7 = 0$
	[4 6 2]	S_4, S_6, S_2	0	0	0	$\vec{V}_0 = 0$

in a stationary state. As a result, a different approach to resolving this issue is required. Wavelet transformations can be divided into two types: continuous and discrete wavelets. Mallet et al. was the first to use multi-resolution wavelet analysis to a problem [23]. Talhaoui et al. [24] performed a similar technique for the identification of rotor problems in the IM. Other papers have utilized the DWT method to discover a number of issues, such as unbalanced eccentricity as well as stator turn short circuits [25, 26].

The importance of automated damage detection is growing for a variety of reasons, the much more notable of which being the human factor's inadequacy, as well as environmental pressures. The major goals of this work are to diagnose a BRB defect and to assess the severity of the issue while the IM is in closed loop drive with constant speed. The V/F control approach is used to attain a constant decoupled control [27, 28]. The speed regulator output signal and stator phase current will be subjected to DWT investigation as a defect identification technique. This approach was used in order to provide a good diagnosis despite the constant speed variations. The energy stored for each stage of dynamic energy may be utilized to assess the intensity of the fault and differentiate among defect and regular fluctuation.

For all frequencies and loading circumstances, DWT is appropriate for a variable size window. Low-frequency

approximation signals were employed to identify BRB defects with short duration time. As a result, fast defect identification is feasible, allowing the equipment to be protected and controlled before it becomes dangerous. Figure 1 shows a block diagram of DWT and energy Eigen value-based BRB fault diagnostics.

To solve many shortcomings with earlier approaches, a solution based on EEV and wavelet packets is proposed in this paper. The key benefit of this system is that it only requires one current sensor. The proposed technique can identify a fault of broken bars with a variable load in real time, because it can determine the number of broken bars irrespective of the motor's operational mode. The most successful method for identifying abnormalities in steady-state, start, and nonstationary signals is to use this method.

In [5], Authors suggest a method for detecting BRB faults under field-oriented control using discrete wavelet coefficients. A reduced dynamic model and stator current spectrum-based fault diagnosis of IM is proposed in [29]. Fuzzy logic controller was presented for examining the performance of drive during BRB failures [30]. This technique reduces sensitivity to electrical parameter fluctuation at each reference point during variable loads. The isolation of BRB faults under low-frequency load fluctuation using Q axis voltage and current component spectrum was proposed in

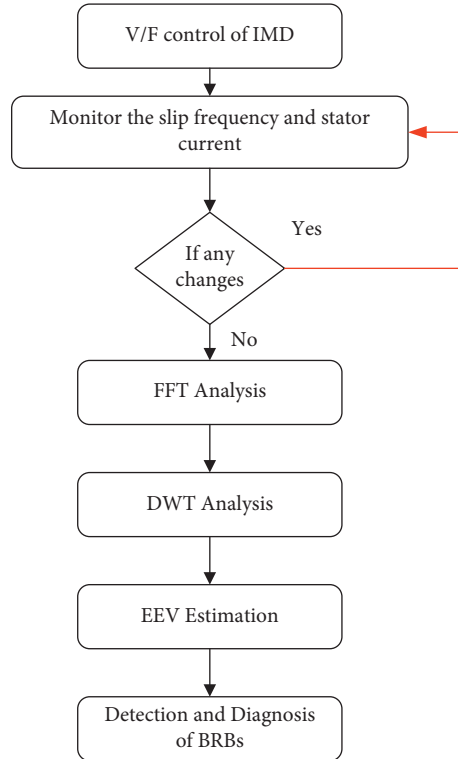


FIGURE 5: Fault diagnosis process.

TABLE 2: Induction motor parameters.

Symbol	Parameter	Values
P_0	Power output	1.1 KW
V_s	Supply voltage	440 V
R_s	Stator resistance	7.86 Ω
R_r	Rotor resistance	6.22 Ω
L_m	Mutual inductance	0.63 H
K_p	Gain constant	60
T_i	Integral constant	180
T_l	Load torque	10 Nm
n_b	Rotor bars	28

[31]. The load torque instability problem offers solutions to BRB failures with the assistance of FFTs. The main objective of this work is to diagnosis the BRB defects using DWT and EEV estimation. In this paper, both FFT and DWT are proposed for the identification of V/F-fed IMD. Then, the fault severity is calculated using EEV computation. This work aids in determining the machine's healthy and malfunctioning states and is also utilized to measure the drives' dynamic response.

The paper is organized as follows: the various signal processing techniques are discussed in Section 2. Section 3 describes the modelling of a BRB failure motor. The dynamic analysis of V/F based IMD is covered in Section 4. Section 5 looked at DWT-based BRB fault diagnosis. The findings and discussion for fault analysis are shown in Section 6, and Section 6 discusses the study's proper conclusions.

2. Signal Processing Techniques Used for Diagnosis

There are two types of defect diagnostic approaches without the use of models. The first is based on signal processing from sensors that measure various electrical and mechanical properties. Another method involves the use of different Artificial Intelligence (AI) algorithms to construct well-developed systems. In industry, signal processing and spectral analysis methods are commonly used to monitor all rotating machineries. In the current situation, employees are maintaining the stability through examining a range of signals of system in order to diagnose problems or deviations. On the other hand, the physical evolution and spectrum of such signals, give enough information for professionals to identify problems and which affects the machine's appropriate operation. The diagnosis by this method needs a proper understanding of the defect and their signs. Hence, the signal processing algorithms are favoured for diagnosing BRB defects.

2.1. FFT. The FFT algorithm is created using DFT. FFT converts a real-time signal to a frequency signal and can also be used to recover high frequency components. Therefore, the estimated magnitude and frequency can be calculated by applying the following equation after collecting a signal through FFT [32].

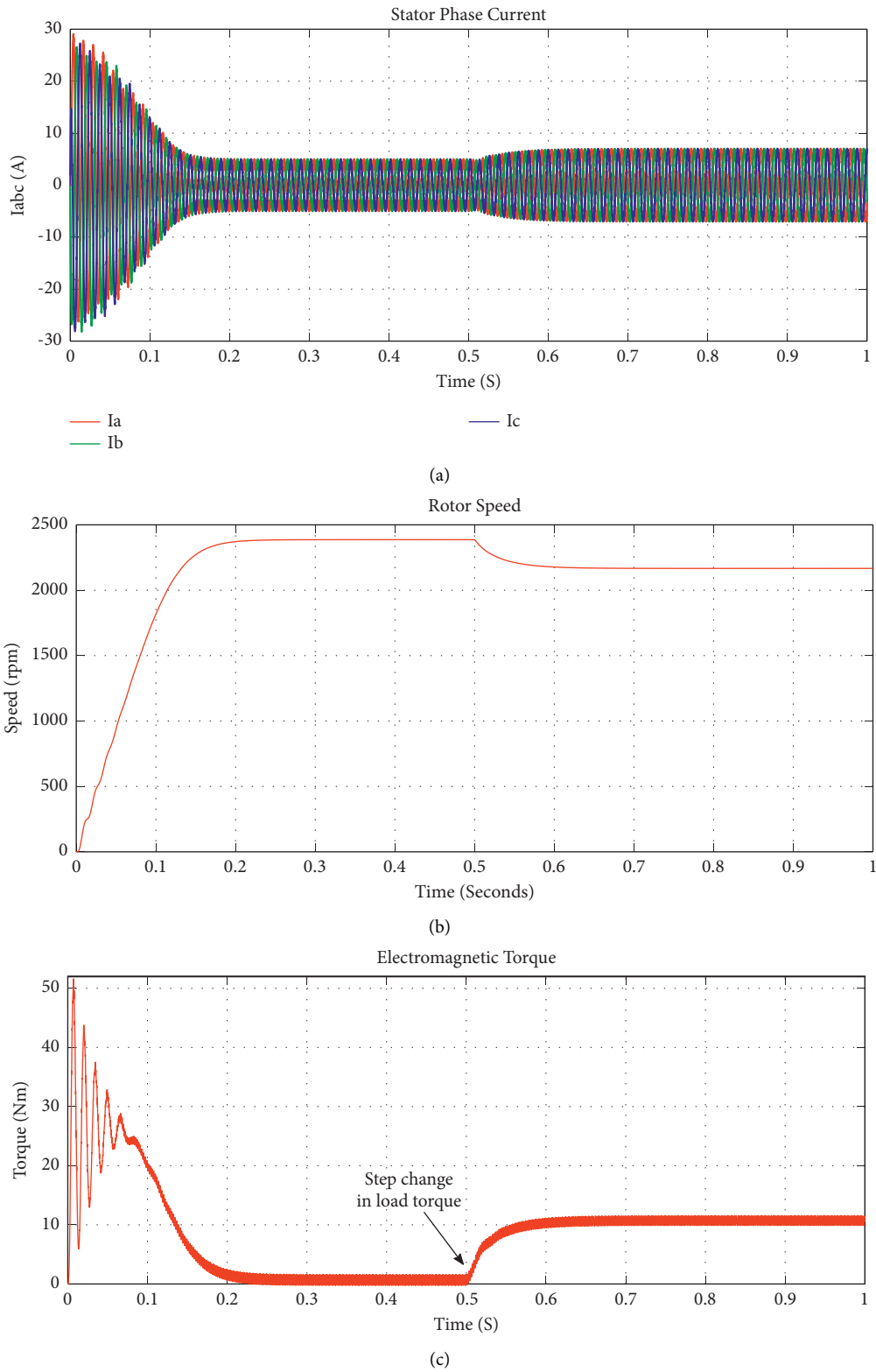


FIGURE 6: Simulation response of V/F control of IM at healthy state. (a) Motor current. (b) Speed. (c) Torque.

TABLE 3: Performance of open loop V/F control of IM under dynamic state: stator current, rotor speed when step change in load torque.

Time-domain parameters	V/F control					
	Fixed load			Full load		
	t_r (ms)	t_s (ms)	M_p (%)	t_r (ms)	t_s (ms)	M_p (%)
Stator current	73	1031	551	77	1030	541
Rotor speed	1727	1031	75	1030	1030	101.5

$$\text{Magnitude spectrum} = \frac{\sqrt{|X|^2 + |Y|^2}}{N}, \quad (1)$$

$$\text{Phase spectrum} = \arctan\left(\frac{|Y|}{|X|}\right).$$

To determine the fault defect, the frequency amounts are eliminated together with amplitude. The amplitude as well as sideband frequency are altered depending on the fault under variable load conditions. The current signal from the machine is extracted and subjected to FFT analysis. Simultaneously, IM runs in a steady-state condition. The frequency components of the current signal are obtained using FFT. It is also used to determine the short circuit between the IM stator windings.

2.2. *DWT*. The DWT is similar to a filter bench and it is used to handle the sampling signals. Figure 2 depicts the DWT decomposition process [11].

The following formulae can be used to compute the level 1 indices:

$$\begin{aligned} a_1 &= \sum_k^l L(k-2l)S_i(k), \\ d_1 &= \sum_k^l H(k-2l)S_i(k). \end{aligned} \quad (2)$$

A next deconstruction stage is created using the a_1 indices. The updated factor can be written as follows:

$$\left\{ a_2 = \sum_k^l L(k-2l)a_1(k), d_2 = \sum_k^l H(k-2l)a_1(k). \right. \quad (3)$$

Decomposition of entire upper levels is completed. The original data is recreated and expressed as follows:

$$S' = a_n + d_n + d_{(n-1)} + \dots + d_1. \quad (4)$$

2.3. *Energy Eigen Value Estimation*. Calculating EEV at every level of decomposition is an effective diagnostic technique for determining the severity of a defect. The EEV is computed using the following equation [33]:

$$E_i = \sum_{k=1}^{k=n} |D_{i,k}(n)|^2, \quad (5)$$

where i is the decomposition level. Each wavelet packet factor in a frequency range has a magnitude band of D ; N is the DWT time of decomposition. The BRB diagnosis technique involves the computation of EEVs, with specific change numbers reflecting the severity of the problem.

3. Modelling of IM with BRB Faults Taken into Account

The healthy state of IM with-reference elements is modelled, and the relevant state equations are established to confirm IM performance [34]. Figure 3 relates the IM to the BRB model in terms of schematic diagram.

The rotor coordinates model of IM is represented as follows:

$$\begin{aligned} \dot{x}(t) &= A(\omega) \cdot x(t) + Bu(t), \\ y(t) &= Cx(t), \end{aligned} \quad (6)$$

$$\text{where } x = [I_{ds} \ I_{qs} \ \Psi_{dr} \ \Psi_{qr}]^T, \quad u = \begin{bmatrix} U_{ds} \\ U_{qs} \end{bmatrix}, \quad \text{and} \\ y = \begin{bmatrix} I_{ds} \\ I_{qs} \end{bmatrix}.$$

$$\begin{aligned} A(\omega) &= \begin{bmatrix} -(R_s + R_{eq})L_f^{-1} & \omega_r & R_{eq}L_m^{-1}L_f^{-1} & -\omega \\ -\omega & -(R_s + R_{eq})L_f^{-1} & -\omega L_f^{-1} & R_{eq}L_m^{-1}L_f^{-1} \\ R_{eq} & 0 & R_{eq}L_m^{-1} & 0 \\ 0 & R_{eq} & 0 & R_{eq}L_m^{-1} \end{bmatrix}, \\ B &= \begin{bmatrix} L_f^{-1} & 0 \\ 0 & L_f^{-1} \\ 0 & 0 \\ 0 & 0 \end{bmatrix}, \\ C &= \begin{bmatrix} 1 & 0 & 0 & 0 \\ 0 & 1 & 0 & 0 \end{bmatrix}. \end{aligned} \quad (7)$$

The corresponding rotor resistance is calculated as follows:



FIGURE 8: Experimental setup.

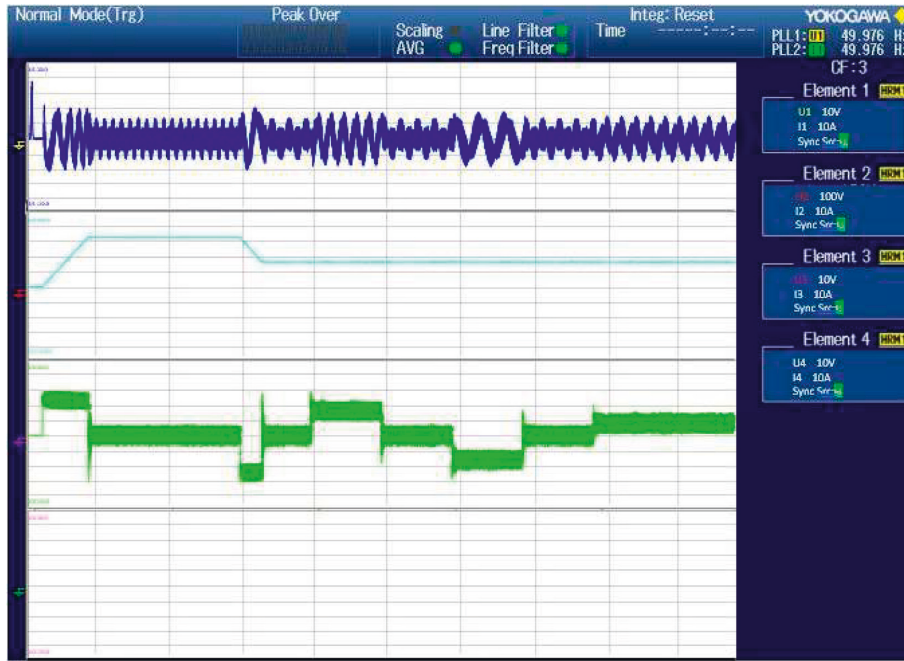


FIGURE 9: Experimental waveform of current, speed, and torque in V/F-fed IM under healthy state.

$$R_{eq} = R_r + \frac{\alpha}{1 - \alpha} K(\theta_0) R_r,$$

$$K(\theta_0) = \begin{bmatrix} \cos(\theta_0)^2 & \cos(\theta_0)\sin(\theta_0) \\ \cos(\theta_0)\sin(\theta_0) & \sin(\theta_0)^2 \end{bmatrix}, \quad (8)$$

$$\alpha = \frac{2}{3}\zeta_0,$$

$$\zeta_0 = \frac{3n_{bc}}{n_b}.$$

4. VSI: SVM Switching

SVM is an advanced modulation system based on eight distinct switching potential combinations of VSI that is commonly achieved by digital signal processing (DSP) or microcontrollers. At the top or bottom of conduction switches, there are six active state (to) and two zero states [35].

In a $d-q$ plane, the eight various states may be characterized as fixed vectors, as shown in Figure 4. The output reference vector can be generated by adding two or more vectors, with each vector's magnitude controlled by time. Table 1 depicts the different switching states and space vector representations.

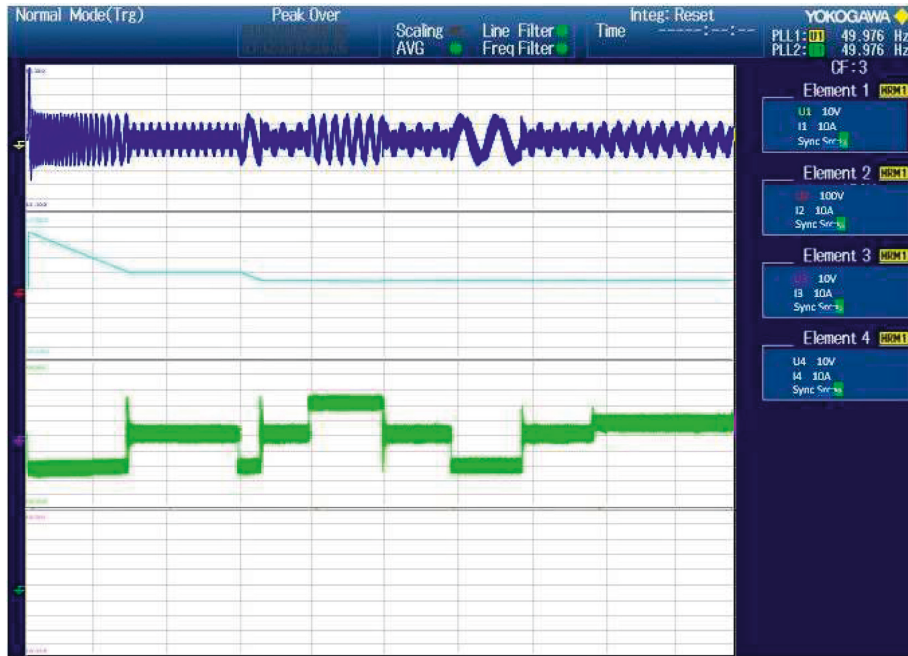


FIGURE 10: Experimental waveform of current, speed, and torque in V/F-fed IM under faulty state.

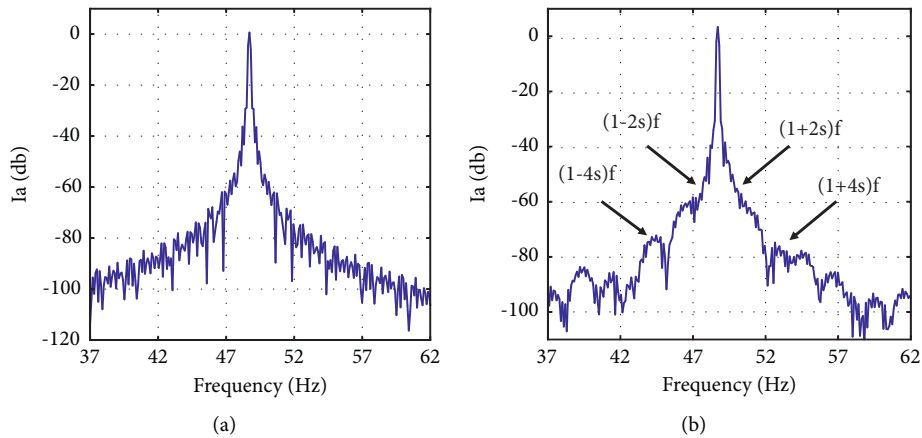


FIGURE 11: FFT analysis of motor current in V/F control of IM at full load condition. (a) Healthy case. (b) 2 BRBs faulty case.

TABLE 4: Frequency and amplitude of motor current in V/F control of IM.

Side band frequency ($s = 0.045$)	Estimated frequency (Hz)	Healthy state		Faulty state	
		Frequency (Hz)	Amplitude (dB)	Frequency (Hz)	Amplitude (dB)
$(1-4s) f_s$	41	43	-82	44	-75
$(1-2s) f_s$	45.5	47	-62	48	-48
$(1+2s) f_s$	54.5	51	-61	52	-50
$(1+4s) f_s$	59	54	-81	55	-70

5. Fault Diagnosis of IMD

The proposed fault diagnosis method is depicted in Figure 5 as a flow chart. The V/F control method is

evaluated using 1.1 kW, 440 V, 28 rotor bars to verify the established BRB model. Table 2 contains the simulation and experimental parameters for IM. The MATLAB function is used to conduct the section of the diode bridge

TABLE 5: Frequency band of wavelet coefficients of V/F fed IM.

Levels	Frequency band
d_1	12250–25000 Hz
d_2	6125–12250 Hz
d_3	3062.5–6125 Hz
d_4	1531.25–3062.5 Hz
d_5	765.625–1531.25 Hz
d_6	382.81–765.625 Hz
d_7	191.40–382.81 Hz
d_8	95.70–191.40 Hz
d_9	47.85–95.70 Hz
d_{10}	23.926–47.85 Hz
d_{11}	11.96–23.926 Hz
d_{12}	5.98–11.96 Hz
a_{12}	2.99–5.98 Hz

rectifier. It is defined as a user-defined function. The RMS voltage, frequency, and time are estimated using the parameters integrated with the function.

5.1. Healthy State of IM. The machine may be controlled using the V/F control system and the SVM technology. IM's load torque and rotor speed are 2400 rpm and 10 Nm, respectively. Figure 6 shows the simulation results for motor current, rotor speed, and electromagnetic torque. When the machine is in good working condition, it produces a high current flow in the transient stage, which then becomes sinusoidal. In response to a step-variation in load torque, the machine's rotor speed achieves the nominal value and gradually drops. The step change in load torque from no load to full load is achieved between 0.5 seconds. A small decrease in IM happens after 0.5 seconds as a result of these load fluctuations. When the load torque varies, the performance of the motor current and rotor speed of the IM is shown in Table 3.

5.2. Faulty State of IM. A simplified state-space model of IM rotor failure is used to simulate the fault state of V/F control. The BRB faults may be seen in the stator current and rotor speed which are shown in Figure 7. After 0.5 seconds, the oscillations in stator current are detected while the machine runs at 2 BRBs failure state. The existence of the inverse field on the rotor ($-s\omega_s$ to $s\omega_s$) causes BRB failure. In stator winding, these two fields can interact with each other, and it increases the frequency components of $2s\omega_s$. This causes oscillations in electromagnetic torque, rotor speed, and stator current shape deviations.

5.3. Experimental Setup and Results. Figure 8 shows the IM experimental setup, which includes a condition monitoring system, a failure simulator, and a TMS320F2812 DSP processor. Gate pulses are sent to the DSP with the code composer studio. Several types of fault tests are performed utilizing a fault simulator to evaluate the efficiency of IM. To investigate the drive performance in a defective state, two tiny holes of 6 mm diameter must be bored in the rotor bars.

The current sensor and the speed sensor send signals to the DSP processor. The sample is then sent to MATLAB for wavelet coefficients.

Figure 9 depicts the healthy state IM experiment results for current, speed, and load torque. The motor current (1 Div. = 2 A) balances respective rated current depending on the load fluctuations. The rotor speed (1 Div. = 100 rpm) response exhibits reduced peak overshoot and the torque (1 Div. = 2 Nm) approaches reference torque in fast. When there is a variation in torque, the oscilloscope records the variation. Figure 10 depicts an experiment V/F supplied driving waveform for both a normal and a defect motor. The motor current is abruptly raised which results in minor oscillations during the transient stage. The speed response is changed at the transient stage due to the influence of the BRB fault. It can be seen that the torque does not retain excellent dynamics.

5.4. FFT Analysis. Figure 11 shows an FFT investigation of motor current both in balanced and defective state. The FFT analysis in MATLAB/Simulink, and also the associated data, has been validated. Depending on the type of defect, the frequency and amplitude portion of harmonic in the motor current changes. Table 4 shows the frequency of sideband elements and amplitude under full load circumstances.

The FFT results demonstrate the potential for signal extraction to identify and localize BRB problems discovered in stator current. FFT has the drawback of potentially losing some time-domain information from the signal. It is challenging to process each frequency channel's assumption when the original signal is decomposed. In order to solve this issue, DWT is proposed for decompose the signal.

Table 5 shows the frequency level band of several wavelet coefficients. It provides a clear interpretation of the variables induced by the BRB fault, as the formation of harmonics during transients and steady-state condition. Figures 12 and 13 illustrate DWT analysis of stator current in healthy and defective states, respectively. The oscillations are the major contributing element for the emergence of transitioning process. There is no oscillation in the system when the wavelet signal intensity is high. In the defective condition, the stator current magnitude has high-level coefficients and variations in coefficients as compared to a healthy condition. The effect of frequency bands is influenced by BRBs failure which causes the coefficient to increase. After decomposing process, the stator current signal is reduced up to 91% in amplitude.

5.5. Energy Eigen Value Computation. The DWT nonstationary analysis shows the presence of faults. The deviation of energy eigenvalue of stator current in each level of DWT provides details regarding fault severity, as illustrated in Figure 14.

The growth in approximation and detail signals, particularly in the level corresponding to the frequency band, is validated through the assessment of energy stored in each

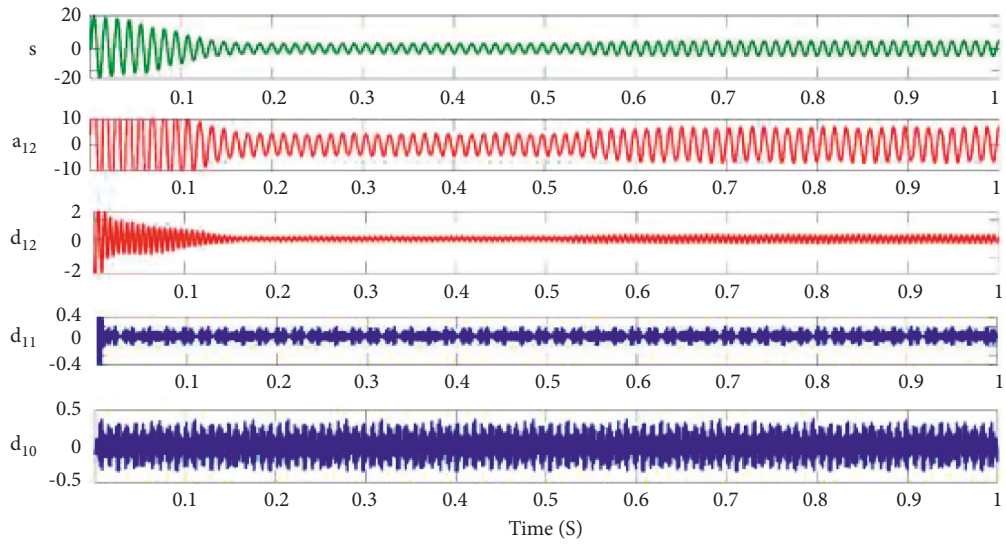


FIGURE 12: DWT of stator current under healthy state in V/F-fed IM.

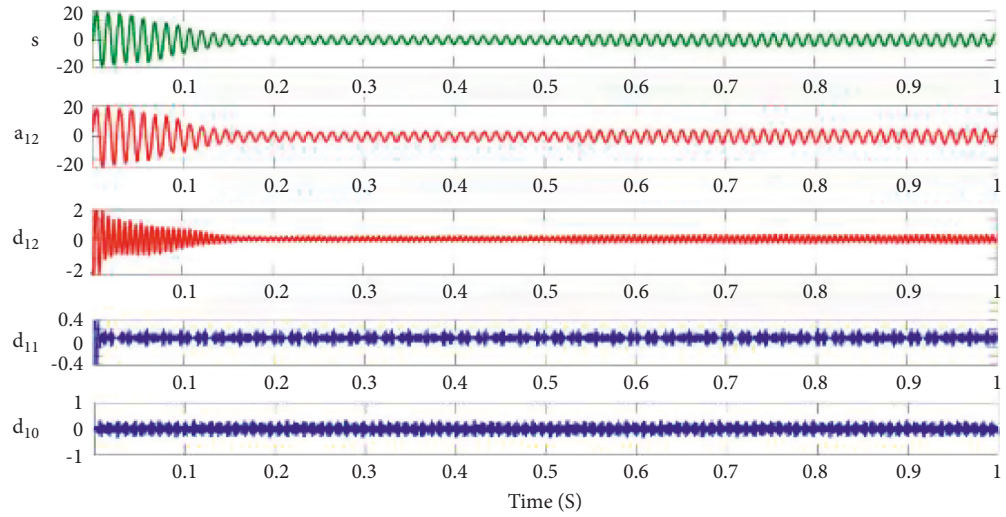


FIGURE 13: DWT of stator current under faulty state in V/F-fed IM.

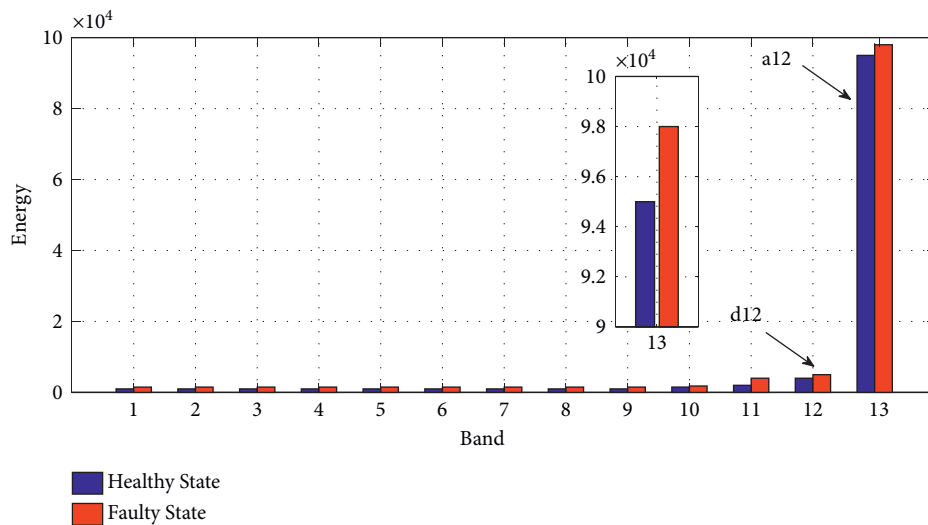


FIGURE 14: EEV of stator current in V/F fed IM.

decomposition level a_{12} . In level 12, the number of deviations is proportional to the EEV. The obtained result is considered as a good fault severity indicator in V/F control of IM.

6. Conclusion

Identifying and diagnosing faults with speed drives is extremely challenging. Rotor bar design is an important aspect of IMD. The machine will get affected due to the fault that occurs in the broken bars with varying loads. This paper focuses on BRB faults and the performance of the induction motor in balanced and unbalanced state. In this paper, BRB fault diagnosis in V/F control of IM is proposed. The magnitude and sideband frequencies are obtained using the FFT method. The magnitude and frequency values are obtained from the FFT outputs. To obtain the stator current and rotor speed, the DWT method is used. By calculating the EEV, we can determine the fault severity. When DWT is applied, the stator current signal of the defective BRB is suppressed to 91% of its original amplitude. The result has proved that DWT and EEV calculation are the effective methods for fault diagnosis, and it is easy to use in motor control applications. In future, the BRB fault diagnosis in vector control methods using advanced regulators will be considered. Also, introducing various observers like sliding model control and backstepping control will be utilized for BRB fault diagnosis in various control methods.

Data Availability

No data were used to support this study.

Conflicts of Interest

The authors declare that they have no conflicts of interest.

Acknowledgments

This study was conducted as a part of the Wollega University, Ethiopia.

References

- [1] D. Gao, X. Lin, and Q. Yang, "Design and application of a fault diagnosis and monitoring system for electric vehicle charging equipment based on improved deep belief network," *International Journal of Control, Automation and Systems*, vol. 20, no. 5, pp. 1544–1560, 2022.
- [2] S. K. Gundewar and P. V. Kane, "Condition monitoring and fault diagnosis of induction motor," *Journal of Vibration Engineering & Technologies*, vol. 9, no. 4, pp. 643–674, 2020.
- [3] A. Allal and A. Khechekhouche, "Diagnosis of induction motor faults using the motor current normalized residual harmonic analysis method," *International Journal of Electrical Power & Energy Systems*, vol. 141, Article ID 108219, 2022.
- [4] M. Abd-el-Malek, A. K. Abdelsalam, and O. E. Hassan, "Induction motor broken rotor bar fault location detection through envelope analysis of start-up current using Hilbert transform," *Mechanical Systems and Signal Processing*, vol. 93, pp. 332–350, 2017.
- [5] T. Ameid, A. Menacer, H. Talhaoui, and Y. Azzoug, "Discrete wavelet transform and energy eigen value for rotor bars fault detection in variable speed field-oriented control of induction motor drive," *ISA Transactions*, vol. 79, pp. 217–231, 2018.
- [6] A. Choudhary, D. Goyal, S. L. Shimi, and A. Akula, "Condition monitoring and fault diagnosis of induction motors: a review," *Archives of Computational Methods in Engineering*, vol. 26, no. 4, pp. 1221–1238, 2018.
- [7] P. Sangeetha, "Rational-dilation wavelet transform based torque estimation from acoustic signals for fault diagnosis in a three-phase induction motor," *IEEE Transactions on Industrial Informatics*, vol. 15, no. 6, pp. 3492–3501, 2019.
- [8] H. Talhaoui, T. Ameid, O. Aissa, and A. Kessal, "Wavelet packet and fuzzy logic theory for automatic fault detection in induction motor," *Soft Computing*, 2022.
- [9] D. Granda, W. G. Aguilar, D. Arcos-Aviles, and D. Sotomayor, "Broken bar diagnosis for squirrel cage induction motors using frequency analysis based on MCSA and continuous wavelet transform," *Mathematical and Computational Applications*, vol. 22, no. 2, p. 30, 2017.
- [10] Q. Fu, S. Yue, B. He, and N. Fu, "Multiple coupled circuit modelling approach for squirrel cage induction machine under single-broken-bar fault with stator winding functions decomposed in $d-q$ rotor reference frame," *IET Electric Power Applications*, vol. 13, no. 7, pp. 889–900, 2019.
- [11] I. Harzelli, A. Menacer, and T. Ameid, "A fault monitoring approach using model-based and neural network techniques applied to input-output feedback linearization control induction motor," *Journal of Ambient Intelligence and Humanized Computing*, vol. 11, no. 6, pp. 2519–2538, 2019.
- [12] O. E. Hassan, M. Amer, A. K. Abdelsalam, and B. W. Williams, "Induction motor broken rotor bar fault detection techniques based on fault signature analysis—a review," *IET Electric Power Applications*, vol. 12, no. 7, pp. 895–907, 2018.
- [13] S. O. Ibrahim, K. N. Faris, and E. A. Elzahab, "Implementation of fuzzy modeling system for faults detection and diagnosis in three phase induction motor drive system," *Journal of Electrical Systems and Information Technology*, vol. 2, no. 1, pp. 27–46, 2015.
- [14] O. A. Imoru, M. A. Bhaskar, A. A.-G. Jimoh, and Y. Hamam, "Diagnosis of stator shorted-turn faults in induction machines using discrete wavelet transform," *African Journal of Science, Technology, Innovation and Development*, vol. 9, no. 3, pp. 349–355, 2017.
- [15] M. Jannati, A. Monadi, N. R. N. Idris, and M. J. Abdul Aziz, "Experimental evaluation of FOC of 3-phase IM under open-phase fault," *International Journal of Electronics*, vol. 104, no. 10, pp. 1675–1688, 2017.
- [16] L. H. B. Liboni, R. A. Flauzino, I. N. da Silva, and E. C. Marques Costa, "Efficient feature extraction technique for diagnosing broken bars in three-phase induction machines," *Measurement*, vol. 134, pp. 825–834, 2019.
- [17] W. Oñate, Y. Gallardo, R. Pérez, and G. Caiza, "Comparative analysis of high frequencies for the broken bar fault diagnosis using MCSA and park's vector demodulation," *Smart Innovation, Systems and Technologies*, pp. 119–130, Springer, Berlin, Germany, 2021.
- [18] A. Verma, P. Arvind, S. Sarangi, J. Kumar, and Anumeha, "Detection of broken rotor bar fault in an induction motor employing motor current signature analysis," *Recent Advances in Power Electronics and Drives*, pp. 523–530, Springer, Berlin, Germany, 2022.

- [19] S.-H. Im and B.-G. Gu, "Study of induction motor inter-turn fault part II: online model-based fault diagnosis method," *Energies*, vol. 15, no. 3, p. 977, 2022.
- [20] R. Senthil Kumar, I. Gerald Christopher Raj, K. P. Suresh et al., "A method for broken bar fault diagnosis in three phase induction motor drive system using artificial neural networks," *International Journal of Ambient Energy*, pp. 1–7, 2021.
- [21] A. El Idrissi, A. Derouich, and S. Mahfoud, "Fault diagnosis of the bearing outer ring of an induction motor under DTC control by using Hilbert filter," *Digital Technologies and Applications*, pp. 802–812, Springer, Berlin, Germany, 2022.
- [22] M. Defdaf, F. Berrabah, A. Chebabhi, and B. D. E. Cherif, "A new transform discrete wavelet technique based on artificial neural network for induction motor broken rotor bar faults diagnosis," *International Transactions on Electrical Energy Systems*, vol. 31, no. 4, 2021.
- [23] Y. Mallet, O. de Vel, and D. Coomans, "Fundamentals of wavelet transforms," *Data Handling in Science and Technology*, pp. 57–84, Elsevier, Amsterdam, Netherlands, 2000.
- [24] H. Talhaoui, A. Menacer, A. Kessal, and A. Tarek, "Experimental diagnosis of broken rotor bars fault in induction machine based on Hilbert and discrete wavelet transforms," *The International Journal of Advanced Manufacturing Technology*, vol. 95, no. 1–4, pp. 1399–1408, 2017.
- [25] J. Guo, Z. Si, and J. Xiang, "A compound fault diagnosis method of rolling bearing based on wavelet scattering transform and improved soft threshold denoising algorithm," *Measurement*, vol. 196, Article ID 111276, 2022.
- [26] F. He and Q. Ye, "A bearing fault diagnosis method based on wavelet packet transform and convolutional neural network optimized by simulated annealing algorithm," *Sensors*, vol. 22, no. 4, p. 1410, 2022.
- [27] S. Datta, A. Chandra, and S. Chowdhuri, "High performance sensor-less V/F control of surface PMSM in voltage vector plane with ZVV injection and SMO-based position estimation method," *Electrical Engineering*, vol. 104, no. 2, pp. 657–666, 2021.
- [28] K. Sundararaju, R. S. Kumar, and I. G. Raj, "Modeling and simulation of neural based speed controller for direct torque control of three phase induction motor," in *Proceedings of the TENCON 2017–2017 IEEE Region 10 Conference*, Penang, Malaysia, November 2017.
- [29] H. Talhaoui, T. Ameid, and A. Kessal, "Energy eigenvalues and neural network analysis for broken bars fault diagnosis in induction machine under variable load: experimental study," *Journal of Ambient Intelligence and Humanized Computing*, vol. 13, no. 5, pp. 2651–2665, 2021.
- [30] B. Saad and A. Goléa, "Direct field-oriented control using fuzzy logic type-2 for induction motor with broken rotor bars," *Advances in Modelling and Analysis C*, vol. 72, no. 4, pp. 203–212, 2017.
- [31] T. Goktas and M. Arkan, "Discerning broken rotor bar failure from low-frequency load torque oscillation in DTC induction motor drives," *Transactions of the Institute of Measurement and Control*, vol. 40, no. 1, pp. 279–286, 2016.
- [32] R. Senthil Kumar and I. Gerald Christopher Raj, "Broken rotor bar fault detection using DWT and energy eigenvalue for DTC fed induction motor drive," *International Journal of Electronics*, vol. 108, no. 8, pp. 1401–1425, 2021.
- [33] S. R. Kapoor, N. Khandelwal, and P. Pareek, "Bearing fault analysis by signal energy calculation based signal processing technique in squirrel cage induction motor," in *Proceedings of the 2014 International Conference on Signal Propagation and Computer Technology (ICSPCT 2014)*, Ajmer, India, June, 2014.
- [34] B. Bessam, A. Menacer, M. Boumechraz, and H. Cherif, "Detection of broken rotor bar faults in induction motor at low load using neural network," *ISA Transactions*, vol. 64, pp. 241–246, 2016.
- [35] F. Acosta-Cambranis, J. Zaragoza, L. Romeral, and N. Berbel, "Comparative analysis of SVM techniques for a five-phase VSI based on SIC devices," *Energies*, vol. 13, no. 24, p. 6581, 2020.

Research Article

A Modified Seven-Level Inverter with Inverted Sine Wave Carrier for PWM Control

Arun Vijayakumar ¹, Albert Alexander Stonier ², Geno Peter ³,
Praghash Kumaresan ⁴ and Elenor M. Reyes⁵

¹Department of Electrical and Electronics Engineering, Sreevidyanikethan Engineering College, Tirupati, India

²Department of Electrical and Electronics Engineering, Kongu Engineering College, Erode, India

³CRISD, School of Engineering and Technology, University of Technology Sarawak, Sibu, Malaysia

⁴Department of Electronics and Communication Engineering, Christ University, Bengaluru, India

⁵Department of Electrical Engineering, Batangas State University, Batangas, Philippines

Correspondence should be addressed to Geno Peter; genopeter@gmail.com

Received 30 May 2022; Revised 9 June 2022; Accepted 5 July 2022; Published 21 July 2022

Academic Editor: Ci Wei Gao

Copyright © 2022 Arun Vijayakumar et al. This is an open access article distributed under the Creative Commons Attribution License, which permits unrestricted use, distribution, and reproduction in any medium, provided the original work is properly cited.

The conventional multilevel inverter necessitates more active switching devices and high dc-link voltages. To minimize the employment of switching devices and dc-link voltages, a novel topology has been proposed. In this paper, a novel minimum switch multilevel inverter is established using six switches and two dc-link voltages in the proportion of 1 : 2. In addition, the proposed topology is proficient in making seven-level voltages by appropriate gate signals. The PWM signals were produced using several inverted sine carriers and a single trapezoidal reference. When compared to other existing inverters, this configuration needs fewer components, as well as fewer gate drives. Furthermore, this module can generate a negative level without the use of a supplementary circuit such as an H-Bridge. As a result, overall cost and complexity are greatly reduced. The proposed minimum switch multilevel inverter operation is validated through simulations followed by experimental results of a prototype.

1. Introduction

The cascaded inverter, which is made up of a series of connected strings of a full-bridge inverter, has been presented in [1]. This structure can be functioned in both symmetric and uneven types based on the input source magnitude. Asymmetrical type inverter configuration required fewer cascaded bridges to achieve more output levels [2]. In [3], a new seven-level inverter scheme is proposed with six semiconductor switches and 3 dc capacitors. However, the voltage balancing of the capacitor is quite challenging. A new MLI topology with series connected dc voltage sources has been presented in [4]. To lower the switching losses, this structure includes a level generation and polarity generation portion. Increasing the output voltage, on the other hand, necessitates the use of more dc sources. In [5], MLI topologies with a capacitor selection

circuit have been presented. However, obtaining distinct dc sources having multiple ratios necessitates the use of a front-end transformer. Transformers less switched capacitor inverter topology have been presented in [6]. However, the determination of capacitance value is quite complex. A 7-level configuration with a dc supply with and series of capacitors, diodes, and power semiconductor switches have been presented in [7]. It also uses a new switching strategy to solve voltage balancing problems in capacitors. However, the proposed configuration has a restriction on high-voltage applications. A medium-voltage hybrid seven-level cascaded inverter topology is presented in [8]. However, the circuit topology is more complicated because it requires a high number of switching devices. A packed U cell inverter configuration is presented in [9, 10] with a lower number of power semiconductor switches to high-voltage applications. However, exploiting power semiconductor switches with

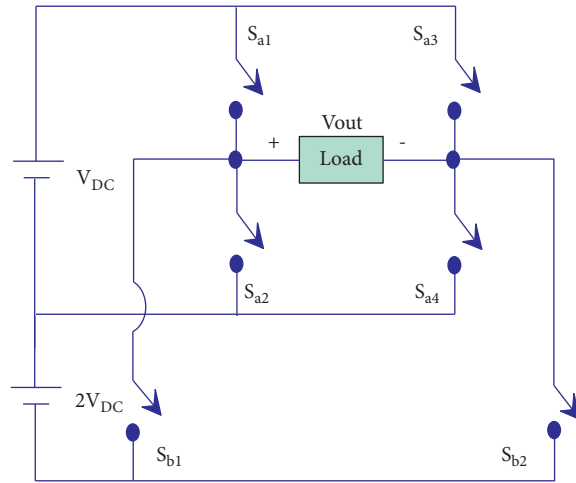


FIGURE 1: Proposed 7-level inverter configuration.

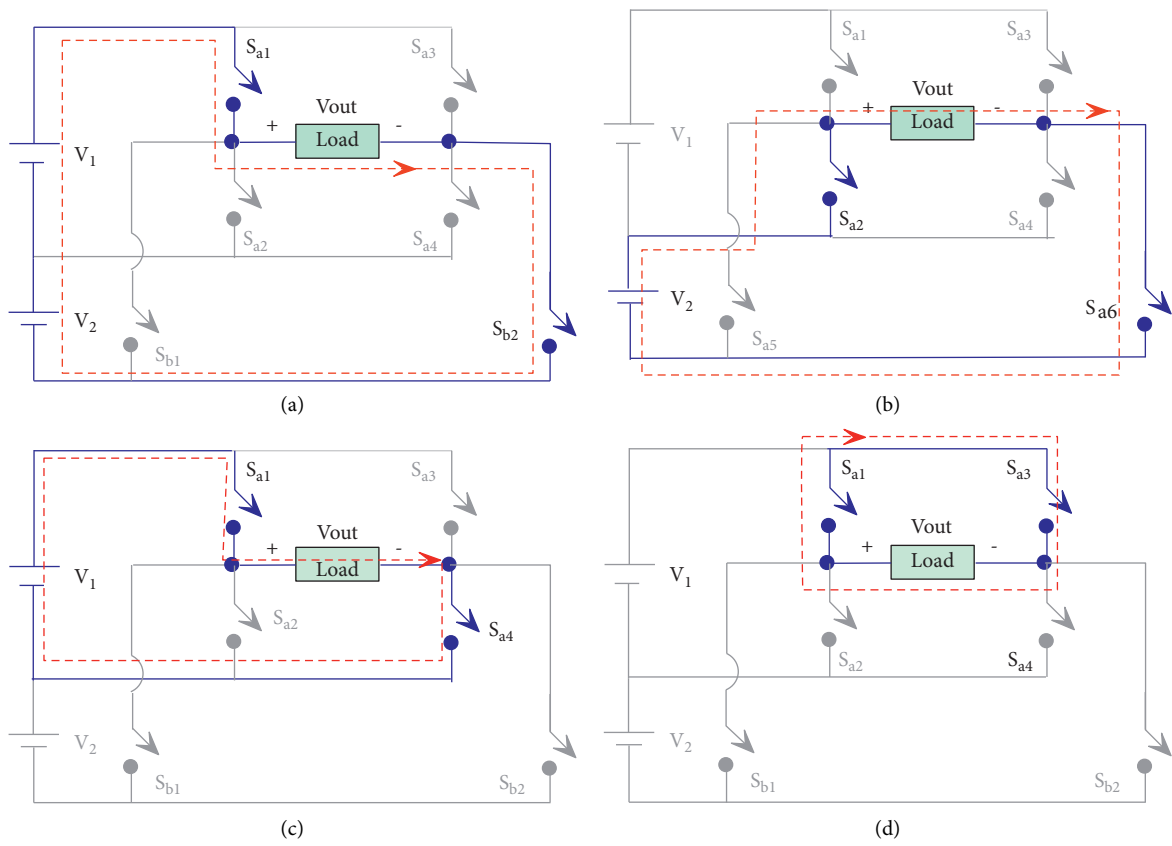


FIGURE 2: Continued.

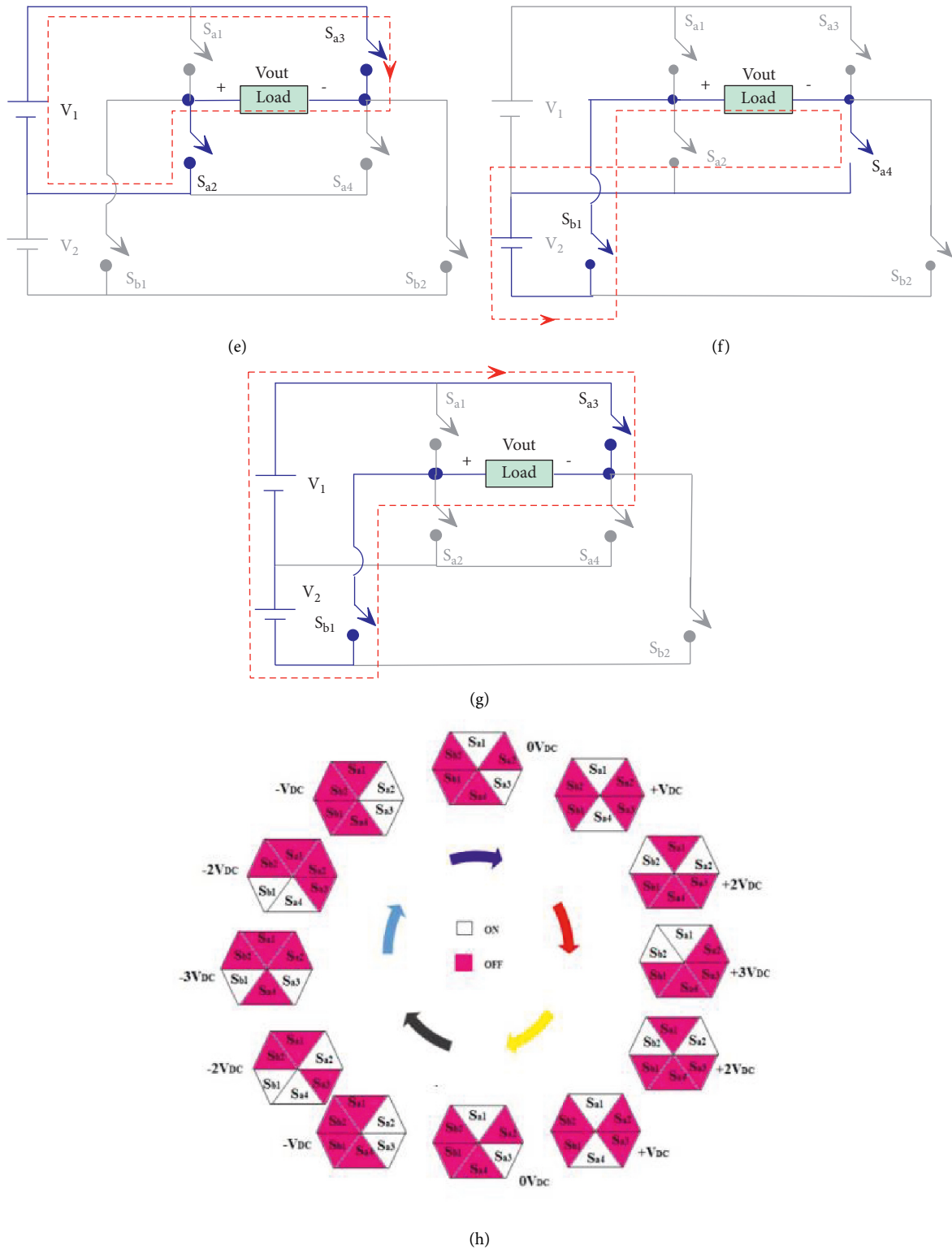


FIGURE 2: (a) Current path and switching plan for making $+3V_{DC}$ at load. (b) Current path and switching plan for making $+2V_{DC}$ at load. (c) Current path and switching plan for making $+V_{DC}$ at load. (d) Current path and switching plan for making $0V_{DC}$ at load. (e) Current path and switching plan for making $-V_{DC}$ at load. (f) Current path and switching plan for making $-2V_{DC}$ at load. (g) Current path and switching plan for making $-3V_{DC}$ at load. (h) Cyclic switching sequence of chosen MLI.

TABLE 1: Voltage stress on switches.

Switch	Voltage stress
S_{a1}	$3V_{DC}$
S_{a2}	$2V_{DC}$
S_{a3}	$3V_{DC}$
S_{a4}	$2V_{DC}$
S_{b1}	$3V_{DC}$
S_{b2}	$3V_{DC}$

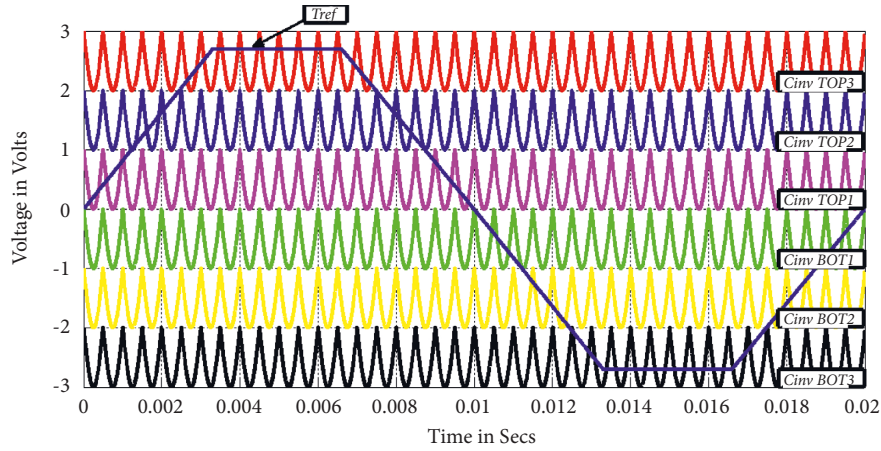


FIGURE 3: Graphic depiction of the PD-PWM scheme with inverted sine carrier and trapezoidal reference waveform.

TABLE 2: Comparison with recent past developed MLIs.

Parameter	Ref. no. [1]	Ref. no. [3]	Ref. no. [4]	Ref. no. [5]	Ref. no. [6]	Ref. no. [7]	Ref. no. [8]	Ref. no. [9]	Ref. no. [10]	Ref. no. [11]	Ref. no. [12]	Ref. no. [13]	Ref. no. [14]	Proposed
N_{Source}	1	1	3	1	1	1	2	1	2	1	1	1	4	2
$N_{capacitors}$	3	3	0	2	3	3	2	1	2	3	3	2	0	0
N_{Switch}	8	8	10	6	10	7	12	6	6	8	10	8	6	6
N_{Driver}	8	8	10	6	10	7	12	6	6	8	10	8	6	6
N_{Diode}	4	0	0	2	0	2	4	0	0	4	0	2	2	0

different ratings and frequencies is crucial. 7-level inverters designed with switched capacitors are described in [11–13]. To enhance the voltage level, however, the voltage across the dc-link capacitor should be enhanced. In addition, to minimize overall harmonic distortion, level shifted, phase shifted, and hybrid pulse width modulation (PWM) approaches are often used. The key challenges with these MLI topologies are improving efficiency by enhancing the quality of power using appropriate control and modulation techniques. Additionally, finding the exact modulation method for any kind of multilevel converter seems to be complicated [2, 14–16]. Drawing inspiration from early research, the article outlines a novel 7-level inverter based on a decreased number of parts, with a series of connected dc sources of binary sequence to achieve maximum capacity from dc sources by an appropriate organization of switches [17]. Symmetrical and asymmetrical MLI with lower switch count and dc sources are presented in [18–21]. However, these topologies need auxiliary circuits to generate negative levels.

The proposed inverter topology has the following merits over the inverter topology presented in recent past years.

- (1) Simple structure with fewer semiconductor components and individual DC sources for each unit has great potential for the application of dispersed generation.
- (2) It does not require any supplementary H-bridge unit to make negative polarity levels. Therefore, the redesign overcomes the restriction on high-voltage applications due to high-voltage stress on H-bridge switches [21].
- (3) Reduction in blocking voltage on switches, a diversity of switches, and heat sinks.
- (4) Modified PWM technique uses trapezoidal reference and inverted sine carrier waveform for the inverter, which enhances the inverter performance by maximizing output voltage and reducing voltage distortion [22].

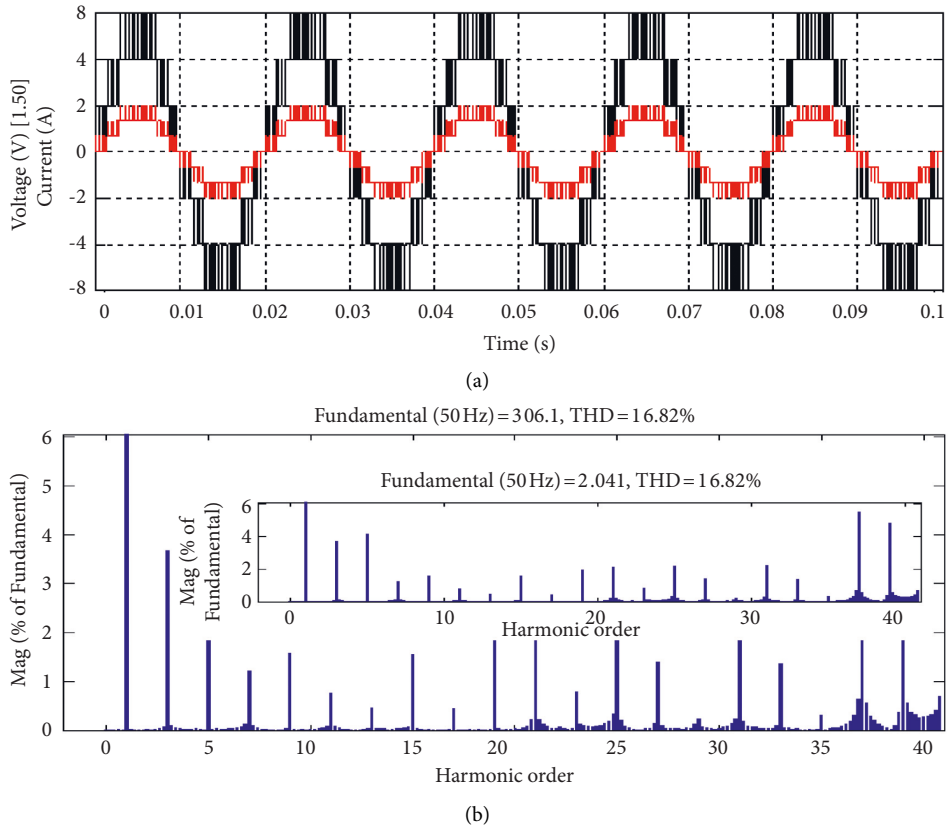


FIGURE 4: (a) Resultant 7-level voltage along with the current for R ($100\ \Omega$) load (simulation). (b) Harmonic spectrum.

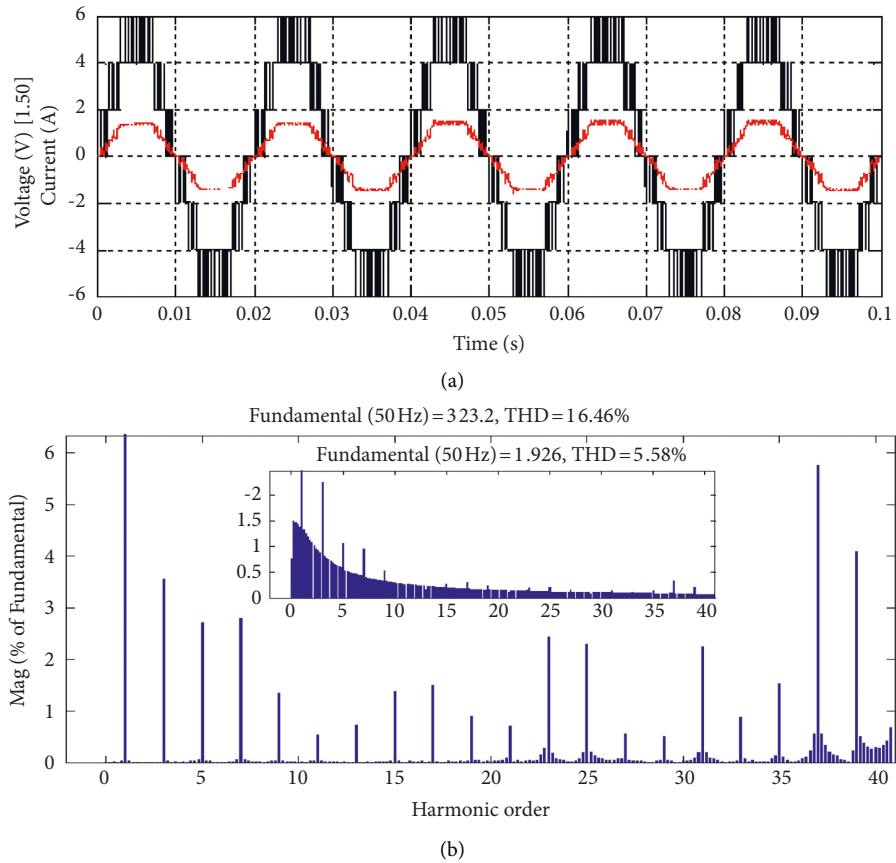


FIGURE 5: (a) Resultant 7-level voltage along with the current for a series RL ($100\ \Omega$ and $240\ \text{mH}$) load (simulation). (b) Harmonic spectrum.

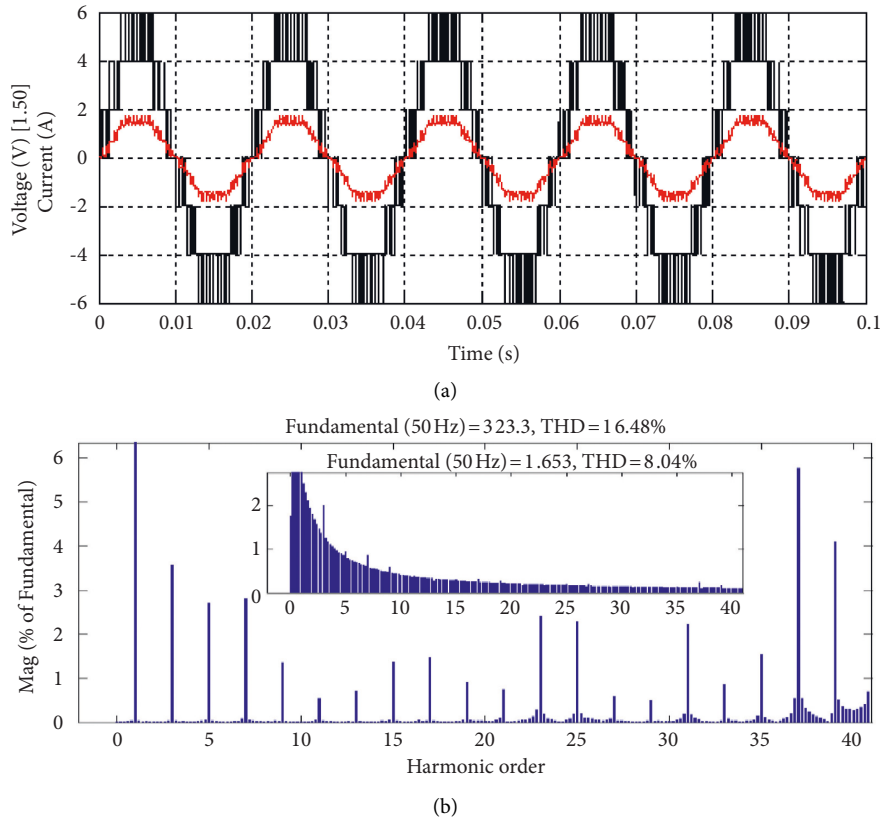


FIGURE 6: (a) Resultant 7-level voltage along with the current for a series RL (100 Ω and 400 mH) load (simulation). (b) Harmonic spectrum.

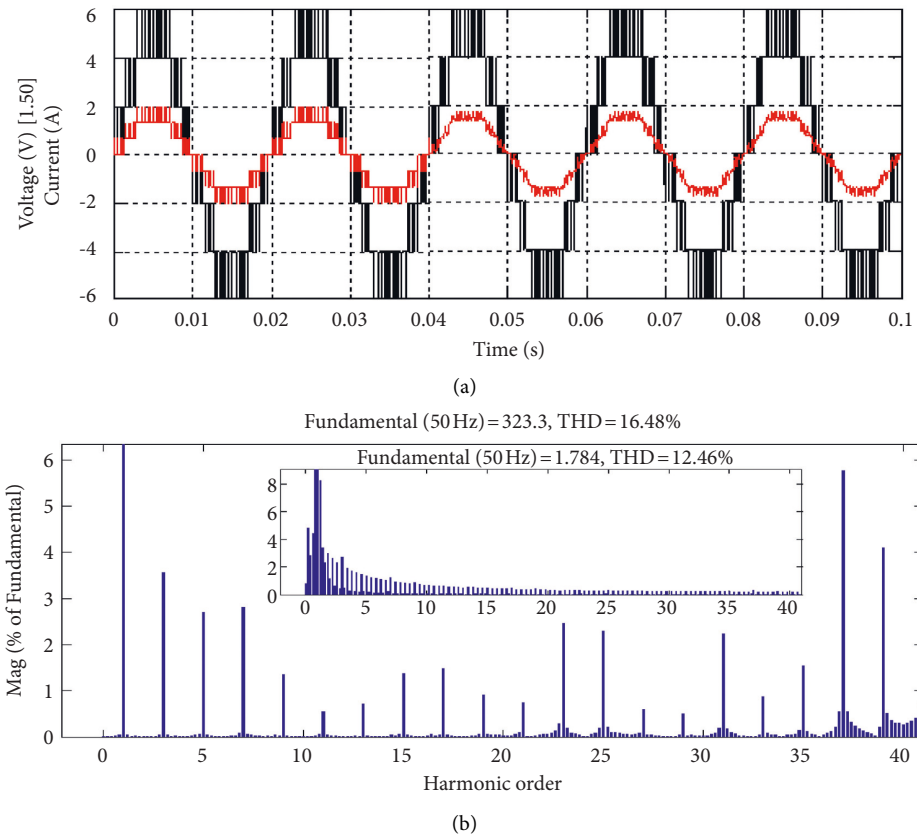


FIGURE 7: (a) Resultant 7-level voltage along with the current for sudden step change $R = 100 \Omega$ to $(R = 100 \Omega, L = 400 \text{ mH})$ load (simulation results). (b) Harmonic spectrum.

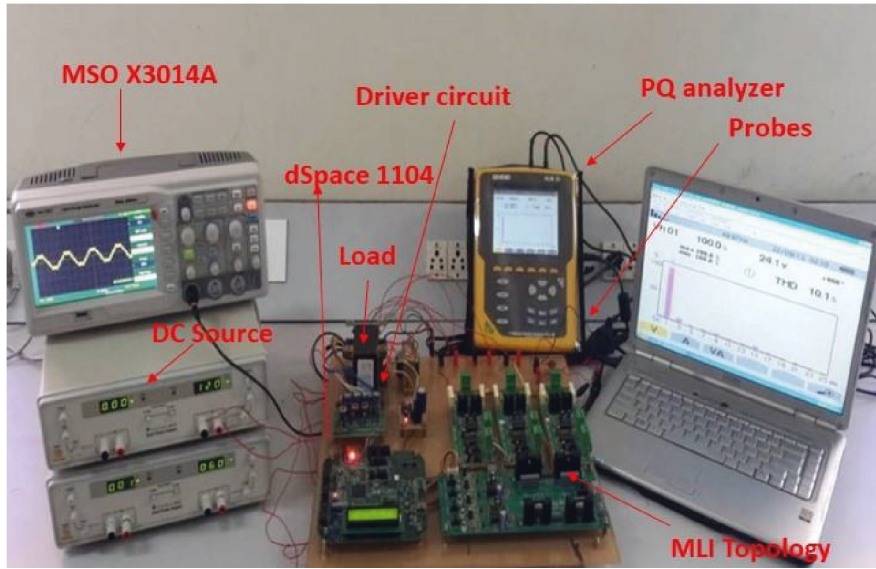
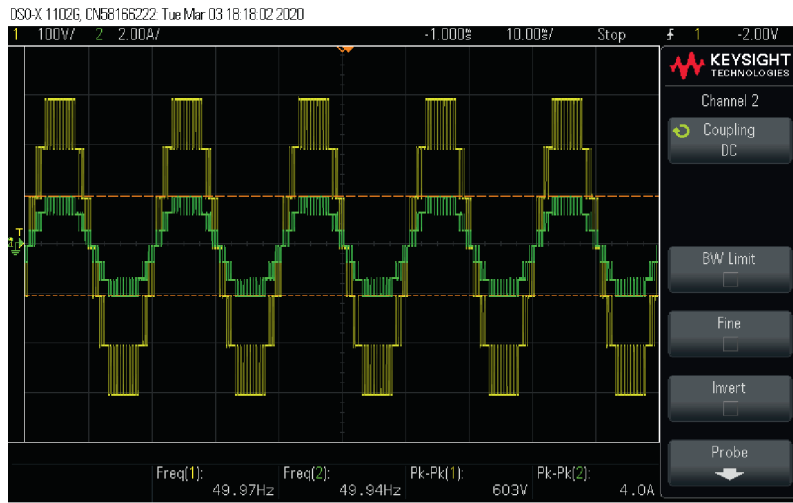
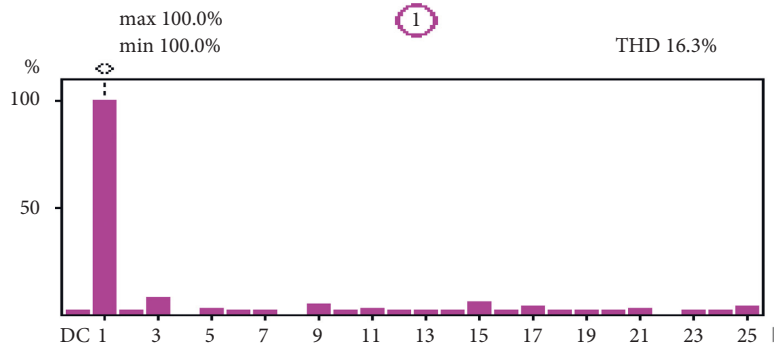


FIGURE 8: Experimental arrangement of proposed seven-level inverter.



(a)



(b)

FIGURE 9: (a) Resultant 7-level voltage along with the current for R ($100\ \Omega$) load (experiments). (b) Harmonic spectrum.

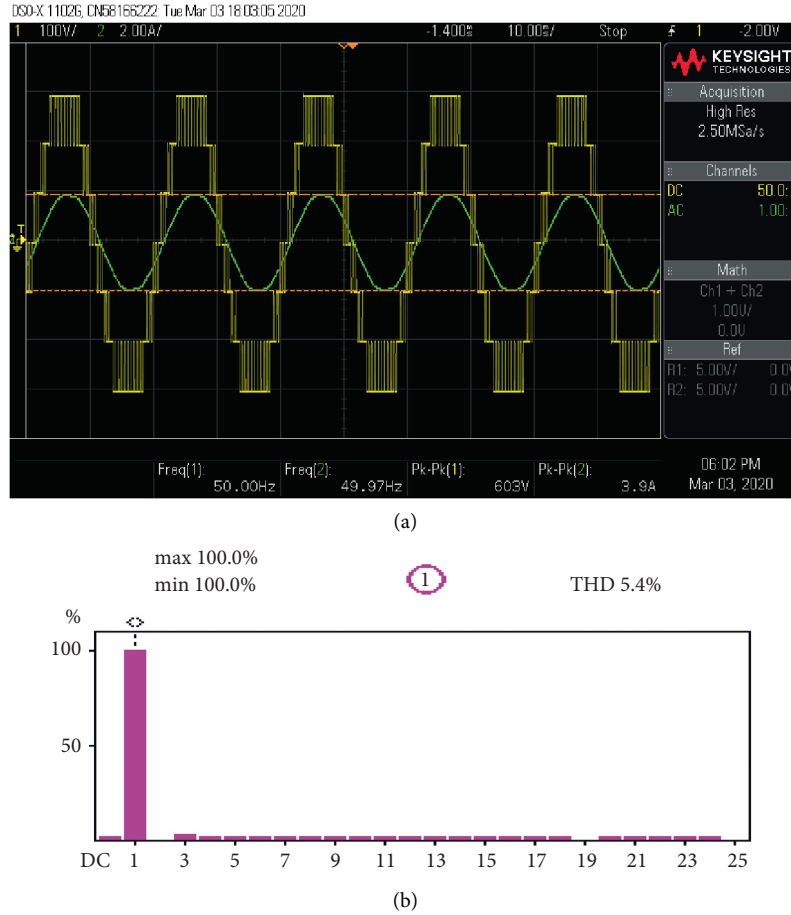


FIGURE 10: (a) Resultant 7-level voltage along with the current for a series RL-load ($100\ \Omega$ and $240\ \text{mH}$) (experiments). (b) Current harmonic spectrum.

The following is the structure of the article: the operation of the proposed configuration and PWM technique is described in Section 2. Sections 3 and 4 discuss the comparative study and results. Conclusions are finally drawn in Section 5.

2. 7-Level Inverter Configuration and PWM Technique

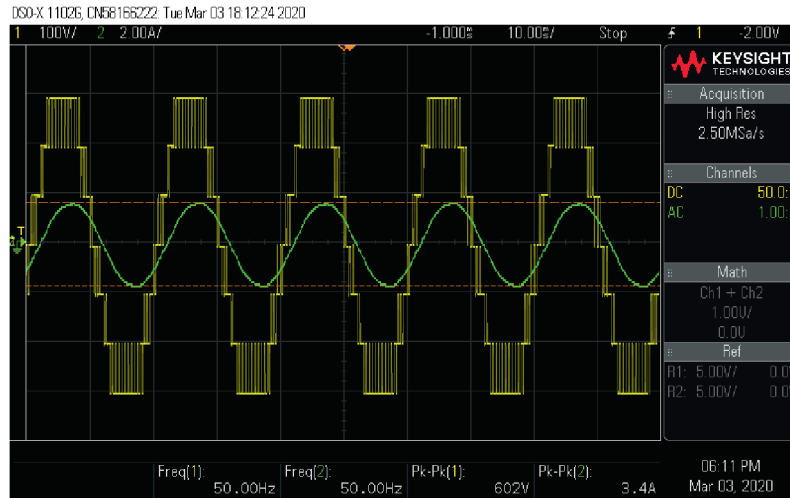
2.1. Proposed Configuration of MLI. Figure 1 displays the proposed structure of a 7-level inverter with a new device arrangement. It is used to extract the seven-level output by choosing the suitable switches and sources. The configuration consists of 'two' dc sources with distinct voltage scales that have a two-fold geometric progression (V_{DC} and $2V_{DC}$), then the output voltage levels $0V_{DC}$, $\pm V_{DC}$, $\pm 2V_{DC}$, and $\pm 3V_{DC}$ can be achieved by choosing the suitable path from switches and dc sources. It consists of six semiconductor switches (Sa1 to Sa4, Sb1, and Sb2) like IGBT and two unequal dc sources of magnitude V_{DC} and $2V_{DC}$. With a proper driving pattern for six switches, it is possible to obtain voltage levels from $-3V_{DC}$ to $3V_{DC}$.

However, the extension of further high levels is quite complex. To avoid a short circuit, the suggested configuration

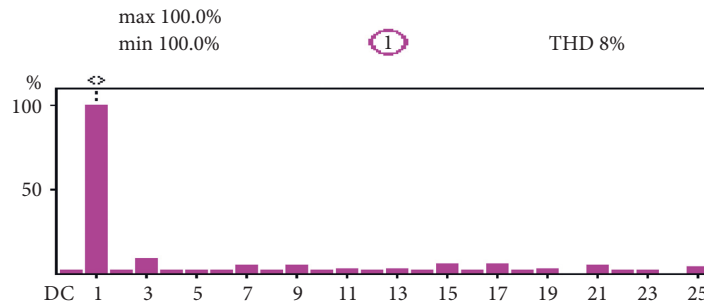
switches (Sa1, Sa2), (Sa3, Sa4), (Sa1, Sb1), and (Sa3, Sb2) should never be switched on at the same period [23].

The current path for each output state and cyclic switching sequence is depicted in Figure 2(a)–2(h). Sa1, as well as Sa3, were switched ON in accordance with the operating modes for maintaining zero level. When Sa1 and Sa4 are turned ON, the output voltage becomes $+V_{DC}$, and then Sa2 and Sb2 are switched ON to produce $+2V_{DC}$ as an output voltage. Sa1 and Sb2 are turned ON to make output voltage as $+3V_{DC}$, then V_{out} becomes $-V_{DC}$ by turning ON Sa2 and Sa3. To synthesize $-2V_{DC}$ as the output voltage, Sa4 and Sb1 are turned ON. Sa3 and Sb1 are turned ON to make an output voltage $-3V_{DC}$. Table.1 shows voltage stress on each switch.

2.2. Proposed PWM Technique. The control strategy uses trapezoidal wave as a reference instead of sine wave and inverted sine waves as a carrier instead of triangular wave. The trapezoidal wave is obtained from triangular wave by limiting its magnitude, which is peak of the triangular wave. Interaction of trapezoidal reference and inverted sine carrier provide wider pulse area compared to conventional sinusoidal PWM scheme, which enhance the fundamental components. The operation of minimum switch multilevel



(a)



(b)

FIGURE 11: (a) Resultant 7-level voltage along with the current for a series RL-load (100 Ω and 400 mH) (experiments). (b) Current harmonic spectrum.

inverter is achieved by proper switching using carrier-based PWM technique named PD-PWM, which is depicted in Figure 3. In this case, a trapezoidal reference wave T_{ref} and six inverted sine carrier C_{inv} (1, 2, 3, ..., 6) are used. The half of the carrier are set above the zero reference C_{inv}^{TOP} (1, 2, 3, ..., $C_{inv}/2$) and remain set below the zero reference C_{inv}^{BOT} (1, 2, 3, ..., $C_{inv}/2$) with same frequency, phase, and amplitude are disposed. Each C_{inv}^* are compared with reference T_{ref} , which produces command signals ($Cs_1, Cs_2, \dots, Cs_3, \dots$). The switching signals are generated by a proper logical combination of command signals.

3. Comparative Study

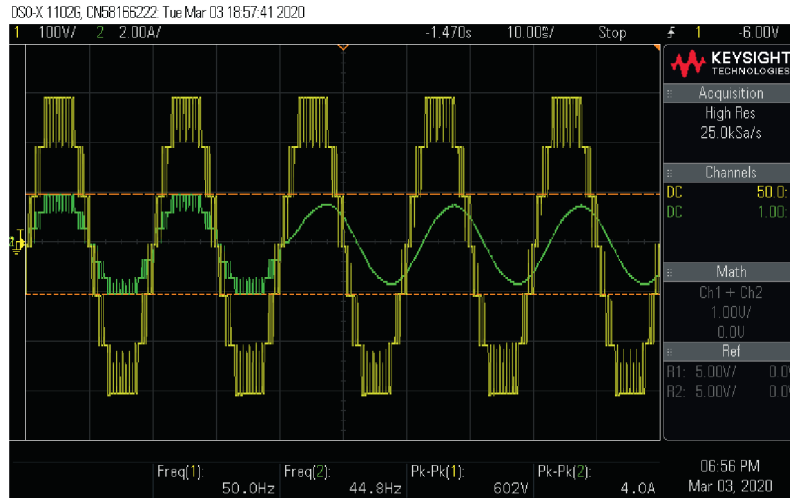
Many reduced switch MLI topologies have been developed in recent past years. To prove the effectiveness of the proposed topology, several parameter (number of sources, switches, driver circuits, capacitors, and diodes) comparisons have been made between the proposed MLI topology and the recently developed topologies which are tabulated in Table 2. Table 2 shows the comparison of different parameters. From Table 1, it is evident that the proposed topology has the best features in the number of power switches, driver circuits, source capacitors, and diode. Based on the aforementioned merits, the proposed MLI requires

the least cost and installation space requirement as compared to other MLI topologies.

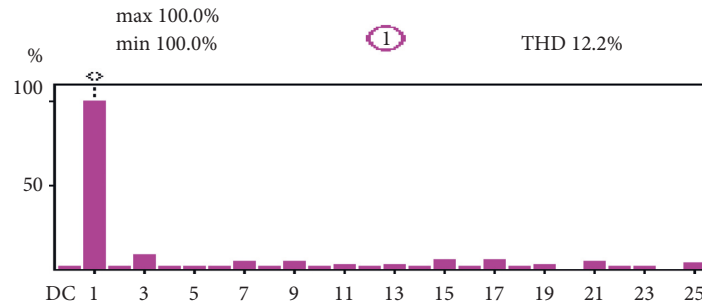
4. Results and Discussions

4.1. Simulation Results. The Simulink-Power system block set has been used to simulate the desired asymmetrical multilevel inverter. Seven-level inverters were simulated for the modulation index value of 1 with various loads and dynamic shifts in the loads. $V_{DC} = 100V$, R load value of 100 Ω , R - L load values of ($R = 100 \Omega$, $L = 240$ mH), and ($R = 100 \Omega$, $L = 400$ mH) are utilized. The carrier switching frequency $f_{carrier} = 2$ kHz.

Figures 4(a) and 4(b) exhibit the resultant waveform of voltage and current for the desired 7L inverter, as well as an FFT chart for the standard resistive load. The seven-level output waveform has voltage magnitudes of 0, $\pm 100V$, $\pm 200V$, and $\pm 300V$. The output voltage THD is 16.82%, and the fundamental peak voltage is 216.4 V. For the R - L load condition ($R = 100 \Omega$, $L = 240$ mH), Figures 5(a) and 5(b) display the load voltage and currents, and also the output current FFT plot. The resultant current has a total harmonic distortion (THD) of 5.58%, as found by a Fast Fourier Transform (FFT) analysis. Furthermore, the testing has been performed using a separate set of R - L load ($R = 100$ ohms,



(a)



(b)

FIGURE 12: (a) Resultant 7-level voltage along with the current for sudden step change $R = 100 \Omega$ to ($R = 100 \Omega$, $L = 400$ mH) load (experiments). (b) Current harmonic spectrum.

$L = 400$ mH) with almost the same amplitude (100 Volts) of dc source for the same inverter configuration. Figures 6(a) and 6(b) show the resulting voltage and current for this load state, and also the resultant current FFT plot. The load current has a THD of 8.04 percent, as revealed by an FFT analysis. The developed inverter configuration has been effectively investigated for the rapid phase.

Transition loads [24]: the load voltage and current for rapid load shifts between $R = 100$ ohms to ($R = 100$ ohms, $L = 400$ mH) at $t = 0.04$ sec, as well as the current FFT plot, are displayed in Figures 7(a) and 7(b). The load voltage appears to remain steady even after a rapid transformation in load. Furthermore, the current in the load is rehabilitated from high to low value. The current harmonic distortion is found to be 12.46% using the FFT analysis.

4.2. Experimental Validation. In this study, a prototype of a seven-level inverter was examined under various loading conditions as well as dynamic variations in load values by setting the modulation index to 1. The MLI configuration consists of two DC sources ($V1 = 100$ V, $V2 = 200$ V) and six IGBT switches which produce 7-level output with the maximum value of 300 V. The other parameters are considered as follows: FGA25N120 IGBT switch, TLP350 driver

circuit, R load value is 100Ω , R-L load value of ($R = 100 \Omega$, $L = 240$ mH), ($R = 100 \Omega$, $L = 400$ mH), and the triggering signal for the IGBT switches is produced by the real-time controller DSpace 1104 in real time. The carrier switching frequency $f_{carrier} = 2$ kHz. Figure 8 depicts an experimental arrangement of the proposed 7L inverter. Figures 9(a) and 9(b) illustrate the resultant voltage and current waveforms for the proposed 7L inverter, as well as the FFT plot for the R load. The output waveform has a magnitude of 0, ± 100 V, ± 200 V, and ± 300 V. The output voltage THD is 16.30%, and the fundamental peak voltage of 213.4 V. For the R-L load ($R = 100$ ohm and $L = 240$ mH), Figures 10(a) and 10(b) show the 7-level voltage pattern and current pattern, as well as the current FFT plot. It can be seen that according to an FFT measurement of resultant current, the percentage of THD is 5.48%. The 7-level inverter arrangement were further investigate with R-L load ($R = 100$, $L = 400$ mH) and 100 V dc sources. Figures 11(a) and 11(b) exhibit the resultant voltage and current, as well as the current FFT plot. The percentage of THD in the resultant current is 8.04 percent, according to an FFT measurement. The effectiveness of the designed inverter structure has been validated for rapid phase-changing loading. The resultant voltage and current for rapid load transitions between $R = 100$ ohms and ($R = 100$ ohms, $L = 400$ mH) at $t = 0.04$ sec, as well as the current FFT chart,

are shown in Figures 12(a) and 12(b), respectively. It can be witnessed that after a quick shift in load, the resultant voltage appears to be stable. Moreover, the resultant current is reduced from a high to a low level. The percentage THD of resultant current is reported to be 12.26 using the FFT.

The aforementioned performance findings reveal that the presented topology is capable of handling a wide range of loads and is also suited for dynamic load changes.

5. Conclusion

In the work, a new multilevel inverter configuration is established using six switches. The suggested topology is a synthesized 7-level output waveform with two uneven dc inputs using trapezoidal reference and inverted sin-carrier-based PD-PWM method. The recommended multilevel inverter performance is confirmed with a variety of loading conditions. Furthermore, the proposed architecture uses merely six switches and eliminates the requirement for a distinct level generation and polarity generation arrangement. Furthermore, the proposed switching approach significantly improves the harmonic spectrum of the output waves under unequal dc links with dynamically changing load conditions. Moreover, the proposed switching method can apply to all types of multilevel inverters and it can be used in applications with higher and lower switching frequencies. The viability of recommended control technique is evaluated experimentally. The results validate the effectiveness of the recommended multilevel inverter configuration and control technique. As an outcome, we believe that the suggested multilevel inverter structure and control technique can provide improved dynamic performance while also lowering overall harmonic distortion and enhancing voltage profile.

Data Availability

The required data can be obtained from the corresponding author upon an email request.

Conflicts of Interest

The authors declare that they have no conflicts of interest.

Acknowledgments

The authors acknowledge and thank the Department of Science and Technology (Government of India) for sanctioning the research grant for the project titled "Design and Development of Solar Photovoltaic Assisted Microgrid Architecture with Improved Performance Parameters Intended for Rural Areas" (Ref. No. DST/TMD/CERI/RES/2020/32 (G) dated (03.06.2021)) under the TMD-W&CE scheme for completing this work.

References

- [1] J. Lai, S. Member, and F. Z. Peng, "Multilevel converters-A new breed of power converters," *IEEE Transactions on Industrial Applications*, vol. 32, no. 3, pp. 509–517, 1996.
- [2] B. P. McGrath and D. G. Holmes, "Multicarrier PWM strategies for multilevel inverters," *IEEE Transactions on Industrial Electronics*, vol. 49, no. 4, pp. 858–867, 2002.
- [3] N. A. Rahim, K. Chaniago, and J. Selvaraj, "Single-phase seven-level grid-connected inverter for photovoltaic system," *IEEE Transactions on Industrial Electronics*, vol. 58, no. 6, pp. 2435–2443, 2011.
- [4] E. Najafi and A. H. M. Yatim, "Design and implementation of a new multilevel inverter topology," *IEEE Transactions on Industrial Electronics*, vol. 59, no. 11, pp. 4148–4154, 2012.
- [5] J. C. Wu and C. W. Chou, "A solar power generation system with a seven-level inverter," *IEEE Transactions on Power Electronics*, vol. 29, no. 7, pp. 3454–3462, 2014.
- [6] A. Tsunoda, Y. Hinago, and H. Koizumi, "Level- and phase-shifted pwm for seven-level switched-capacitor inverter using series/parallel conversion," *IEEE Transactions on Industrial Electronics*, vol. 61, no. 8, pp. 4011–4021, 2014.
- [7] J. S. Choi and F. Kang, "Seven-level pwm inverter employing series-connected capacitors paralleled to a single dc voltage source," *IEEE Transactions on Industrial Electronics*, vol. 62, no. 6, pp. 3448–3459, 2015.
- [8] A. Edpuganti and A. K. Rathore, "Fundamental switching frequency optimal pulse width modulation of medium-voltage cascaded seven-level inverter," *IEEE Transactions on Industry Applications*, vol. 51, no. 4, pp. 3485–3492, 2015.
- [9] J. I. Metri, H. Vahedi, H. Y. Kanaan, and K. Al-Haddad, "Real-time implementation of model-predictive control on seven-level packed U-cell inverter," *IEEE Transactions on Industrial Electronics*, vol. 63, no. 7, pp. 4180–4186, 2016.
- [10] H. Vahedi, M. Sharifzadeh, and K. Al-Haddad, "Modified seven-level pack U-cell inverter for photovoltaic applications," *IEEE Journal of Emerging and Selected Topics in Power Electronics*, vol. 6, no. 3, pp. 1508–1516, 2018.
- [11] C. H. Hsieh, T. J. Liang, S. M. Chen, and S. W. Tsai, "Design and implementation of a novel multilevel dc-ac inverter," *IEEE Transactions on Industry Applications*, vol. 52, no. 3, pp. 2436–2443, 2016.
- [12] J. Liu, X. Zhu, and J. Zeng, "A seven-level inverter with self-balancing and low-voltage stress," *IEEE Journal of Emerging and Selected Topics in Power Electronics*, vol. 8, no. 1, pp. 685–696, 2020.
- [13] Y. Ye, W. Peng, and Y. Yi, "Analysis and optimal design of switched-capacitor seven-level inverter with hybrid PWM algorithm," *IEEE Transactions on Industrial Informatics*, vol. 16, no. 8, pp. 5276–5285, 2020.
- [14] K. P. Panda, S. S. Lee, and G. Panda, "Reduced switch cascaded multilevel inverter with new selective harmonic elimination control for standalone renewable energy system," *IEEE Transactions on Industry Applications*, vol. 55, no. 6, pp. 7561–7574, 2019.
- [15] V. Jammala, S. Yellasiri, and A. K. Panda, "Development of a new hybrid multilevel inverter using modified carrier SPWM switching strategy," *IEEE Transactions on Power Electronics*, vol. 33, no. 10, pp. 8192–8197, 2018.
- [16] V. Arun and N. Prabakaran, "Induction motor drive with trinary DC source asymmetrical inverter," *International Journal of Recent Technology and Engineering*, vol. 8, no. 2, pp. 5484–5490, 2019.
- [17] P. Geno Peter and M. Rajaram, "An enhanced Z-source inverter topology-based permanent magnet brushless DC motor drive speed control," *International Journal of Electronics*, vol. 102, no. 8, pp. 1289–1305, 2015.
- [18] M. S. O. Yeganeh, P. Davari, A. Chub, N. Mijatovic, T. Dragičević, and F. Blaabjerg, "A single-phase reduced

- component count asymmetrical multilevel inverter topology,” *IEEE Journal of Emerging and Selected Topics in Power Electronics*, vol. 9, no. 6, pp. 6780–6790, 2021.
- [19] A. Chappa, S. Gupta, L. K. Sahu, S. P. Gautam, and K. K. Gupta, “Symmetrical and asymmetrical reduced device multilevel inverter topology,” *IEEE Journal of Emerging and Selected Topics in Power Electronics*, vol. 9, no. 1, pp. 885–896, Feb. 2021.
- [20] G. Peter and A. Sherine, “Induced over voltage test on transformers using enhanced Z-source inverter based circuit,” *Journal of Electrical Engineering*, vol. 68, no. 5, pp. 378–383, 2017.
- [21] S. R. Khasim and C. Dhanamjayulu, “Design and implementation of asymmetrical multilevel inverter with reduced components and low voltage stress,” *IEEE Access*, vol. 10, pp. 3495–3511, 2022.
- [22] D. ShunmughamVanaja and A. A. Stonier, “A novel PV fed asymmetric multilevel inverter with reduced THD for a grid-connected system,” *International Transactions Electrical Energy Systems*, vol. 30, no. 4, 2020.
- [23] G. Peter, A. Sherine, and S. B. Iderus, “Enhanced Z-source inverter-based voltage frequency generator to conduct induced over voltage test on power transformers,” *IJPELEC*, vol. 12, no. 4, p. 493, 2020.
- [24] G. Peter, K. Praghash, A. Sherine, and V. Ganji, “A combined PWM and AEM-based AC voltage controller for resistive loads,” *Mathematical Problems in Engineering*, vol. 2022, Article ID 9246050, 11 pages, 2022.